Single-Electron transport in Focused Electron Beam Induced Deposition (FEBID)-based nanostructures

Dissertation
zur Erlangung des Doktorgrades
der Naturwissenschaften

vorgelegt beim Fachbereich Physik
der Johann Wolfgang Goethe - Universität
in Frankfurt am Main

von

Giorgia Di Prima
aus Messina, Italien

Frankfurt am Main 2022
(D 30)

Vom Fachbreich Physik der
Johann Wolfgang Goethe - Universität zur Dissertation angenommen
Dekan: Prof. Dr. Harald Appelshäuser

Gutachter: Prof. Dr. Michael Huth
Gutachter: Prof. Dr. Jens Müller
Datum der Disputation: _____

To you

Contents

Abbreviations

AC	Alternating Current
AFM	Atomic Force Microscopy
AM-AFM	Amplitude Modulation mode of Atomic Force Microscopy
AS-ALD	Area-Selective Atomic Layer Deposition
BIPS	Beam Induced Polishing and Sputtering
BSE	BackScattered Electrons
c-VRH	correlated Variable-Range Hopping
CCD	Charge-Coupled Device
CVD	Chemical Vapour Deposition
DC	Direct Current
DCM	DiChloroMethane
DI	DeIonized
EBL	Electron Beam Lithography
EDX	Energy Dispersive X-ray spectroscopy
ES-VRH	Efros-Shklovskii Variable-Range Hopping
ESD	ElectroStatic Discharge
FDM	Fused Deposition Modeling
FEBID	Focused Electron Beam Induced Deposition
FEG	Field Emission Gun
FIB	Focused Ion Beam
FSE	Forward Scattered Electrons
GA	Genetic Algorithm
GIS	Gas Injection System
HLN	Hikami-Larkin-Nagaoka
HMDS	HexaMethylDiSilazane
HOMO	Highest Occupied Molecular Orbitals
HV	High Vacuum
IGP	Ion Getter Pump
IVC	Inner Vacuum Chamber
LD	Laser Diode
LMIS	Liquid Metal Ion Source
LUMO	Lowest Unoccupied Molecular Orbitals
MTL	Mass Transport Limited
NDP	Nano Device Prototyping
NMT	Nanomanipulator
NNH	Nearest-Neighbour Hopping
NP	Nanoparticles

NTP	Normal Temperature and Pressure
PE	Primary Electrons
PEG	Poly(Ethylene Glycol)
PET	PolyEthylene Terephthalate
PI	Proportion-Integration
PSPD	Position Sensitive Photo Diode
PVD	Physical Vapour Deposition
QPC	Quantum Point Contact
RMS	Root-Mean-Square
rpm	rotations per minute
RRL	Reaction Rate Limited
RRR	Residual Resistance Ratio
SA	Self-Assembly
SE	Secondary Electrons
SEB	Single-Electron Box
SEM	Scanning Electron Microscopy
SET	Single-Electron Transistor
TCR	Temperature Coefficients of Resistance
TEM	Transmission Electron Microscope
UHV	Ultra High Vacuum
UVL	UltraViolet-Lithography
vdW	van der Waals
VRH	Variable-Range Hopping
VTI	Variable Temperature Insert
WKB	Wentzel-Kramers-Brillouin

Introduction

Advances in electronics miniaturization are solving technology challenges across markets by reducing loss of performance, increasing signal speed and allowing dense integration. In this scenario, the aim of controlling matter even to the atomic-scale has risen a stronger motive for advanced nanofabrication techniques, sowing the seed for nanotechnology. This new field of research and innovation has been considered to have a very high potential in delivering energy efficient, smaller and lighter products at significantly reduced costs.

In the words of Richard Smalley, Nobel laurate in chemistry, who in June 1999 commented: *"The impact of nanotechnology on the health, wealth, and lives of people, will be at least the equivalent of the combined influences of microelectronics, medical imaging, computer-aided engineering and man-made polymers developed in this century"* [1]. Such extraordinary impact on so many research fields is connected to the fact that at these small scales, the macroscopic forces of physics and chemistry have other relevance. By engineering and manipulating conventional materials, the obtained nanomaterials exhibit novel unique features that can be very different from their macroscale counterparts, such as increased strength, durability, conductivity, distinctive plasmonic properties and chemical resistance. Moreover, quantum phenomena arising from the size reduction of the basic elements exhibit characteristic effects, which are of special interest for fundamental research and future applications. Eventually, further advances will allow novel functions that were originally unforeseen by conventional techniques.

It follows that, in the last decades, increased research engagement has been dedicated to the development of manufacturing processes which allow for precise manipulation of matter, compatibility with other device components and integration of the new nano-elements, such as fullerenes, nanotubes, nanoparticles and graphene in microdevices for the manifold application portfolio of miniaturized electronic elements.

Most of the technical methods used to manufacture nano- and microstructures are based on the generation of duplicable patterns in a complex planar fashion. In particular, nanotransfer printing and lithography techniques, which involve several process steps, allow stable and reproducible nanofabrication. For this reason, they have been largely

applied in semiconductor industry for highly-resolved chip production. However, the use of chemicals and numerous steps involving radiation exposure and different temperature baking treatments make these techniques not suitable to be applied in conjunction with sensitive materials or for fast prototyping purposes. Consequently, direct-writing techniques have attracted more attention in the last years. In particular, Focused Electron Beam Induced Deposition (FEBID) is considered for nanopatterning applications because of its direct-write character, bottom-up approach, large variety of applicable materials, high-resolution capabilities (sub 10 nm lateral resolution) and minimal surface damage [2]. By scanning the electron beam on any kind of material, 2D and 3D nanostructures can be fabricated by the dissociation of the molecules of a gaseous precursor in the focal point of the electron beam. A solid deposit forms on the beam target point. This technique resembles the same bottom-up approach of the mainstream Fused Deposition Modeling (FDM) 3D printing machines in the macroscale. In the same way, very highly-resolved and complex shapes with excellent 2D and 3D design correspondence can be achieved on the nanoscale.

With its direct character, the technique can be considered as an alternative to Electron Beam Lithography (EBL) for fabrication of devices involving sensitive nanomaterials and as a convenient technique for Nano Device Prototyping (NDP) of complex shaped structures.

However, as a particular type of electron induced local Chemical Vapour Deposition (CVD), FEBID offers a wide spectrum of material deposition possibilities using numerous precursors, which are mostly organometallic compounds. It follows that FEBID suffers from the inclusion of organic fragments in the deposits as a consequence of the incomplete dissociation of the used organometallic precursors. The presence of carbon contamination negatively impacts the electronic and optical properties of the deposited material. Consequently, the low metal content of the deposits and a relative low throughput reduce FEBID applicability.

As an important example, big effort has been devoted by the FEBID research community in the development of approaches to improve the electrical conductivity of FEBID structures obtained by the use of one of the most employed FEBID precursors: Trimethyl(methylcyclopentadienyl)platinum(IV), $Me_3PtCpMe$(IV). Besides FEBID, this precursor has been largely employed in Atomic Layer Deposition (ALD) in combination with O_2 because of its high vapor pressure, good stability and simple molecule structure. These characteristics combined with the thermal energy contribution and the catalytic effect of platinum for oxygen atoms, make the release of the organic compounds from the molecule quite straightforward in order to accomplish pure Pt deposition.

In the case of Pt-C FEBID deposits, it has been similarly demonstrated that by employing O_2 or H_2O as oxidising gases, either by local gas injection or as background

gas, in combination with electron irradiation or heating, the complete removal of carbonaceous fragments in the deposit can be accomplished [3–5].
Such catalytic purified Pt FEBID nanostructures can be used directly for contacting applications or serve as seed layers for pure Pt thin film growth. A highly versatile technique consists of using $Me_3PtCpMe$ and O_2 as reactive gases for the Pt Area-Selective Atomic Layer Deposition (AS-ALD) process on purified Pt FEBID deposits. In this way, subnanometric layers of pure Pt can be grown on defined structures by alternating reactant exposures on the heated substrate. The technique has maskless design machining capability of arbitrary complex structures, spatial resolution in the nanoscale and easy integration capacity. In this work, a novel approach towards *in situ* monitoring of AS-ALD of metals, in particular platinum, using the electrical conductance of the growing layer as new probed quantity is presented [6].

The aim of this work is to investigate the FEBID capability in the nanofabrication of very sensitive devices which require high-resolution and control by the use of suitable materials. In this scenario, single-electron devices, as for example gold Nanoparticles (NP) arrays and the Single-Electron Transistor (SET), have appeared as suitable candidates to test the fabrication and material performances of FEBID-based devices. Such interest can be traced back to the fact that in the last decades single-electron devices have been considered as replacement for silicon transistors on account of their ultra-low-power range with a high level of device integration [7–12]. Moreover, the appealing fabrication challenge lies in the highly controlled definition of the metallic islands with a diameter far below 100 nm and in the fine tuning of the tunnel couplings among the islands and the drain/source leads. However, it is important to note that with minimum feature sizes less than 10 nm, increasingly challenging fabrication barriers concerning the island and the tunnel junctions have to be taken into account.
By using catalytically purified Pt FEBID deposits, electrical contacting of UltraViolet (UV)-lithographically defined pads to Au-NP arrays has been achieved in order to investigate the single-electron transport properties of self-assembled multibody systems. NP arrays contacted between two electrodes behave as networks of Coulomb blockade-type tunnel junctions with a distribution of threshold energies due to the network of single nanoparticles forming the domain. However, Pt co-deposit is a consequence of the FEBID technique itself, giving the formation of trapped charges around the nanoparticles promoting cotunneling effects that disturb the single-electron transport through the whole array. For this reason, a different type of approach has been used for the fabrication of SET devices.
The method proposed in this work consists of using FEBID for the island definition between pre-fabricated SET electrode structures. The Pt-C island itself is a system of Pt-grains (2 - 3 nm in size) embedded in a amorphous-carbon matrix [13]. The island's

nano-granular structure allows, in conjunction with *in situ* tuning of the inter-grain tunnel coupling by post-growth electron irradiation, to study the effect of the island's peculiar electronic properties (driven by its granularity composition) on the SET device performance. In this way, it is possible to understand the cooperative physical phenomena that take place when the interdot coupling between neighboring particles is tuned together with the degree of long-range Coulomb interactions. A localized Ar^+-etching has been necessary in order to remove the Pt-C co-deposit halo in proximity of the island and avoid transport disturbance factors. The quality of the devices and the reliability of the nanofabrication methods have been directly evaluated through the observation of the characteristic features of single-electron transport as Coulomb blockade, diamonds and oscillations at very low-temperatures (down to 0.3 K) [14].

This work is structured as follows: Chapter 1 provides the basis for the theoretical understanding of single-electron transport in granular metals. In this way, the reader will become familiar with concepts and terms defining the single-electron transport in granular metal systems addressed in this work, such as nanoparticle arrays (Section 1.3) and Pt-C FEBID nanostructures (Section 1.4). This theoretical introduction serves as the basis to comprehend the origin of global transport properties arising from local charging-mediated tunneling. The described theoretical background is preparatory to the interpretation of the experimental results obtained by the electrical characterization of the samples reported in Chapter 3 for the nanoparticle arrays and in Chapter 4 for the SET devices. Special focus is set at the end of Section 1.4 to describe the particular case of single-electron transport in the SET and its characteristic electrical features.

The second chapter provides an overview of methods and process techniques used for the fabrication and analysis of micro- and nanostructures. Initially, in Section 2.1, the manufacturing process of the macroscopic chip on which the nanostructures are fabricated is described. The chip serves as electrical interface to perform the electrical characterization of the nanostructures. Afterwards, in Section 2.2, the main technical instruments used for the fabrication and analysis of the nanostructures are reported. The methods include Scanning Electron Microscopy (SEM), Focused Ion Beam (FIB) and further related indispensable techniques for the topographic and compositional analysis of the nanostructures, such as Atomic Force Microscopy (AFM) and Energy Dispersive X-ray spectroscopy (EDX).
In Section 2.3, the nanofabrication and optimization methods which have been used to obtain the experimental devices presented in this work are outlined. In Subsection 2.3.1, the basic principle of the FEBID technique employed for the fabrication of Pt-C deposits from the precursor $Me_3PtCpMe$ is given. Special emphasis is given to the description of the relevant interaction mechanisms of the electrons with the precursor molecules and

the substrate. Moreover, the main drawbacks of the technique, such as co-deposit formation in proximity to the defined pattern and low metal content of the obtained deposit, are outlined. Accordingly, the curing post-growth treatments of Pt-C FEBID deposits used in this work to increase the deposits electrical conductivity are described.
One technique is the electrical irradiation of the Pt-C FEBID deposits. The method fine tunes the inter-grain coupling strength allowing to adjust the electrical conductivity from an insulating to a metallic state [15]. Such optimization has been used in this work to increase the conductivity of Pt-C FEBID dots used as islands for SET fabrication. This application is described in detail in Chapter 4.
The second technique is a catalytic purification of the Pt-C FEBID structures [4]. This purification technique uses the catalytic activity of Pt in combination with O_2 exposure and high substrate temperature to oxidise and remove the carbonaceous component of the deposits. Purified Pt FEBID deposits have been used afterwards as electrical contacts in nanoelectronics applications, such as for contacting Au-NP arrays. This application is described in detail in Chapter 3.
However, the catalytic purified Pt FEBID structures present a highly porous structure due to the massive loss of the carbonaceous matrix from the FEBID deposited material. To strengthen the contacts and promote selective growth of Pt on highly-resolved nanometric features, purified Pt FEBID deposits have been used as seed layer for maskless Pt AS-ALD inside the chamber of the dual-beam FIB-SEM. This method and the relative electrical conductance based monitoring technique developed in this work are outlined in Subsection 2.3.2.
The last reported nanofabrication techniques are nanoparticles drop casting and ion etching techniques. Nanoparticles drop casting has been used in order to obtain self-assembled nanoparticle arrays that have been later contacted with the purified Pt FEBID deposits. Focused Ga^+-beam milling and localized Ar^+-etching have been used in order to design and polish the SET devices. The fabrication and characterization description of these samples can be found in Chapter 4.
Finally, Chapter 2 ends with the electrical and magneto-transport characterization measurements description (Section 2.4). Such measurements have allowed not only process monitoring during the nanofabrication but, additionally, they delivered an important feedback of the quality of the device nanofabrication providing the observation of single-electric transport and in general the electrical characterization of the obtained devices. Such characterization measurements have been conducted in an ^{3}He-cryostat. The description of the cryostat setup is given in Subsection 2.4.1.

In Chapter 3 the first experimental single-electron-based devices are described. Au-NP arrays consist of monolayers of thiol-PEG ligated gold nanoparticles (diameter = 12.5 nm), synthesized and deposited by drop-casting from solution onto Si/SiO_2

substrates in close proximity to UV-lithographically defined gold electrodes. The Au-NP arrange in triangular lattices with domain sizes up to 1 μm. In particular, in order to contact the gold electrodes to the NP arrays, Pt purified FEBID deposits have been used as contact elongations. In the weak-coupling framework, single electron charging becomes significant, leading to Coulomb blockade behavior and the localization of electrons on individual particles. The overall global transport properties arising from local charging-mediated tunneling have been then investigated with electrical transport measurements at low-temperature. Unfortunately, Pt co-deposit is a consequence of the FEBID technique itself giving the formation of trapped charges around the nanoparticles promoting cotunneling effects and disorder compromising single-electron transport among the nanoparticles. For this reason, a second approach has been employed in order to succeed with the demanding fabrication of SET.

The new approach and the operation results of the obtained SET are described in Chapter 4. The method consists of using four pre-patterned contacts in a cross configuration and mill them with a Focused Ga^+-Ion Beam in order to obtain a SET device geometry with two gate electrodes. Afterwards, a Pt-C island is placed between the milled electrodes using FEBID and subjected to a post-growth irradiation step. The co-deposit is later etched away by using a localized Ar^+-milling in a pulsed fashion.
By means of the electron irradiation of the island material, the tunnel coupling strength inside the island and between the leads can be finely tuned and stable SET operation is accomplished. Moreover, depending on the irradiation dose, different operation regimes of the SET can be achieved.

Chapter 1

Theoretical background

The electrical properties of NP arrays (Chapter 3) and Pt-C FEBID material used as SET island (Chapter 4) are based on the concept of single-electron transport in granular metals.
In this chapter a theoretical description of the single-electron transport within granular metals is given to assist the following interpretation of the electrical characterization of the granular metal systems fabricated in this work.
In the first section, a general introduction on single-electron transport in granular metals is provided (Section 1.2). Afterwards, the single-electron transport taking place in a NP lattice (Section1.3) and in a Pt-C FEBID deposit is described (Section 1.4). The chapter ends with an accurate theoretical description of a single-electron device - Single-Electron Transistor (SET) - and its operating principle (Section 1.5.2).

1.1 Granular metals

Granular conductors consist of close-packed granules (nanocrystals) in an insulating matrix. Whereas the metal particles range their size usually from a few to several hundred nanometers, metallic granules are often considered as artificial atoms with programmable electronic properties [16]. Thereby, granular metals form a new class of materials combining the individual and collective properties of coupled nanocrystals. More specifically, the electrical transport is based on the electron tunneling among neighbour grains through the dielectric medium. Detailed information about the tunneling mechanism theory can be found in Appendix B.
Granular metals are particularly interesting to study and be used in technological applications since their electronic properties are the results of electron confinement and tunable cooperative effects of disorder. By varying the size and shape of the grains, quantum confinement effects can be modified. Because of their versatile electrical

properties, granular metals have been extensively used in a broad spectrum of nanotechnological applications and in fundamental studies of disordered solids [16].
Over the years, several fabrication techniques have been used to fabricate granular metals, such as co-sputtering of metals and insulators and partial metal ALD on insulator substrates [17]. A widely employed technique, that gained increasing interest in the last decade and guarantees a high level of order and homogeneity in the grain size, consists in the fabrication of granular conductors through self-assembled colloidal nanocrystals [18, 19]. In this type of systems, metallic nanoparticles are separated by organic ligands serving as dielectric medium.
Details about the single-electron transport in this type of systems are given in the following Section (1.3). In particular, self-assembled nanoparticle arrays have been investigated in conjunction with FEBID-based electrodes elongations in Chapter 3.
Apart from that, Huth and collaborators [2, 20] explain that also FEBID materials originated from organometallic precursors as, for example, from the $C_5H_4CH_3Pt(CH_3)_3$ precursor (more information about this precursor and its use in FEBID can be found in Subsection 2.3.1.2) are behaving as granular metals with distinct electrical features. For instance, their electrical behavior can be well tuned through a post-growth electron irradiation treatment [15, 21]. In Section 1.4, FEBID materials as granular metal systems and their electrical properties are described in detail.

1.2 Single electron transport in granular metals

The electronic transport in granular metals is governed by the interplay between the diffusive intra-grain electron motion and the inter-grain tunneling. In addition, the grains involved in the electron transport are subjected to a sequential charging induced by the electron tunneling. The energy model of this type of system can be described with the Hamiltonian:

$$H = H_0 + H_t + H_c\,. \tag{1.1}$$

where H_0 includes the intra-grain kinetic and potential energies, H_t describes the tunneling between grains and H_c comprises the charging energy. A detailed description of this model can be found in the work of Likharev *et al.* [7] and Beloborodov *et al.* [22].
The interaction of disorder, confinement effects and fluctuations are described by different quantities e. g. the inter-granular tunnel conductance between the grains g, the single-grain Coulomb charging energy E_c, the mean level spacing of electronic levels within a single grain δ, and the mean electronic lifetime within the grain $\tau_0 = \hbar/g\delta$ (also called *relaxation time*).
The charging energy is equal to the change in energy of the grain when one electron is added to the grain or removed from the grain. This characteristic energy has a crucial

role for the transport properties in the insulating regime when the electric charge in the single grain is quantized and the electrons are localized in the grain.
The capacitance of a grain can be realistically approximated with that of a sphere:

$$C_0 = 4\pi\epsilon_0\epsilon_r a \tag{1.2}$$

where ϵ_0 and ϵ_r are the permittivity of vacuum and the dielectric constant, respectively and a is the radius. Accordingly, the charging energy is described by the equation

$$E_C = \frac{e^2}{2C_0} = \frac{e^2}{8\pi\epsilon_0\epsilon_r a} \tag{1.3}$$

where e is the electron charge.
To give an idea about the energy scale we are dealing with, it is important to point out that the charging energy of grains with a diameter in the few 10 nm range is in the several meV to 10 meV range and will increase to above 50 meV as soon as the grain diameter drops to below a few nm.
Single-electron charging effects can take place in single junctions (or in an array of junctions) if the tunnel conductance g, is smaller than the conductance quantum

$$G_0 = 2\,e^2/h \approx (13k\Omega)^{-1} \tag{1.4}$$

where h is the Planck constant. This condition ensures that charges can be transported through the junctions by tunneling and the electron is sufficiently localized in the grain. In this way, charge states of the junction are well-defined. It is worth notice that, g is dimensionless and expressed by normalization to the conductance quantum G_0 :

$$g = \frac{G}{(2e^2/h)} \tag{1.5}$$

where G is the average tunnel conductance between neighbouring grains.
By approximating a tunnel junction by a resistor and a capacitor in parallel, we can express the energy-time uncertainty principle where the (dis)charging time due to the tunneling $\tau \approx R_t C$ (where R_t is the ohmic resistance and C is the capacitance of the tunnel junction) has to be sufficiently long allowing the corresponding uncertainty in energy being smaller than the charging energy E_C:

$$\Delta E\,\tau \sim \frac{e^2}{C} R_t C = e^2 R_t \gg h\,. \tag{1.6}$$

The change in energy stored in the electrostatic field between the metal particle and the environment associated with a tunnel event is given by

$$\delta E = E_{fin} - E_{ini} = \frac{(Q_0 + e)^2}{2C} - \frac{Q_0^2}{2C} = \frac{e(Q_0 + e/2)}{C} \,. \tag{1.7}$$

where E_{fin} and E_{ini} are the final and initial energy, respectively. Q_0 is the initial charge present in the island.
The tunnel event occurs when it is energetically favorable and the condition $\Delta E < 0$ has to be satisfied.
Remembering that $e < 0$, it follows

$$Q_0 > -\frac{e}{2} \,\text{and}\, V > -\frac{e}{2C} \tag{1.8}$$

where V is the electric potential.
Repeating for the opposite polarity, it can be found that in order for the tunnel event to occur, the following condition has to be satisfied:

$$-\frac{e}{2C} < V < \frac{e}{2C} \,. \tag{1.9}$$

A tunneling current will only flow when a sufficiently large voltage ($\mid V \mid > \mid e \mid /2C$) exists across the metal particle and the next metal object. This effect is called *Coulomb blockade* and it shows a distinctive feature in the current-voltage (I-V) characteristic. The voltage value, for which a tunnel current is established, is called *threshold voltage* V_t.
In Figure 1.1, an illustrative Coulomb blockade example is depicted. No current flows through the junction inside the blockade region ($-V_t : V_t$). The particular case of the Coulomb blockade effect for a single metal island between two tunnel junctions is described in the Single-Electron Transistor theory in Subsection 1.5.2.

Temperature plays an important role in the observation of Coulomb blockade phenomena by providing energy to the system. In this way, the tunnel energy gap is easier to overcome. It follows that, in order to observe the Coulomb blockade, the charging energy has to be larger than the thermal energy:

$$\frac{e^2}{2C} \gg \frac{1}{2} k_B T \tag{1.10}$$

where k_B is the Boltzmann constant and T is the system temperature.
For example, for a nanoscale sphere capacitor with its radius about 12 nm (like the Au-NP used in this work), a capacitance of 2.712 aF and a charging energy of $E_C = 29$ meV has been calculated (Section 3). Considering that thermal energy at room temperature is nearly 26 meV, the condition $E_C \gtrsim 7 k_B T$ should be roughly satisfied in order to observe the Coulomb blockade effect. This means that for $T \lesssim 43$ K single-electron transport

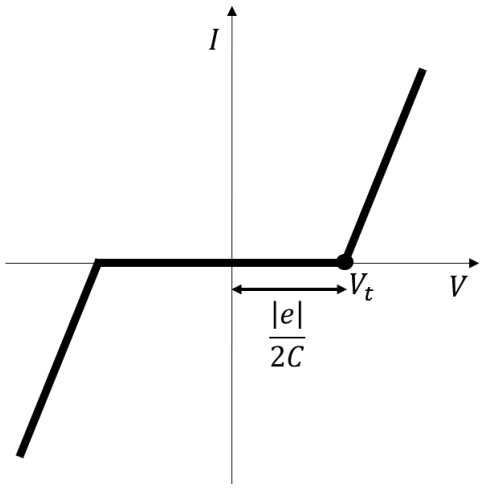

Figure 1.1: Schematic picture of the Coulomb blockade in an I-V characteristic. The tunnel current starts to flow as soon as $|\ V\ | > |\ V_t\ |$.

is expected to take place through a single nanoparticle. For this reason, in order to investigate the single-electron transport properties of granular metals the use of a cryo-system is necessary. A description of the ^{3}He-cryostat used for the electrical investigations conducted in this work can be found in Subsection 2.4.1.

The semiclassical approach to describe the Coulomb blockade regime as demonstration of the electric charge quantization is known as *orthodox theory* [7]. In this theory, a kinetic equation is derived for the distribution function describing the charge state of the junctions' system. The orthodox theory has proven to be very valuable since the transport properties of metallic tunnel junctions, where size quantization effects are negligible, have been explained in a well-acknowledged semiclassical fashion [23–26].

Additionally to the orthodox theory, in the theory of electronic transport in granular metals elaborated by Beloborodov and collaborators [16], assumptions on the system energy conditions have been given. For example, the mean level spacing of electronic levels at the Fermi energy in a single grain δ is the smallest energy scale and the condition $E_c > k_B T >> \delta$ is always satisfied. This can be explained by the fact that δ is inversely proportional to the volume of the grain:

$$\delta = (D(E_F)V)^{-1} \tag{1.11}$$

where V is the grain volume and $D(E_F)$ is the density of states at the Fermi energy. Whereas E_c is inversely proportional to the radius. For this reason and considering the high density of energy states in metals, the energy discreteness of the electronic levels within a single grain due to electron confinement and the relative quantum size effects can be neglected except for extremely low-temperatures.

Finally, the relaxation time (τ_0) of the electron inside the grain is particularly important

since, through the characteristic energy $\Gamma = \hbar\tau_0^{-1}$, τ_0 is related to the tunnel conductance g and δ by the relation: $\Gamma = g\delta$. The energy Γ can be considered as the 'smearing' of the energy levels inside the grain as well as the inverse of the electron escaping rate [16].

The electronic properties of granular systems can be tuned by modifying the strength of electron tunnel coupling between conductive neighbour grains *via* microscopic parameters. This is done by changing the arrangement of the grains, the amount of them and the dielectric material in which they are embedded. In this way, granular metal systems can behave as relatively good metals for $g > g_c = (1/2\pi z)\ln E_c/\delta$ (with z coordination number, which is the number of neighbours for a site on the array) or insulators when $g < g_c$. g_c is the critical coupling strength and $g_c \approx 1$.

From the definition of a granular metal, it follows that $g < g_0$, where g_0 is the intra-grain conductance that is always larger than 1 ($g_0 >> 1$). g_0 originates from the diffusive motion of electrons inside the metallic grain and the scattering on impurities and irregular boundaries.

It is noteworty to mention that the fine matrix tunability permit to study in detail the metal-insulator transition for this type of new class of materials that exhibit a wide spectrum of transport behaviors ranging from the hopping conductivity to those typical of a Fermi liquid. A graphical description of the transport behavior spectrum is reported as a phase diagram in Figure 1.2 [22, 23].

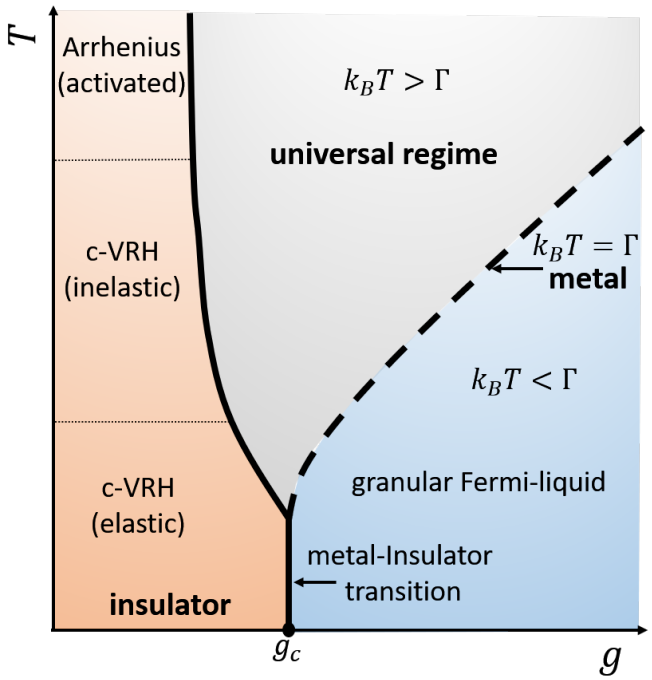

Figure 1.2: Schematic phase diagram of the transport behavior for granular metals. Readapted from [20, 22].

In the graph, a crossover between three different phases is taking place at $g = g_c$. The conductivity can show either insulating behavior for $g << g_c$, or a strong tunnel coupling limit at higher temperatures. The latter becomes a dimensionality dependent granular Fermi liquid behavior at low-temperatures for $g >> g_c$. The different regimes cross each other in a so called *metal-insulator transition* at $g = g_c$. The three distinct phases displayed in the diagram are:

- For $k_B T < \Gamma$, the Fermi-liquid phase of homogeneous disordered metals.
- For $k_B T > \Gamma$, the high-temperature phase governed by the local single-grain physics.
- For $g < g_c$, the insulating phase characterized by the activation behavior of the conductivity, inelastic cotunneling (at higher temperatures) and elastic cotunneling (at lower temperatures).

It is possible to distinguish three types of disorder in granular metals [27]:

- global structural disorder in the array topology,
- local structural disorder in the inter-particle coupling and
- local charge disorder due to random, immobile charges - *trapped charges* - in the dielectric material where they are embedded.

The effect of disorder and irregularities in the grain positions and in the tunnel coupling strength is different whether the system is a metal or an insulator. In a conducting system where the coupling between grains is sufficiently strong, these effects are negligible. In contrast, the effects are crucial in an insulator system where the tunnel coupling is low.

1.2.1 Weak-coupling regime

In the weak-coupling transport regime, the single-grain Coulomb charging energy E_c has a key role. The transport is related to the classical single-electron transport effect taking place e. g. in a Single-Electron Box (SEB) between the electrons' reservoir and a metallic grain connected to it (details about the SEB are given in the Subsection 1.5.1). With the presence of the tunnel junctions, the well-known phenomenon of the Coulomb blockade occurs and it produces a decrease or the strong vanishing of electrical conductance for biases under a certain threshold [28]. A schematic representation of the blockade feature in the current-voltage characteristic that is relative to the single-electron transport through the tunnel junction has been given in Figure 1.1.
In the case of arrays of weakly coupled grains, where $g << 1$, the insulating regime is established and the electrical behavior is well described by the orthodox theory predicting the exponential suppression of the conductance at low-temperatures since

electrons in the grains are quantized and the transport is mediated by each electron hopping from grain to grain. The orthodox theory associates a periodic granular array in the regime of weak-grain-coupling to an exemplary intrinsic Mott semiconductor [29]. According to this model, carrier charges are localized on dopant sites i with energies E_i. The current can be generated when the carriers acquire energy thermally and they are hopping to another site with energy gap $\Delta E_{ij} = E_j - E_i$. Hopping to the nearest neighbour site is not always the most favorable process, since there is a large probability of finding sites at larger distances, r_{ij}, where the energy gap ΔE_{ij} is lower. The cooperation of these two (next-neighbour and hopping) tunnel processes leads to a fractional exponent dependence as it is described in Equation 1.14. Such a transport mechanism is known as Variable-Range Hopping (VRH). However, due to the electrostatic energy cost involved in the hopping transport, the theory predicts a hard energy gap Δ_M (Mott gap) in the excitation spectrum. The result is a next-neighbour like tunneling transport described by an Arrhenius-like conductivity (Nearest-Neighbour Hopping (NNH)):

$$\sigma(T) = \sigma_0 \exp\left[-\frac{\Delta_M}{k_B T}\right], \text{ for } T << \Delta_M \tag{1.12}$$

where σ_0 is the high-temperature conductivity and the hopping length is given by the distance between nearest neighbors. The activated charge transport of the Arrhenius type eventually results in an insulating state at low-temperatures due to the Coulomb blockade effect for highly ordered arrays. In this type of systems, the Coulomb interaction energy ΔE_{ij}, associated with electron hopping from a filled site i ($E_i < E_F$) to an empty site j ($E_j > E_F$) increases following the equation

$$\Delta E_{ij} = E_j - E_i - \frac{e^2}{4\pi\epsilon_r\epsilon_0 r_{ij}} > 0 \tag{1.13}$$

where the last term is the Coulomb attraction of an electron-hole pair located at sites j and i and ΔE_{ij} can be seen as the net energy change associated with the charge transfer process. The condition $\Delta E_{ij} > 0$ requires that the two sites i and j are separated by a distance $r_{ij} > \frac{e^2}{4\pi\epsilon_r\epsilon_0\Delta E_{ij}}$. Therefore, there is a hard Coulomb gap (or Hubbard energy gap) at the Fermi level, making the density of states equal to zero at the Fermi level. However, it is important to point out that the activation behavior is usually not observed in real granular metals, which present structural and potential disorder caused by background charges. The experimentally most observed conductivity follows the law

$$\sigma(T) = \sigma_0 \exp\left[-\left(\frac{T_0^{ES}}{T}\right)^{1/2}\right] \tag{1.14}$$

which resembles the Efros-Shklovskii Variable-Range Hopping (ES-VRH) law derived for doped semiconductors and strong correlations [30]. In the equation

$$T_0^{ES} = \beta \frac{e^2}{\kappa \xi k_B} \tag{1.15}$$

where $\beta = 2.8$ (numerical coefficient), $\kappa = 4\pi\epsilon_0\epsilon_r$ is the tunneling decay dielectric constant and ξ is the decay length of localized electron states. The hopping distance r_{hop} and the hopping energy gap ΔW_{hop} follow as

$$r_{hop} = \frac{1}{4}\kappa \left(\frac{T_0^{ES}}{T} \right)^{1/2} ; \tag{1.16}$$

$$\Delta W_{hop} = \frac{k_B}{2} (T_0^{ES} T)^{1/2} . \tag{1.17}$$

If both E_i and E_j are close to the Fermi level, then ΔE_{ij} is small and r_{ij} is large. In other words, the concentration of sites close to E_F should be very low and in particular has to vanish at the Fermi level [31]. The reduction of density of states near the Fermi level results in a 'soft' Coulomb gap. The ES-model only applies when hopping occurs between sites inside the soft Coulomb gap. Outside of the Coulomb gap, the density of states is constant, and the conductivity is described by the Mott model ($\sigma \propto \exp -T^{-1/4}$). The critical temperature T_C, for a transition from ES- to Mott-VRH, is expressed by the equation

$$T_C = 4\Delta W_{hop}^2 / k_B^2 T_0 . \tag{1.18}$$

For many years scientists could not explain why the temperature dependence of granular metals should follow a stretched exponential behavior. Later on, Beloborodov *et al.* [16] hypothesized that the cause of the mismatch between theory and observation has to be traced back to the disorder contribution and the charged impurities present in the system. Therefore, fluctuations in size, capacitance and tunnel resistance of individual islands tend to average out the effect of single-charge tunneling. In particular, the observation of the Efros-Shkovloskii behavior in place of the usual Mott-VRH temperature dependence reflects the smearing out of the hard energy gap in the electron spectrum and the establishing of a soft gap resulting from the strong long-range Coulomb correlations [24]. Moreover, the transport described by the Equation 1.14 takes into account higher-order (not restricted to next neighbor) tunneling, the so-called *cotunneling*. This hopping mechanism is therefore also mentioned as correlated Variable-Range Hopping (c-VRH) and was first discussed by Averin and Nazarov [32]. The inclusion of the cotunneling effect in the VRH model has received strong support by experiments on long-range ordered nanocrystal arrays [25, 26].

Cotunneling Cotunneling is the viable conduction channel while Coulomb blockade prevents direct sequential tunneling for $V < V_t$. In other words, the cotunneling effect increases the average distance over which the electrons can hop *via* virtual electrons in a sequence of grains bypassing the Coulomb blockade barrier. Figure 1.3 depicts how the transport takes place *via* several grains in the c-VRH regime. The transport takes place through the grains thanks to a strong reduction of the effective charging energy E_C, as there is no charge accumulation in the grains which take part in the cotunneling sequence. In the lower part of Figure 1.3 (b) an electron energy diagram of the grains describes how the electrons hop elastically and inelastically through virtual electronic states *via* a sequence of grains. The total tunneling distance r^* is larger than the distance between neighboring grains.

Depending on the temperature, the hopping conductivity is dominated by either elastic or inelastic cotunneling processes. The elastic cotunneling dominates at very low applied electric fields ($V < \sqrt{E_c \delta}$) and temperatures, while the inelastic cotunneling occurs for tunneling at high-temperatures or fields ($V > \sqrt{E_c \delta}$).

The elastic cotunneling mechanism transfers the electron charge *via* tunneling through an intermediate virtual state on the metal grain where an electron has the same energy entering and leaving the grain. In the inelastic cotunneling process, the energy of the electrons before and after the tunneling is not maintained producing an electron-hole excitation. Representative sketches of the two cotunneling processes are given in Figure 1.4.

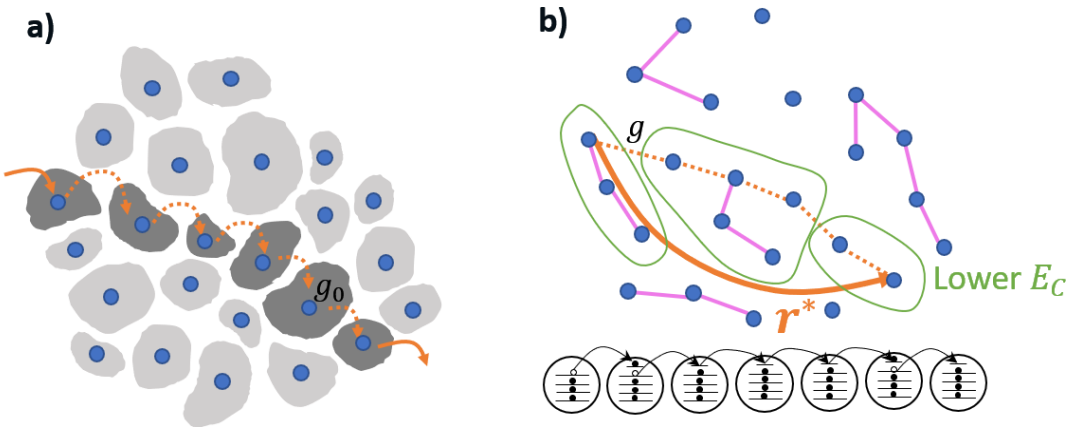

Figure 1.3: a) Schematic of the charge transport in a granular metal in the c-VRH regime through a cotunneling grain sequence. b) A map chart of the energy favorable electron tunneling in the metal grain system reported in (a). In the lower part of the picture, an electron energy diagram of the grains. Adapted from [20, 33].

The localization length (or attenuation length) ξ determines the activation temperature T_0 in Equation 1.14 and it can be still extracted from Equation 1.15.

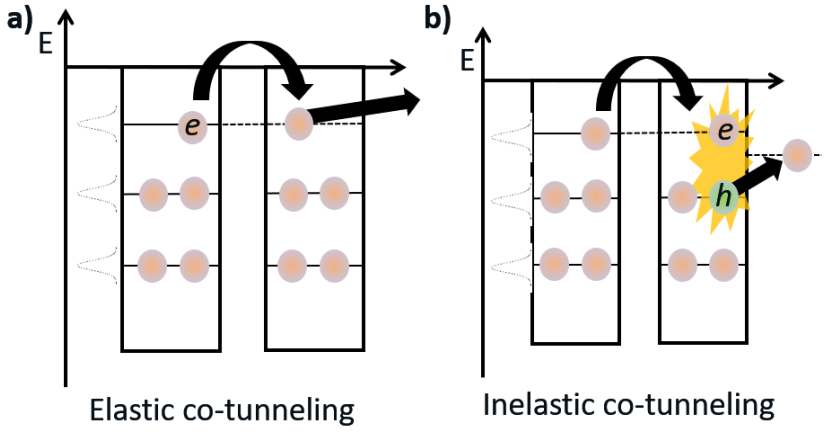

Figure 1.4: Energy diagram representation of the tunneling process between two grains (potential wells) for the cotunneling processes. a) Elastic cotunneling process: the electron tunnels through an intermediate virtual state in the grain leaving the grain with the same energy as it came. b) Inelastic cotunneling process: the electron coming out of the grain has a different energy than the incoming one. An electron-hole excitation is left in the grain which absorbs the energy difference.

ξ has different descriptions for the elastic and the inelastic cotunneling mechanism. In the elastic cotunneling regime, ξ_{el} can be derived by

$$\xi_{el} = \frac{2L}{ln(\bar{E_C}\pi/c_{el}g\delta)} \tag{1.19}$$

with the boundary condition for the c_{el} factor $1/2 \leq c_{el} \leq 1$ [34]. $L = 2a$ is the grain diameter, δ is the energy level spacing in the grain and g is the inter-grain conductance. It is important to notice that ξ and then T_0 do not depend on temperature for elastic cotunneling and $T_0 \propto e^2/\kappa\xi_{el}$.
For the limit of zero applied bias, the cotunneling events span a typical distance, r^*. This distance is given by

$$r^*/d_{c-c} = \left(\frac{E_C}{k_BT}\frac{\xi a}{d_{c-c}^2}\right)^{1/2} \tag{1.20}$$

where d_{c-c} is the particle center-to-center spacing.
For the inelastic cotunelling mechanism ξ_{inel} is given by

$$\xi_{inel} = \frac{2L}{ln(\bar{E}^2/16\pi c_{in}g(k_BT)^2)} \tag{1.21}$$

with the boundary condition $1/4 \leq c_{inel} \leq 1$ [24, 34].
In the inelastic cotunneling condition, ξ_{inel} grows with temperature and $T_0(T) \propto e^2/\kappa\xi_{inel}(T)$.
It is then possible to determine the hopping distance r_{inel}, over which a cotunneling

event takes place:

$$r_{inel} = \sqrt{\frac{E_c}{k_B T}\xi a} = \sqrt{\frac{e^2 \xi}{4\pi\epsilon_0\epsilon_r k_B T}}\,. \tag{1.22}$$

r_{inel} decreases with increasing temperature until reaching the inter-grain distance and the conductivity reduces to the Arrhenius type of temperature dependence.

1.2.2 Strong-coupling regime

If the electrical coupling between the grains is strong ($g \geq g_c$), the electrons propagate easily through the array, the charge quantization is negligible and metallic behavior is clearly observable in the sense that $lim_{T\to 0}\,\sigma(T) > 0$.
For intermediate temperatures ($T \geq k_B\Gamma$) in the strong-coupling regime, the system behaves quite similar to common disordered metals with the effective diffusion coefficient $D_{eff} = \Gamma L^2$ (with L, grain size) depending on the tunnel coupling between the grains. The conductivity can be then expressed by the Einstein relation

$$\sigma = 2e^2 D_{eff}(L^d\delta)^{-1} \tag{1.23}$$

where d is the dimensionality of the granular array and the factor 2 is due to the spin [35]. The diffusion coefficient depends on the Coulomb interactions and two conductivity corrections are found in the distinctive temperature regions $T > \Gamma$ (1) and $T < \Gamma$ (2). The conductivity corrections are expressed in the equation

$$\sigma = \sigma_0\left(1 + \frac{\delta\sigma_1}{\sigma_1} + \frac{\delta\sigma_2}{\sigma_2}\right)\,. \tag{1.24}$$

The first correction is given by

$$\delta\sigma_1 = -\sigma_0 \frac{1}{2\pi d g} \ln\left[\frac{gE_C}{\max(T,\Gamma)}\right] \text{ [23]} \tag{1.25}$$

where $\sigma_0 = 2e^2 g a^{2-d}$ is the classical Drude conductivity of granular metals. The second correction to conductivity varies depending on the system dimensionality:

$$\delta\sigma_2 \approx \begin{cases} \frac{\sigma_0\alpha}{12\pi^2 g}\sqrt{\frac{T}{\Gamma}} & \text{if d = 3,} \\ -\frac{\sigma_0}{4\pi^2 g}\ln\frac{\Gamma}{T} & \text{if d = 2,} \\ -\frac{\sigma_0\beta}{4\pi g}\sqrt{\frac{\Gamma}{T}} & \text{if d = 1} \end{cases} \tag{1.26}$$

where $\alpha \approx 1.83$ and $\beta \approx 3.13$ are constants [36].
At high temperatures ($T > \Gamma$), the correction $\delta\sigma_1$ grows logarithmically with decreasing

temperature.
In the low-temperature regime ($T < \Gamma$), the first correction remains constant and temperature independent. The system resembles a disordered Fermi liquid [36, 37] and the conductivity can be described by the Altshuler-Aronov model with localization type corrections [38].

1.3 Single-Electron transport in a NP array

A nanoparticle (NP) array is a periodical granular assembly of particles identical in size and shape that can exhibit various degrees of order/disorder. In comparison with general granular metals, the disorder is lower and the coupling between the grains could be strongly affected by it.
NP arrays are commonly referred to as 'artifical solids' with tunable electronic, magnetic and optical properties. These properties originate from single-electron charging and quantum confinement energies on the individual particle level. These systems behave as networks of Coulomb-blockade-type tunnel junctions with a distribution of threshold energies [39].
Through the assembling process, the arrangement of the nanoparticles can be modified and, by the use of molecules to cap or cross-link the nanoparticles, the inter-NP spacing can be adjusted in order to establish a precise degree of coupling [31]. The variation of the tunneling process due to capping ligands is described in the following Subsection 1.3.1.
The inter-granular electron coupling can be described *via* the *tunneling matrix* of the system through the definition of mutual capacitances and resistances. By varying the arrangement parameters, the length and type of the capping ligands, NP assemblies can exhibit a broad range of charge transport behaviors from Arrheinius to hopping and even to metallic behavior.
In metal NP arrays, disorder arises even for perfectly ordered particle arrangements due to defects in the host material or in the underlying substrate. These defects produce local traps or barriers of varying strength that surround the particles, resulting in a variation of local nanoparticle potentials. It follows that the local potential variation may directly affect the global threshold voltage. However, the quenched charge disorder is only a perturbative effect and electrons still propagate in an array through a network of junctions with randomly varying threshold voltages. Therefore, the overall array current-voltage characteristic appears to be robust against background charge disorder and exhibit a non-zero effective threshold voltage V_t.
The high order of control and flexibility of this type of systems has led to deeper understanding of fundamental charge transport phenomena, such as Metal-Insulator

Transition (MIT) and VRH. Therefore, NP arrays have been extensively used in numerous applications, such as chemical/biological sensing [40, 41], charge switching devices [42], catalysis [43], etc.

Nanoparticles can be fabricated in the laboratory by physical (e. g., vapor deposition and laser ablation) or chemical methods (e. g., metal-salt reduction, sol-gel process, pyrolysis). In the case of capped nanoparticles, the capping molecules are anchoring on the surface of the NP when they are in contact with a stabilizing solution of reducing agents.
There are several techniques that have been used to prepare NP assemblies on surfaces. The common methods employed in studies involving charge transport through NP assemblies are drop-casting [44], Langmuir methods [45], Cross-Linking Precipitation [46] and stepwise Self-Assembly (SA) [47]. A simple theoretical approach to describe the NP ensamble of highly ordered films of homogeneous size-distributed nanoparticles is taking into account the single NP capacitance and the cross-capacitances to the neighbour nanoparticles [48]. In this model the neighboring nanoparticles are approximated as a conducting continuum separated from the central NP, having radius R, by an insulating shell with a constant separation lenght, s. A sketch of a NP array is shown in Figure 1.5. This representation describes best the NP systems studied in this work in Chapter 3.
The capacitance and the charging energy of the single NP can then be approximated as

$$C = 4\pi\epsilon_0\epsilon_r \left(\frac{1}{R} - \frac{1}{R+s}\right)^{-1} = 4\pi\epsilon_0\epsilon_r \frac{R(R+s)}{s}\,; \tag{1.27}$$

$$E_C = \frac{e^2}{8\pi\epsilon_0\epsilon_r} \frac{s}{R(R+s)}\,. \tag{1.28}$$

Through the separation s and the dielectric constant ϵ_r, the ligands influence directly the charging energy E_C:

$$\begin{cases} \frac{\Delta E_C}{E_C} = -\Delta R \left(\frac{1}{R} - \frac{1}{R+s}\right) \approx -2\frac{\Delta R}{R} & \text{if R} \gg \text{s} \\ \frac{\Delta E_C}{E_C} = -\Delta s \left(\frac{1}{s} - \frac{1}{R+s}\right) = \Delta s \left(\frac{R}{s(R+s)}\right) \approx \frac{\Delta s}{s} & \text{if R} \ll \text{s} \end{cases} \tag{1.29}$$

and, as soon as ϵ_r increases, E_C decreases:

$$\frac{\Delta E_C}{E_C} = -\frac{\Delta\epsilon_r}{\epsilon_r}\,. \tag{1.30}$$

Those theoretical results have been successfully confirmed in experimental studies [49–51]. Moreover, an exponential dependence of the film conductivity from the constant

separation s between the nanoparticles has been observed [52, 53]:

$$\sigma \sim e^{-\beta s} \tag{1.31}$$

where β is the decay constant per unit length. This behavior is consistent with the one reported in single-molecule tunneling studies (Equation 1.51 in Subsection 1.3.2).
However, the electron transport in real NP assemblies is influenced by the different degree of disorder and the most common temperature dependent electron transport behavior exhibited by NP assembly is Arrhenius at sufficiently high-temperatures.
For this reason, local conductances can be expressed as

$$g_{loc} = e^{-\beta s} e^{-E_c/k_B T} . \tag{1.32}$$

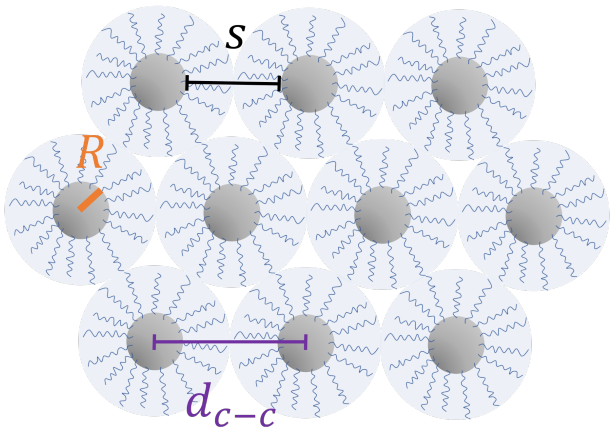

Figure 1.5: Sketch of a triangular NP assembly in which the nanoparticles are separated by capping ligands. The main lattice parameters, such as NP radius R, center-to-center distance d_{c-c} and nanoparticles separation s, are displayed in the figure.

As a result, the assembly can be modeled as a serial and parallel combination of local conductances forming a Maxwell matrix of capacitances C_{ij}, where structural disorder can give rise to variations in s, E_C and g_{loc}. Even minimal variation of these parameters or the presence of impurities can generate background charges that can cause local fields and shift of NP charging energies [51]. The effect of this type of disorder has been investigated with Monte Carlo simulations for dot-arrays [49, 54, 55]. In the simulations' model, the involved capacitances are a constant capacitance C among neighboring dots and between the leads and adjacent dots, and a capacitance C_{gate} between each dot and the back gate. The back gate is placed underneath the hole array. The diagonal elements of the capacitance matrix, C_{ij}, are the sum of all capacitances associated with a nanoparticle. The off-diagonal elements are the mix of the interparticle capacitances. If Q_i is the charge

on any given nanoparticle, the charging energy is

$$E_C = \frac{1}{2}\sum_{i,j}(Q_i + q_i)C_{ij}^{-1}(Q_j + q_j) + V_L Q_L + V_R Q_R + \sum_i V_i^{ext} Q_i \text{ [56]} \tag{1.33}$$

where $Q_{L,R}$ and $V_{L,R}$ are the charges and the voltages of the left and right lead, respectively. The effective offset charge in the nanoparticle q_i gives an indication of the disorder from charged impurities in the neighborhood. The voltage V_i^{ext} is the external voltage applied to lead i. In the model, localized charges in the organic matrix or in the sample substrate can introduce random relative energy shifts of the system electronic levels that can strongly influence the transport properties of the nanoparticle assembly. This effect modifies the potential landscape experienced by the nanoparticles and adds up to the externally applied bias voltage.

By applying the semiclassical picture to large arrays of nanoparticles with a random distribution of local chemical potentials, Middleton and Wingreen [49] explained that a steady-state current flow is only established once there is at least one continuous path connecting one side of the system with the other. The onset of steady-state transport then corresponds to finding the lowest-energy system-spanning path. Using analytical arguments as well as Monte Carlo simulations, the researchers found, that for the limit of negligible thermal energies ($T \to 0$), conduction only occurs beyond a global threshold voltage:

$$V_{t,array} = \alpha N E_C \tag{1.34}$$

where N is the number of nanoparticles spanning the gap between the electrodes and $\alpha = 0.2 - 0.5$ is a pre-factor that depends on dimensionality and array geometry. For example, for triangular lattices $\alpha = 0.227$, for honeycomb lattices $\alpha = 0.3019$ and for square lattices $\alpha = 0.338$ [57]. Hence, the global threshold value scales with distance across the system, but it is independent on the details of the barrier size distribution.

As a result, the scientists found that the steady-state transport current displays a power law scaling in the I-V curve at $T = 0$ for arrays of conducting nanoparticles having a capacitance C small enough to satisfy $e^2/C > k_B T$:

$$I \propto (V/V_t - 1)^{\zeta} \tag{1.35}$$

where V_t is the threshold voltage of the Coulomb blockade and ζ is a scaling parameter that depends on the structure of the array and the distribution of trapped charges.

The power-law dependence on $V - V_t$ emerges as a consequence of the electrons percolation through the array *via* a multitude of branching paths that navigate local Coulomb blockade thresholds and optimize the total charging energy cost.

The Middleton and Wingreen model and its extensions only apply to the large bias limit

and do not consider thermally activated charge excitations. The low bias conductances across 'nonerased' local thresholds are assumed to be exponentially suppressed and, as a result, the global low bias conductance is effectively controlled by the largest threshold along the optimal path. Since this path can avoid high charging energy costs to some extent by branching for 2D close-packed arrays, the relevant activation energy is not the array charging energy but instead $U \approx \upsilon\, eV_t(0)$ where $0.2 \leq \upsilon \leq 0.5$ [55, 57]. Moreover, the sequential percolation of charge through next-neighbor grains leads to the observation of an activated Arrhenius behavior of the conductance $\sigma(T) = \sigma_0 \exp[-U/k_B T]$ [27, 57]. This simplified picture neglects processes that involve charge transfer over distances larger than a single particle (such as in the case of cotunneling) but it is applicable at sufficiently high-temperatures where the near zero-bias conductance follows a simple activated Arrhenius behavior [26]. The simulations have shown that the trapped charges are stationary and they do not change with increasing bias, thus this system property is referred to as *quenched charge distribution* [49].

The numerical simulations predict $\zeta \approx 2$ for finite 2D arrays in the semiclassical picture. The value of ζ found in numerous experiments lies in the range $2.2 < \zeta < 2.8$ [27, 55, 58–60]. The cause of the value discrepancy may depend on the order of disorder. However, at low temperature numerous experiments [24, 26, 32] showed that $\sigma(T)$ crosses over to a stretched exponential form:

$$\sigma(T) \sim \exp(-\sqrt{T_0/T})\,. \tag{1.36}$$

This behavior echoes the VRH behavior described in Section 1.2.1.

Accordingly, it is energetically favorable for the system in case of low temperatures that electron charge transfer occurs *via* virtual states through several neighbour particles by a cooperative tunneling as a single-quantum event. Beloborodov *et al.* [16] explained that the electrostatic disorder, unrelated to grain-size variations but caused by charged defects in the insulating matrix or in the substrate, is responsible for lifting the Coulomb blockade and for the finite density of states near the Fermi energy resulting in the dependence Equation 1.36. Resulting both from the ES-VRH model and the newer approaches based on cotunneling, T_0 is related to a localization length ξ (decay length of the electronic wave function) through

$$T_0 = \frac{2.8e^2}{4\pi\epsilon_r\epsilon_0 k_B \xi} = \frac{2.8E_C R}{k_B \xi}\,. \tag{1.37}$$

This equation is just describing the same behavior explained by Equation 1.15 for metal grains.

It follows that the typical hopping distance r^* in the limit of zero applied bias is

$$r^* = \left(\frac{E_C R\xi}{k_B T}\right)^{1/2} \tag{1.38}$$

as shown in [16]. In terms of the number of tunnel junctions involved j^*, this distance is given by $j^* = r^*/d_{c-c}$, with d_{c-c} center-to-center distance between neighbouring grains [26]. Substituting T_0 from the Equation 1.37 in Equation 1.38, the relation of j^* in terms of T_0 and T is obtained:

$$j^* = r^*/d_{c-c} = \left(\frac{T_0}{2.8T}\right)^{1/2} \frac{\xi}{R}\,. \tag{1.39}$$

It is worth mentioning that in this framework, $j^* \propto \sqrt{T}$.
Nevertheless, NP assemblies can also show weakly coupled behavior with a temperature dependence of the conductance that is not exactly Arrhenius or VRH. These relationships can be summarized by the equation

$$g \approx \exp\left[-\left(\frac{T_0}{T}\right)^{\nu}\right] \tag{1.40}$$

where T_0 is a constant and $0 < \nu < 1$. $\nu = 1$ represents the Arrheinus behavior and $\nu = 1/2$ the ES-VHR.
In the elastic cotunneling scenario, the theory predicts the 'easy' power-law scaling of Equation 1.35. For inelastic cotunneling, the I-V curve follows a power-law in which the exponent depends on the number of junctions involved:

$$I \sim V \left[\frac{g_{loc}}{h/e^2}\right]^{j^*} \left[\frac{(eV)^2 + (k_B T)^2}{E_C^2}\right]^{j^*-1}. \tag{1.41}$$

For temperatures $E_C > \frac{eV}{j^*} > k_B T$ and mesoscopic islands, the equation predicts $I \sim V^{1+2(j^*-1)} = V^{2j^*-1}$. This behavior has also been observed in experiments [25, 32, 61].
Other researchers, such as Elteto and collaborators [57], concentrated their efforts on the extension of the approach of Middleton and Wingreen [49] to finite temperatures and investigated how the temperature modifies the transport in the metal arrays. This model is called *percolation theory*.
The scientists estimate in their work how many small barriers, overcome by temperature, have percolated across the system. In this way, an upper limit is established on the global threshold as a function of temperature. The percolation theory could explain the results of experimental studies reporting that V_t decreases linearly with increasing temperature [55, 62, 63].
In the model, a sequential fraction of junctions $p(T)$, due to thermal rising, can overcome their junction charging energy and behave as ohmic elements. Hence, $p(T)$ is the fraction

of junctions that has been effectively linearized and it is expressed by the equation

$$p(T) = 2 \int_0 b k_B T P(\Delta E)\, d\Delta E \tag{1.42}$$

where $b = 2.4$ is a coefficient calculated by the probability of occupied states below and of occupied states above the Fermi level in each nanoparticle and $P(\Delta E)$ is the probability density. In this way, increasing temperature activates more and more transport channels. At a certain temperature T^*, there are just enough local junctions linearized to span the array at zero bias and remove the global threshold.
This means that with increasing temperature, the non-linear I-V characteristic, described by Equation 1.35, has been linearly shifted until, at T^*, a finite zero-bias conductance $g_0 \equiv dI/dV|_{V=0}$ is observed. The $p(T)$ is also increasing with T. At T^*, the fraction $p(T^*)$ becomes large enough to build a network of ohmic junctions through the array and finally V_t is zero.
Above T^*, when the global threshold disappears along the optimal path, there are still many other paths that have finite thresholds and are accessible at higher bias. These thresholds will keep decreasing linearly with temperature as more and more steps are linearized by thermal fluctuations.
The dependence of V_t on T can be expressed as

$$V_t(T) = V_t(0)[1 - p(T)/p(T^*)] \text{ for } T < T^* . \tag{1.43}$$

Equation 1.43 can also be written as

$$V_t(T) = V_t(0)[1 - \eta T] \tag{1.44}$$

where $\eta = 4.8 k_B / p_c \bar{E_C}$, p_C is a parameter dependent on the array geometry (e. g. for a triangular lattice $p_c \approx 0.347$) and $\bar{E_C}$ is the average of charging energies in the array.
In the semiclassical regime it was found that $V_t(T) = V_t(1 - T/T^*)$ [26].
With Elteto's assumptions the formula becomes

$$V_t(T) = V_t(0) - 4.8 V_t(0) P(0) k_B T \tag{1.45}$$

where $P(0)$ is the distribution of $\Delta E = 0$ energy costs.
It is important to mention that another dependence was found experimentally by Bezryadin *et al.* [64]. The researchers explored how the power law scaling of the I-V curves is affected by structural disorder in the array and they observed that the threshold voltage decreased in their 2D arrays of gold nanoparticles as $V_t(T) \equiv V_t(0) - N k_B T/e$. They motivated the result explaing that random quenched disorder leads to universal behavior that is independent of the details of the barrier

height distribution. In this regard, the scientists demonstrated for a 2D metal nanocrystal array that the scaling exponent of the I-V curves remains unaffected by temperature. It follows that arrays are much more robust and forgiving as compared to other systems with a single threshold that might be significantly influenced by the surrounding environment. This result has been confirmed by various experiments [27, 55, 62, 64].

On a separate note, Elteto and collaborators [57], differently from Middleton and Wingreen [49], investigated electrical transport in metal arrays in the case of nearest-neighbor capacitive coupling. In their study, the scientists found that, depending on the interparticle distance, the contribution of next nearest-neighbor interactions can become significant and correlations between energy steps may become important. To calculate the nearest-neighbor capacitive coupling effect of the single nanoparticle capacitance C_0, the scientists considered the electrostatic energy of a 10 sphere system of capacitors in a triangular lattice (Figure 1.6):

$$E = \frac{1}{2}\sum_{i,j}(q_i + Q_i)C_{ij}^{-1}(q_j + Q_j) \tag{1.46}$$

where the q_i are quenched offset charges and the Q_i are mobile charges (equal to an integer multiple of e or 0). The C_{ij}^{-1} are elements of the inverse capacitance matrix. Nonetheless, C_{11}^{-1} does already include contributions from coupling to nearest neighbors if such coupling is present. The energy difference before and after tunneling will then be

$$\Delta E = e(q_1 - q_2)C_{11}^{-1}\,. \tag{1.47}$$

Considering the subsystem with 10 spheres in Figure 1.6, where the two central sites (1 and 2) are participating in the tunneling event and their 8 surrounding neighbor elements have $Q_j = 0$ for $j > 2$, the energy difference becomes

$$\Delta E = e(q_1 - q_2)(C_{11}^{-1} - C_{12}^{-1} + eC_{12}^{-1}(q_3 + q_4 + q_5 - q_7 - q_8 - q_9)\,. \tag{1.48}$$

The maximum value for ΔE is achieved if the appropriate limiting values ($+e/2$ or $-e/2$) are inserted for the q_i. This gives

$$\Delta E_{max} = e^2 C_{11}^{-1}(1 + 2\gamma) \tag{1.49}$$

where $\gamma = C_{12}^{-1}/C_{11}^{-1}$.

Note that the system energy cost associated with a tunnel event is not just equal to the change in chemical potential of a single site, but the different polarization charges q_i give rise to a distribution of energy costs ΔE.

Elteto and collaborators provided a graph showing the effect of coupling on the 1-1 and 1-2 elements of the inverse capacitance matrix. The graph has been adapted in Figure 1.7. As it can be seen, if $d_{c-c}/R > 3$, the correction of C_0 in the case of nearest-neighbor capacitive coupling remains within 10% and, depending on the applications, it could be commonly neglected. Considering the low impact of this capacitance correction in the system description, the nearest-neighbor capacitive coupling effect has been omitted on the system capacitance calculation of the NP assemblies investigated in this work and described in Chapter 3 for which the condition $d_{c-c}/R > 3$ is satisfied.

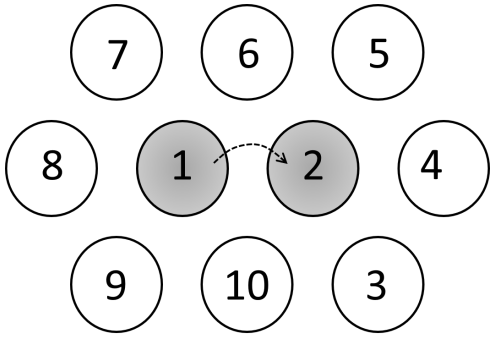

Figure 1.6: Sketch of a ten-sphere triangular lattice in which the single-electron transfer is taking place between spheres 1 and 2. Figure adapted from [57].

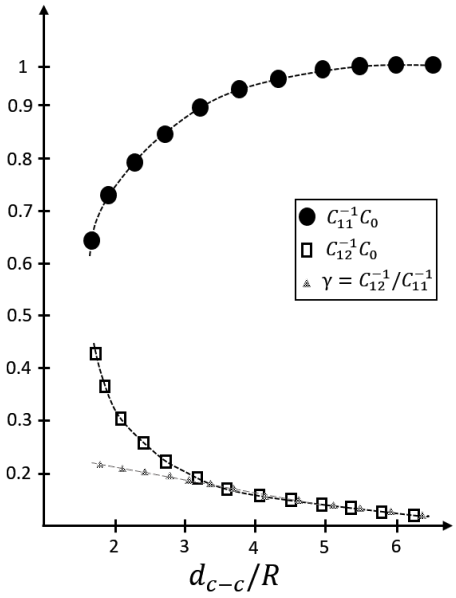

Figure 1.7: In the graph the effect of coupling on the inverse capacitance matrix for a 10-particle triangular system (Figure 1.6), normalized by the self-capacitance of the isolated sphere C_0, is displayed. Adapted from [57].

In Middleton and Wingreen theory [49], the factor $E_C = e/C_0$ was derived by an increase of

the local potential by one full electronic charge, leading to Equation 1.34 for the uncoupled case. With capacitive coupling, the increase in local potential, due to an electronic charge, will be less as it effectively spreads out over neighbors.
Equation 1.34 can then be modified considering the cost in bias per up-step $V_0 \approx eC_{11}^{-1}$ as

$$V_t(0) = \alpha N V_0 \approx \alpha N e C_{11}^{-1} . \tag{1.50}$$

This assumption can find a proof in the effective charging energy extracted from the Arrhenius fit of the temperature dependence of conductance curve $g_0(T) = g \exp[-U/k_B T]$ where $U \approx 0.2\Delta E_{max}$.
In the nearest-neighbor capacitive coupling scenario, the constant α in Equation 1.34 is the minimal number of up-steps in the optimal path at $T = 0$ divided by the length of the array. This definition differs from the conclusion of Middleton and Wingreen [49], which define $\alpha = V_t(0)C_0/Ne$. The two definitions only agree in the uncoupled case.

Another aspect to consider is the one related to NP arrays showing metallic behavior. In order to exhibit global metallic behavior, an assembly of metal nanoparticles must cross a percolation threshold. When the percolation threshold is overcome, the strongly coupled nanoparticles that form metallic clusters combine to form at least one continuous, sample-spanning metallic pathway. Although at or just above the percolation threshold, the sample may be dominated by nonmetallic conduction, as $T \to 0\,\mathrm{K}$, nonmetallic pathways freeze out and at $T = 0\,\mathrm{K}$, the electrical conductance results only from the metallic pathway contribution [31]. Typical observations of this behavior are the ones reported from Trudeau *et al.* [65]. The scientists observed that NP films above a threshold fraction of filled sites exhibited high conductivities and metallic behavior. However, below the threshold, conductivities were thermally activated. In this way, they gave proof of a MIT driven by percolation.

1.3.1 Influence of the ligands on the electric transport in a NP array

The improvement of conductivity of weakly coupled NP assemblies, in which metal-molecule-metal junctions were involved, has been largely demonstrated [66–69]. It followed that this configuration became the preferred one for NP assembly applications.
Studies of molecularly linked metal-NP assemblies showed that the ligands can strongly change the mutual tunneling coupling among the NP and MITs can be investigated as a function of inter-NP separation [50, 70, 71].
It is interesting to point out that metallic behavior can be tuned not only with shorter ligands but also with an higher number of NP layers. For example, Liu *et al.* [72] have

reported the highest conductance observed in Au-NP assemblies, $\sigma = 2 \times 10^5\,\Omega^{-1}cm^{-1} \approx 0.5\,\sigma_{Au}$ where $\sigma_{Au} = 4.5 \times 10^5\,\Omega^{-1}cm^{-1}$. The NP assembly consisted of 15 layers of 4.8 nm Au-NP assembled using an ionic layer-by-layer method. The Temperature Coefficients of Resistance (TCR), $TCR \equiv (1/R)(dR/dT)$ reported for metallic NP assemblies is also lower than the one observed in bulk. The observation of lower σ and TCR in those NP films compared with the corresponding bulk metal suggests that electron scattering processes are strongly enhanced in NP assemblies. Elastic electron-scattering decreases zero-temperature conductivity of samples, which in turn gives rise to smaller values of TCR.
The separation between nanoparticles in the NP assemblies studied in this work is maintained by the presence of Poly(Ethylene Glycol) (PEG) capping ligands HS-PEG-COOH (MW 10 kDa, $C_{12}H_{26}S$) forming metal-molecule-metal tunnel junctions. In the following subsection, the case of this particular tunnel junction is described.

1.3.2 Metal-Molecules-Metal junction

Taking into account the theoretical description of a classical tunnel junction given in Appendix B.1, the tunneling transmission probability for a metal-molecules-metal junction depends on the aligment of the energy level in the first nanoparticle with respect to the Highest Occupied Molecular Orbitals (HOMO) and Lowest Unoccupied Molecular Orbitals (LUMO) where the energy difference between the orbitals is known as *HOMO-LUMO gap*. In this case, the effective work function becomes $E_{LUMO} - E_F$ if the conduction is dominated by electron transport and $E_F - E_{HOMO}$ if the conduction is dominated by hole transport instead [73]. The presence of molecules between the nanoparticles rather than vacuum (and the SiO_2 underneath them) reduces the tunneling potential barrier height. Moreover, it determines the inter-NP surface-to-surface separation and a clear Coulomb blockade response consistent with double-layer charging of the metal-electrolyte interface.
The theoretical treatment mostly used for the traditional molecular model of charge transfer in donor-bridge-acceptor was proposed by Mc Connell [74] for nanoparticles in solution. The rate of charge transfer in the molecule χ_{CT} is given by

$$\chi_{CT} \approx \exp(-\beta') \, r_{DA} \tag{1.51}$$

where r_{DA} is the distance between the donor and the acceptor, and

$$\beta' = \frac{2}{d_{bridge}} \ln\left(\frac{\Delta E_B}{V_B}\right) . \tag{1.52}$$

In Equation 1.52, d_{bridge} is the length of the bridge unit, ΔE_B is the energy of the mediating states relative to the ground state and V_B is the coupling energy between two adjacent units.
Thereafter, Nitzan [75] derived the model of the molecular electronic structure for the case of molecules attached to electrodes.
The molecular conductance can then be expressed as

$$g_{mol} \approx \frac{8e^2}{\pi^2 \Gamma_D \Gamma_A} \frac{\chi_{CT}}{DOS} \tag{1.53}$$

where Γ_D and Γ_A are the donor and acceptor levels' widths, respectively (by taking into account the energy level coupling to the electrodes) and DOS is the density of vibronic molecular states. Their results have found remarkable agreement with the experiments [76].
Another interesting result is the one of Samanta *et al.* [77]. The scientists proposed a method of calculating a tunneling resistance assigned to a single organic molecule. By using a Green-function-based method, they calculated the transmission function of electrons across an aryldithiol molecule that binds two Au metal surfaces, which in turn gives a resistance value using the Landauer formula [78]. The method, proposed by Samanta and collaborators for calculating the resistance of a single organic molecule, can be used to calculate the ligand resistance of the nanoparticle systems described in Chapter 3. Differently from the work of Samanta *et al.* [77], who used aryldithiol molecules as tunneling separators, HS-PEG-COOH (MW 10 kDa) are employed in the present work. The calculated transmission function Υ of the molecule barrier is approximated by

$$\Upsilon^n(E) \approx \sum_1^n \Upsilon^1(E) = n\Upsilon^1(E) \tag{1.54}$$

where n is the number of the repeated molecule units (12 units, for the molecule used in this work). The conduction through the molecule will generally involve tunneling rather than propagation and the tunnel transmission coefficient can be calculated from

$$\Upsilon^1(E) \sim \exp(-2\sqrt{m_e E_g} l_{mol}/\hbar) \tag{1.55}$$

where E_g is the molecule energy gap, l_{mol} is the molecule length (circa 5 nm, in the presented case) and the resistance R_{mol} per molecule is derived by the modified Landauer formula

$$R_{mol} \sim (12.9\, k\Omega) \exp(0.7245\sqrt{E_g} l_{mol})\,. \tag{1.56}$$

1.4 FEBID technique for granular metals fabrication

An intense field of research pursued since 1996 covers the investigation of electron transport in Focused Electron Beam (FEB) deposited lines from organometallic precursors in analogy with the theory of electrical conductivity in granular metals [79, 80]. Gazzadi, Frabboni, de Teresa and Huth discussed some investigations on the electrical conduction mechanisms of FEBID material in [81]. Additionally, the researchers described the correlation between conductivity and the metal-to-carbon ratio of nanocrystalline compounds, such as the FEBID deposits obtained by the dissociation of organometallic precursor molecules. They reported that the resistivity of deposited lines varies over a wide range, namely $(10^{-6} - 10^{8})\,\Omega\,cm$. An example is given for the deposits obtained by the $C_5H_4CH_3Pt(CH_3)_3$ precursor. The same precursor has been used for FEBID nanofabrication reported in this work. The deposited material consists of small Pt-grains with a diameter of 2-3 nm embedded in a carbonaceous medium. Namely, Pt atomic content in Pt-C FEBID deposit is 16-26 at.% [82, 83] and its resistivity is around $10^7\,\mu\Omega\,\mathrm{cm}$. The matrix is amorphous carbon, which is known to behave as a semiconductor with a energy gap of about 2 eV [84, 85]. Therefore, as-grown Pt-C FEBID deposits are nano-granular metals whose electrical transport is the result of the interplay of diffusive charge transport inside the Pt-grains and thermally assisted tunneling between those grains [20].
Besides the many fundamental physical questions about this particular type of granular-metal system, the highest interest for this type of material is mainly correlated to the use of it for technical applications by virtue of its downscaling capabilities and tunability. In particular, different techniques may change the electric properties of the carbonaceus matrix, consequently changing the conductivity of the deposit. In Subsection 2.3.1.4, the post-growth irradiation of FEBID deposits is described. This technique has been used in this work to precisely tune the electronic inter-grain-coupling strength in the SET island system. The effect of the treatment on the SET functioning is reported in Section 4.3.

1.5 Single-electron transport in devices

In this Section, the concept of single-electron transport in devices is introduced. Particular attention is devoted to the description of a peculiar device which bases its operation on the single-electron transport. This device is the Single-Electron Transistor (SET). The name *single-electron transistor* comes from the observation that the transistor turns on and off again every time a single electron is added to it. Before

describing the SET in detail, an introduction about a simpler and preparatory device, the Single-Electron Box (SEB), is given.
Single-electron effects in devices have been studied now for more than two decades. A large interest has been dedicated to this subject since many of the single-electron effects can be described within simple perturbation theory and direct application of these systems was found in the framework of voltage-biased tunnel junctions.
The first experiments on single-electron devices are well summarized in the book *Single Charge Tunneling* [86]. The systems presented are based on the concept of using tunnel junctions for electron charge partition on an isolated electrode (island). Details about the electron tunneling through one and more than one tunnel junction are given in Appendix B.
In order to find evidence of single-electron transport in the I-V characteristic, the particular feature of Coulomb blockade should be observed. The condition for single-electron tunneling observation can be determined with the semi-classical orthodox theory, formulated by Averin and Likharev [7, 28]. The orthodox theory has been already described in Subsection 1.2.1. The Equation 1.6 describes one condition. In the equation, the resistance R_t of the tunnel barriers should be much higher than the quantum of resistance:

$$R_t \gg \frac{h}{e^2} = 25.81281\,k\Omega\,. \tag{1.57}$$

In the Equation, h is the Planck constant and e is the elementary charge. This condition sets a lower limit of the barrier 'opacity'. It ensures that the island is weakly coupled to the metallic contacts and that the charge inside the island is quantized. In this way, the degree of localization depends only on the fact that one electron at the time is tunneling in or out of the island.
The second condition to observe single-electron tunneling is that the system temperature has to be lower than the island charging energy, $E_C = \frac{e^2}{2C}$:

$$E_C \gg k_B T\,. \tag{1.58}$$

If this condition is not satisfied, the tunnel process can be thermally activated.
Many of the measurable consequences of the single-electron effect depend on the interplay of a discrete number of tunneling electrons and changes of the polarization charge on the capacitors in a continuous way by the applied gate voltages. The description of simple systems based on tunnel junctions are following.

1.5.1 Single-Electron Box (SEB)

The conceptually simplest device, for which single-electron effects are observed, is the Single-Electron Box (SEB) [87]. A schematic of the relative circuit is shown in Figure

1.8(b), where the tunnel junction is depicted as a resistor R and a capacitor C in parallel (Figure 1.8 (a)).
The device consists of a metallic island (the box) coupled *via* a tunnel junction J with a source electrode and *via* a capacitor with a capacitance C_G to a gate voltage source V_G. While no voltage is applied on the gate, the system is charge neutral and no excess electrons are on the island (Figure 1.9 (a)). As soon as a voltage V is applied, electrons will be 'pumped' onto the island through the tunnel junction in discrete steps $n = \pm 1, \pm 2, ...$ (Figure 1.9 (b)).

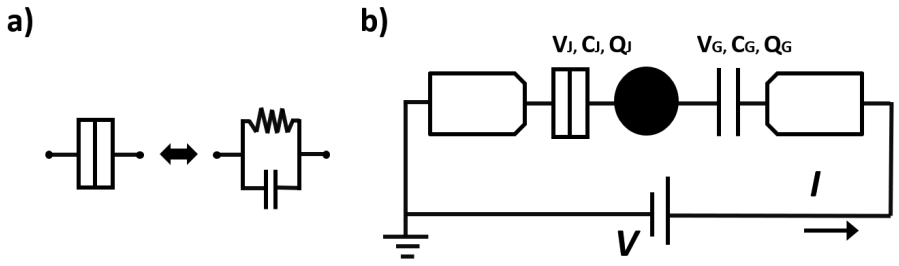

Figure 1.8: a) Circuit representation of a tunnel junction as a resistor and a capacitor connected in parallel. b) Circuit representation of a SEB.

While the total number of electrons on the island is an integer, the charge is spatially distributed with opposite sign on the capacitors plates: $-ne = Q_G - Q_J$. Kirchhoff's voltage law to the circuit is applied to obtain the condition: $V_J + V_G - V = 0$ where $V_J = \frac{Q_J}{C_J}$ and $V_G = \frac{Q_G}{C_G}$. It follows that:

$$Q_J = \frac{C_J}{C_\Sigma}(C_G V + ne)\,; \tag{1.59}$$

$$Q_G = \frac{C_G}{C_\Sigma}(C_J V - ne) \tag{1.60}$$

where $C_\Sigma = C_J + C_G$.
When an electron tunnels from the junction to the island, the energy $E_C = \frac{e^2}{2C_\Sigma}$ is required. The island charge changes from $-ne$ to $-ne - e$ and n increases to $n + 1$.
Accordingly, the tunnel junction charge changes as follows:

$$\Delta Q_J = Q_{J,final} - Q_{J,initial} = \frac{C_J}{C_\Sigma} e\,. \tag{1.61}$$

In a similar way the change of the charge on the gate capacitor is given by $\Delta Q_G = Q_{G,final} - Q_{G,initial} = -\frac{C_G}{C_\Sigma} e$ implying that the island charge changes by $-e$ and $\Delta Q_G - \Delta Q_J = -e$.

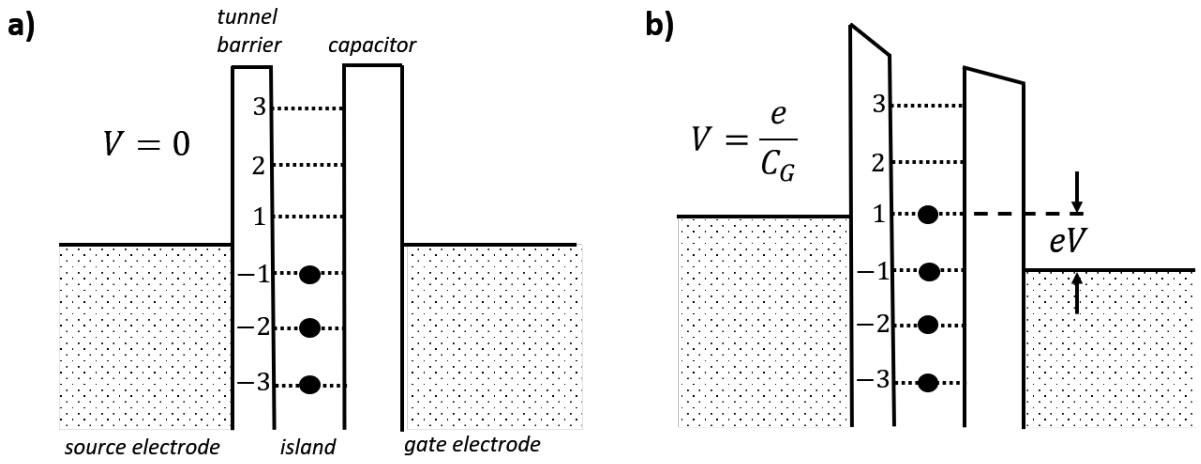

Figure 1.9: Energy diagram for the single-electron box when no bias is applied (a) and as a bias voltage V is applied (b). Adapted from [87].

The charging energy E_Σ on the island is derived from Equation 1.59 and 1.60 and it is expressed as

$$E_\Sigma = \frac{Q_J^2}{2C_J} + \frac{Q_G^2}{2C_G} = \frac{Q_G^2}{2C_G} + \frac{(Q_G + ne)^2}{2C_J}\,. \tag{1.62}$$

The energy that determines the transport of electrons through a single-electron device is the Helmholtz free energy F, which is defined as the difference between the stored energy and the work done by the power sources W. Thus, the total energy used to charge an island with an electron is: $F = E_\Sigma - W$ where $W = \int_{\Delta t} V_{DS} I(t) = \Delta Q_G V$. If $C_G \gg C_J$, the Helmholtz free electrostatic for $V = 0$ is just $F(Q_G) \equiv E_\Sigma$ and its parabolic trend is shown in Figure 1.10 (a) for several island charge states.

The change in Helmholtz free energy, that a tunnel event causes, determines the probability of this tunnel event. Thereby, the change in free energy is defined as the difference of the free energy after the tunnel event (final) and the free energy before the tunnel event (initial), $\Delta F = F_f - F_i$. The number of electrons in the box at equilibrium can be found by imposing the condition $\frac{\partial F}{\partial n} = 0$.

Since physical systems tend to occupy lower energy states, a transition to a state with lower free energy produces a negative change in free energy. From the electrostatic rules, the change in Helmholtz free energy of the circuit connected to a single-electron tunnel event ΔF_{add} is given by the sum of the change in the electrostatic energy of the island and the work done by the source V on the circuit:

$$\begin{aligned} \Delta F_{add} = F_{final} - F_{initial} + W = \frac{(-(n+1)e)^2}{2C_\Sigma} - \frac{(-ne)^2}{2C_\Sigma} + V\Delta Q_G \\ \Rightarrow \Delta F_{add} = \frac{e}{C_\Sigma}\left(-C_G V + ne + \frac{e}{2}\right) \end{aligned}\,. \tag{1.63}$$

In a similar way, the change in electrostatic energy of the circuit ΔF_{sub}, when an electron tunnels off the island, is:

$$\Delta F_{sub} = \frac{e}{C_\Sigma}\left(C_G V - ne + \frac{e}{2}\right) . \tag{1.64}$$

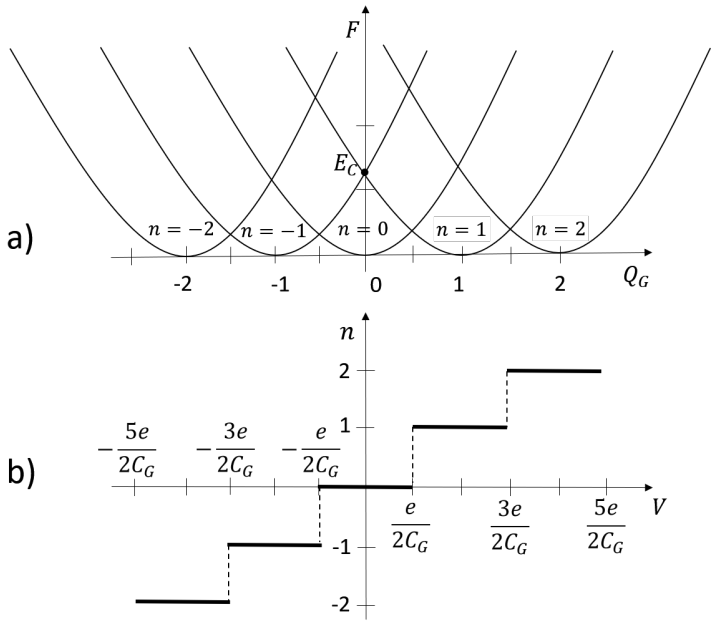

Figure 1.10: Charge builds up in a single-electron box. a) The Helmholtz free energy of the system for various charge states n at V=0 if $C_G \gg C_J$. b) Island charge n *vs.* supply voltage V. An integer number of charges can be stabilize in the box for specific voltage ranges.

The two changes in the electrostatic energy in the circuit, ΔF_{add} and ΔF_{sub}, are used to calculate the rate of electrons tunneling onto or off the island [86]:

$$\Gamma = \frac{1}{e^2 R_J} \frac{-\Delta F_{add}}{1 - \exp(\Delta F_{add}/k_B T)} . \tag{1.65}$$

This formula is one of the main results of the *orthodox theory* for single-electron effects [7]. In the case that $T = 0\,\mathrm{K}$, the equation becomes

$$\Gamma = \begin{cases} \frac{-\Delta F_{add}}{e^2 R_J}, & \text{if } \Delta F_{add} < 0 . \\ 0, & \text{if } \Delta F_{add} > 0 . \end{cases} \tag{1.66}$$

Considering ΔF_{sub}, similar expressions for the removing tunneling rate can be derived. Equation 1.66 defines the edge of the Coulomb blockade at $T = 0$ as

$$(n - \frac{1}{2})e < C_G V < (n + \frac{1}{2})e\,. \tag{1.67}$$

In this way, n and V adjust so that the condition 1.67 is satisfied and n, depending on V, has stable values (Figure 1.10(b)).
It is important to notice that the single-electron box can transfer integer numbers of electrons but in order to hold a precise number (e. g. $n = 1$) of electrons on the island, it is necessary to apply a specific bias voltage (e. g. $e/2C_G < V < 3e/2C_G$), as it is visible from the plateau regions in Figure 1.10 (b) corresponding to integer n numbers of electrons in the box.

1.5.2 Single-Electron Transistor (SET)

A particular device in which single-electron effects can be used for local electrostatic potential or very sensitive charge monitoring is the Single-Electron Transistor (SET). A SET consists of a conducting island which is tunnel-coupled to source and drain leads. Through the action of a gate capacitively connected to the island, only an integer number of electrons can tunnel among source, island and drain. The separation between the components is in the classical theory a border which cannot be overcome by electrons and no current can flow. The idea that the Coulomb blockade in the double tunnel junction source-island-drain can be overcome with a gate electrode was proposed by several authors [7, 28]. However, it was not until 1987 that Fulton and Dolan [88] created the first SET for which the gate effect was demonstrated. Few years after, Korotkov *et al.* [89] proposed a model that describes the electron transport through the dot. Afterwards, Kouwenhoven further extended the model in his work [90]. Therein, the electrostatic behavior of the dot is modelled by capacitors to the source, drain, and gate terminals and it is nowadays the mostly used model.
The interest in electronic elements based on single-electron effects grew fast and the devices have been even proposed as replacement for silicon transistors on small-scale integrations [8–10, 12, 28].
In addition, their applications spread on different fields. As a matter of fact, researchers have been using SET devices as ultra sensitive electrometers [91–94], memory devices and logic switches [95–103], chemical sensors [104, 105] and molecule-based transistors [106, 107].
The circuit of a SET can include more than one gate terminal. In this work, two gates have been used in the SET design. Representation of the classical and the used circuit are given in Figure 1.11 (a) and (b), respectively.

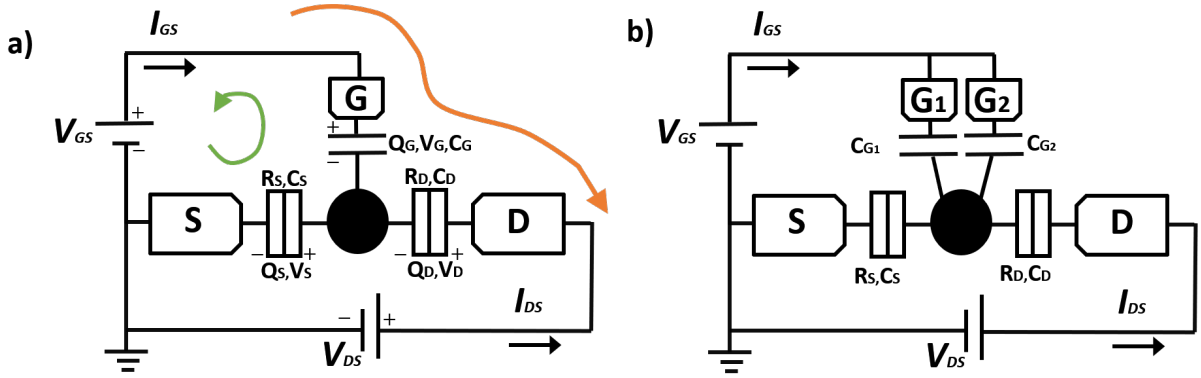

Figure 1.11: Equivalent circuit of a SET with one (a) and two gates (b).

The circuit of the SET can be initially simplified considering the easier circuit of the double tunnel junction with only the metal island between the leads and no gates. The simplified circuit is shown in Figure 1.12 (a).

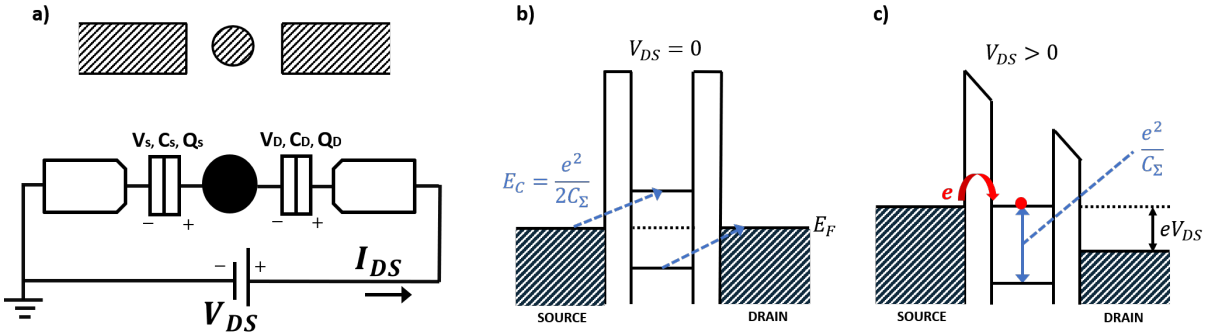

Figure 1.12: a) Schematic drawing of source/metal island/drain junction structure and the corresponding circuit. Band gap diagrams of the double tunnel barrier for $V_{DS} = 0$ in (b) and $V_{DS} > 0$ in (c). The gap in the density of states of the island can be overcome as soon as the system has enough energy to overcome the Coulomb charging energy which prohibits tunneling into and out of the island below the threshold voltage.

The Coulomb blockade model describes how due to Coulomb interactions on the electrons in the metal particle, for current to flow, an energy cost (charging energy) $E_C = q^2/2C_\Sigma$ has to be overcome in order to add an electron or hole of charge $q_e = \pm e$ to the particle. In the equation, $C_\Sigma = C_S + C_D$ is the total capacitance.
A schematic band gap diagram of the source/metal island/drain is shown in Figure 1.12 (b) and (c), for two junctions with equal capacitances for the case $V_{DS} = 0$ and $V_{DS} > 0$, respectively. As it is possible to be seen from the band diagrams, there is an energy gap in the island density of states. Considering the tunneling of an electron or a hole, the

gap width is e^2/C_Σ.
In Figure 1.12 (b), the double-tunnel junction energy band diagram is in equilibrium (no bias applied) and the coulomb gap of width e^2/C_Σ in the density of states appears in the island at about the Fermi energy. In this way, no states are available for electrons to travel into. When a bias is applied (Figure 1.12 (c)) and the voltage overcomes the charging energy of the island, an electron can tunnel on the island.
When a gate is added to the circuit, the effect of the gate electrode can easily be understood looking at the energy band diagram of Figure 1.13. The gate voltage modifies the position of the Fermi level on the island. Depending on the gate voltage, the top of the energy gap can be made to lie above, below or even at the Fermi levels of the source or of the drain.

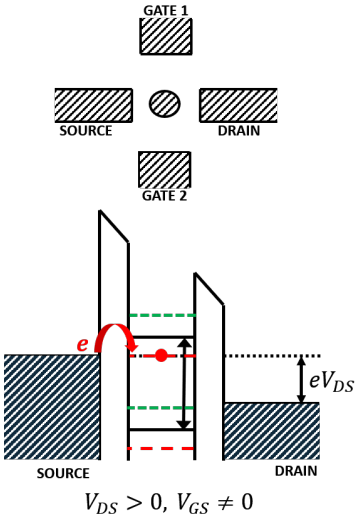

Figure 1.13: Schematic drawing and energy band diagram of a SET when $V_{DS} > 0$ and V_{GS} varies in order to shift the Fermi energy level of the source electrode on the left tunnel junction and allow an electron to tunnel from the source to the metal island.

1.5.2.1 Electrostatic energy change in the circuit

The electrostatic relations in the case of the SET circuit, for which two gate leads are used to control the charge inside the island (Figure 1.11 (b)), will be now described.
The following theoretical model was proposed by Ingold and Nazarov [86, 87]. In their model, the scientists described the electrostatic energy change associated to an electron tunneling on or off the island across the two tunnel junctions under the influence of an electrodynamic environment.
From the island, the capacitances C_S, C_D, C_{G_1} and C_{G_2} are connected in parallel. In particular it is possible to simply for the following calculations the gate capacitance as

$C_G = C_{G_1} + C_{G_2}$ and in general consider the two gates as a single one $G = G_1 + G_2$ since the two gate capacitances act in parallel and are connected to the same gate voltage source V_{GS}.
It is important to remember that the stray capacitance C_0 has to be taken into account due to the proximity of the electronic components. The different charges on the source, drain and gate (Q_S, Q_D and Q_G) are respectively

$$Q_S = C_S V_S;\ Q_D = C_D V_D;\ Q_G = C_G V_G\,. \tag{1.68}$$

The electron tunneling allows a discrete number of electrons to accumulate on the island. It follows that the net charge on the island can be expressed as the number of electrons on the island plus an offset charge (Q_0) in this way:

$$Q = nq_e + Q_0 = Q_S - Q_D - Q_G\,. \tag{1.69}$$

In the semiclassical model, the discrete index n and the continuous charge Q have well-defined values and they are not quantum quantities. Q_0 is an unintentional background polarization charge that usually exists in real structures due to work-function differences and random charges trapped near the island. This additional charge is the cause of the asymmetric experimental I-V characteristics. Moreover, those charges in large amounts can compromise the functionality of the device and their uncertainty represents a severe problem in the fabrication of the single-electron-based device technology.
The energy stored in the capacitors is

$$E = \frac{1}{2}\left(\frac{Q_S^2}{C_S} + \frac{Q_D^2}{C_D} + \frac{Q_G^2}{C_G} + \frac{Q_0^2}{C_0}\right)\,. \tag{1.70}$$

Applying Kirchhoff rules to the circuit, the following conditions are obtained:

$$\begin{aligned} -V_{DS} - V_{GS} + V_G + V_S = 0 \ &, \text{ green arrow loop in Fig. 1.11 (a)}\,; \\ V_{GS} - V_G + V_D - V_{DS} = 0 \ &, \text{ orange arrow loop in Fig. 1.11 (a)} \end{aligned} \tag{1.71}$$

Solving Equations 1.69 and 1.71, the charges can then be rewritten as

$$\begin{aligned} Q_S &= C_S\frac{C_D V_{DS} + C_G V_{GS} + Q}{C_\Sigma}\,; \\ Q_D &= C_D\frac{V_{DS}(C_S + C_G) - C_G V_{GS} - Q}{C_\Sigma}\,; \\ Q_G &= C_G\frac{V_{GS}(C_S + C_D) - (C_D V_{DS} + Q)}{C_\Sigma} \end{aligned} \tag{1.72}$$

where $C_\Sigma = C_S + C_D + C_G + C_0$, and the stored energy is

$$E = \frac{1}{C_\Sigma}\left[C_G C_D (V_{DS} - V_{GS})^2 + C_S C_D V_{DS}^2 + C_S C_G V_{GS}^2 + Q^2\right] . \tag{1.73}$$

As soon as one electron tunnels onto the island from the source lead through the first junction, the change in the stored energy is

$$\Delta E = \frac{(nq_e)^2 - ((n+1)q_e)^2}{2C_\Sigma} = -q_e^2 \frac{2n+1}{2C_\Sigma} . \tag{1.74}$$

In the model, it is assumed that electrons, that tunnel through one junction, immediately relax due to carrier-carrier scattering. In this way, resonant tunneling through both barriers simultaneously is neglected. A sequential tunneling model is therefore adopted. When charge tunnels across a junction, the power supply must do work transferring charge. This work is calculated by integrating the power delivered to the junctions:

$$W = \int_{\Delta t} V_{DS} I(t) = \int_{\Delta t} V_{DS} \frac{dq}{dt} dt = \Delta Q V_{DS} \tag{1.75}$$

where ΔQ is the total charge transferred from the power supply during the charging period Δt. Before an electron tunnels, n electrons are on the island, the initial voltages across the junctions J_{SI} and J_{ID} are V_S^{in} and V_D^{in} and the initial charges on the two junctions are Q_{SI}^{in} and Q_{ID}^{in}, respectively. If one electron tunnels onto the island through junction J_{SI}, the voltage drops across the two junctions are:

$$V_S^{fin} = \frac{1}{C_\Sigma}(V_{DS} C_D + (n+1)q_e) = V_S^{in} + \frac{q_e}{C_\Sigma} ; \tag{1.76}$$

$$V_D^{fin} = \frac{1}{C_\Sigma}(V_{DS} C_S - (n+1)q_e) = V_D^{in} - \frac{q_e}{C_\Sigma} . \tag{1.77}$$

The work of the power supply and the Helmholtz free electrostatic energy barrier for adding an electron from the source electrode are:

$$W_S = \frac{-q_e C_D}{C_\Sigma} V_{DS} \text{ and } \Delta F_{S\to I} = E_C - W_S = E_C - \frac{q_e C_D}{C_\Sigma} V_{DS} . \tag{1.78}$$

The resulting charge stored by junction J_{ID} is then

$$Q_{ID}^{fin} = C_D V_D^{fin} = C_D V_D^{in} - \frac{C_D q_e}{C_\Sigma} = Q_D^{in} - \frac{C_D q_e}{C_\Sigma} . \tag{1.79}$$

On one side, the change on J_{SI} is associated with the tunnel event. On the other side, the change in charge stored by junction J_{ID} is $\Delta Q_D = Q_{ID}^{fin} - Q_{ID}^{in}$ and it is provided by

the work of the power supply

$$W_D = V_{DS}\frac{-q_e C_D}{C_\Sigma}\,. \tag{1.80}$$

The Helmholtz's free electrostatic energy barrier for an electron leaving to drain is

$$\Delta F_{I\to D} = E_C - W_D - eV_{DS} = E_C + \frac{q_e C_D}{C_\Sigma}V_{DS} - eV_{DS}\,. \tag{1.81}$$

In the same way the charge changes on the gate capacitor, ΔQ_G, and the work done from the power supply on the gate, W_G, can be derived as:

$$\Delta Q_G = C_G\frac{q_e}{C_\Sigma};\; W_G = \Delta Q_G V_{GS} = \frac{C_G q_e}{C_\Sigma}V_{GS}\,. \tag{1.82}$$

The change in the total Helmholtz's free energy associated with the electron tunneling through junction J_{SI} is

$$\Delta F_t(SI) = \Delta F - (W_D + W_G) = -q_e^2\frac{2n+1}{2C_\Sigma} - C_D\frac{q_e}{C_\Sigma}V_{DS} - C_G\frac{q_e}{C_\Sigma}V_{GS}\,. \tag{1.83}$$

Similarly, it can be calculated for $V_{DS} < 0$. It follows that, moving out an electron from the island towards the drain costs the electrostatic energy difference:

$$\Delta F_t(ID) = q_e^2\frac{2n-1}{2C_\Sigma} + q_e\left(1 - \frac{C_D}{C_\Sigma}\right)V_{DS} + q_e\frac{C_G}{C_\Sigma}V_{GS}\,. \tag{1.84}$$

At zero temperature, a tunnel event will only occur if the change in energy is negative. The condition $\Delta F_t > 0$ has to be satisfied for $\Delta F_t(SI)$:

$$q_e\left(n + \frac{1}{2}\right) - (C_D V_{DS} + C_G V_{GS}) + Q_0 > 0\,. \tag{1.85}$$

In a similar way, the condition in order to tunnel an electron out from the island through junction J_{ID} can be found from

$$q_e\left(-n + \frac{1}{2}\right) - V_{DS}(C_S + C_G) - C_G V_{GS} - Q_0 > 0\,. \tag{1.86}$$

The suppression is overcome for $\mid V_{DS} \mid \geq V_{DS}^{th} \equiv \min\left(\frac{q_e}{2C_S};\frac{q_e}{2C_D}\right)$ in the case that $V_{GS} = 0$ and $Q_0 = 0$ and $n = 0$. After this limitation, the drain-source current $\mid I_{DS} \mid$ rises rapidly with increasing $\mid V_{DS} \mid$.
A graph explaining the different regions of the Coulomb blockade in terms of energy barrier diagrams is reported in Figure 1.14.

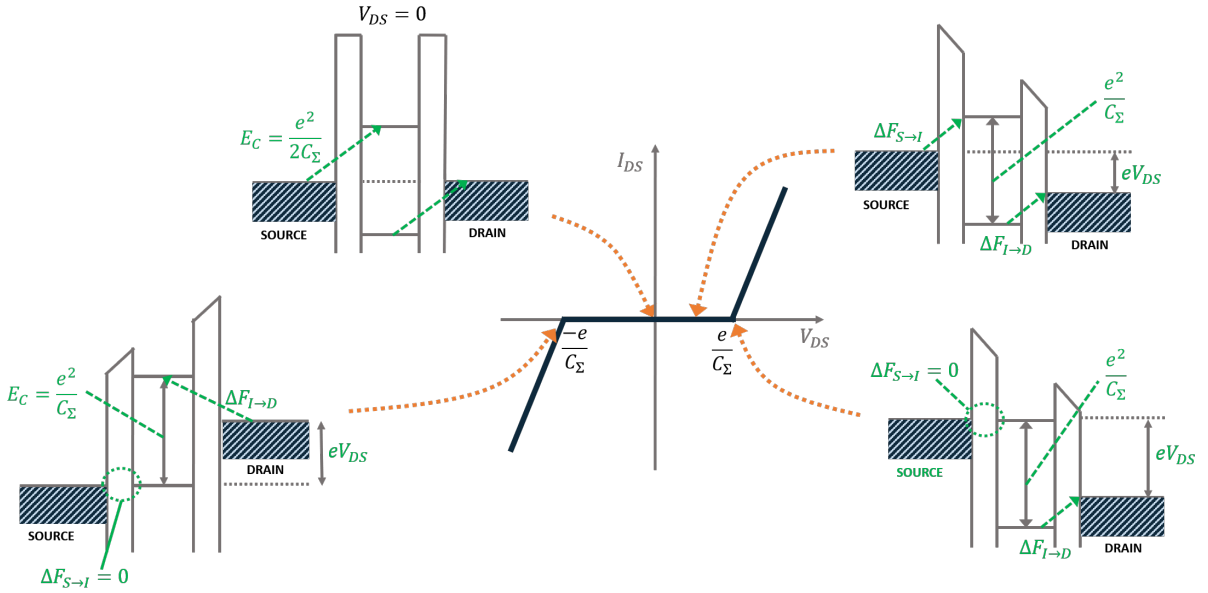

Figure 1.14: Theoretical representation of the expected non linear I-V characteristic for $V_{GS} = 0$ and $Q_0 = 0$ and $n = 0$ in the case that $C_\Sigma = 2C_S = 2C_D$. The energy diagrams of the corresponding I-V curve regions along the V_{DS} range are additionally sketched out. Adapted from [108].

Coulomb Staircase: When the tunnel junctions are not symmetric (such that either the capacitances or the tunneling resistances are different), the probability, that an electron after tunneling the first junction remains in the island and does not have enough energy to overcome the next junction energy gap, is high.
As shown in Figure 1.15 (b), when $V_{DS} \leq -e/C_\Sigma$, one electron tunnels into the island, the island charge increases by one electron ($n = 1$) and the Fermi energy in the island grows by e^2/C_Σ. In particular, the Coulomb gap of width e^2/C_Σ in the density of states aligns the leads Fermi energy. In this way, no states are available for electrons to travel into. Hence, a particular feature will display in the I-V characteristics: the *Coulomb staircase*.
Assuming for example that the capacitances are still equal but the tunneling resistances are quite different $R_{di} > R_{is}$, the island remains in a charge state corresponding to the voltage range for which Equation 1.86 is not satisfied. Under this condition, the current is approximately controlled by the voltage drop across the second junction. Therefore, the current increases accordingly by an amount given by

$$\Delta I \approx \frac{\Delta V_D}{R_{di}} = \frac{e}{C_\Sigma R_{di}} \,. \tag{1.87}$$

An exemplary sketch of the I-V characteristic of a SET, in which the Coulomb staircase is visible, is given in 1.15 (c).

In particular, the first step-like increase corresponds to the probability $p(n = \pm 1)$ of having one excess charge on the island beginning to increase from the state of Coulomb blockade where the excess in charge is 0. At the same time, the probability $p(n = 0)$ of having no excess charge decreases. In a similar way for the subsequent steps, the probability of having two, three, etc excess charges $p(n = \pm 2, 3, etc)$ starts to rise from zero, meanwhile the no excess charge probability $p(n = 0)$ decreases.

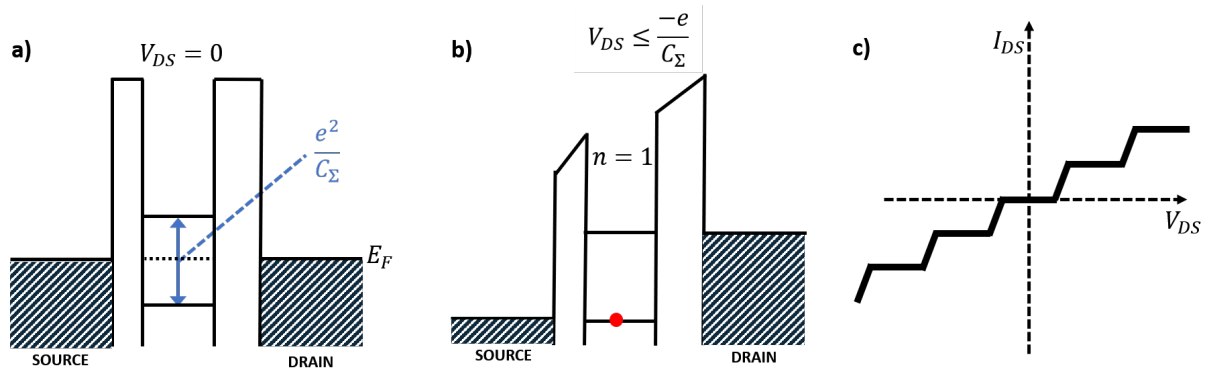

Figure 1.15: The energy diagram of a double tunnel junction with non symmetric junctions is shown in equilibrium (a) and under an applied bias V_{DS} between source and drain (b). Since the second junction needs more energy to be crossed, the electron has high probability to remain blocked on the island, not having enough energy to overcome the energy gap of the junction on the right.

Coulomb Oscillations: Through the action of V_{GS}, the electrostatic potential of the island is shifted and can be tuned in order to make a tunneling event possible (Figure 1.16(a)). For example, for positive V_{GS}, negative charge is accumulated on the island in a step-like fashion as sketched in Figure 1.16(b). In this way, an electron can tunnel onto the island from the source, when the Helmholtz free energy for an electron on the island is lowered and it compensates E_C:

$$\Delta F_{S\to I} = E_C - e\frac{C_G}{C_\Sigma}V_{GS} = 0\,. \tag{1.88}$$

The condition leads to the establishment of a threshold voltage

$$V_{GS} = \frac{E_C}{eC_G/C_\Sigma} = \frac{e}{2C_G}\,. \tag{1.89}$$

Hence, unlike a conventional transistor in which the charge increases continuously, the charge on a SET island increases in discrete steps and this behavior is reflected in the conductance between source and drain. Moreover, the gate is the only electrode contributing to the change of electrostatic energy of the island. Evidence of the correlation between single charge increase and the observation of Coulomb blockade

oscillations due to V_{GS} is given in Figure 1.16.
By a small fixed applied V_{DS} and an increasing/decreasing V_{GS}, a directed current is measured between source and drain when the condition in Equation 1.88 is satisfied. It follows that I_{DS} *vs.* V_{GS} presents periodically spaced peaks, as shown in Figure 1.16(b). As seen in Figure 1.16(b), the current increases and decreases periodically in V_{GS}. The peak positions are equally spaced in gate voltage with separation $\Delta V_{GS} = e/C_G$. The increase in gate voltage is the one necessary to add one electron to the island. Between peaks, the number of electrons on the dot remains a stable integer value. As long as $eV_{DS} < k_B T$, the width of these peaks will be limited by thermal broadening and therefore the periodic behavior smears out at temperatures greater than the energy width of the Coulomb blockade regime. Additionally, the nth peak multiplied by the charge of the electron e would be the energy difference between the two states. The energy change can then be written as

$$\frac{C_G e V_G(n)}{C_\Sigma} + B = E(n+1) - E(n) \tag{1.90}$$

apart from a constant B. In the equation, $E(n)$ and $E(n+1)$ are the total energy of the island with n and $n+1$ electrons, respectively.

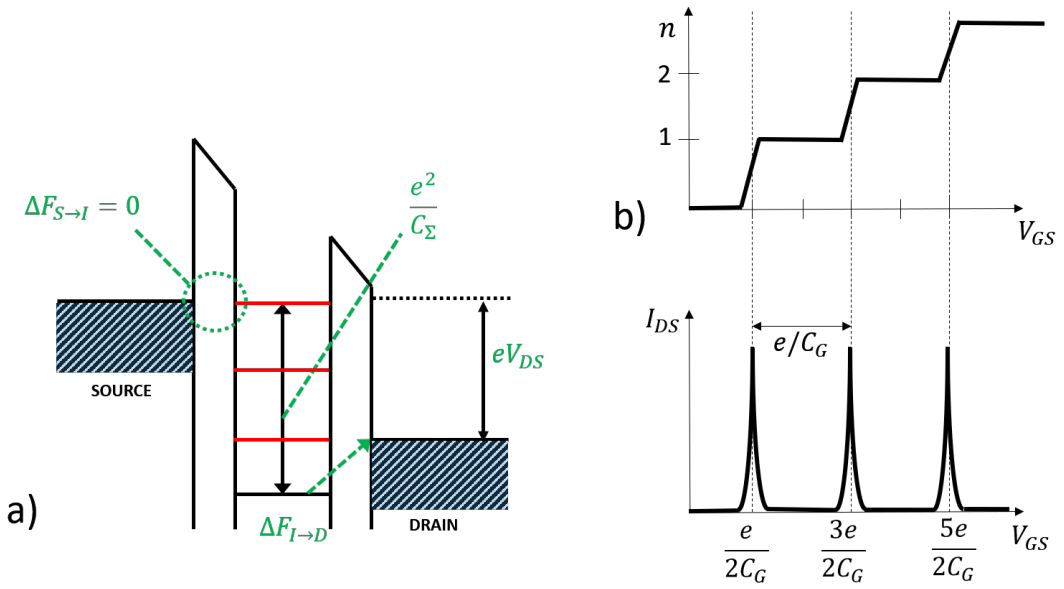

Figure 1.16: a) The effect of V_{GS} is displayed in the band diagram of the source-island-drain system. Applying a voltage V_{GS} induces a shift on the electron levels inside the island. An electron is 'pumped' into/out of the island when the level reaches the Fermi level of one of the two electrodes. b) The staircase like behavior of the single increment of the electron number in the island is shown with correspondence to the relative measured I_{DS} peak for a fixed applied V_{DS} and an increasing V_{GS}.

Coulomb Diamonds: Energy quantization evidence can be observed by measuring the tunneling current at fixed V_G as a function of V_{DS} (Figure 1.17).
The combination of the two conditions Equation 1.85, Equation 1.86 and the effect of V_{GS} creates no-current parallelepiped regions in the V_{DS}/V_{GS} plane, known as *Coulomb diamonds*.
From the initial shift of the maximum Coulomb blockade region in the I-V characteristic, the initial charge on the island, Q_0, can be calculated with the following equation:

$$Q_0 = C_G \times \left(\frac{e}{C_G} - \Delta V_{GS,initial}\right). \tag{1.91}$$

As soon as the Fermi energy rises, higher energy levels on the island are overcome and more current flows since additional channels are established for the electron tunneling on the island.
When the bias voltage V_{DS} is symmetric, $\frac{V_{DS}}{2} = V_S = -V_D$, the diamonds will look squared. For an asymmetric bias, the fours lines corresponding to $\Delta F_t = 0$ and the charge state $n = 0$ are plotted in Figure 1.17.
The width of the Coulomb diamond along the V_{GS} axis is e/C_G. On the vertical axis V_{DS}, the maximal extension of the Coulomb diamond is $\pm q_e/C_\Sigma$.

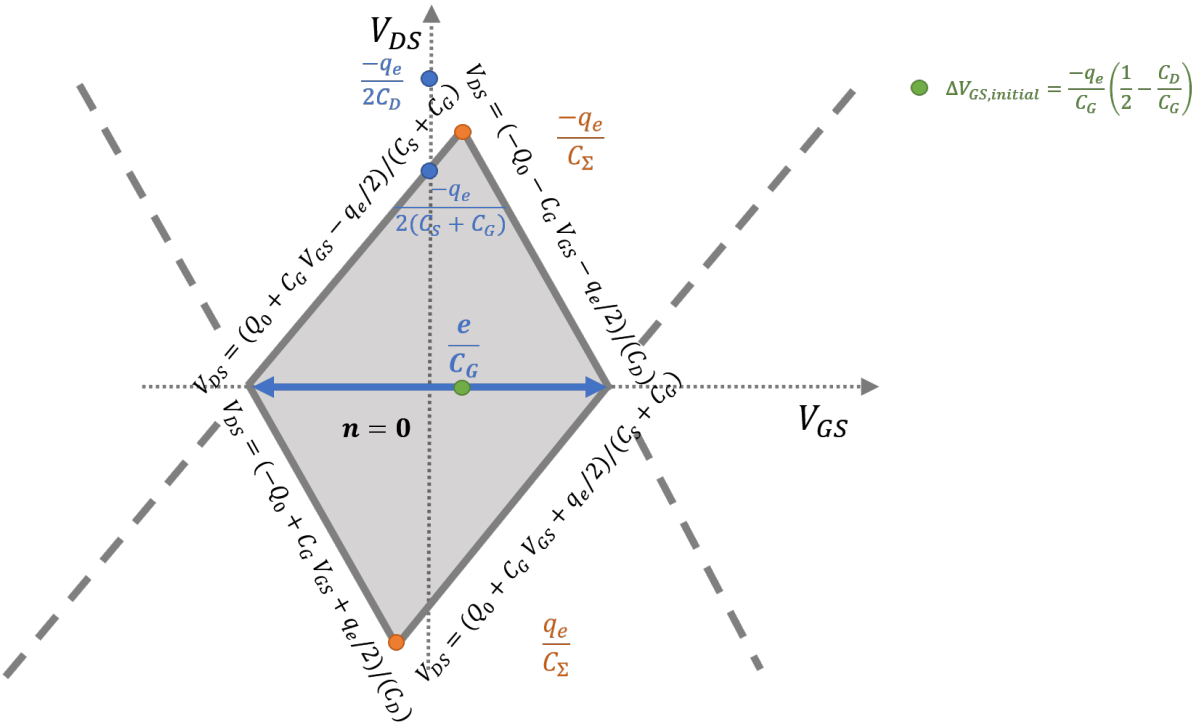

Figure 1.17: Sketch of the Coulomb diamond for a SET with asymmetric tunnel junctions. In the diamond regions tunneling is forbidden by the Coulomb blockade at low temperatures and no charge is held stable on the island ($n = 0$). The borders of the regions are found by setting $\Delta F_t = 0$.

On the left and on the right of the region in Figure 1.17, there are other Coulomb blockade regions with exclusive stable charge states on the island (-1, 1 electron and so on). These blockade regions are indicated in Figure 1.18. In the surrounding regions, more charge states can exist. Hence, the diamond corners correspond to the single-electron tunnel through the device, that leads to the suppression of the Coulomb blockade and the relative current peak observation in the Coulomb oscillations plot.

It is important to notice that the diamonds can look like symmetrical rhombus shaped

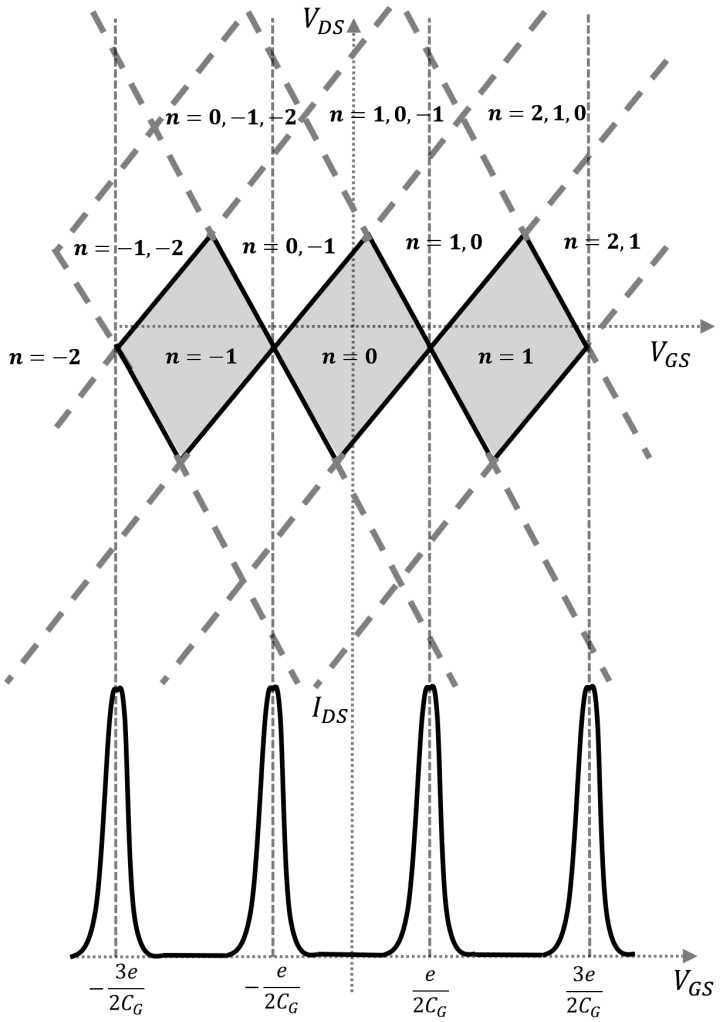

Figure 1.18: Coulomb diamonds plane. n charge states correspond to the different diamond regions. The diamonds corners coincide with the current peaks of the device.

regions when $C_D \approx C_S$ and $C_G \ll C_D$, C_S. Such a feature corresponds the one reported in the experimental measurements in the Section 4.2. This information about the device, can be directly extracted analysing the charge stability diagram.

As it has been shown in Figure 1.17, the diagram linear relations present two slopes:

$$\frac{dV_{DS}}{dV_{GS}}_{\Delta F_{I\to D}=0} \approx \frac{C_G}{C_S + C_G}\,, \tag{1.92}$$

$$\frac{dV_{DS}}{dV_{GS}}_{\Delta F_{S\to I}=0} \approx -\frac{C_G}{C_D}\,. \tag{1.93}$$

In the case of symmetrical blockade diamonds, these lines will cross in the same point. From equalizing the conditions, the capacitance relations of the device ($C_D \approx C_S$), can be directly acquired. In Figure 1.19, the case of the symmetrical rhombic blockade region is sketched.

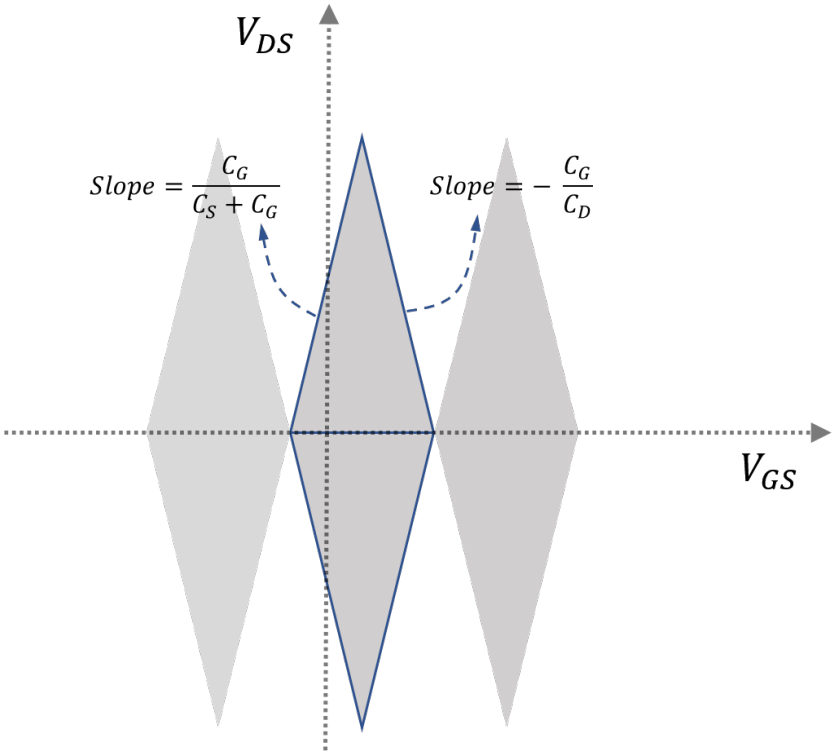

Figure 1.19: Symmetrical blockade diamonds are depicted. The distinctive shape can be observed only when $C_D \approx C_S$ and $C_\Sigma \approx C_S + C_D \approx 2C_D$, C_S. This is the case of the SET devices fabricated in this work, whose electrical behavior is described in Section 4.2.

Chapter 2

Methods and Techniques

Before presenting the main results of this work, it is necessary to provide a description of how these results have been experimentally obtained. Therefore, in this chapter the methods and techniques used for the fabrication and characterization of the several samples are described. The chapter begins with a description of the techniques used for the fabrication of contact-pads on Si-SiO_2 substrates applied as platform for the following nanofabrication step (Section 2.1). The first Section is followed by Section 2.2 describing the main instruments used for the nanofabrication and the topographic/compositional analysis. The different sample nanofabrication techniques are then presented in the following Section 2.3. Finally, in the last Section 2.4, the characterization techniques used to perform electrical transport and magneto-transport measurements are discussed.

2.1 Chip fabrication

In this section, the preparation of the chip on which the samples have been nanofabricated and electrical characterized is described. The chip consists of a Si-SiO_2 substrate on a metal pins equipped printed circuit board. Cr-Au electrodes by UV-lithography and DC magnetron sputtering of Cr-Au in conjunction with lift-off are defined on the substrate. The metal pins on the board match perfectly the socket adapters in the SEM and in the ^{3}He-cryostat in order to allow external electrical measurements on the nanofabricated devices. A description of the contact-pads fabrication follows (Subsection 2.1.1 and 2.1.2). Afterwards, the chip assembling procedure will be described (Subsection 2.1.3).

2.1.1 UltraViolet-Lithography (UVL)

UltraViolet-Lithography (UVL) is a commonly used micro-fabrication technique to transfer a geometric pattern from a mask to a wafer surface [109].

The pristine substrate is coated with a UV-light-sensitive material (photoresist) that is afterwards exposed to UV light with a specific pattern defined by the photomask. This technique combined with baking and development treatments allows to engrave the exposed (for positive photoresist) or not exposed (for negative photoresist) pattern into the photoresist layer. For the process described in this work, negative photoresist and two exposure-baking steps have been used in order to obtain a slight undercut and avoid sharp free standing edges of the further deposited material. Masks used for negative photoresist contain the negative of the pattern to be transferred and the UV exposure causes the negative resist to become polymerized and not soluble in the developer.
The technique has been used to fabricate a 24 finger contacts design on the provided substrates.
The substrates consist of P-doped (100) insulated silicon with a 200 nm thick thermally grown SiO_2 layer. The substrates are commercially available (CrysTec GmbH) and their working surfaces have been epitaxially polished by the supplier. The as-supplied substrates have been cut from wafers to a size of $10\times10\,\mathrm{mm}^2$ with a thickness of approximately 0.625 mm.

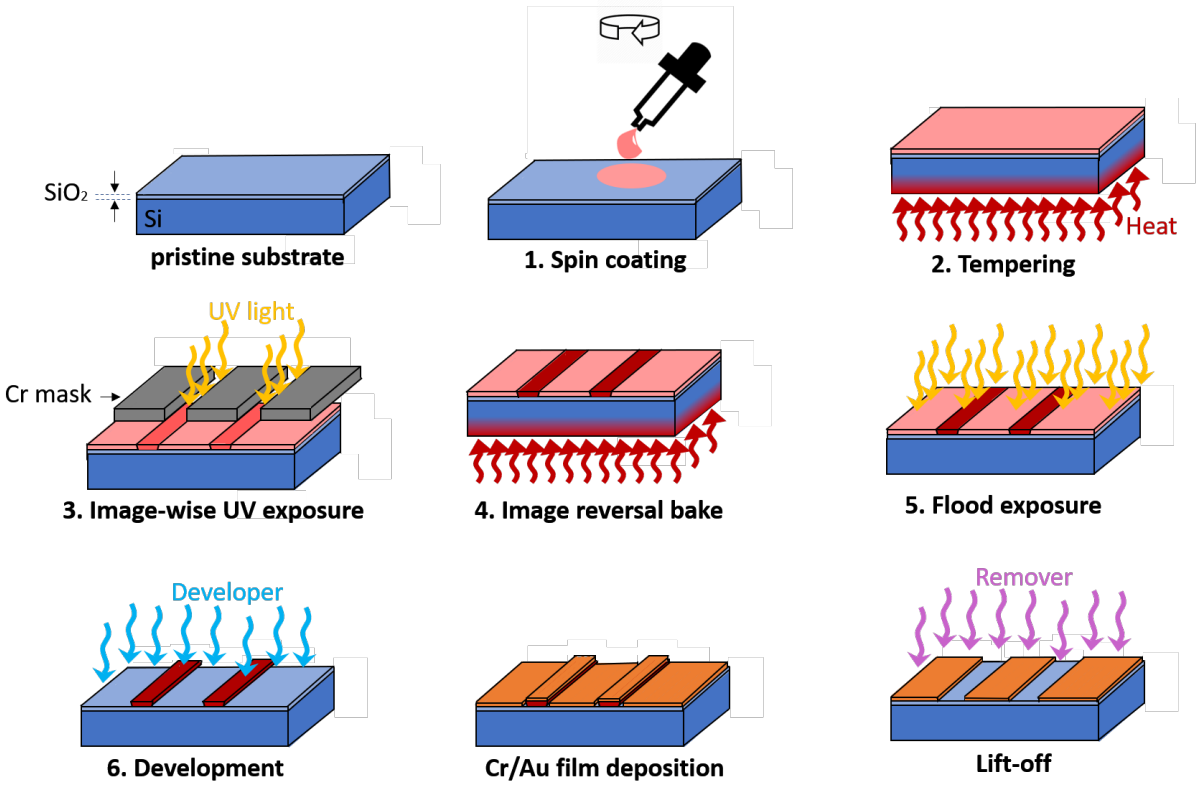

Figure 2.1: The UV-lithography process combined with the lift-off of magnetron sputtered Cr-Au contacts has been accomplished following the depicted steps.

The UVL process consists of the following procedure steps:

1. Substrate cleaning Firstly, the substrates have been cleaned following a consistent cleaning procedure in order to remove the protective wax layer left from the supplier. The procedure consists of sonication in acetone (99.9 %, Merck KGaA) for 15 min, in distilled DeIonized (DI) water for 5 min and finally in isopropylalcohol (99.8 %, Merck KGaA) for 5 min.

2. Spin coating The cleaned substrate surface has been uniformly covered with a image reversal polymer-based UV photoresist (AR-U 4040, ALLRESIST GmbH) by spin coating. During the spin coating process, 1 - 2 drops of the photoresist are spread evenly on the substrate that is rapidly spun. The parameters for the spin coating have been: 3 s duration at 2000 rotations per minute (rpm), followed by 57 s at 6000 rpm. After the coating, the substrate is treated with two cycles of baking and UV irradiation following the photoresist information sheet [110].

3. Tempering The first bake is required to evaporate the excess solvent. The baking is conducted placing the substrate on a hot plate at 85°C for 2 min.

4. Image-wise UV exposure The first UV irradiation (70 mJ/cm^2) or image-wise UV exposure of the substrate is conducted with a Cr mask (on a glass surface) between the Hg-Xe UV lamp and the substrate. The Cr mask has been accurately aligned and it is brought in direct contact with the photoresist on the substrate. The used Cr mask has the positive pattern of the final expected contacts' structure. The distance between the fingers in the center of the pattern is 3 μm.

5. Image reversal bake A second bake is needed in negative processes to harden the exposed photoresist. The amine in the exposed areas reacts with the indenecarboxylic acid and a cross-linking results in making exposed areas alkali-insoluble. The bake has been performed placing the substrate on a hot plate at 115°C for 5 min.

6. Flood exposure The second UV irradiation (180 mJ/cm^2) is conducted without the Cr mask. During flood exposure, the alkali-soluble indenecarboxylic acid is formed in the up to this step unexposed areas. Nevertheless, cross-linked structures remain unchanged.

7. Development Finally, the substrate takes a bath in a solution 2:1 of developer (AR300-35, ALLRESIST GmbH) and distilled DI water for 60 s. Therefore, the photoresist is removed from the first irradiation unexposed regions and the development produces a negative image of the Cr mask.

The interplay of the exposure dose, reversal bake temperature and development time results in a sharper or less pronounced undercut. Later, Cr-Au thin films are deposited over the entire substrate, covering both the photoresist and the resist-free areas of the substrate. This process is described in detail in the next Subsection 2.1.2. In Figure 2.1 the performed lithography and lift-off processes are shown in schematic steps.

2.1.2 DC magnetron sputtering of Cr-Au contacts and lift-off

In this work, Direct Current (DC) magnetron sputtering has been used for the metallic thin film deposition of the electrical contacts. This technique is a Physical Vapour Deposition (PVD) manufacturing process that can offer the deposition of high-quality metal films onto most of common surfaces.
The deposition is a passive film growth mechanism on the substrate of atoms ejected from a target surface by bombardament with the ions of a localized cold plasma [111–113]. An important advantage of sputter deposition is that even materials with very high melting points are easily sputtered.
The sputtering process begins when a substrate (anode), that is going to be coated, is placed in a High Vacuum (HV) chamber containing an inert gas such as argon and a negative voltage is applied to a target source material (cathode) that will be deposited onto the substrate surface (Figure 2.2). The target has high purity and is larger in size than the substrate in order to improve deposited material uniformity.
A high DC voltage between anode and cathode is applied in order to establish a high electric field between the two electrodes. The cathode in DC discharge must be an electrical conductor, since an insulating surface will develop a surface charge that will prevent ion bombardment of the surface. This condition implies that DC sputtering can be used to sputter simple electrically conductive materials such as metals. In the electric field region the gas breaks down to conduct electricity when a certain minimum voltage (striking voltage) is reached by the glow discharge phenomenon. The breakdown voltage for a given gas is a function of the pressure in the chamber and the distance between the anode and the cathode; it can easily be calculated by Paschen's law [114]. By a large electric field, the ions of the plasma are accelerated towards the target. The high-energy impact of the ions on the target material induces neutral atoms, charged atoms and electrons to be emitted from the target surface by energy and momentum transfer. The sputtered atoms ejected from the target surface have high kinetic energy (1 - 10 eV) that allows them to cross the plasma and condense on the substrate, leading to good adhesion and high uniformity of the deposited film. Moreover, an advantage of DC sputtering is that the plasma can be established uniformly over a large area, so that a solid large-area ejection source can be established.

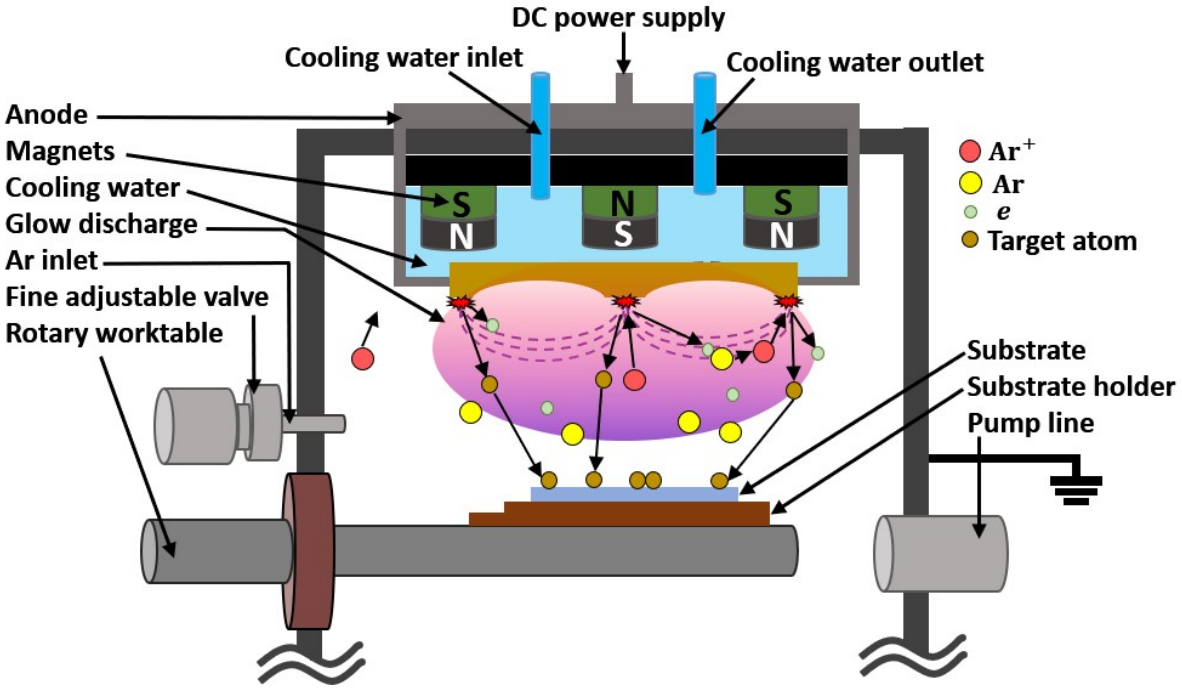

Figure 2.2: Schematic representation of the DC magnetron sputtering process. In a HV chamber, an Ar-plasma is generated in close proximity to a metal target by letting Ar in the chamber and applying an electric potential between the target and a substrate placed just a few cm away. The positively charged Ar-ions are accelerated towards the target and sputter off atoms from the target surface. The sputtered atoms will then travel towards the substrate forming a thin metal film.

In order to increase the efficiency of the target sputtering process and avoid sputtering of the substrate, the plasma is confined next to the target surface. By using an appropriate arrangement of magnets behind the target, a magnetic field (200 - 500 Gauss) is added to the DC sputtering system that can maintain secondary electron motion in the vicinity of the target surface. This type of sputtering is called *magnetron sputtering*. The Lorentz force exerted on the electrons let them spiral about the magnetic field lines (parallel to the target surface) so that they have more chance of undergoing an ionizing collision thus enabling the plasma to be operated at a higher density. As a result of the increased ionization efficiency, the process can be performed at a lower operating pressure (typically 10^{-3} mbar compared to 10^{-1} mbar) and lower operating voltage (typically about 500 V compared to about 2 - 3 kV) than in the basic sputtering mode [113].
Due to the high collision energy and density, the target can become extremely hot. By incorporating an appropriate cooling system, the target is cooled down avoiding thermal damage of the target, the magnets and the substrate as well.
The sputtering yield (S, number of atoms ejected from the target surface per incident ion) depends on the setup conditions, such as voltage and current (sputter power) at

which sputtering takes place and on the target and ion characteristics, such as the target material composition, atom binding energy, energy and angle of ion incidence. The sputtering yield increases with ion incidence angle up to approx 80° due to the decrease in the scan depth of incident ions following the relation $S \propto 1/cos\theta$. The outcome of the sputtering is the deposition of a set of atomic layers resulting in a thin metal film, whose thickness depends on the sputtering time.

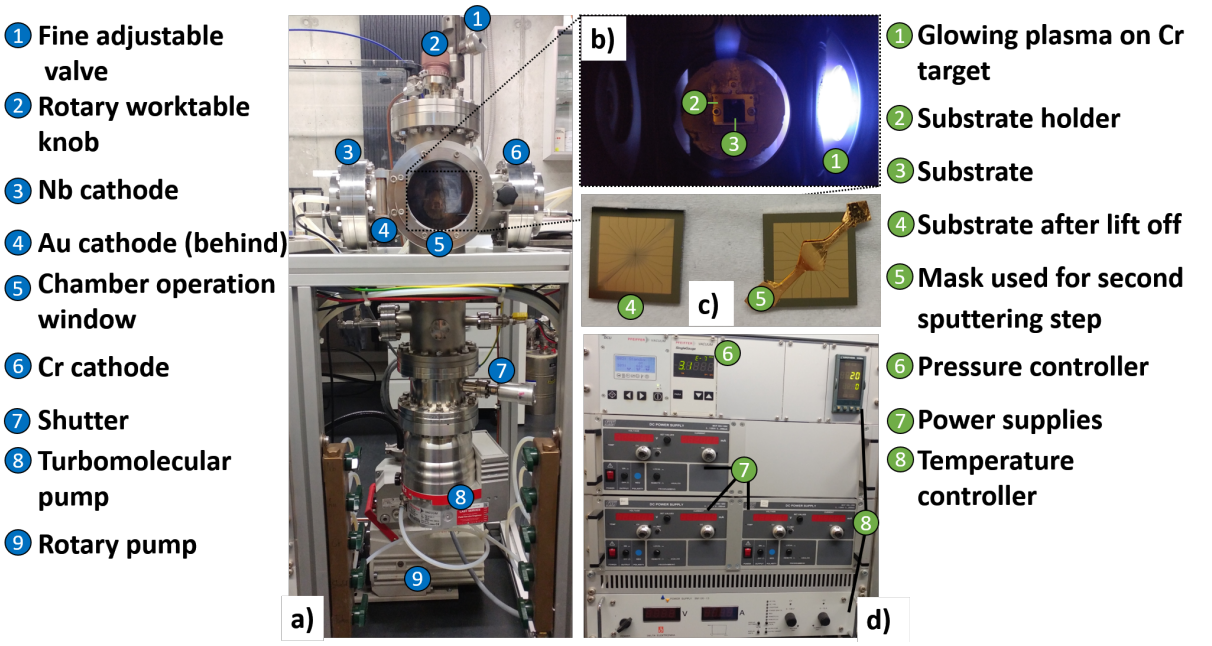

Figure 2.3: a) Photograph of the DC magnetron sputtering setup. b) Inset: The inside of the chamber when the Cr sputtering process is taking place. The substrate will be turned facing the target as soon as the operator wants to start the metal deposition on the target. The Ar-plasma next to the target is enlightening the chamber with the element-characteristic violet plasma glow. c) On the left, a substrate after lift-off. The shadow effect of the sputtering mask used in the second sputtering step is recognizable. On the right, a substrate with the PET mask before the second sputtering step. d) Power supply units and controllers of the electrical setup components.

The setup used for the deposition of Cr-Au contacts defined by UVL on the substrates consists of a custom-built DC magnetron sputtering chamber and the electronic instruments, such as DC power supplies for the targets, pressure and temperature controllers. A photograph of the DC magnetron sputtering setup used in this work is shown in Figure 2.3 (a). The HV chamber made of stainless steel is connected through a fine adjustable valve to a gas inlet tube for the Ar supply. The chamber is a 6-way spherical cross where three flanges on the horizontal axis are equipped with 2-inch Cr, Au and Nb targets of 99.99% purity. The bottom flange is connected to the pumps

(turbo molecular pump and rotary pump). A movable shutter is placed between the turbo molecular pump and the rest of the chamber in order to protect the turbine of the turbomolecular pump from sputtered material deposition. The target is bolted directly to the cathode body. Behind the target, one magnet is positioned at the central axis working as one magnetic pole. The other pole is formed by a ring of magnets around the outer edge of the target. The magnets and the back of the target are water cooled.
On the central vertical axis of the vacuum feedthrough the chamber has a rotary worktable. The substrate processed by UVL, after being attached on a customized holder, is positioned on the electrically-grounded worktable at the same height as the targets. By means of the rotating worktable, the substrate can be positioned directly in front of the target during the sputtering process and it is maintained at room temperature. Before sputtering, the chamber has been evacuated in order to reach a background pressure in the range of 7.5×10^{-8} - 3.4×10^{-7} mbar. Just before the sputtering process, the Ar is supplied into the chamber and a direct current voltage is applied between the cathode and anode by a DC power supply. Since the distance between the target and the substrate is fixed, the pressure and voltage have to be adjusted for the sputtering of the different targets.
Because of the weak adherence of the Au layer, a Cr sputtered film is used as adhesive intermediate layer between the Au layer and the substrate surface. The Cr sputtering has been conducted applying a potential around -360 V at a chamber pressure of 7×10^{-2} mbar. At these conditions, the plasma is stable turning into a constant deposition rate of about 16.5 s/nm. For the Au sputtering, a potential around -380 V has been used. A pressure of 1.6×10^{-2} mbar has been maintained in the chamber to reach a constant deposition rate of about 3 s/nm. On the same substrate, two sputtering steps have been carried out. The first one consists of the deposition on the whole substrate of Cr-Au film having a thickness of about 35 nm. Cr sputtering lasted for 180 s leading to the deposition of about 11 nm. Au sputtering has been conducted for 70 s producing about 24 nm of Au film. The second sputtering step has been carried out with a mask (obtained by a PolyEthylene Terephthalate (PET) transparency film) covering the central area of the substrate. In this region, the FEBID nanostructures are later on deposited. On the second step, only Au has been sputtered for 300 s leading to the deposition of about 100 nm Au film.
These two steps have been necessary in order to maintain in the central region of the substrate about the same height between the electrodes and the very thin FEBID nanostructures. The thin electrodes have been particularly crucial to reduce the mechanical stress of the FEBID deposit region overlapping the electrodes used to establish electrical contact. Moreover, the thicker Au layer of the contact-pads on the outer part of the substrate is especially useful during the ultrasonic wedge bonding step to avoid bonding through to the Si/SiO_2 substrate. The thickness calibration of the

sputtered films and the Cr-Au contacts thickness has been confirmed by AFM investigations.

After the Cr-Au film sputtering, the substrates have been subjected to a lift-off step. It consists in leaving the substrate in a remover bath (AR 300-76, ALLRESIST GmbH) at 80°C for 2 h. During this time, the photoresist under the film get dissolved and the sputtered metal layer on it is stripped away, whereas the rest of the sputtered film deposited directly onto the substrate remains intact.
Afterwards, sonication for 15 min in a new bath of remover has been carried to reduce the height of upstanding edges which resulted from lift-off. The remover has been afterwards rinsed off with DI water and the substrate has been dried with a N_2 blow gun. Finally, the chip has been cleaned in a solution of H_2O_2 and H_2SO_4 in a 1:3 ratio (piranha solution) to remove surface contaminants.

2.1.3 Chip assembly

After the contact-pad preparation, the substrates have been assembled on ceramic board supports with 24 contact Cu-pins covered with Au. The obtained carrier chip can be directly mounted in a socket on a custom-built heatable stage adapter for the dual-beam SEM-FIB and on a ^{3}He-cryostat sample rod adapter. The substrate contacts are connected to the 24 carrier chip Au-plated contacts by Au wires (Heraus GmbH) having a thickness of 32 μm using wedge bonding, which relies on the application of ultrasonic power to establish the connection.
The substrates have been secured with screw Cu-clamps on a Cu-block which is fixed on the board. On the Cu-block and next to the substrate, a temperature sensor Pt-1000 [115] is attached to monitor *in situ* the temperature during the Pt-C FEBID catalytic purification and AS-ALD experiments. The Cu-block has been successively screwed against the copper part of the socket in order to have optimal thermal coupling and the same electrical ground potential as the dual-beam SEM-FIB stage and of the ^{3}He-cryostat sample rod. The socket is connected *via* a vacuum feedthrough to the electrical measurement setup. External switches are connected between the chip electrodes and the electrical sources in order to force the electrodes to ground when needed. In this way, *in situ* electrical measurements can be conducted with external current/voltage sources on the nanodevices fabricated in the center of the substrate and connected to the Cr-Au contacts.
In Figure 2.4 (a), a chip on the dual-beam SEM-FIB heatable stage adapter is shown. The heatable stage adapter can be directly mounted in the center of the eucentric stage inside the dual-beam SEM-FIB system (Figure 2.4 (b)) and it allows to carry *in situ* electrical measurements up to 350°C. By a cable-bus using a feedthrough, the 24 pins

are connected to the outside electrical measurement setup. In Figure 2.4(c) a calibration sample is placed on the carrier chip attached to the ^{3}He-cryostat sample rod.

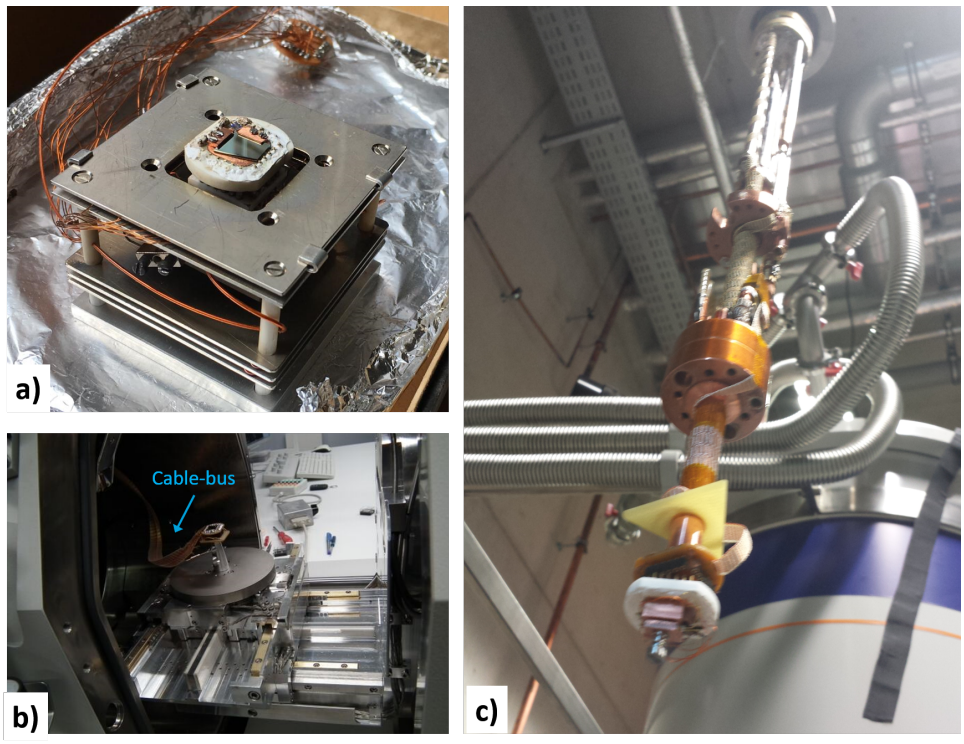

Figure 2.4: a) The temperature-controlled ceramic carrier chip is placed on a heatable dual-beam SEM-FIB stage adapter. b) The inside of the FEI dual-beam SEM-FIB is shown. The adapter shown in a) will be placed in the middle of the stage and connected to the external electrical measurement setup by a cable-bus through a vacuum feedthrough. c) A temperature calibration sample is attached by a ceramic carrier chip on the ^{3}He-cryostat sample rod.

2.2 Instruments for nanofabrication and topographic/compositional analysis

Most of the nanofabrication methods described in the following section (Section 2.3) are based on the use of a SEM and a FIB. In this section, the two instruments and their functions are described (Subsection 2.2.1). Apart from that, the SEM has been used for its conventional purpose, such as the morphological investigation of the samples. In the following subsections, the description of the other analytical techniques used to investigate the samples is given.

The SEM morphological analysis has been actually combined to a compositional investigation, such as EDX. The analysis can be directly performed *in situ* in the

dual-beam SEM-FIB. The EDX technique is described in Subsection 2.2.2.
Topographic investigations by the use of a AFM are also conducted in order to fully characterize the samples. The AFM method is described in Subsection 2.2.3.

2.2.1 Scanning Electron Microscope (SEM) / Focused Ion Beam (FIB)

A SEM is an electron microscope that produces images of a sample by scanning the surface with a focused beam of electrons. By the interaction of the electrons with the atoms at various depths within the sample, electrons are emitted from the sample with different energies and trajectories. These electrons are collected in detectors providing signals used to produce an image [116, 117].
Beside the conventional use of a SEM as topographical analysis instrument, its rastering electrical beam is used in the FEBID nanofabrication method, which is described in Subsection 2.3.1.
The SEM used in this work is equipped with a Field Emission Gun (FEG) in which a sharply pointed Tungsten emitter (tip radius of about 100 nm) protrudes 250 μm from the suppressor electrode. The emitter is a Schottky type cathode in which the electrons are ejected by thermionic emission. The tungsten tip is covered with a layer of zirconium oxide, which reduces the work function [118]. The source is maintained in Ultra High Vacuum (UHV) at about 6×10^{-10} mbar by an Ion Getter Pump (IGP) [119]. The energy and the current of the electron beam can be adjusted from 0.5 to 30 keV and from 1 pA to 20 nA, respectively. In the vicinity of the anode, the electron beam cross-section (the crossover) is in the 10-50 μm range. In order to produce a sharp image, the beam diameter has to be smaller. For this reason, one or two condenser and objective electrostatic/electromagnetic lenses and apertures are used to accelerate, (de)magnify and converge the electron beam crossover and focus it onto the specimen surface where finally the beam spot will be about 1 nm to 5 nm in diameter.
The lens system consists of a condenser lens, an objective lens, scanning coils and monopole magnetic immersion final lens. As optical lenses in a light based microscope are used to change the path of the light in a desired direction, the electrostatic/electromagnetic lenses in a SEM are used to shape and deflect the trajectory of the electrons by the action of an electromagnetic field.
The electrostatic lenses consist of electrodes separated by very small distances in order to generate very high electric fields. Electromagnetic lenses are constructed with ferromagnetic materials and a tight copper wire wound into a coil producing a magnetic field with a focal length that can be changed by varying the current through the coil.

The scanning coils are two pairs of electromagnetic deflection coils. They are used to scan

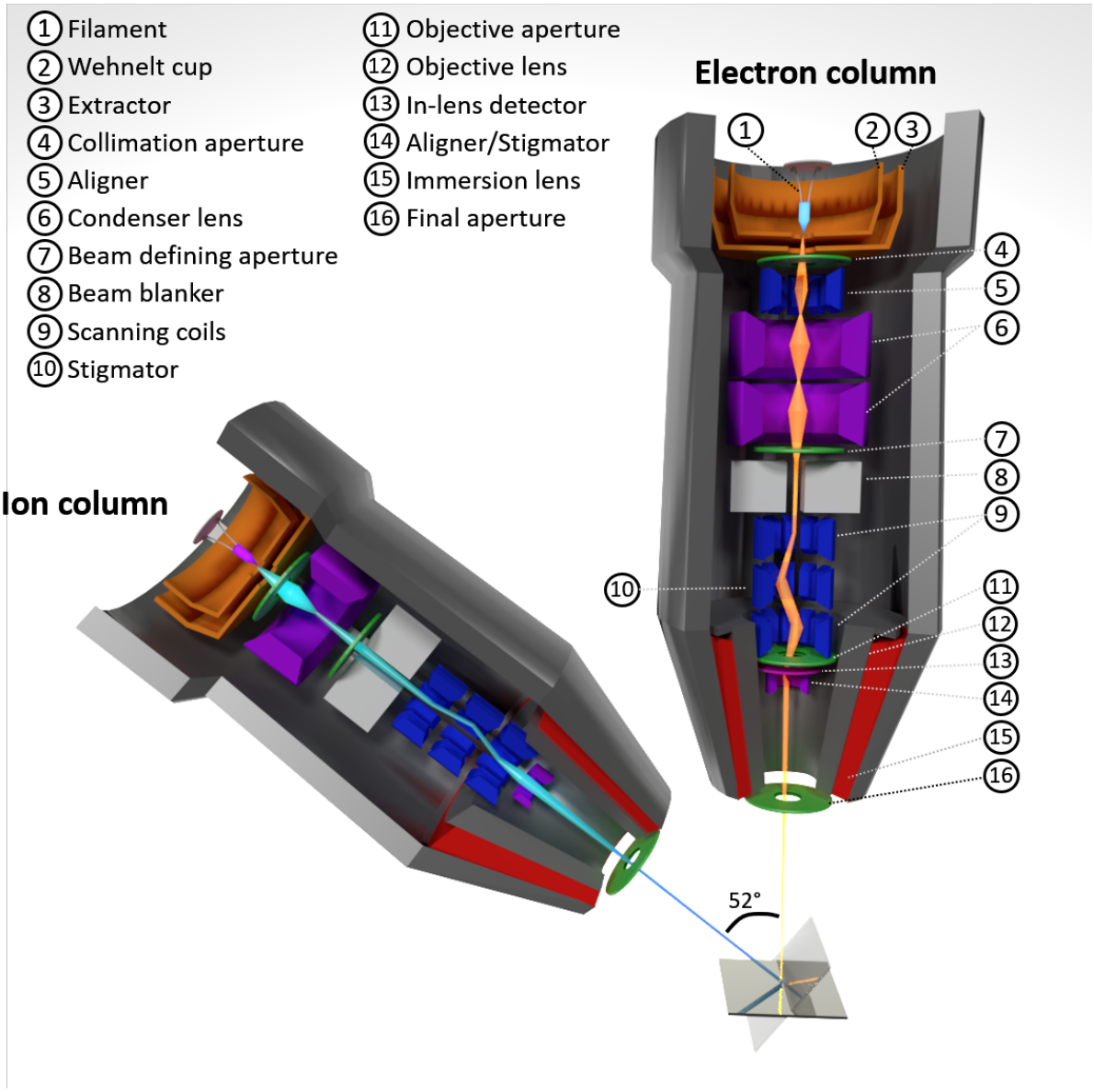

Figure 2.5: Schematic illustration of the dual-beam SEM-FIB. The two columns present similar components and they are outlined in the picture. A dual-beam system is a compact and complete solution for analytic and manufacturing purposes at the nanoscale.

the electron beam in a raster scan pattern and deflect the electron beam horizontally and vertically over the specimen surface to construct the image point-by-point and line-by-line.
An immersion lens can be used to further lower the diameter of the beam and provide better resolution. It establishes a magnetic field with short focal length in the proximity of the specimen surface providing a high-resolution SEM mode.
The objective, scanning and immersion coils are embedded in a pole piece made of high magnetic permeability material that serves to direct the magnetic field. The column, in which the condenser and objective lens fields act, is evacuated by a second IGP in order to maintain the vacuum to the 9×10^{-8} mbar range. An exemplary sketch of the dual-beam SEM-FIB system with the highlighted components is shown in Figure 2.5.

Electron beam and target interaction As soon as the electron beam reaches the target surface, the Primary Electrons (PE) of the beam will interact with the atoms of the target generating several interaction products. The main products of the interaction are Secondary Electrons (SE), BackScattered Electrons (BSE), Auger electrons, and a variety of X-rays [120, 121]. When the primary beam hits a solid target, elastic and inelastic collisions are taking place. The elastic scattering processes lead to beam broadening *via* changes in electron trajectory directions, whereas inelastic collisions manifest as energy losses *via* ionization (secondary electron generation), plasmon excitation, molecule dissociation, phonon scattering (heat), and characteristic X-rays emission along the primary electron trajectories with the sequential transfer of energy to other electrons in the specimen. A representative schematic of the interaction product generation depending on the distance from the PE beam impact point is given in Figure 2.6.
The incident primary electron beam interacts with atoms having different depth in the sample depending on the energy of the primary beam and the atomic number of the sample atoms [122]. The interaction region has typically a droplet-shaped volume with a depth range up to a few μm. The higher the primary electrons acceleration voltage is, the deeper the electrons can travel in the material and the interaction volume will be bigger. Moreover, the higher the Z atom number of the atom material is, the sooner the primary electrons propagation will be stopped in the material and the interaction volume will be reduced.
The inelastic interaction between primary beam electrons and sample atoms leads to SE generation and subsequent escape of the SE from the sample into the vacuum. The high-energy PE, which after inelastic collisions travel into the sample, are finally escaping the sample material with an energy $> 50\,\text{eV}$. Those electrons are called BackScattered Electrons (BSE) since they are scattered back in the pole piece direction. The emitted low-energy electrons, called secondary electrons with a cut-off

conventionally set to $< 50\,\text{eV}$, have their origin in the sample.
SE emission arises due to loosely bound electrons in the valence or conduction band of the sample atoms. There are primarily two kinds of SE generated from the sample labelled as SE I and SE II. The SE I are generated in the near proximity of the primary beam point of impact. Differently, the SE II are generated by the BSE away from the PE impact point. The position of SE II emission depends on the energy cascade and inelastic interaction that the primary electron is experiencing [123]. In this process, other by-products as Auger electrons and X-rays are generated. However, only those SE and Auger electrons, which are within 100 nm from the surface, can escape from the sample and be detected. In addition to SE I and SE II, another type of SE, identified as SE III, is generated when high-energy BSE, that emerge from the sample, strike the objective pole piece or the chamber walls and generate SE from these surfaces. These electrons could introduce a background signal and artefacts in the detector signal [124].

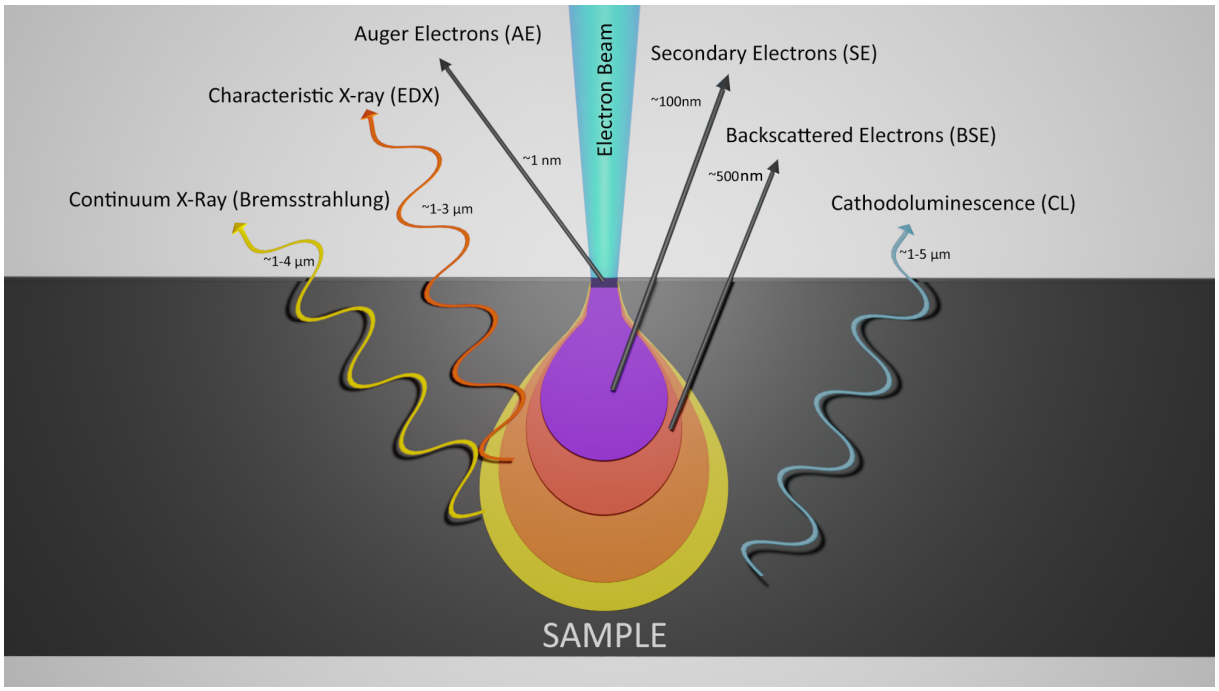

Figure 2.6: The interaction volumes for generation of SE, Auger electrons, BSE, characteristic X-rays, continuum X-rays, and *Cathodoluminescence (CL)* X-rays.

A schematic representation of the generation mechanism of the electrons, that have been described so far, is available in Figure 2.7 (a). The electrons, that after this interaction have enough energy to leave the substrate surface have a characteristic energy spectrum. A typical energy spectrum of these electrons, BSE and SE, is shown in Figure 2.7 (b).

To help the microscopists with the interpretation of imaging, microanalysis and EBL

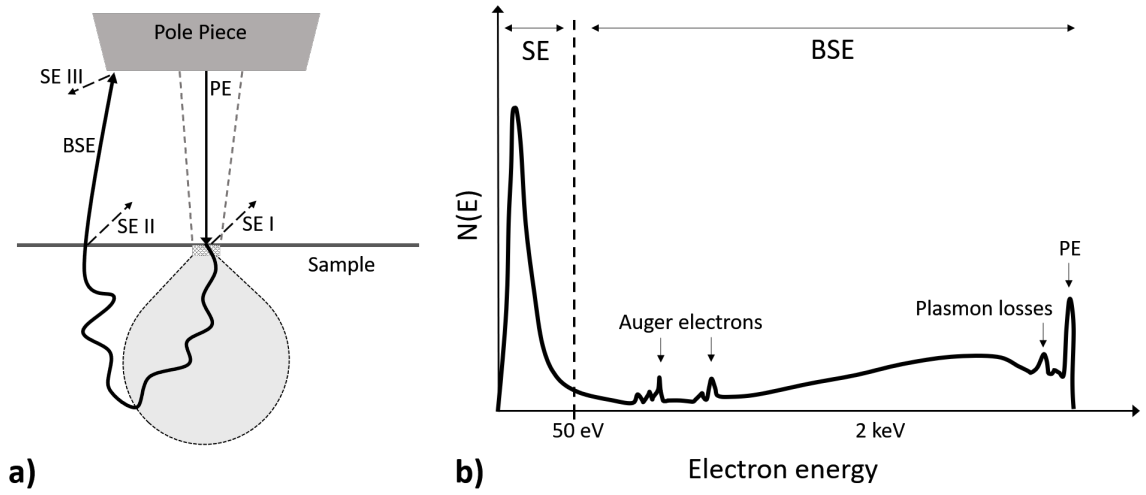

Figure 2.7: a) Sketch of the generated BSE and SE from the collision of the primary beam with the sample. Different types of SE: SE I, SE II and SE III are produced depending on their generation position with respect to the PE impact position. b) A typical energy spectrum of electrons emitted from the substrate. Adapted from [121].

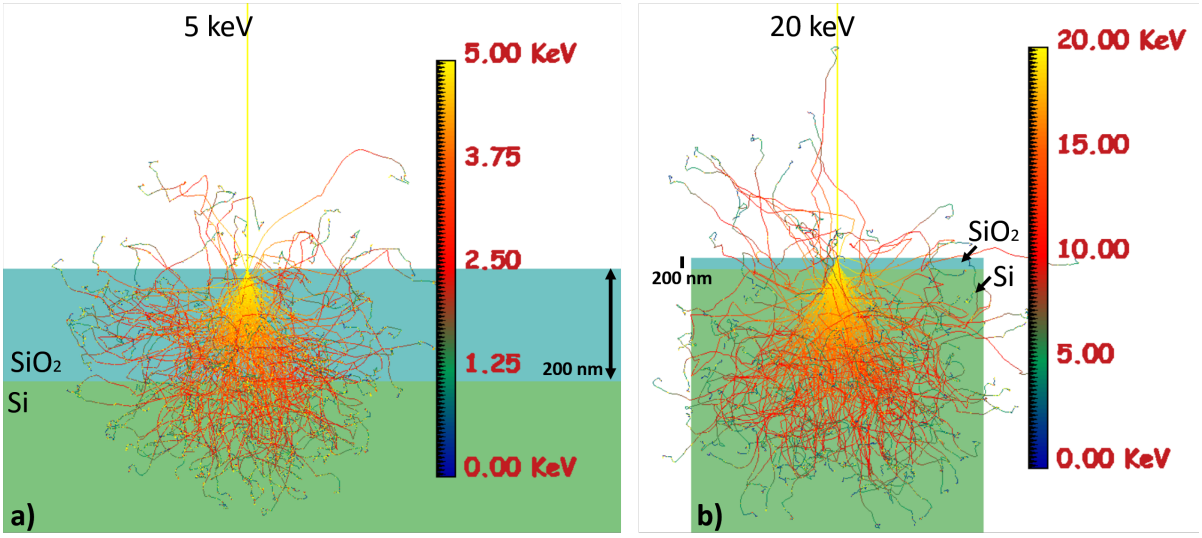

Figure 2.8: The free software version of CASINO 3.3.0.4 has been used for the simulations of the interaction volume of beams with the typical PE energies (5 (a) and 20 (b) keV) on a Si/SiO_2 substrate as used in this work. 200 of the 1000 primary electrons interacting trajectories in 5 μm^3 substrate have been simulated.

applications, Monte Carlo simulations have been widely used to predict the propagation of a primary electron beam in a material. A very successful simulation software of the electron propagation in materials, *CASINO*, has been developed by Drouin [125]. The findings of this simulations field are also particularly helpful for understanding the deposit formation in FEBID. In Subsection 2.3.1, the deposit formation theory in FEBID is described.

In Figure 2.8, the simulations conducted with the two main primary beam acceleration voltages (5 and 20 kV) and substrate configuration (Si substrate covered with 200 nm of thermal grown SiO_2) used for the research work reported here are shown. It is possible to notice how different the size of the interaction volume is in the two cases. For 5 kV (Figure 2.8 (a)), an interaction volume of less than 500 nm in diameter results from the simulation. Moreover, the rapid color change of the trajectories indicate a quite drastic energy loss inside the material. On the contrary, the simulated interactions for a 20 kV primary beam acceleration voltage show a wider spreading of the electron trajectories in the substrate, reaching almost 5 μm in depth (Figure 2.8 (b)).

The dual-beam chamber is equipped with different detectors, which collect the emitted products of the interaction of the primary beam with the sample in the vicinity of the beam hitting point. The different interaction products provide different types of information about the sample.

For example, in-lens electron detectors can detect SE and BSE that come back to the primary beam direction. In particular, the in-lens secondary electron detector is used to detect SE I electrons generated near the upper region of the interaction volume and therefore they provide direct information of the sample surface. In this case, the SE are re-accelerated and focused through the electromagnetic objective lens field towards the in-lens detector. There, they hit a scintillator and generate photons that are finally directed through a light guide and transferred to a photomultiplier. The obtained photons will generate signals that after the amplifier action will be analysed by the computer generating an image.

The in-lens BSE detector is a solid state (or semiconductor) detector. It consists of a doped semiconductor material (usually silicon) and is placed directly above the sample. This detector collects the high-energy back scattered electrons. Considering the different nuclei sizes between heavy and light elements, sample materials with elements composed of a higher atomic number (Z) yield more backscattered electrons than lower Z elements. When a high-energy BSE hits the semiconductor material, it generates electron-hole pairs paying the band gap energy of the silicon (1.1 eV). Therefore, the number of electron-hole pairs generated is proportional to the energy of the incident electrons. The output current signal is then amplified and analyzed by the computer producing a compositional map of the specimen.

The Everhart-Thornley detector is positioned near the beam target. It collects the SE,

as they are low energetic electrons generated in the vicinity of the sample surface. The detector consists of a Faraday grid, a scintillator and a photomultiplier.
Additionally, characteristic X-rays are collected from the specimen by an EDX detector. An illustrative sketch of the described detectors is shown in Figure 2.9.

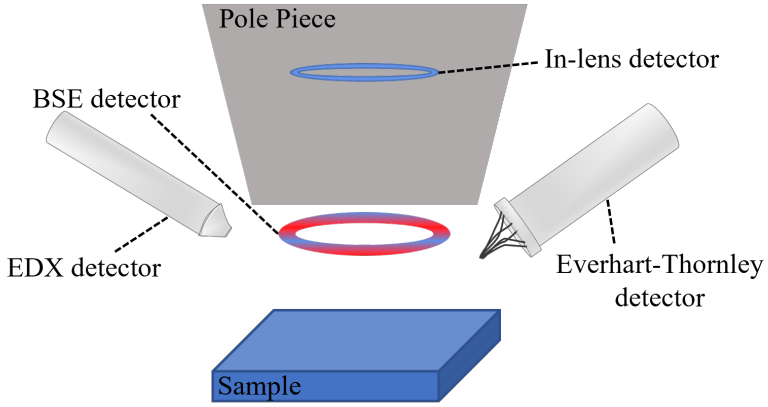

Figure 2.9: Basic types of the detectors available in a SEM chamber.

The microscope used in this work is a FEI dual-beam SEM-FIB Novananolab 600. The instrument consists of a system with both electron and ion beam columns, allowing the same feature to be investigated using both beams. The FIB is tilted at 38° from the electron beam column. The source of ions is a Liquid Metal Ion Source (LMIS). Gallium provides the best combination of low vapor pressure, large atomic number, and ease of use. Heated gallium flows to the tip of a Tungsten needle where an electric field ionizes the Ga atoms and causes field emission of the ions. The Ga^+-gun has adjustable energy (5 - 30 keV) and current (1 pA - 20 nA). The FIB column is connected to an IGP which maintains the pressure of 6×10^{-8} mbar.
Beside the source type and the use of different electromagnetic lenses (since the deflected charge particles are different), the SEM and the FIB are very similar. Therefore, a detailed description of the FIB operation is omitted for redundancy. The interaction processes and products resulting from the collision of the primary ion beam with the sample surface are, beyond the one described for the electron beam, the ejection of specimen atoms (milling), ion implantation, structural defects creation, heating, etc. Details about the ion beam interaction with the sample and in particular its milling effect are provided in Subsection 2.3.4.1. An exemplary sketch of the components of the SEM and FIB for the dual beam system used in this work has been already shown in Figure 2.5.
In the chamber the sample is mounted on an eucentric stage which can be translated in x, y, and z direction as well as rotated around the y- and z-axis, respectively. On the stage, the sample can be mounted using a special *in situ* electrical measurement

adapter. Electrical measurements are also possible on a heatable stage adapter used, for example, for the catalytic purification of FEBID deposits (Subsection 2.3.1.4) and AS-ALD experiments (Subsection 2.3.2). Photographs of the electrically heatable stage adapter and the electrical adapter (without heating option) have been already shown in Figure 2.4(a) and (b), respectively.

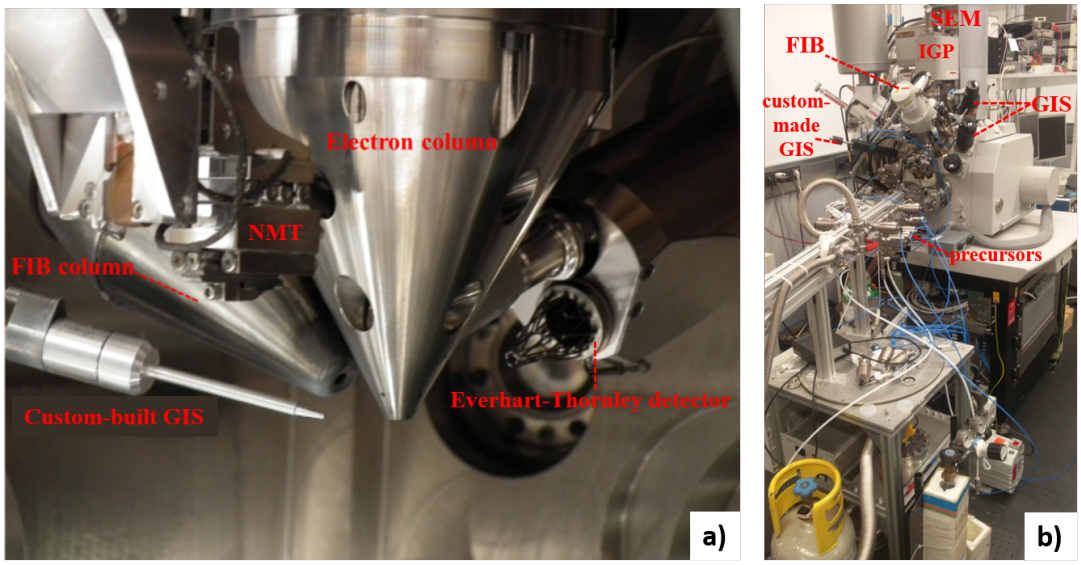

Figure 2.10: a) Inside view of the dual-beam SEM-FIB Novananolab 600. b) Photograph from the outside of the dual-beam system. Some of the visible options are listed in the figure.

In addition, the SEM is equipped with four commercial and one custom-built Gas Injection System (GIS). The custom-built GIS has been used for the catalytic purification of FEBID deposits (Subsection 2.3.1.4) and AS-ALD (Subsection 2.3.2) to provide O_2 in the proximity of the sample surface. By the use of a turbomolecular pump and a rotary pump, the base pressure in the chamber is about 3×10^{-7} mbar.
In the chamber a Charge-Coupled Device (CCD) camera, an air plasma generator and a mass spectrometer are also present. In addition, a Nanomanipulator (NMT) and an *in situ* AFM can be mounted in the chamber when needed. Photographs of the inside and of the outside of the FEI dual-beam SEM-FIB Novananolab 600 used in this work are shown in Figure 2.10 (a) and (b), respectively. The instrument, thanks to the increasing available options, has become in the course of the years a very complete and versatile tool.

2.2.2 Energy Dispersive X-ray (EDX) spectroscopy

EDX spectroscopy is an analytical chemical characterization technique that is conducted

inside the chamber of a SEM. By using a dedicated detector, characteristic X-rays generated in the core of the interaction volume of the primary beam with the material, are collected (see Figure 2.6) [117].
The compositional characterization capability of this analysis is based on the generation of energetically distinctive X-rays only depending on the material atom with whom the electron interacts. Every element has a unique atomic structure leading to a unique set of energies on its electromagnetic emission spectrum.
The principle of this analysis technique is based on the stimulated ejection of electrons and characteristic X-rays from the sample when the primary electron beam interacts with the sample atoms. In an interaction, an electron originally positioned in the inner shell (K shell) of the atom can be ejected. In order to reduce energy, the vacancy of the ejected electron will be occupied by an electron belonging to a more energetic shell. This process goes along with the emission of an X-ray having as energy the difference between the higher energy shell and the lower energy shell. The energy shells are characteristic for every atom, therefore a precise compositional analysis of the sample can be obtained by collecting the X-rays ejected from the sample. An additional Bremsstrahlung energy background signal is present in the energy spectrum. An exemplary sketch of the described X-ray generation process is shown in Figure 2.11 (a).

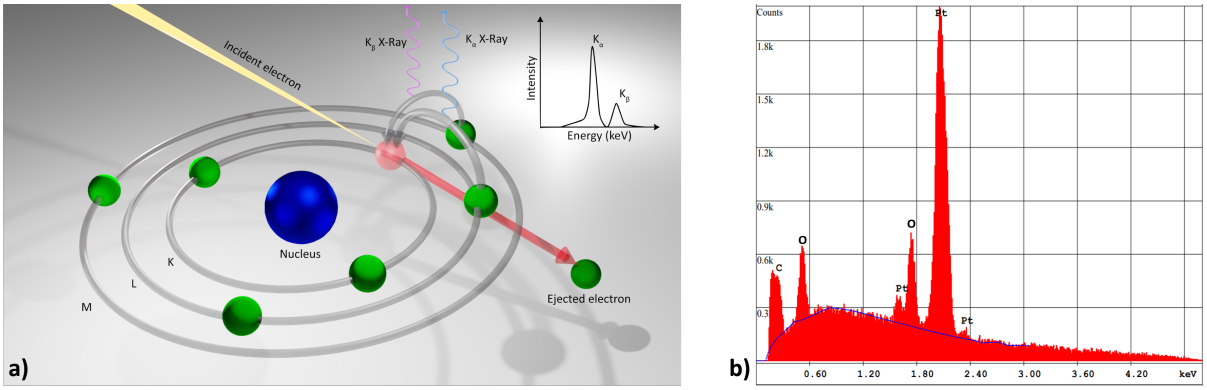

Figure 2.11: a) X-ray generation process: 1) The energy transferred to the atomic electron leads to its ejection leaving a hole behind. 2) Its position is filled by another electron from a higher energy shell and the characteristic X-ray is released. b) A typical EDX spectrum. Blue line: Bremsstrahlung energy spectrum is shown as additional signal background.

The X-rays are collected by the respective detector and analysed by the energy-dispersive spectrometer. The X-rays are therefore differentiated in energy and most of the elements of the periodic table can be detected by this technique. The quantity of X-rays emitted by each element is reported in an EDX spectrum on the y-axis as counts. The peak area is therefore directly proportional to the concentration of the element (mass or atomic fraction). The position of the peaks in a EDX spectra is

described by the empirical Moselay Law [126]. As a result, information about elemental composition and relative concentration in the specimen region on which the primary electron beam is focused are directly extracted. In Figure 2.11 (b), a typical EDX spectrum, that has been collected on a $1.5 \times 1.5\,\mu m^2$ purified Pt FEBID structure with 5 keV accelerated electron beam, is shown.
As typical beam parameters, 5 kV and 1.6 nA have been used for the measurements reported in this work. Depending on the beam energy applied, only some elements can be detected. For this reason, the beam energy used for the analysis should be at least greater than twice the energy of the characteristic X-rays of the material under examination in order to detect a certain element. The use of a small acceleration voltage for the EDX analysis ensures near-surface generation of X-rays. In this way, compositional investigations on nanostructures with limited thickness on a substrate can be conducted.
An EDAX Genesis 2000 EDX spectrometer, that is mounted directly to the FEI dual-beam SEM-FIB NovaNanoLab 600, has been used for the analysis. The X-rays ejected from the sample are collected by an X-ray detector in close proximity to the sample (Figure 2.9). The Si(Li) detector is a p-i-n device formed by lithium drifting of p-type silicon. The semiconductor crystal needs to be cooled to cryogenic temperatures with liquid nitrogen. Cooling the detector minimizes noise and increases the peak resolution. Moreover, the low temperature increases the life time of the detector, since Li diffuses towards the surface at room temperature, degrading the material over time. The X-rays are converted into voltage signals by electron-hole pairs generation in the semiconductor crystal. The signals are then processed by a pulse processor that removes noise by averaging the incoming signal. The output from the pulse processor is passed to a multi-channel analyser for data display. The energy range of the spectrum is divided into the channels and the respective X-rays energies are assigned to them. The data is displayed in the EDAX software as a spectrum showing the number of X-rays (counts) assigned to each energy channel [127].
EDX measurements have been particularly useful during the optimization of the FEBID and AS-ALD combined technique. The compositional monitoring of the deposited, purified and sequentially grown material gave direct proof of the effectiveness of the process. The results of these analysis are shown in Subsection 2.3.2.

2.2.3 Atomic Force Microscopy (AFM)

AFM is a topography imaging technique with nanometer resolution [128]. The method is based on the scanning action of a probe - cantilever - on the surface of the investigated nanostructure and on the feedback loop used to adjust parameters needed

to image the surface. By using attractive and repulsive interaction forces between the few atoms attached to the cantilever tip and the sample atoms (which are located as close as 0.1 - 100 nm), the profile of a sample can be mapped in the x, y and z direction. The sharp tip of the cantilever (5 - 10 nm radius) is scanned over the sample surface and it can be either in contact with the sample (static or contact mode) or it oscillates in close proximity to the surface of the sample (dynamic or tapping mode). When the cantilever tip is close to the sample, it experiences an attractive force. Then, the force becomes repulsive at a certain point. In particular, there are three main contributions as attractive forces. These are the short-range chemical force, the van der Waals force and the electrostatic force. On the other hand, repulsive forces are Pauli exclusion and electron-electron Coulomb interaction forces. Whereas the effective ranges of these forces are different, one of them is dominant depending on the cantilever distance from the sample surface.

Static mode is the original and simplest mode to operate an AFM. The possible configurations of static mode are operation in constant force and in constant height. In constant force mode, the cantilever deflection is the feedback parameter and the force can be estimated by using Hooke's law. In constant height mode, the probe maintains a fixed height above the sample and there is no force feedback. Constant height mode is typically used in atomic resolution AFM.

In the dynamic mode, the cantilever is driven with a sinusoidal motion at a fixed excitation energy by a piezo-actuator. The cantilever behaves as a damped spring or a single harmonic oscillator vibrating close to its resonance frequency. Typical resonance frequencies, due to the small size of these cantilevers, are in the kilohertz up to Megahertz range. The interaction of the tip with the sample changes the effective spring constant of the cantilever altering the cantilever's vibrating amplitude, phase and resonance frequency. These changes are used as feedback parameters. Because the cantilever operates at resonance and interacts with the sample as the probe 'taps' along the surface, it is a non-invasive method in comparison to contact imaging modes in which direct contact between cantilever tip and sample can deform the sample surface and/or the tip.

In order to detect the cantilever bending motion at a specific location (x, y), optical deflection techniques are commonly used. A laser beam from a Laser Diode (LD) is focused on the back side end of the cantilever, and the reflected beam is aligned at the center of a Position Sensitive Photo Diode (PSPD). When the cantilever is bent, the beam path is shifted and generates the intensity difference between the upper and lower photodiodes (A-B signal). This signal is fed to a Proportion-Integration (PI) controller to control the bending angle of the cantilever through a z-piezo-actuator. An illustrative sketch of the AFM principle and of the described operation modes is shown in Figure 2.12.

In this work, an EasyScan 2 (Nanosurf) AFM has been mainly used in dynamic mode to measure the thickness of the FEBID seed layers and of the AS-ALD grown nanostructures. In particular, the used dynamic mode is an Amplitude Modulation mode of Atomic Force Microscopy (AM-AFM), which uses the oscillation amplitude as feedback parameter [129]. The substrate and the AFM have been isolated from the environment by a vibration isolation platform and an acoustic isolation coverage. *Ex situ* high-resolution AFM measurements on AS-ALD nanostructures have been also conducted with a Nano Wizard 3 Ultra (JPK) available in the group of Prof. Dr. Alexander Heckel in the Institute for Organic Chemistry and Chemical Biology, Goethe University, Frankfurt am Main, Germany.

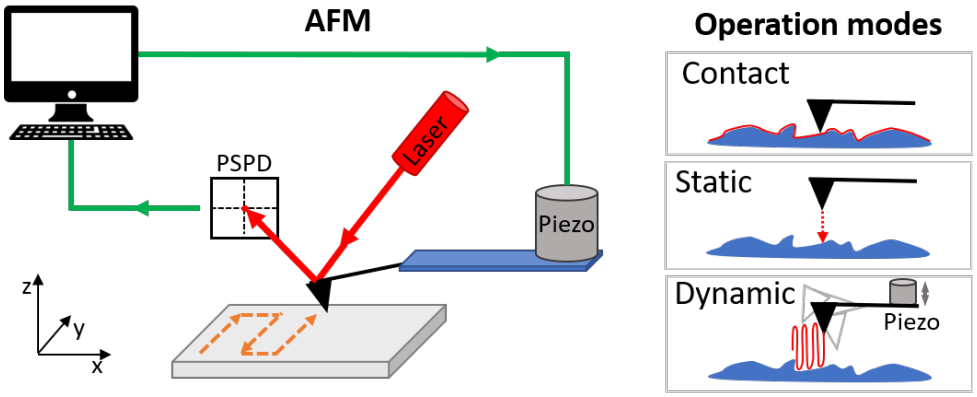

Figure 2.12: On the left, explanatory graphical representation of the AFM working principle and setup. On the right, descriptive sketch of the AFM operation modes.

2.3 Nanofabrication techniques and optimizations

This section describes the nanofabrication methods employed in this work.
Firstly, the section reports the nanofabrication technique that has been mostly used: Focused Electron Beam Induced Deposition (FEBID, Subsection 2.3.1). Secondly, the section covers the techniques that have been used in combination with FEBID, such as electron irradiation of Pt-C FEBID deposits and catalytic purification of Pt-C FEBID deposits (Subsubsection 2.3.1.4). A separate Subsection (2.3.2) is dedicated to a more complex technique: AS-ALD on purified Pt FEBID seed layers.
Finally, the methods, which are required together with FEBID and its combined techniques for the fabrication of the nanosystems investigated in this work, are introduced. For instance, drop casting nanoparticle deposition (Subsection 2.3.3) and ion etching by Ga^+ and Ar^+ (Subsection 2.3.4) are presented.

2.3.1 Focused Electron Beam Induced Deposition (FEBID)

In the last decades, the rapid growth of nanotechnology and the increasing demand of controlled fabrication of nanostructures ignited the interest in FEBID. Curiously, the idea of FEBID originated from the observation of unwanted hydrocarbon contamination deposits during routine sample examination with the electron beam and it has been limited for a long time to lithography mask reparation.
Thanks to its high flexibility, FEBID provides direct-write synthesis of functional structures with complex patterning geometry and nanometer resolution on (and with) a wide variety of materials [20, 81, 130].
FEBID can be considered as a local electron-beam induced CVD with the decomposition of a gaseous precursor caused by the interaction of the electron-beam with a solid substrate.
The process takes place in the vacuum chamber of a SEM or a Transmission Electron Microscope (TEM). The molecules of a precursor are brought in close proximity to a substrate by the small capillary of a GIS. The energy, which is transferred from the electron-beam (scanning the substrate surface) to the adsorbed precursor gas molecules, dissociates the precursor into a volatile and non-volatile part. On the substrate, the non-volatile fragments pile up causing local material growth, whereas the volatile fragments desorb from the surface and are pumped away from the chamber. Sub-nanometer resolution of FEBID deposits has been reached with TEM [131–133]. On the other hand, the minimal resolution reported for FEBID in a SEM on a bulk substrate is 3 nm [134, 135].
Most precursors that are used for FEBID have been designed as CVD precursors. A group apart is formed by those precursors based on the carbonyl (CO) group, such as $Fe(CO)_5$, $Co_2(CO)_8$, $Mo(CO)_6$, $W(CO)_6$, $HCo_3Fe(CO)_{12}$, etc. Furthermore, the increasing interest on the technique encourages the research of suitable FEBID precursors and the deposition of binary metal alloys by the simultaneous or cycled use of two precursor gases [136–139]. An extensive list of FEBID precursors has been compiled by Silvis-Cividjian [140].
Depending on the precursor, final deposits allow a diverse range of applications such as nanolithography [141, 142], lithography-mask repair [143, 144], protection coverage for TEM investigations [145], fabrication of attachments in mechanics [146], nano optics [147–149], magnetic applications [150–153], tunable disordered systems [15], functional scanning probe microscopy tips fabrication [154, 155], superconductor material deposition [156, 157], atomic layer seeding [6, 158], nanoscale stress-strain sensors assembly [159, 160], or gas and humidity sensors fabrication [161, 162]. Moreover, FEBID applications portfolio increases every year with new challenging creative ideas.
The deposition process can be described as an interplay of the surface physical

mechanisms of the molecules and the electrons interaction with the material (substrate and precursor molecules) [163] and is based on three physical/chemical processes: *substrate-precursor molecule interaction, electron-substrate interaction* and *electron-precursor molecule interaction*. The description of these processes will follow in the next paragraphs.

Substrate-Precursor molecule interaction: At the beginning of the FEBID process, the precursor molecules physisorb on the substrate where four key processes are assumed to determine the surface density of adsorbed molecules here considered for cylindrical symmetry, $N(r,t)$ [2, 20, 163]. The four processes are:

1. Adsorption from the gas phase governed by the precursor flux J, the sticking probability s and coverage N/N_0, where N_0 is the maximum monolayer density,
2. Surface diffusion from the surrounding area to the irradiated area governed by the diffusion coefficient D and the concentration gradient,
3. Thermally-induced desorption,
4. Electron-stimulated desorption of the physisorbed molecules after a residence time τ (depending on the materials and temperature of precursor and substrate),
5. Molecule dissociation followed by desorption of volatile organic ligands. This process is governed by the electron flux profile $f(r)$ and the energy-integrated dissociation cross-section σ. More details on the decomposition factor are given in the following paragraph *Electron-Precursor molecule interaction*.

Figure 2.13 gives a graphical overview of the FEBID process and the described adsorption mechanisms. Hence, the molecule adsorption rate $\partial N/\partial t$ for Lagmuir regime (i. e. max. one monolayer) is:

$$\frac{\partial N(r,t)}{\partial t} = \underbrace{sJ(1-\frac{N(r,t)}{N_0})}_{\text{Adsorption}} + \underbrace{D(\frac{\partial^2 N(r,t)}{\partial r^2}+\frac{1}{r}\frac{\partial N(r,t)}{\partial r})}_{\text{Diffusion}} - \underbrace{\frac{N(r,t)}{\tau}}_{\text{Desorption}} - \underbrace{\sigma f(r) N(r,t)}_{\text{Decomposition}} \quad (2.1)$$

Electron-substrate interaction: At a second stage, the electron beam rasters the substrate surface and a deposit is formed. The precursor molecules can be dissociated by many species of electrons which happen to circulate in their proximity. For this reason, it is important to understand how the deposition process is influenced by the spatial and energy distribution of the electrons involved in the process.
In the dedicated paragraph of Subsection 2.2.1, the different products originating from the primary beam interaction with a substrate have been described and in Figure 2.7 all

the electrons involved in the interaction are graphically indicated (a) with their energy spectrum (b). Moreover, the simulations shown in Figure 2.8 of the interaction volume depending on the PE energy show how large the electron back-emission surface from the substrate is.

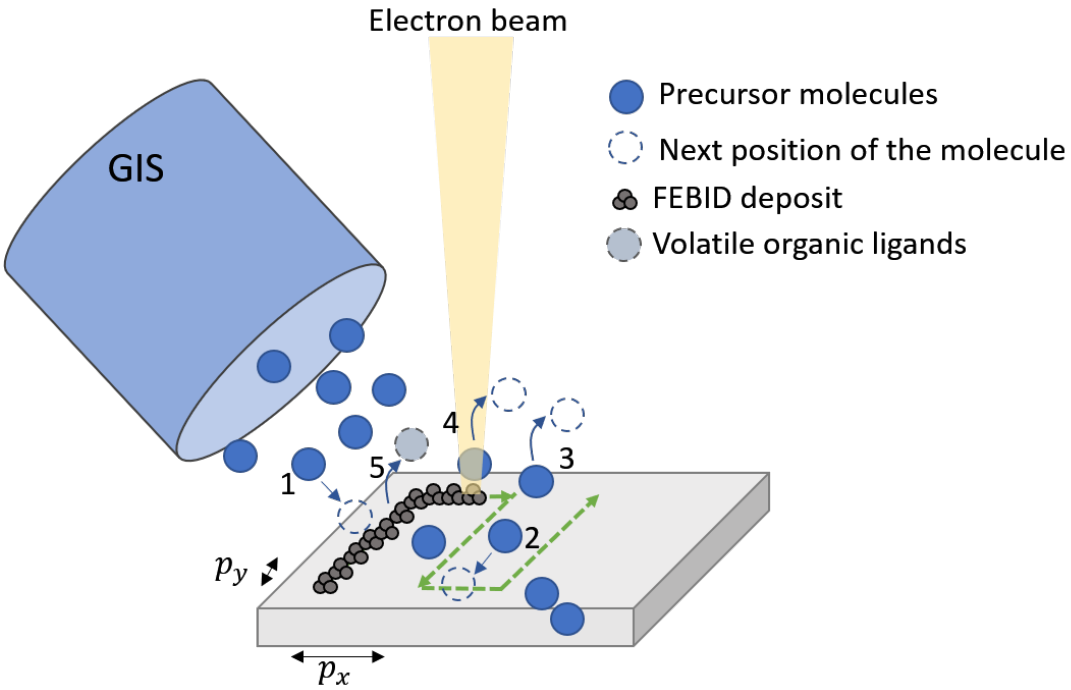

Figure 2.13: Illustrative representation of the FEBID process. Precursor molecules are supplied by a GIS and physisorb (1) on the surface. There, they are diffusing on the substrate surface (2). Some of them will desorb by thermally- (3) and/or electron-induced processes (4). As a result, a solid deposit will form on the substrate position scanned by the electron beam and volatile ligands will be released (5). The beam is scanning the substrate surface following a strategy described by the patterning parameters. p_x and p_y are the line spacing and step size, also known as pitch in x and y direction, respectively. Figure inspired by [20].

Electron-Precursor molecule interaction: The emitted electrons, crossing the substrate-vacuum interface with a suitable energy to dissociate the precursor molecules, break the molecules that physisorb in their proximity and the deposit forms on the substrate. Many studies have been carried out to elucidate the specific type of electrons responsible for the dissociation of surface adsorbed molecules and the following deposition [82, 130, 164]. An important piece of information has been gained through Monte Carlo simulations and experiments. In particular, they gave an exhaustive explenation of the complex physical phenomena involved in the deposition taking into account factors such as the electron flux as well as their spatial and energy distribution,

the cross-section of the precursor as a function of electron energy, the precursor residence time and the electron-beam-induced heating [164–169]. From these results, the important role of the secondary electrons in the deposition rate and also in the spatial distribution and resolution of the deposits has been demonstrated.
In brief, the model assumes second-order kinetics of molecule dissociation by electrons [163]. The probability that an electron induces the scission of a bond in a precursor molecule depends on the electron energy and is generally expressed as a cross-section $\sigma(E)$. Its calculation is a complex matter and it has been studied for different precursors extensively [81]. From the electron-impact dissociation cross-section and Equation 2.1, it is possible to derive the deposition rate $R(x)$ in units of molecules per unit area per unit time at any site on the surface situated at a distance x from the incident point of the primary beam. $R(x)$ is governed by the formula

$$R(x) = \int_0^{E_0} N(x)\sigma(E)f(E,x)dE \tag{2.2}$$

as provided by [170].
$\sigma(E)$ is experimentally found to show a maximum at a certain energy in the range of a few tens of eV. In this range of energy, cross-sections for dissociative electron-molecule interactions are observed for many FEBID precursors [130, 171]. At the same time, the distribution of secondary electrons has a maximum in the same range of energy (Figure 2.7 (b)) resulting in secondary electron interactions to be the main cause of precursor molecules dissociation. It is important to mention the work of van Dorp [172], who reported a detailed study on the electron-induced dissociation cross-section of the FEBID precursor $Me_3PtCpMe$ used in this work.
For FEBID, the whole electron relevant energy range causing molecular fragmentation is 1 meV (slowed-down SE) up to keV (PE, FSE and BSE). The different electron-molecule interaction processes taking place in FEBID can be summarized as shown in Table 2.1.
In FEBID, DEA processes are most efficient close to the SE energy peak resulting in the deposition of very stable neutral fragments [164]. The ratio of relevant secondary electrons and precursor flux, in conjunction with precursor residence time and diffusion coefficient determine the precursor density on the growing surface. The precursor density controls the growth regime. Accordingly, the FEBID deposit composition and morphology depends on different types of growth regime.

Process type	Electron-molecule interaction
Elastic scattering	$e^-(E_0) + AB \rightarrow AB + e^-(E_0)$
Vibration Excitation (VE)	$e^-(E_0) + AB \rightarrow AB(v) + e^-(E_{res})$
Electronic Excitation (EE)	$e^-(E_0) + AB \rightarrow AB^* + e^-(E_{res})$
Dissociative Electron Attachment (DEA)	$e^- + AB \rightarrow A^\bullet + B^-$
Neutral Dissociation (ND)	$e^- + AB \rightarrow A^\bullet + B^\bullet + e^-$
Dissociative Ionization (DI)	$e^- + AB \rightarrow A^\bullet + B^+ + 2e^-$
Bipolar Dissociation (BD)	$e^- + AB \rightarrow A^- + B^+ + e^-$

Table 2.1: Electron-molecule interaction processes relevant for FEBID [171]. E_0 is the PE kinetic energy and E_{res} is the residual kinetic energy of an electron after the process. The neutral ground state (AB) is depicted along with the volatile state of the molecule ($AB(v)$). Anionic dissociated molecule parts ($A^{+/-}$, $B^{+/-}$), electronically excited molecule states (AB^*) and neutral ions ($A^\bullet$, $B^\bullet$) are obtained as products from the different interactions.

The FEBID growth regimes can be mainly divided into two extremes: (1) the Mass Transport Limited (MTL) regime, in which more potentially dissociating electrons are available than precursor molecules and (2) the Reaction Rate Limited (RRL) regime in which the situation is reversed and the abundance of precursor molecules on the surface is higher compared to potentially dissociating electrons [2]. For an optimal geometrical and compositional uniform structure deposition, it is important to tune the FEBID writing parameters such as dwell time, pitch, refresh time, precursor temperature and beam current [173, 174].

Finally, an exemplary representation of the different type of electrons involved in the deposit formation is given in Figure 2.14 (a). Depending of where the electrons reach the interface with vacuum, a material deposition is initiated at that place. The deposit (and related co-deposit) formation dependence from the SE II and BSE generation region is described according to [175, 176]. The SE II and BSE originated in the deposit (SE II-D and BSE-D) mostly cause the broadening of the structure on the top volume. On the other hand, SE II and BSE generated from the substrate (SE II-S and BSE-S) are mostly responsible for initial deposit and co-deposit formation. In addition, also other electrons as Forward Scattered Electrons (FSE) produced by forward scattering of PE in the growing deposit can generate indirectly other deposition events.

In Figure 2.14 (b), a sketch in section view of a deposit is shown where the deposit areas, which are formed by the interaction of precursor molecules with SE originating from different target regions, are highlighted. The initial material deposition is initiated from the interaction of SE and BSE, that are generated in the substrate and reach the surface-vacuum interface, with the precursor molecules found in their proximity. This material builds the inside of the FEBID deposit (red region). As soon as the deposit

increases its volume, the PE strike first on the deposit generating there SE, BSE and FSE and afterwards they reach the substrate. The further deposition of material on top of the deposit itself is then generated both from the interaction of precursor molecules with the electrons leaving the deposit and from the substrate (grey region). In this way, material deposition can continue mainly on the deposit itself or in its vicinity forming a co-deposit.

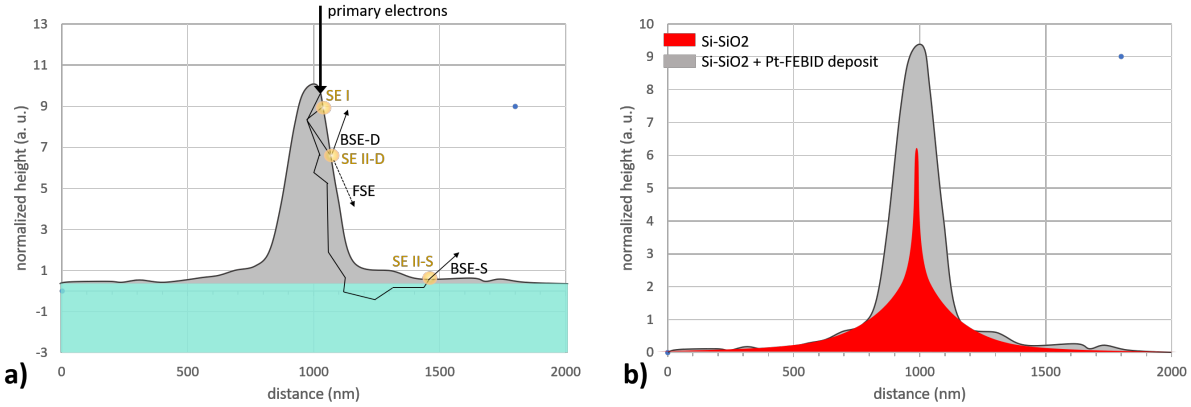

Figure 2.14: a) The different type of SE, BSE and FSE generated from the FEBID deposit and the substrate are shown. b) Exemplary sketch of the deposit formation. Colors are used to highlight the deposit volumes which are obtained by the interaction of physisorbing precursor molecules with SE and BSE arising from different regions. Adapted from [175].

2.3.1.1 Technical parameters of the writing process

The growth rate, composition, and structure of FEBID deposits are influenced by several parameters that govern the writing process and can be set from the SEM operator. They are the primary-beam energy or acceleration voltage E_0 (1 - 30 keV), the beam current I (5 pA - 24 nA), the dwell time t_D (50 ns - 100 ms) as the time for which the electron beam is held stationary on a particular point of the surface, the pitch p_x, p_y (1 - 100 nm) (Figure 2.13) as the distance between the center of neighboring dwell points in x and y direction, and the passes as the number of loops for which the writing pattern is repeated, n_L.

There are other important parameters that influence the writing process: the refresh/replenishment time t_r that is the time period for which the writing is paused between two successive loops, the writing strategy for the pattern (e. g. raster or serpentine), the writing strategy for multiples patterns (e. g. parallel or sequential writing) and parameters influencing the flux of the precursor such as the heating temperature of the precursor $T_{precursor}$ and the (vertical and planar) distance between the GIS and the target position. In this work, the FEBID fabrication strategy and setup

reported in the experimental sections, are described by the previously listed writing parameters. When not specified, an isotropic pitch (in x, and y) has been used.

2.3.1.2 $C_5H_4CH_3Pt(CH_3)_3$ Precursor

In the present work, $C_5H_4CH_3Pt(CH_3)_3$ or $Me_3PtCpMe$(IV) (Me: methyl, Cp: cyclopentadienyl), Trimethyl(methylcyclopentadienyl)platinum(IV) has been used as organometallic precursor for Pt deposition in FEBID and AS-ALD. The molecular structure of the precursor is shown in Figure 2.15.

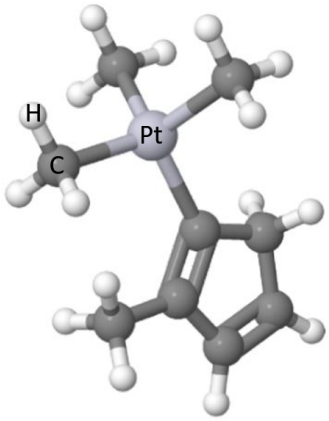

Figure 2.15: The molecular structure of $C_5H_4CH_3Pt(CH_3)_3$ obtained by Jmol [177], an open-source Java viewer for chemical structures in 3D.

This Pt-based precursor has been popular for CVD and ALD [178, 179] applications since pure platinum films can be obtained from it [180], whereas FEBID structures created from the same precursor lead to a Pt content of 16-26 at.% [82, 83].
Studies about the interactions between metal orbitals and orbitals of the ligand can provide valuable insight into how organometallic molecules react after electron stimulation or higher temperature [181]. The dissociation process for $Me_3PtCpMe$ in FEBID strongly depends on the beam energy. Moreover, environmental factors like residual gas in the process chamber and the associated partial pressures of the precursor gas have a strong influence on the final deposit composition.
The dissociation of the parent compound due to electron interaction results in the reduction of platinum atoms and the evolution of gas phase methane and hydrogen while polyhapto unsaturated hydrocarbon ligands result in incorporation of carbon atoms from the π-bound ligand into the deposit [182]. Moreover, from single electron-molecule collision studies involving $Me_3PtCpMe$, Engmann *et al.* [183] traced the loss of a single methyl group as the primary fragmentation channel in a DEA process expressed by the

Equation:

$$MX + e^- \rightarrow [MX]^{-*} \rightarrow M + X^- \tag{2.3}$$

It results in Pt atoms aggregating to fcc nanocrystals (diameter: 2 - 3 nm) in competition to reticulation (network formation) of the organic ligand fragments. The carbon reticulation reactions can result in a chemically and mechanically very stable amorphous hydrogenated carbon network providing 1 nm scale distance between the metal grains [13, 163]. Namely, the amorphous-carbon network surrounds the metal nanocrystals and limits their aggregate size. Therefore, the presence of the carbon contamination negatively impacts the electronic and optical properties of the deposited material for most applications.

In the last years, big efforts have been dedicated in finding new approaches to control the electron-initiated chemistry of precursor molecules that enables a complete dissociation. In the case of $Me_3PtCpMe$, experiments of Pt-C FEBID [13, 184, 185], simulations of Pt-C FEBID [166, 167, 176] and mass spectrometric detection experiments for dissociation cross-section determination [172, 182] have been done in order to understand the process and improve the metal content in the deposits. As a matter of fact, the research about the best writing parameters to reach the highest Pt-concentration has been carried out leading to contradictory results. According to Plank *et al.* [186], the dwell time, beam energy and defocus have little effect on resistivity and composition. On the other hand, Botman *et al.* [187] have shown an improvement of Pt concentration, based on increasing the beam current. The differing results suggest that the process conditions such as partial precursor pressure and residual gas contribution of the process chamber have a strong influence on the final deposit composition [20]. This conclusion has to be taken into account for further improvements of the technique.

Technical characteristics: The precursor consist of white/transparent crystals (98 %, CAS Number: 94442-22-5 Merck KGaA). It has high volatility, since its vapor pressure has been estimated to be about 0.54 kPa at 373 K and its melting point is 23°C at a vapor pressure of 0,071 hPa [188]. The molecular weight is 319.31 amu.

For the FEBID process, the precursor is treated with vacuum heating at 44°C inside an Omniprobe GIS for circa 60 min prior to deposition in order to convert this compound into a gaseous state. The precursor in gaseous state has been injected into the dual-beam FIB-SEM chamber by means of a capillary with 0.5 mm inner diameter at a tilt angle to the substrate surface of circa 74°. The capillary has been held at a distance of 100 μm, both vertically from the substrate surface and horizontally from the center of the SEM field of view. The substrate is maintained at room temperature since it has been demonstrated that the deposit chemical composition is independent of substrate temperature or electron

fluence [189]. The composition of the FEBID deposits as deduced from EDX analysis has been 24 at.% of Pt and 76 at.% of carbon, which is typical for the used setup [4].

2.3.1.3 Proximity effect (Co-deposit formation)

The ability to interconnect different nanostructures is crucial to nanocircuit fabrication efforts. Despite FEBID's ability to generate a range of different nanostructures for nanolithography and prototyping applications, FEBID is not without its shortcomings. It is well-known that although FEBID provides very defined structures, it has the disadvantage of yielding an inner and outer co-deposition halo in close proximity to the defined structure caused by precursor dissociation beyond the incident beam location [131, 135, 190, 191].

Different studies [175, 176, 192] have shown that these broadening deposition effects have been mainly caused by substrate related BSE and SE II (BSE-S and SE II-S). An example of this effect can be seen in Figure 2.14. In addition, Schmied and collaborators [176] found that the shape of the inner and outer halos depend on the primary beam energy. Their crucial outcome can be summarized saying that intermediate primary energies (as e. g. 20 kV) can lead to significant edge broadening as a consequence of substrate related backscattered electron contribution resulting in distinct plateaus around the intended deposit. An exemplary sketch of those effects is given in Figure 2.16.

It has been suggested in order to avoid proximity exposure by BSE and SE, to use thin substrates such as carbon or silicon nitride membranes, which transmit primary electrons without large inelastic energy loss. Alternatively, the use of very small exposure times and high accelleration voltages on bulk samples should be preferred. These conditions will reduce the volume of SE next to the incident point, since only SE produced near the surface will be able to escape the surface. The most probable escape depth λ of SE is independent of the primary electron energy (as long as $E_0 >$ first ionization energy), it is proportional to the first ionization energy and approximately inversely proportional to the electron density of the element [193]. Furthermore, high primary beam energy generates minimal BSE-related proximal deposition due to the low BSE yield and the large BSE radius.

In the present work, we used bulk substrates for which only increasing the primary beam energy is beneficial to avoid co-deposit formation. A strategy compromise had to be found between the use of short or long dwell time in combination with multiple or few passes, respectively. The best strategy suited for the different type of application has been therefore evaluated in order to avoid 'smudge' or charge drift effects on the final structure.

For the fabrication of the conducting nanostructures presented in the experimental

sections, the proximity effect in Pt-C FEBID has been a major drawback. As a matter of fact, in Appendix C.1, it is underlined that co-deposit between FEBID electrodes can lead to leakage currents. Nevertheless, in Chapter 4 the successful use of localised Ar^+-etching to erase co-deposit formed in conjunction with the Pt-C FEBID of a dot, which has been used as island for the fabrication of functioning SET devices, is proposed. The localized Ar^+-etching provides a slight erosion of the dot and its surrounding. Consequently, it produces the eradication of undesired charge trapping in localized states near the nanoisland.

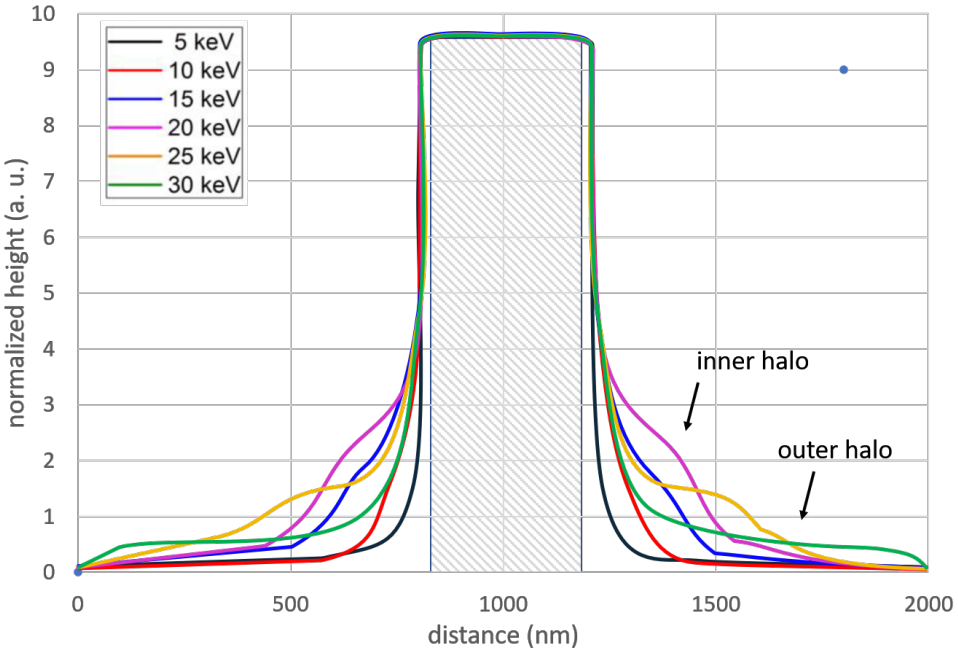

Figure 2.16: Exemplary sketch of co-deposit formation depending on the primary beam energy. The striped area represents the ideal deposit shape expected from the defined pattern. Adapted from [176].

2.3.1.4 Post-growth treatments of FEBID deposit from $C_5H_4CH_3Pt(CH_3)_3$ precursor

Despite the flexibility and processing capabilities of Pt-C FEBID from $Me_3PtCpMe$ precursor, some significant drawbacks limit the scope of its current applications. One of the major limitations is that the nanostructures contain organic contaminations resulting in relatively high resistive material ($\rho \sim 10^7\,\mu\Omega\,\mathrm{cm}$) [21, 187]. The high material resistivity prevents the direct application of such deposits as nanoelectrodes [194].

Several developments over the last decade have brought significant progress into advancing the conductivity of Pt-C FEBID deposits from $Me_3PtCpMe$. The different curing methods can be separated in post-growth techniques and *in situ* parallel

treatments. On the one hand, post-growth methods comprise pulsed laser light exposure [195], electron beam post-growth irradiation [15, 21, 196, 197], annealing (300° - 500°C) with O_2 exposure, air or H-radicals reactive atmosphere [4, 198, 199] and a combination of the listed methods at a lower substrate temperature (120°C) [200] or even at room temperature [5, 201, 202]. On the other hand, *in situ* parallel treatments consist of simultaneous supply of O_2 and Pt precursor in one step [3, 202] and laser-assisted deposition [203].
In the following paragraphs, the two methods employed in this work to improve the conductivity of FEBID deposits from the $Me_3PtCpMe$ precursor are described. They comprise electron beam post-growth irradiation and post-growth catalytic purification.

Post-growth electron beam irradiation of Pt-C FEBID deposits The first experimental evidence that the Pt-C FEBID material changes its conductivity upon post-growth electron beam irradiation has been given by Schwalb *et al.* [159]. In their study, the scientists offer a direct application of this material property demonstrating that the sensitivity of strain-sensor elements fabricated by FEBID employing $Me_3PtCpMe$ depends on the electrical conductivity of the elements. Later on, Porrati *et al.* [21] and Sachser *et al.* [15] offered accurate studies about the change of conductivity for as-grown FEBID structures and gradually post-growth e-beam irradiated structures up to the maximum irradiation dose $6.72\,\mu\mathrm{C}\,\mu\mathrm{m}^{-2}$. The results of Sachser *et al.* are adapted in Figure 2.17. With their work, the scientists demonstrated how delocalization effects due to tunneling and the tendency for localization can be finely tuned from insulating to metallic behavior by using the post-growth electron irradiation. The remarkable result has been the obtained wide range of conductivity tunability of the electron irradiated Pt-C FEBID material. In the results reported, the samples' conductivity at room temperature varied over three orders of magnitude ranging in absolute values from $16\,\Omega^{-1}\,\mathrm{m}^{-1}$ to $1.25\times10^{5}\,\Omega^{-1}\,\mathrm{m}^{-1}$.
The criterion described by Moebius [204] to analyse the logarithmic derivative of the conductivity $w = d\,ln\sigma/d\,lnT$ has been used in order to reliably distinguish the transition between metallic and insulating behavior. Moreover, they observed that the change of the structures' resistivity at room temperature varies over three orders of magnitude reaching $800\,\mu\Omega\,\mathrm{cm}$. This remarkable result has been attributed to microstructural changes of the deposit matrix. As TEM [205] and Micro-Raman [206] investigations proved, the matrix tends to be subject to a continuous carbon loss, graphitization and formation of bigger crystallites by coalescence. Accordingly, the number of sp^2 hybridized carbon bonds ($1s \rightarrow \pi^*$, graphite) increases at the expense of sp^3 bonds ($1s \rightarrow \sigma^*$, diamond) [207]. Therefore, the increase of electrical conductivity is attributed to the improved inter-grain tunnel coupling due to an effective reduction of the tunneling barrier height as consequence of the matrix graphitization. The carbon

loss is ascribed to an electron beam-induced reaction of carbon with residual oxygen gas and/or water vapor present in the SEM chamber and to an induced diffusion of the few embedded O_2 molecules in the deposit, that reacting with the amorphous-carbon matrix, are finally leaving the surface of the deposit as CO [208].

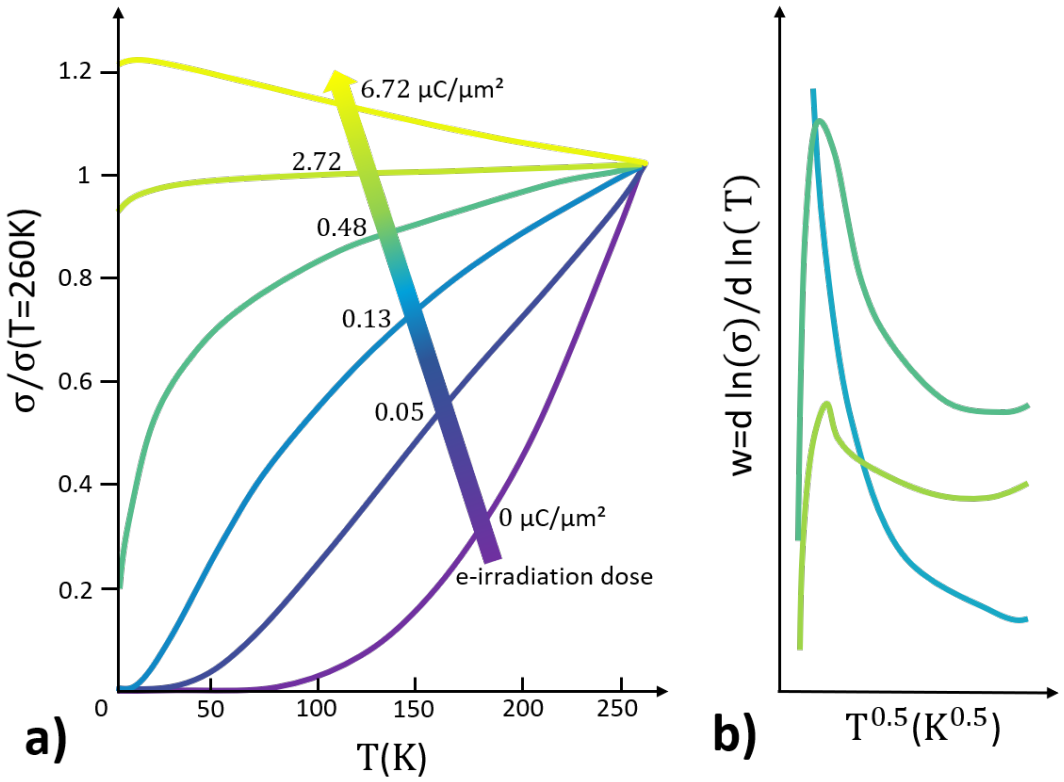

Figure 2.17: a) Normalized temperature-dependent conductivity curve for Pt-C FEBID deposits irradiated with an increasing dose up to 6.72 μC μm^{-2}. b) Representative example of the logarithmic derivative $w = d\,ln\sigma/d\,lnT$ trend of the samples reported in (a). The characteristic trend evolution of w allows to distinguish for samples in the MIT whether the material tends to behave more as an insulator or a metal. Samples exhibiting a cusp-like trend tend to have a metallic behavior. Adapted from [15].

For thin structures and high irradiation dose, a complete carbon loss has been observed by Frabboni *et al.* [197]. In their work, they explained that even local heating and knock-on effects on the organic matrix are assisting the carbon loss process [209, 210].
It is important to point out that an irradiation treatment, that would promote metallic behavior, on large areas (several microns) would cost several hours. Furthermore, high irradiation doses may induce structure broadening and degradation of the lateral resolution. For this reason, the application of such a treatment to increase the conductivity of Pt-C FEBID devices is limited.
In this work, post-growth electron beam irradiation has been employed in order to

increase the conductivity of a Pt-C FEBID dot used as island for SET fabrication. By the use of different irradiation doses (1 and $3\,\mu C\,\mu m^{-2}$) the tunnel coupling strength inside the island and between the leads has been tuned so that the effect of the island's electronic granularity on the SET device performance could be studied. The results of the described application are reported in Section 4.3.
Because of the versatile option to measure *in situ* the resistance of the deposits, the irradiation could be started/interrupted by using the output pin of the source meter connected to the BNC connector of the SEM beam-blanker as soon as a defined time or resistance value is reached. Consequently, the source meter can be programmed to send a digital I/O signal to the OUT pin connected to the beam-blanker. In particular, an interesting application of the programmable source meter and beam blanker functionality during the irradiation process is that as soon as the source meter measures a user defined resistance value of the probed structure, a I/O signal is sent through the OUT pin to the beam blanker that electrostatically blanks the electron beam and interrupts the irradiation. This function is particularly useful for step-like or long irradiations. For short and very accurate irradiation doses, such as the one required for the irradiation step on the Pt-C FEBID island in the SET devices, the measurement and the blanking is too 'slow' in comparison to the speed of the irradiation effect. For this reason, defined irradiation doses have been used for the fabrication of Pt-C FEBID-based SETs. Details of the electron irradiation application on Pt-C FEBID SET islands are given in Subsection 4.1.4.

Catalytic purification of Pt-C FEBID deposits The catalytic purification of Pt-C FEBID structures developed by Sachser *at al.* [4] has been used in this work for the fabrication of pure Pt-nanostructures employed in two separate projects. Firstly, the purified Pt FEBID nanostructures have been used as functional seed layer templates for the following AS-ALD process (Subsection 2.3.2). Secondly, the purification of Pt-C FEBID nanostructures has been used in order to obtain *in situ* metal bridge leads between the pre-patterned Cr-Au contacts defined by UVL and the randomly placed nanoparticle assemblies deposited on the surface of the chip substrate from a Au-NP solution by drop casting (Subsection 2.3.3). The electrical characterization of the assemblies built by Au-NP dropcasting and electrical contacting with purified Pt FEBID contacts can be found in Chapter 3.
This purification technique uses the catalytic activity of Pt in combination with O_2 exposure and high substrate temperature to oxidise the carbonaceous component of the deposits. In addition, *in situ* conductance measurements during the purification process have been used to monitor the progress of the process.
For the purification process, the substrate, on which Pt-C FEBID nanostructures have

been written, has to be heated to 150°C inside the dual-beam FIB-SEM chamber. This temperature has been reached by employing a heatable stage adapter equipped with electrical contacts mounted onto a ceramic carrier chip allowing for temperature control of the sample in the range of 22 - 350°C (Figure 2.4 (a)). After the FEBID process, a pause of 2 h has been introduced to pump the residual precursor molecules from the system. At a later time, the temperature has been increased with a rate of 2°C/min to 150°C. A multi-channel gas injection system with an end inner diameter of 0.5 mm and automated valve control [211] has been brought in close proximity to the substrate surface to provide a localized O_2 exposure on the FEBID deposits. The O_2 needle has been kept at an angle of 26° to the sample surface, at a distance of 100 μm above the sample and of 100 μm from the SEM center of view. The O_2 has been provided on the sample surface in a pulsed fashion. Every pulse was lasting for 5 min followed by a pause of 5 min in which the oxygen has been pumped from the system. During the O_2 exposure, the chamber pressure has been increased to 1.5×10^{-5} mbar. The total duration of the purification process has been 160 min and deposits in an area of up to about 2×10^5 μm^2 got purified in parallel. The final resistivity of the structures is 79.5 $\mu\Omega$ cm [4], which is about a factor of 8 larger than that for bulk Pt (10.4 $\mu\Omega$ cm [35]). The low resistivity is a remarkable achievement considering that the initial FEBID seed layer has a chemically purity of only 24 at.% of Pt.

The increase in conductance during the process has been monitored in a 4-pole configuration on one of the nanostructures subjected to the process (SEM picture of the structure is shown on the inset of Figure 2.18 (a)). The purification process runs until the conductance reaches a plateau, which electrically validates the purification of the structures. In Figure 2.18 (a) a typical conductance measurement result during the described purification process is shown. From the curve analysis, it is possible to follow the chemical reaction steps occurring during the process. For the first 1 - 2 oxygen exposures, we can observe that the conductance increase associated to the O_2 exposure is rather low. This effect can be traced back to the small ratio of exposed Pt grains on the surface of as-grown Pt-C FEBID structures. Later, a strong conductance increase can be observed after every oxygen exposure during the pauses. During these periods, the catalytic properties of Pt enable the chemisorption of oxygen, leading to the thermally activated oxidation of carbon at the Pt-C interface. It follows that the CO molecules are released from the deposit. In the final stage, the conductance saturates. This result can be explained by the fact that in the case of a thin deposit, it gets entirely purified or generally the CO desorption is hindered by chemisorbed oxygen blocking the CO molecules attempt to leave the inner level of the deposit by the small channels between neighboring Pt grains. The process results in the removal of the carbonaceous matrix and a pronounced volume reduction with a densification of the Pt-C FEBID structures and their evolution to pure nanoporous Pt structures (Figure

2.18(b)). Although, the definition of the structures after the purification is maintained, the deposits are very thin and porous. For this reason in this work, a subsequent step, namely AS-ALD, has been used to add pure Pt layers onto the metallic FEBID-based nanostructures (Subsection 2.3.2). The purity of the final Pt structures has been also demonstrated by EDX compositional analysis. The results are reported in Figure 2.23 as metal content improvement proof of the fabrication technique promoted in this work.

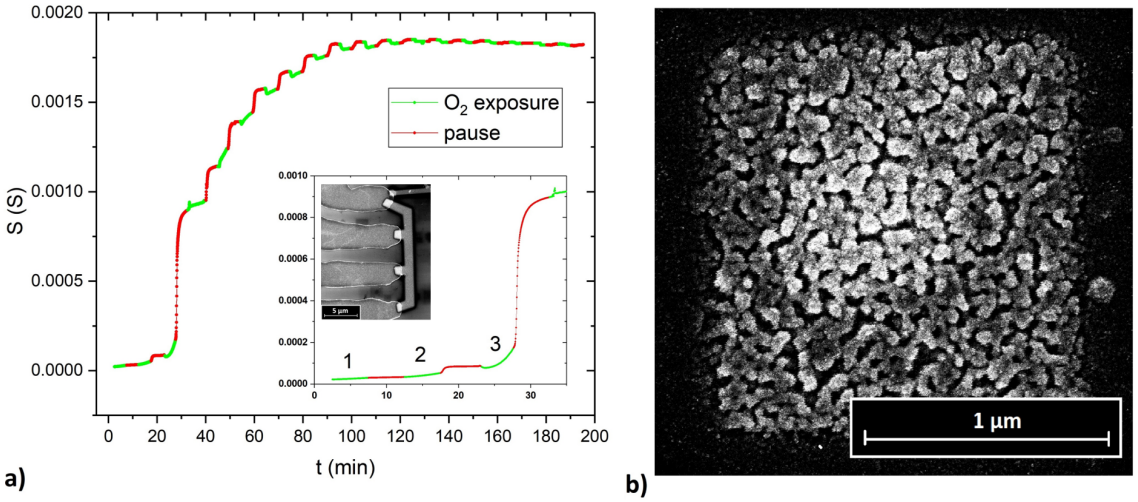

Figure 2.18: a) Overview of the measured time-dependent electrical conductance curve during the catalytic purification process at 150°C and lasting for 160 min. Inset: magnification of the first purification cycles and SEM image of the probed structure. After the O_2 exposure of the third cycle, the conductance shows a rapid relative increase of 85%. b) SEM image of a Pt deposit after purification. The nanoporous morphology of the purified samples is clearly visible.

2.3.2 Area-Selective Atomic Layer Deposition (AS-ALD) on purified Pt FEBID seed layers

In the last decades with the growing complexity of nanodevices, big effort has been devoted in the development of innovative nanomanufacturing approaches that could offer dimension control and material purity, ideally in conjunction with scalability. Techniques as EBL, microcontact and nanotransfer printing serve the purpose having mainly the drawbacks of many processing steps and the use of chemical solutions that can lead to compatibility issues with sensitive surfaces [212–214].

ALD, on its own, is a process for depositing highly uniform and conformal thin films by alternating exposures of a surface to vapors of two chemical reactants which chemisorb on the surface [215]. This succession of different gas-exposures on the surface of the

nanostructures represent one ALD cycle that normally deposits a monolayer or less of material.

Pt ALD relies on surface nucleation generated by catalytic reactions allowing the deposition of pure Pt by subjecting the substrate to alternate exposures of Pt precursor ($Me_3PtCpMe$) and O_2 flux. In this way, pure and low resistive ($12.2 \pm 0.3\,\mu\Omega\,\mathrm{cm}$) Pt films are deposited with submonolayer accuracy of the film thickness but without intrinsic control of the film growth in lateral dimensions [179, 216]. It follows that, Pt ALD is not a suitable technique for contacting applications.

In order to promote AS-ALD, approaches based on masking by resist films [217] or self-assembled monolayers [218] are mostly used. However, the use of resist materials and different chemicals can lead to compatibility issues with sensitive surfaces and elongate the nanofabrication time. For this reason, the use of a method involving no other chemicals use was driving the choice to conduct maskless AS-ALD in this work.

In this regard, AS-ALD on Pt-C seed layers has been introduced by Mackus and collaborators [158, 219–221] as low-invasive and highly versatile new bottom-up methodology for area-selective fabrication of pure Pt thin film growth on isotropic nanoscale.

In this work, *in situ* AS-ALD has been employed on purified Pt FEBID nanostructures for the fabrication of functional metal nanostructures [6]. Differently from most other AS-ALD methods, the combinatorial FEBID-ALD approach relies on locally stimulating catalytic Pt ALD growth instead of using masking techniques for specific area deactivation. Thus, the combination of FEBID and AS-ALD merges the advantages of both techniques, such as the high-resolution patterning capability of FEBID and the high-purity deposition of Pt layers with good thickness control of AS-ALD.

In the setup used, the *in situ* ALD technique is a fully automated process. Moreover, *in situ* electrical conductance monitoring during the AS-ALD cycling process has been used to optimize and control with high accuracy the course of the process. A description of the conductance monitoring technique and the informations that can be obtained from it, such as height increase and preservation of selectivity, is presented in Subsection 2.3.2.4.

The multistep technique consists of:

1. Pt-C FEBID of structures.
2. Catalytic purification. The Pt-C FEBID structures result to be C-free.
3. Pt AS-ALD on the Pt FEBID used as seed layers. Pt layers are grown on the structures.

In Figure 2.19 the whole fabrication process is represented. As initial step in the AS-ALD of Pt, the substrates have been subjected to a prior treatment (piranha

cleaning) in order to avoid that any impurity present on the substrate surface could initiate platinum growth, becoming a favorable nucleation point during ALD. Afterwards, rectangular-shaped FEBID seed layers have been written in high-resolution mode bridging pre-patterned Cr-Au electrodes. In order to guarantee stable electrical contacts during the AS-ALD experiments, conductance monitoring has been always done on purified FEBID seeds written with a dose of 3.45 nC μm^{-2} using electron beam parameters: 5 keV (beam energy), 1.6 nA (beam current), 20 nm (pitch), 1 μs (dwell time) and 3000 passes. This structure has been also taken as monitoring reference in the previous catalytic purification step. In addition, the same monitoring and electrical properties analysis have been conducted on seed layers written at lower doses in the range 0.2 - 0.9 nC μm^{-2} using as beam parameters: 5 keV (beam energy), 400 pA (beam current), 10 nm (pitch), 100 μs (dwell time) and the respective calculated number of passes. The next step consisted in purifying the FEBID seed layers for later use in the AS-ALD process with the method described in the previous Subsection 2.3.1.4.

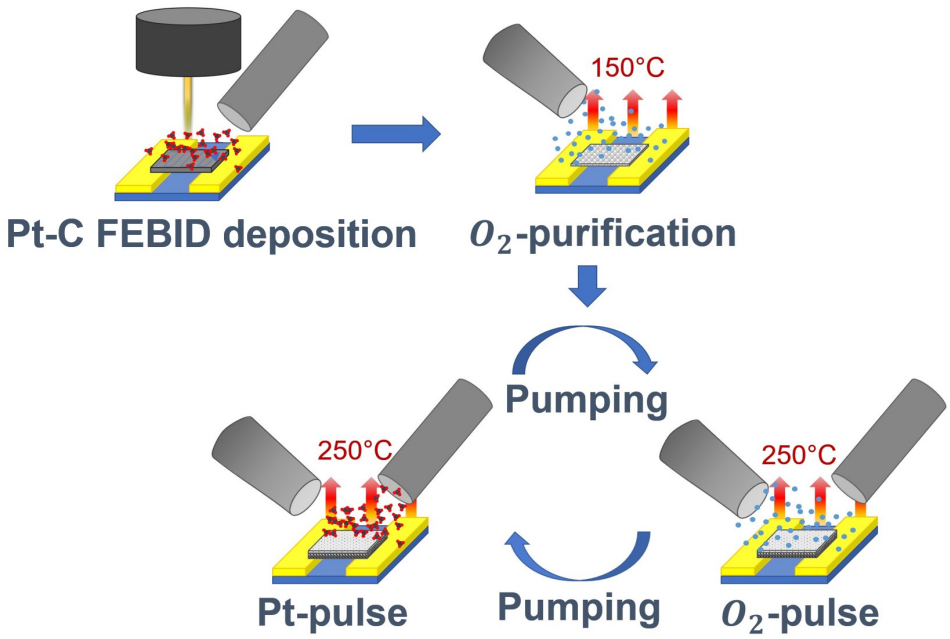

Figure 2.19: Schematic of the fabrication process steps used in this work to obtain pure Pt structures for nanoscale electrical contacting purposes. Initially, Pt-C FEBID structures are deposited. Subsequently, the catalytic purification described in Subsection 2.3.1.4 is conducted. Finally, cycle-fashion AS-ALD is carried out using purified Pt FEBID deposits as seed layers.

The ALD has been performed selectively on the Pt FEBID post-treated nanostructures inside the dual-beam FIB-SEM FEI Nova Nanolab 600 at a temperature of 250°C. The purified Pt FEBID structure is used as seed layer defining the desired lateral Pt thin film shape for the following Pt ALD process using $Me_3PtCpMe$ and O_2 as reactive

gases. For the AS-ALD inside the dual-beam FIB-SEM chamber, the same gas injectors, that are used for the Pt-C FEBID and the catalytic purification steps, have been employed for the corresponding Pt precursor and O_2 exposures. For the ALD process, the capillaries have been adjusted to 100 μm and 300 μm vertical distance to the substrate surface for the O_2- and Pt-GIS, respectively. The pressure of the chamber has been kept stable to 1×10^{-5} and 1.3×10^{-5} mbar during the Pt and O_2 pulse, respectively. A typical ALD cycle consists of 1 min Pt precursor dosing, followed by 1 min pumping, 1 min O_2 exposure and again a pumping step of 1 min. These times have been then modified in the self-optimization process. As a result of the localized process, Pt ALD growth was taking place on an area of about 300 μm^2, whose diameter is determined by the flux profiles provided by the gas injection system for the precursor and oxygen flux, respectively.

In Figure 2.20 (a) a SEM image and a 3D reconstructed vision (in the inset) of the two inserted capillaries is shown. In addition, an investigation of the intensity and direction of the Pt precursor and O_2 flux has been conducted, in order to estimate the ALD process area (Figure 2.20 (b)). For the flux simulation of the two pipes, the software developed from Friedli [222] has been used. The parameters used for the simulation are: number of molecules (10^6), angle and vertical distance between exit surface of Pt-GIS and substrate surface (57° and 300 μm), angle and vertical distance between exit surface of O_2-GIS and substrate surface (26° and 100 μm).

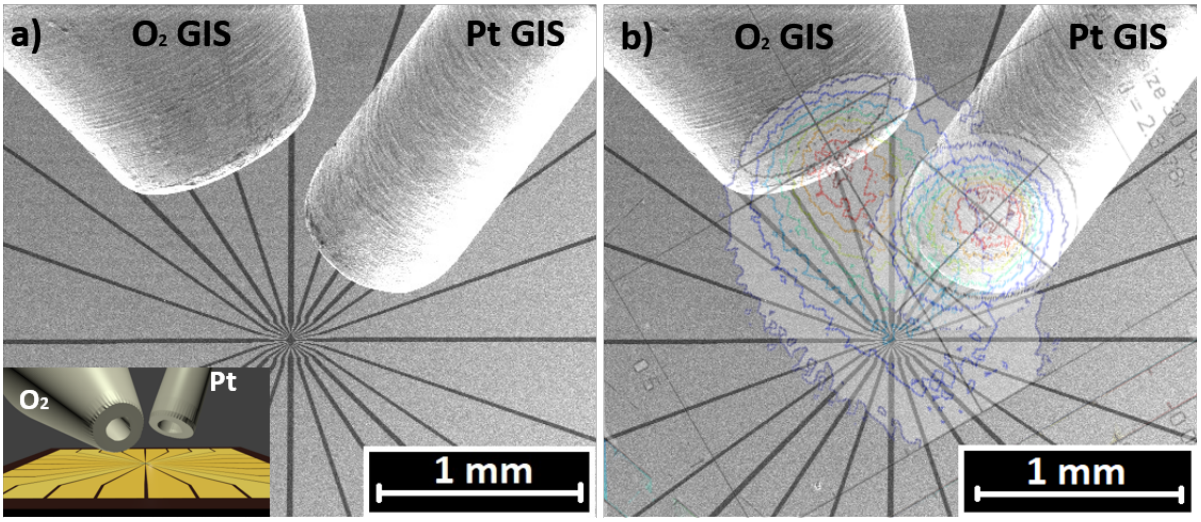

Figure 2.20: a) SEM image of the GISes configuration during the course of the AS-ALD process. The center of the substrate is the target of both GIS exposures. Inset: 3D sketch of the capillaries and substrate setup created with the open-source 3D software Blender [223]. b) The SEM picture reported in (a) is shown with the relative gas supply simulation performed with the software developed from Friedli [222].

In addition to the fabrication and conductance monitoring development of the combined technique, the electrical properties of the obtained nanostructures have been investigated *in situ* in the chamber of the dual-beam FIB-SEM at room temperature and inside a ^{3}He-cryostat. In Appendix A, the results of the low-temperature electrical characterization of the obtained structures are reported.

Chemical reactions of Pt Atomic Layer Doposition (Pt ALD) In the last years, numerous research groups continued to study extensively the complex Pt ALD surface reaction mechanisms [179, 224–228]. The following reaction mechanism has been proposed for the oxidative decomposition of $Me_3PtCpMe$ in the temperature range of 200 - 350 °C for the related ALD process [179, 224]:

$$Pt(s) + O_2(g) \rightarrow Pt - O_x \tag{2.4}$$

$$C_5H_4CH_3Pt(CH_3)_3(g) + Pt - O_x \rightarrow Pt(s) + CO_2(g) + H_2O(g) + other\ byproducts \tag{2.5}$$

The Pt-O_x species represents oxygen that is adsorbed on the platinum surface and reacting with $Me_3PtCpMe$ releases CO_2, H_2O and possibly other byproducts (as presented in the equation). However, because of the limited amount of oxygen in the adsorption layer, the ligands may not be completely oxidized. The remaining hydrocarbon species are then oxidized during the following pauses. After complete oxidation of the ligands, a new layer of adsorbed oxygen should thus form on the platinum surface. This cycle is then repeated during the film growth. In Figure 2.21 the described reactions are graphically shown.

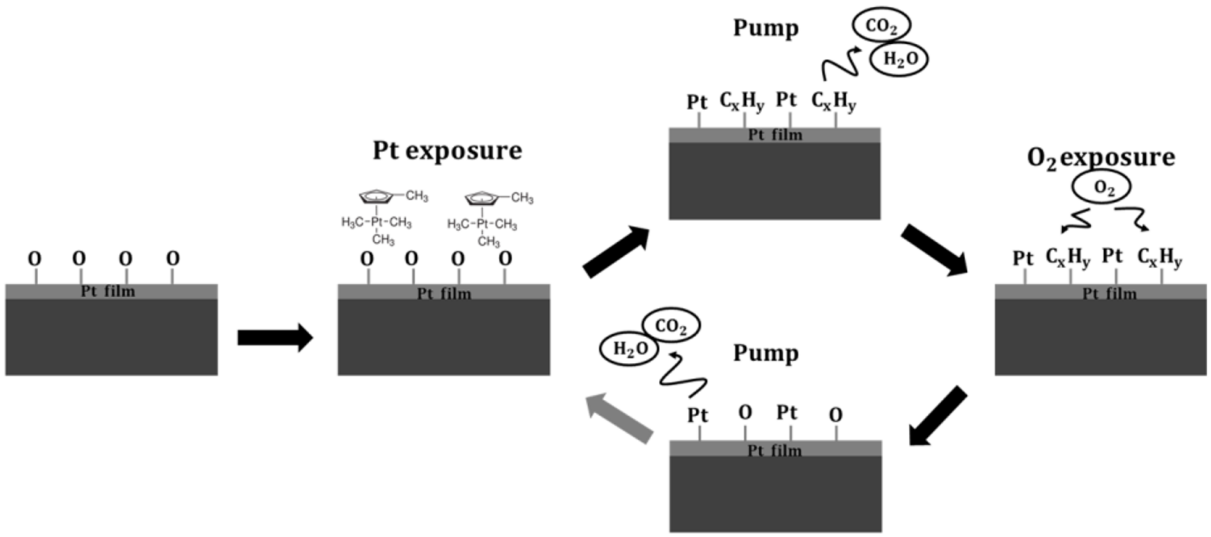

Figure 2.21: Sketch of the reactions taking place during a Pt ALD process. The deposition of Pt atoms in every ALD cycle is mainly assisted by CO_2 and H_2O gaseous emission.

Extending the process analysis, Kessels *et al.* [225] describe with higher complexity the possible reaction mechanism at 300°C:

$$2\,Me_3PtCpMe(g)+3\,O(ads) \rightarrow 2\,Me_2PtCpMe(ads)+CH_4(g)+CO_2(g)+H_2O(g) \quad (2.6)$$

$$2\,Me_2PtCpMe(ads) + 24\,O_2(g) \rightarrow 2\,Pt(s) + 3\,O(ads) + 16\,CO_2(g) + 13\,H_2O(g) \quad (2.7)$$

By balancing the carbon containing volatile reaction products, approximately 1 C-atom per precursor molecule has been found to be on average removed during the precursor pulse. This occurs through combustion of the ligands by chemisorbed oxygen producing CO_2 and H_2O, as well as through the production of CH_4, with an observed CH_4/CO_2 ratio of 1:1. During the subsequent O_2 exposure step, the remaining hydrocarbon ligands, that constitute 87% of the precursor carbon, are combusted by O_2 gas.

Compositional analysis of the fabricated structures The compositional evolution of the structures after the different steps of the combined fabrication technique has been investigated with EDX. EDX analysis and relative compositional results have been conducted on $1.5\times1.5\,\mu m^2$ structures written by an 5 keV accelerated electron beam with a beam current of 1.6 nA, using dwell time 1 μs, pitch 20 nm and 6000 passes. The structures have been investigated by EDX (collecting at least 2000 counts on Pt peak) after deposition, after purification and after 120 ALD cycles. From the EDX spectra comparison in Figure 2.22, it is directly possible to observe how dramatically the relative C and Pt compositional peaks of a structure as deposited (a) and at the end of the AS-ALD (b) changed. In the spectra, Si and O peaks are visible but their compositional amount have not been taken into account by the addressed analysis of the Pt/C ratio. Those Si and O peaks appear also different in the spectra because after the catalytic purification the deposit lost in volume and the EDX measurement on the structure after AS-ALD collects more signal from the substrate. It follows that after deposition, the material consists of 24.3 at.% of Pt and 75.7 at.% of C. The reversed compositional situation is observed as soon as the material is purified. The purified structure shows 75.9 at.% of Pt and 24.1 at.% of C. The presence of C is related to the deepest deposit layer that did not get purified since the structure is relatively thick (150 nm). After 120 cycles of ALD, the amount of Pt indeed slightly improved with 79.3 at.% of Pt and 20.7 at.% of C. These results are graphically summarized as histogram plot in Figure 2.23.

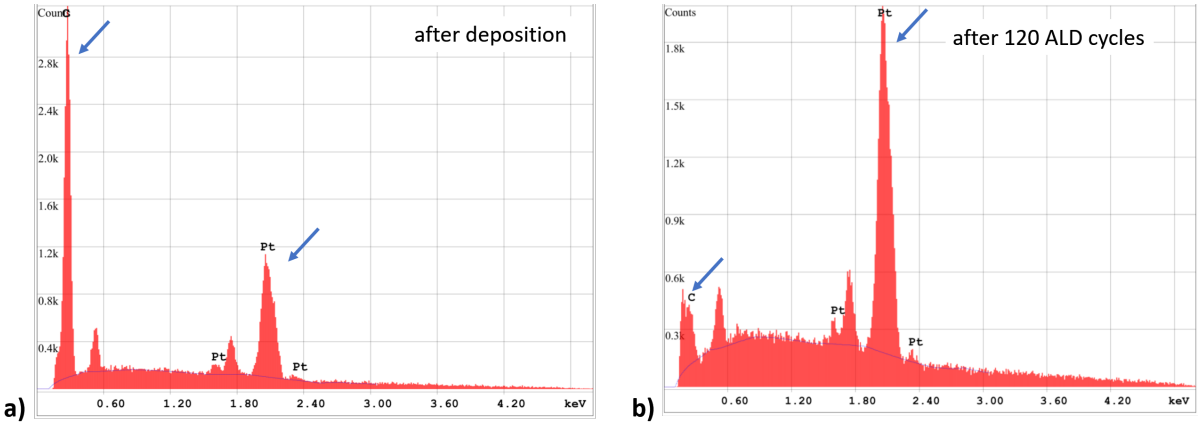

Figure 2.22: EDX spectrum of a structure written by FEBID with the $Me_3PtCpMe$ precursor as deposited (a) and after catalytic purification and 120 cycles of Pt AS-ALD (b). It is noticeable how the Pt/C ratio turns over between the two spectra. The unidentified peaks belong to Si and O (substrate).

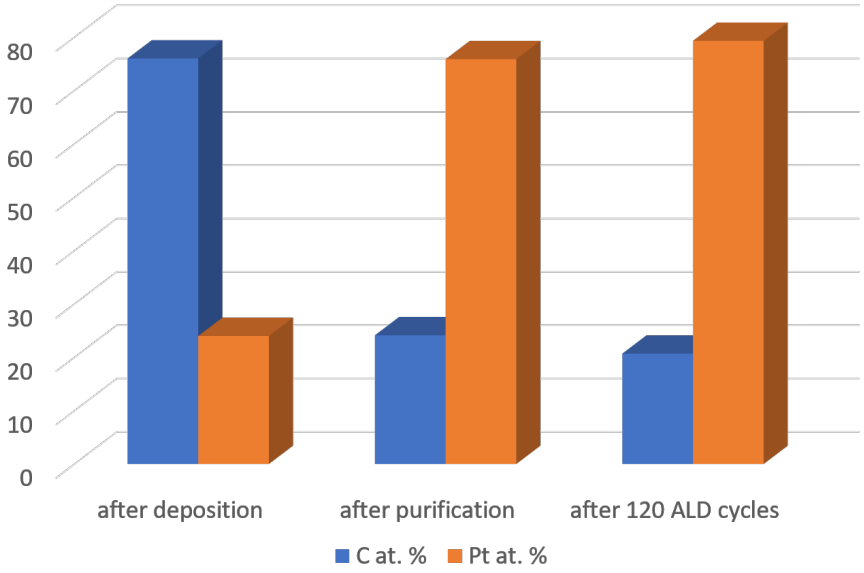

Figure 2.23: Compositional results of EDX measurements after every step of the combined fabrication technique: after deposition, after purification and after AS-ALD. A drastic change in the Pt/C ratio can be observed between the first two steps. After ALD, the structure shows a smaller improvement of the Pt content. The corresponding EDX spectra after deposition and after AS-ALD are shown in Figure 2.22.

Final structures To give an idea of a typical structure fabricated by the multistep technique, in Figure 2.24 a SEM image of Sample 1 is shown. Sample 1 has been written with a FEBID dose of $0.9\,\mathrm{nC}\,\mu\mathrm{m}^{-2}$, subjected to catalytic purification and to 153 AS-ALD cycles. After the catalytic purification the sample thickness has been about 7 nm. The 153 AS-ALD cycles have been conducted with a stable chamber pressure during O_2 exposure of 1.3×10^{-5} mbar. Sample 1 presented an average final thickness of 11.7 ± 1.5 nm. As it can be noticed in the inset of Figure 2.24, the final structure is not smooth and a significant Root-Mean-Square (RMS) roughness of 3.2 ± 0.5 nm has been measured in the central area of 550×150 nm^2. This roughness value is significantly larger than for Pt layers grown in dedicated ALD reactors whose RMS roughness is reported to be around 0.6-0.8 nm after 153 ALD cycles on Si substrates with an initial RMS roughness of 0.3 nm [216, 229]. The roughness of the obtained samples is a consequence of the initial roughness of the purified Pt FEBID seed layer used for the AS-ALD. In accordance with the results of Sachser and collaborators [4] about the purified Pt FEBID structures, the carbon removal from the FEBID deposit matrix, promoted by the catalytic purification, leads to the formation of pores. These cavities at the end of the conducted AS-ALD are likely not totally filled.

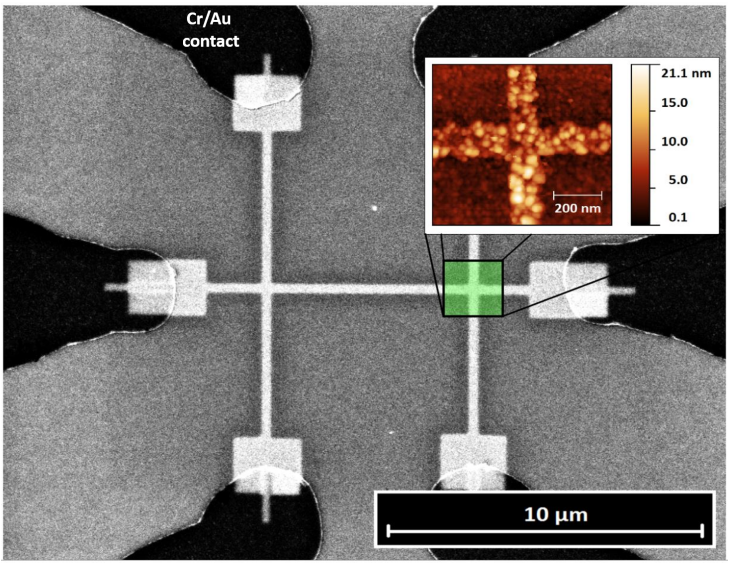

Figure 2.24: SEM image of the 6-probe structure (Sample 1) obtained after the AS-ALD whose monitoring is shown in Figure 2.33. Inset: AFM image of the corresponding location, that is highlighted in the main SEM picture. The roughness of the structure is related to the formation of deep pores during the previous catalytic purification step. The Figure is reported with permission from [6].

In addition, the 'bump' effect is also visible on samples that have been very thin (about 2 nm) at the beginning of the AS-ALD process (FEBID dose $0.3\,\mathrm{nC}\,\mu\mathrm{m}^{-2}$), but that have been subjected to more ALD cycles (400 cycles). In Figure 2.25 AFM

measurements of the last mentioned structure are shown. This result shows that it is not possible to reach smooth structures with this technique in the available setup. Even on very thin samples, which are subjected to a high amount of cycles, the nanostructure surface cannot be filled up by the AS-ALD of Pt-layers. It is worth mentioning that further increase of the number of ALD cycles is not recommended, since it extends even more the duration of the ALD process (already lasting more than 26 hours for 400 ALD cycles) and increases the probability of unselective growth.

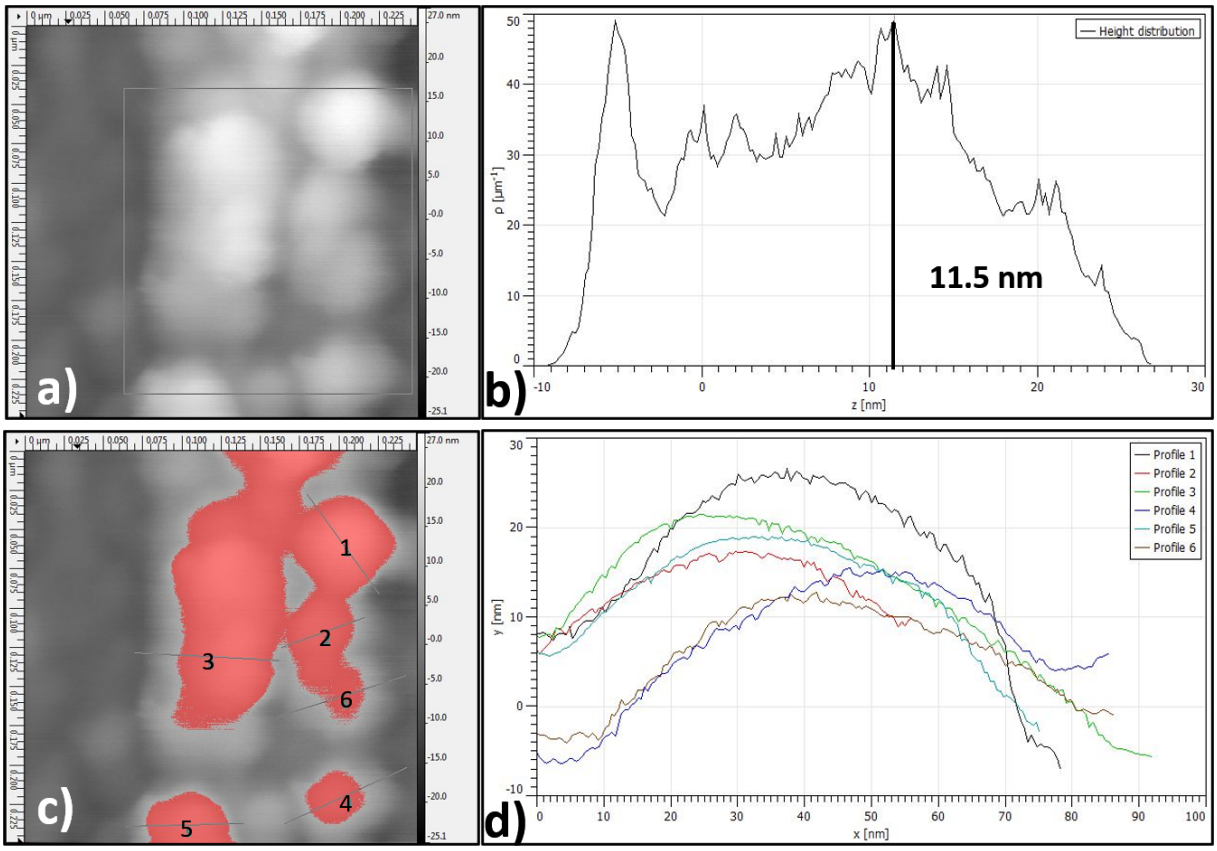

Figure 2.25: a) AFM measurement of a sample written with a FEBID dose of $0.3\,\mathrm{nC}\,\mu\mathrm{m}^{-2}$ and subjected to catalytic purification, followed by 400 Pt ALD cycles. b) Height distribution of the region selected in (a). The height of the sample is not homogeneous. c) With a masking filter the 'bump' character of the structure morphology is highlighted. d) Profile measurements of the grains, that are highlighted in (c), show that the measured clusters have similar dimension and relative height.

The room-temperature resistivity of the material is $12.2 \pm 0.3\,\mu\Omega\,\mathrm{cm}$. This value is quite comparable to the resistivity of Pt also fabricated *in situ* by AS-ALD ($11 \pm 2\,\mu\Omega\,\mathrm{cm}$) [220] or in a dedicated ALD reactor ($13 \pm 1\,\mu\Omega\,\mathrm{cm}$) [216] and to the bulk resistivity of Pt ($10.4\,\mu\Omega\,\mathrm{cm}$) at 215 K [35]. The resistivity value of the obtained samples have been calculated using SEM and AFM measurements of the sample volumes and taking the

nanoporous morphology for the very thin layers into account. The electrical characterization of the obtained structures is presented in Appendix A.

2.3.2.1 Area-Selective Atomic Layer Deposition (AS-ALD) development in the dual-beam FIB-SEM chamber

Generally, ALD is run in dedicated reactors, in which the reactants exposures can be precisely carried out and inert gas purges (e. g. Ar pulses) are executed between the precursor pulses in order to avoid interaction among the different reactants. In this way, high pressures (1 - 10 mbar), high substrate temperatures (150 - 350°C) and short time cycles (less than 1 s) can be used to run an efficient and fast ALD process on several substrates (50-500 substrates) [230].
Since ALD is a common technique used for thin film production on free surfaces, different conditions have to be established to trigger the selective deposition of material on mask-less regions. In the case of AS-ALD with FEBID fabricated seed layers, the selectivity is determined by the unbalanced condition of the catalyzed promotion of Pt deposition reactions on already prepared Pt-structures against the inability of Pt to wet the oxide surface of the substrate (SiO_2) [231, 232].
Previous studies on the nucleation process taking place at the beginning of ALD have shown that on SiO_2 the ALD initiates as island growth (Volmer-Weber) and it is mainly influenced by substrate temperature, O_2 flux [215, 233, 234] and the presence of impurities/defects which act as favorable nucleation points and will influence the overall growth behavior.
It must be considered that a dual-beam FIB-SEM chamber has setup limitations that make the establishment of a Pt AS-ALD process challenging. The substrate temperature of 250°C used during the AS-ALD process is the maximum stable temperature reachable with the available setup and it has been chosen following the results of Erkens, Knoops and collaborators [216, 235]. The scientists demonstrated that the growth of platinum is relatively constant between 250-300°C.
Impurities that work as favorable nucleation points have been avoided dipping the substrate in a piranha solution of H_2O_2 and H_2SO_4 with 1:3 ratio before inserting it in the dual-beam FIB-SEM chamber.
As it has been reported in literature [216, 236], Pt ALD can be conducted in a defined substrate temperature and O_2 flux range, the so called 'ALD window' [215].
In the case of AS-ALD on Pt FEBID, Mackus and collaborators [158, 219–221, 236] pursued extensive studies of the area-selective platinum growth on the FEBID seed layers explaining that the selectivity is depending on the different type of surface reactions taking place on the seed layers and on the surrounding dielectric material. Moreover, the scientists found correlation between the area-selective character of the

metal growth and both, seed layer thickness and O_2 flux. With regards to the gas flux dependence of the Pt growth, in the experimental work reported here, a strong influence of the Pt flux on the growing process has not been noticed. On the contrary, the significant effect of the O_2 flux on the Pt growth during AS-ALD has been confirmed. Therefore, for AS-ALD the O_2 flux has been dosed with particular care and pauses have been introduced to pump the system between the different reactant exposures.
In this work a fine tuning of the optimal O_2 flux for the used setup has been performed. The O_2 flux has been controlled indirectly measuring the base pressure of the SEM. The *in situ* conductance measurement on the seed layers has been used as monitoring method to collect a direct feedback on conductance variations driven by the O_2 exposure. In this way, an optimization of the growth conditions and direct control of the selective growth can be carried out (details are given in Subsection 2.3.2.4). The extracted height increase observed in the given setup is in the range $\Delta h = 0.2\text{-}0.4$ Å per cycle. The height increase varies depending on the different growth conditions. This result has been confirmed by *ex situ* AFM thickness measurements.
The best base pressure value induced by the O_2 flux for which stable and selective AS-ALD has been obtained in the used setup is 1.3×10^{-5} mbar. It has been observed that varying this value by 20 % is enough to strongly slow down the growing process or to promote Pt deposition all over the substrate. In addition, the pause between the precursor and O_2 exposure has been also found to be crucial for the process. In the present study, it has been observed that due to too short pauses between the different gas exposures, the nucleation of Pt during the ALD has been promoted on the area directly subjected to the Pt flow.
Following the results of Mackus *et al.* [221], a characterization of the minimal FEBID dose of a Pt purified deposit to promote AS-ALD has been carried out in the available setup. The researchers found that the minimal Pt FEBID dose necessary to have enough Pt in order to start *ex situ* catalytic ALD growth on the FEBID seed layers is $2\,\mathrm{nC}\,\mu\mathrm{m}^{-2}$. In the experiments reported in this work, it has been observed that in a sample written with a FEBID deposition dose of $0.4\,\mathrm{nC}\,\mu\mathrm{m}^{-2}$, in which current was not flowing at the beginning of the process, electrical contact grew during the AS-ALD and it has been well monitored by the *in situ* conductance measurement performed during the AS-ALD process. In Figure 2.33 (b) the result of this observation is reported. In addition, also samples written with a lower dose ($0.3\,\mathrm{nC}\,\mu\mathrm{m}^{-2}$) and not conducting before the AS-ALD, have shown at the end of the process to be conducting. Therefore, it can be assessed that in the used setup purified structures written with a minimal writing dose of $0.3\text{-}0.4\,\mathrm{nC}\,\mu\mathrm{m}^{-2}$ have enough nucleation material to initiate AS-ALD growth.
In Figure 2.26 a series of deposits subjected to 250 cycles of ALD is shown. The deposits have been written with a dose in the range $0.1\text{-}0.5\,\mathrm{nC}\,\mu\mathrm{m}^{-2}$. From the BSE overview image (a), a bright $\approx 2\,\mu$m halo of co-deposit in the vicinity of the deposit is

recognisable. The Pt originated from FEBID co-deposit initiated Pt ALD growth. Studying the minimal FEBID dose necessary to initiate ALD growth is important in order to preclude the growth of Pt on co-deposit during ALD and perform AS-ALD just on the FEBID structures. In particular, in Figure 2.26 (b) a remarkable contrast change can be noticed between the deposits written with a dose of $0.2\,\mathrm{nC}\,\mu\mathrm{m}^{-2}$ and $0.3\,\mathrm{nC}\,\mu\mathrm{m}^{-2}$, respectively. The increase of brightness is an indication of an increased Pt amount. Indeed, FEBID deposits written with a minimal dose of 0.3-0.4 $\mathrm{nC}\,\mu\mathrm{m}^{-2}$ had enough Pt to initiate electrical contact during the AS-ALD (see Figure 2.33(b)). The difference in the FEBID minimal dose founded by Mackus *et al.* [221] and the one reported in this work depends on the different setup parameters (temperature, O_2 flux, pause duration, etc) and the different type of initial structures (Pt-C FEBID and Pt purified FEBID structures, respectively).

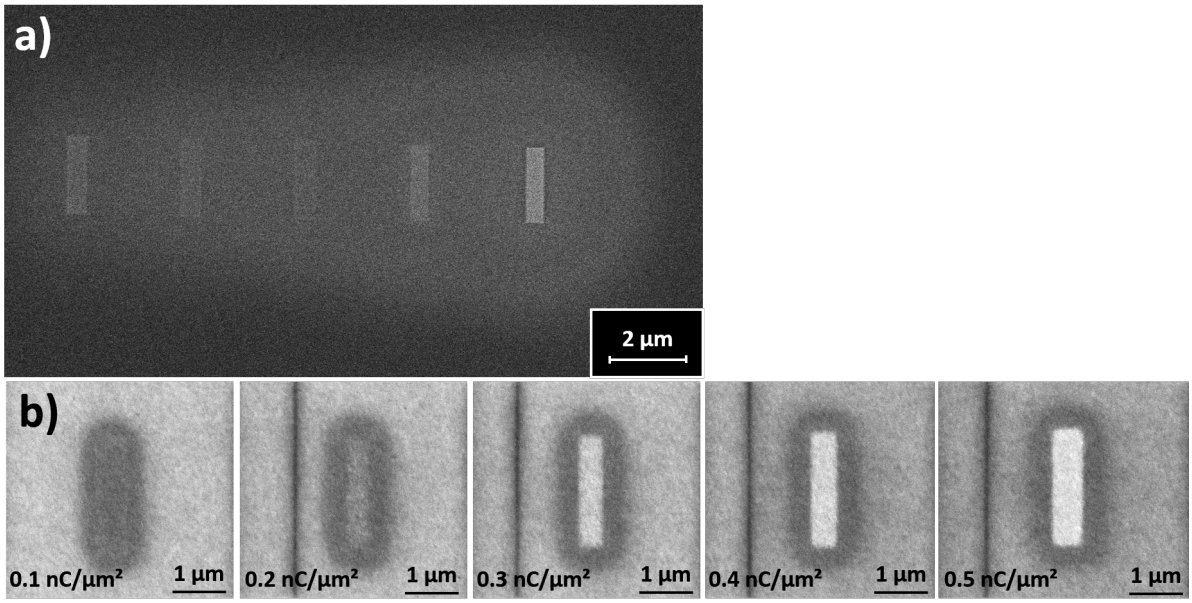

Figure 2.26: a) BSE detector image of Pt purified FEBID deposit written with dose $0.1, 0.2, 0.3, 0.4, 0.5\,\mathrm{nC}\,\mu\mathrm{m}^{-2}$ (from left to right) and subjected to 250 cycles of ALD. The BSE image gives information on the material composition. The bright $\approx 2\,\mu\mathrm{m}$ halo around the structures is Pt co-deposit. b) SE detector image of the single deposits. A remarkable contrast change is apparent between the deposits written with a dose of $0.2\,\mathrm{nC}\,\mu\mathrm{m}^{-2}$ and $0.3\,\mathrm{nC}\,\mu\mathrm{m}^{-2}$, respectively. The grey lines are the border of the area subjected to previous snapshots.

Cluster-like Pt ALD growth by *e*-activation on chemically treated substrate areas It is worth mentioning that unselective Pt ALD growth has been experienced during the research of the best process conditions. Substrates, on which the central Cr-Au contacts have been fabricated with EBL, have been subjected to a fast

cluster-like Pt growth during Pt ALD. In particular, it has been observed that in the substrate central region Pt nucleation has been promoted. This region has been SEM photographed before the ALD process. By an SEM picture, the photographed area is exposed to a dose lower than $1\,\mathrm{pC}\,\mu\mathrm{m}^{-2}$. This final effect could be directly dependent on the presence of EBL resist residue that has been activated from the electron irradiation of the SEM picture.

In Figure 2.27, optical and SEM images of a substrate, on which the Pt deposition during ALD has not been area-selective, are shown. The area, on which the most Pt deposition took place, has been the region subjected to the direct O_2 flux. This deduction is confirmed by the precursor flux simulations performed with the molecule flux simulation software from Friedli [222] and shown in transparency on Figure 2.27 (a). From the image contrast and EDX analysis, it has been confirmed that the material clusters are made of Pt. Moreover, sharp edges of material delimit the areas that have been subjected to SEM imaging at the end of the purification procedure and before starting the ALD process. For the process a chamber base pressure of 1.7×10^{-5} during the O_2 exposure and a pause of only 15 s between the two reactant exposures have been used. Therefore, it can be deduced that the fast Pt cluster-like deposition during the first cycles of Pt ALD has been initiated by both the high O_2 flux and the *e*-activation of chemical residues.

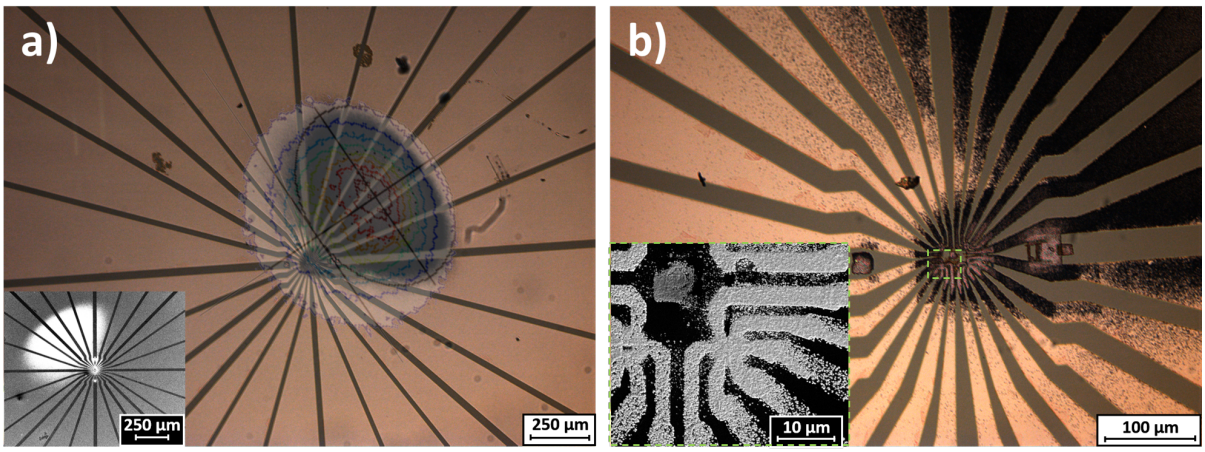

Figure 2.27: a) Optical microscope image of the substrate. The O_2 flux incidence area, simulated with the GIS simulator software from Friedli [222], is shown. The simulated data confirms that on the area subjected to the O_2 exposure, fast cluster-like Pt growth during ALD has been promoted. In the inset a SEM image of the same substrate is shown. b) Optical image close up on the center of the substrate. Sharply delimited areas on which Pt growth has been promoted can be observed. Those areas have been, before the ALD process, SEM photographed. Inset: SEM closeup of the selected area. The optical microscope and SEM images are mirrored along the vertical axis.

2.3.2.2 HexaMethylDiSilazane (HMDS) primer

With the intention of optimizing the Pt ALD process and suppress the ALD growth on the substrate surface besides the Pt FEBID purified seed layers, not only the O_2 flux during the process has been reduced but an attempt to deeply clean and prime the substrate surface before writing the seed layers has been made.
After Cr/Au have been fabricated on the surface of a Si/SiO_2 substrate (details about the technique can be found in Section 2.1), the substrate has been etched in a piranha solution (H_2O_2 : H_2SO_4 = 1:3) in order to remove organic or metallic impurities from the surface substrate. Afterwards, HexaMethylDiSilazane (HMDS) - $(CH_3)_3SiNHSi(CH_3)_3$ has been deposited on the substrate in order to turn the surface from hydrophilic to hydrophobic and prime it for the next fabrication step.
HMDS is commonly used on semiconductor surfaces to bond the Si-atoms of the molecule to the O-atoms of oxidized surfaces (in this case SiO_2), releasing ammonia [237]. HDMS is mainly used in semiconductor industry to make chip surfaces water-repellent. It builds non-polar methyl groups on the substrate surface and improves the surface photo-resist wetting and adhesion properties. However, more interesting uses for the study presented in this work are including HMDS deposition as pre-treatment step for ZnO ALD on glass substrate [238]. This step elongated the initial ALD growing delay. Moreover, HMDS has been used as prime step before FEBID deposition of Au (by $Au(CO)Cl$ precursor) [239] and Pt (by $Me_3PtCpMe$ precursor) [200].
The HMDS deposition has been conducted with HMDS vapor in a custom-built vacuum chamber. A photograph of the constructed reaction chamber is shown in Figure 2.28 (a). The reaction chamber has been built in order to recreate the process conditions of a HDMS oven [237]. A metal reservoir has been filled with HMDS (HexaMethylDiSilazane reagent grade ≥99%, Sigma-Aldrich) in an inert atmosphere (N_2 flowbox). The reservoir has been connected to the chamber with a manual valve. The chamber has been pumped to a pressure of about 3×10^{-5} mbar. The substrate has been heated by thermal radiation and reached a stable temperature of 90°C. The temperature has been measured with a Pt-1000 sensor in the proximity of the substrate (max. 5 mm apart). The substrate has been subjected to a dehydratation bake followed by the HDMS deposition. The HMDS vapor has been introduced inside the chamber by opening the manual valve. HDMS should then chemically bond with the substrate surface as a monolayer. The substrates were hydrophobic after the process (as it is possible to be noticed from Figure 2.28 (b)). The substrates after the HMDS have been contacted on the carrier chip and directly inserted in the SEM. By the SEM investigation, it has been discovered that HMDS has been not deposited homogeneously on the substrate surface. Circular stains could be found on the substrate. A SEM picture of the stains is shown in Figure 2.28 (c). Nevertheless, a fabrication process attempt has been carried out.

FEBID deposits have been written between the Cr-Au contacts in the center of the substrate and the structures have been subjected to catalytic purification and Pt ALD. The fabrication parameters used for this run (such as O_2 flux, O_2 exposure time, pause duration after a gas exposure, distance of the GIS to the substrate, etc) have been the optimized parameters to achieve AS-ALD. It quickly became clear that not only the HMDS step was not improving the selectivity of the ALD process but it has been even counter-productive. In Figure 2.28 (d), it can be noticed that, also in this case, *e*-activation effects drove Pt clusterization. The regions subjected to a short electron irradiation by a SEM picture, that has been taken after the purification step and before ALD, present an high density of Pt clusters after only 5 Pt ALD cycles.
As a consequence of the unsuccessful attempt, the use of HDMS prime has not been further pursued. As it has been speculated for EBL processed substrates (Figure 2.27), it can be considered that also HMDS (as EBL resist rest) promotes a fast Pt cluster-like formation during Pt ALD on regions that have been briefly activated by electron irradiation by SEM pictures. This result furthermore underlines the effort that is requested by the establishment of AS-ALD in the available setup and it points out how crucial the interplay of the process variables are.

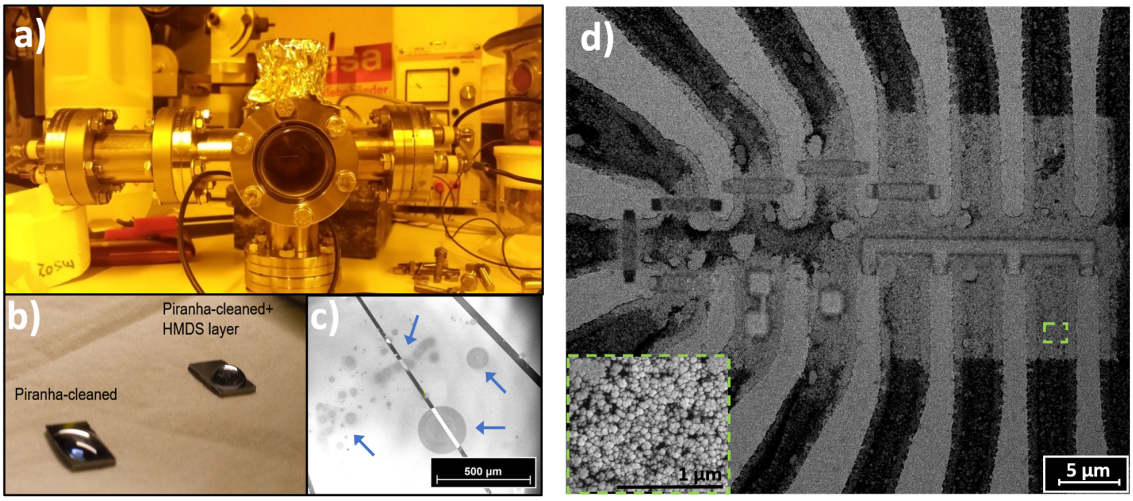

Figure 2.28: a) Photo of the custom-built HMDS chamber. b) Two Si/SiO_2 substrates after the piranha solution cleaning step (on the left) and after the HMDS deposition (on the right). The substrate surface after the HMDS is hydrophobic. c) SEM picture of the uneven HMDS deposition on the chip surface. Stains of HMDS are recognisable (indicated in the picture with blue arrows). d) SEM picture of the HMDS-treated chip subjected to few (5) Pt ALD cycles. A Pt cluster-like deposition on *e*-activated regions is visible. A similar effect has been observed on chips fabricated with EBL (Figure 2.27 (b)).

2.3.2.3 Co-deposit by ALD

Fabrication tests have been conducted to evaluate the AS-ALD method as fabrication approach for high-resolution SET nanostructures. In order to obtain well-defined structures, high acceleration voltage, such as 20 keV, and a small beam current of 150 pA have been used during the FEBID process. In addition, for the FEBID writing process a low number of passes (5), long dwell time (1 ms) and relative small pitch (5 nm) ensured high lateral resolution of the seed layer. The FEBID deposition yield at so high beam acceleration is lower than the one reachable with smaller acceleration voltages (as e. g. 5 keV). This effect has been well described by De Teresa *et al.* [13]). For this reason, a higher FEBID writing dose (about 15 nC μm^{-2}) than the initial dose used for the common AS-ALD process (0.2 - 0.9 nC μm^{-2} by 4 keV and 400 pA beam parameters, for the samples fabrication previously described in the main Section 2.3.2) has been employed in order to obtain 4 nm high purified seed layers. The writing pattern parameters and the geometry has been uploaded in the software patterning engine of the FEI dual-beam FIB-SEM software in a bitmap format. After catalytic purification, AS-ALD has been conducted for 120 cycles with exposure times O_2 - 60 s ; pause - 20 s ; Pt precursor - 20 s ; pause - 20 s. The base chamber pressure during O_2 exposure has been maintained at 1.8×10^{-5} mbar. The GIS and substrate configuration has been the same as described in Subsection 2.3.2. Several patterns have been written with the same dose but different design (different size of the gap between the electrodes). AFM measurements confirmed that about 3 nm of Pt have been grown on the seed layers.

In Figure 2.29, SEM pictures (a)(b)(c) and the respective AFM measurement (d) of a SET shaped nanostructure are shown. A co-deposit halo is directly recognizable from the change in contrast of the region. The affected area is a disk of about 7 μm radius around the pattern. Such a wide halo is a consequence of the high acceleration voltage used. Details about the primary beam energy dependence of co-deposit formation in FEBID can be found in Subsection 2.3.1.3.

It is possible to notice that the halo is darker after deposition (Figure 2.29 (a)) and lighter after Pt ALD (Figure 2.29 (b) and (c)). This brightness change in the SE detector picture has to be traced back to the co-deposit compositional change in the different fabrication steps. After deposition the co-deposit consists mainly of C. On the contrary, after Pt ALD the co-deposit lost C and Pt-atoms initiate Pt ALD growth, resulting in higher electron collection from the Everhart-Thornley detector and therefore showing high brightness. A closeup of one structure indicated in (b) is shown in (c). The use of optimized beam parameters leads to high-resolution structures. For the same structure, an AFM measurement is shown in (d). It is important to point out that, during the SEM picture, a carbon layer from the residual chamber atmosphere gets

deposited on the structure. A trace of this layer can be recognized in the respective AFM measurement in Figure 2.29 (d). In the 3D view, it is evident how the interaction of the AFM cantilever and the different materials is producing an AFM artefact showing the picture region as it would be below the substrate level.

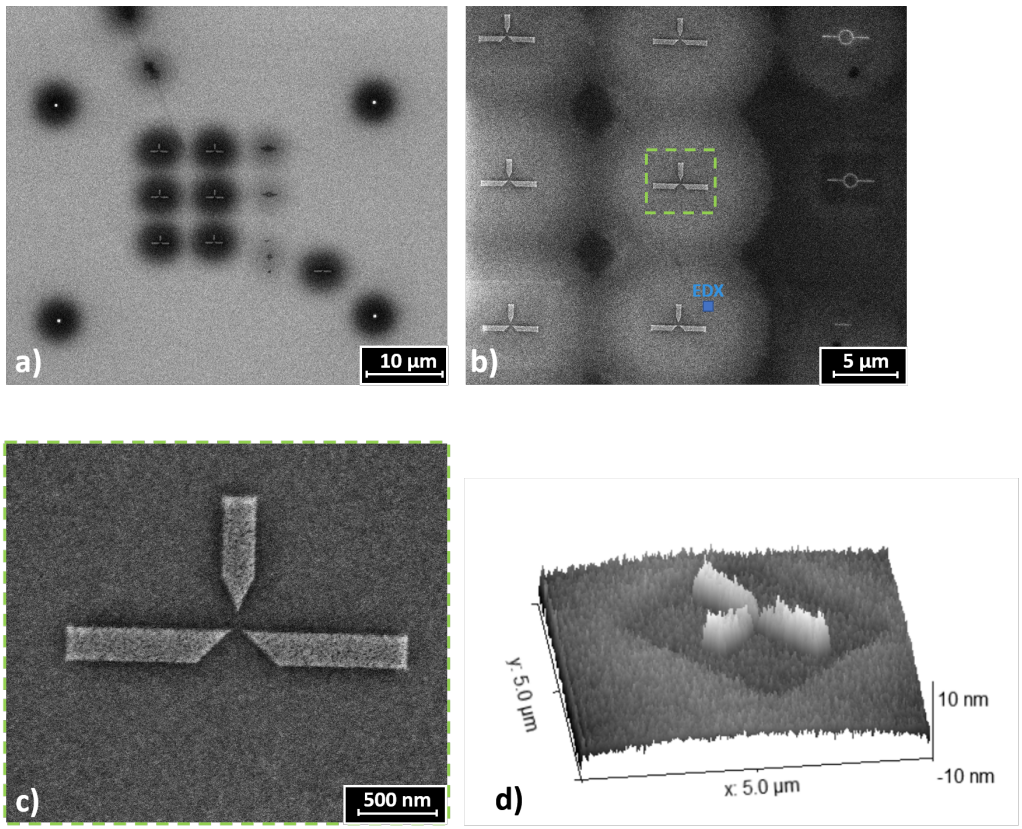

Figure 2.29: SET design test structures written with Pt-C FEBID. SEM picture of the structures (a) after deposition (b) after 120 ALD cycles with high O_2 flux exposure. In light blue is indicated the point on which the EDX measurement reported in Figure 2.30 has been conducted. c) Closeup of the highlighted structure in (b). d) AFM measurement of the structure in (c). The structure has a thickness of about 7 nm. A compositional AFM artefact shows the area subjected to the picture (c) as sunk into the substrate.

An EDX measurement has been conducted on a $1.5 \times 1.5\,\mu m^2$ region indicated in light blue in Figure 2.29 (b), collecting about 5500 counts and using 5 keV and 1.6 nA as beam parameters. The result of the EDX measurement is reported in Figure 2.30. The compositional analysis yields to 58.1 at.% of O, 39. at.% of Si, 2.2 at.% of Pt and 0.5 at.% of C. The 2.2 at.% of Pt is attributed to the Pt FEBID co-deposit layer grown with ALD on the substrate surface.

This test have shown again that the O_2 flux used in the Pt ALD has been too high (1.8×10^{-5} mbar SEM chamber base pressure during O_2 exposure) and unselective Pt ALD growth has been initiated on the co-deposit. It is important to remember that Pt

AS-ALD has been obtained with a chamber pressure during O_2 exposure in the range 1 - 1.3 $\times 10^{-5}$ mbar. However, it can be noticed that the structures maintain the typical lateral high-resolution feature of FEBID structures written with the optimized beam parameters. This result encourages the use of the combined technique for high-resolution nanofabrication.

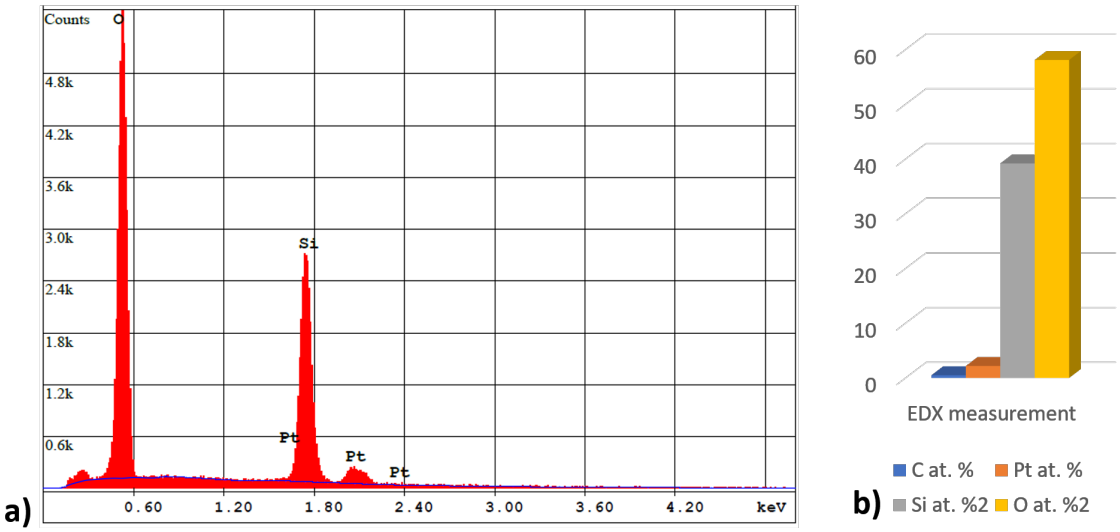

Figure 2.30: a) The EDX spectra and the quantified material composition (b) on the light blue indicated point of Figure 2.29 (b). The investigated location is 1 μm apart from one of the nanostructures. 2.2 at.% of Pt has been detected at this location, proving that enough Pt-atoms, which are present in the FEBID co-deposit, worked as seeds for Pt ALD growth.

However, the establishment of a nanogap between two patterned contacts is the key challenge for SET fabrication. By using electrical measurements, the electrical isolation of structures written between two Cr-Au contacts (nearby the test structures shown in Figure 2.29) has been investigated in order to assess if the Pt co-deposit next to the defined structure established electrical transport channels. The structures have been written and subjected to the same purification and Pt ALD process as the nanostructures shown in Figure 2.29.
The test structure has been written in a 'narrow constriction' fashion with 40 nm distances between the contacts in the pattern design. An SEM picture of the structure with the respective closeup is shown in Figure 2.31. The final gap between the contacts can be estimated from the inset in Figure 2.31 to be about 30 nm.
An interesting behavior of the structure has been observed taking I-V characteristics inside a ^{3}He-Cryostat at 2 K. Switching to different slopes can be observed in the I-V characteristics reported in Figure 2.32 (a). This feature is typical for Quantum Point Contact (QPC) effects. In literature [240], experimental and theoretical studies predict

and confirm that the conductance through a single Pt atom would be quantized in units of $G_0 = 2e^2/h$, the conductance quantum. In the performed measurements, an unspecific peak of the extracted conductance slopes has been found around the not integer value of 1.35 G_0 (Figure 2.32 (b)). This result could be connected to the formation of Pt atomic chains enhanced by the presence of Pt atoms in the narrow constriction. Therefore, it would be reasonable to expect that electromigration could drive the establishment of Pt atomic chains. However, the peculiar feature in the I-V characteristics could also be connected to a bad contact interface between the Au contacts (about 35 nm high) and the very thin Pt nanostructures (about 7 nm) or it can be traced back to the different working functions of the two materials (Au and Pt). This interface issue of very thin purified FEBID structures is also discussed in Appendix C.1.

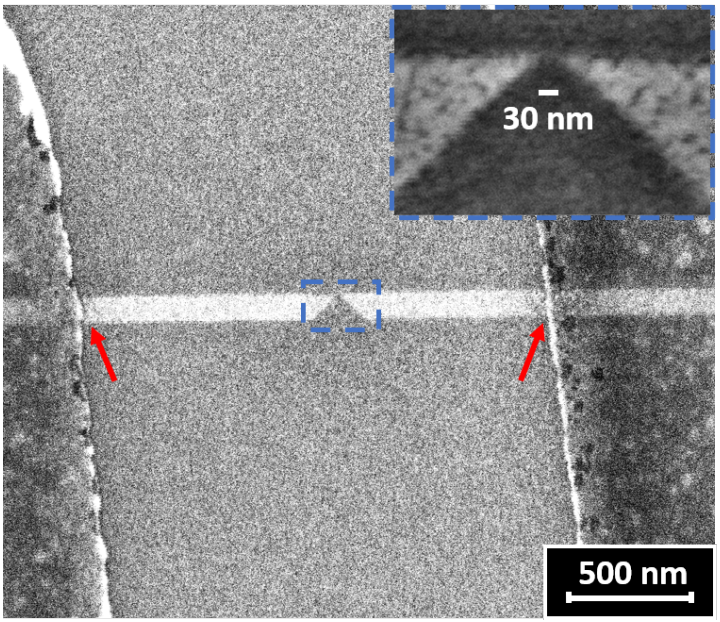

Figure 2.31: SEM picture of a nanostructure written between two Cr-Au contacts. Inset: closeup of the gap region. At the end of the Pt ALD, the final gap between the two patterned tips is estimated to be about 30 nm. The interface regions, which are responsible for the bad physical contact between the Cr-Au electrodes and the Pt nanostructure, are indicated with red arrows.

As a consequence of the nanofabrication method limitations and having considered the time requested to optimize the fabrication process for such a high-definition demanding nanostructure, as can be a SET, it has been decided to dedicate a separate project to the challenge of fabricating high-resolution nanostructures with this technique [241]. A dedicated ALD reactor is better suited for the optimization of Pt AS-ALD instead of the precious FEI dual-beam FIB-SEM system available in the research group. The results obtained in this work serve as basis for this follow-up project.

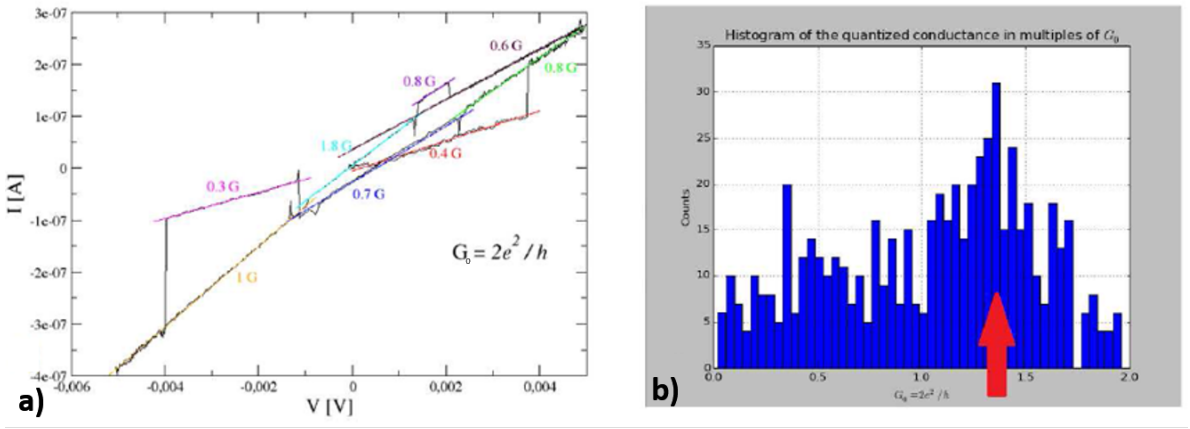

Figure 2.32: a) I-V characteristics of the nanostructure shown in Figure 2.31. The measurements have been conducted inside a ^{3}He-Cryostat at 2 K. Different slopes have been observed and summarized in the histogram in (b). The most frequent slope has been found at the value of 1.35 G_0. For QPC, the conductance is quantized in units of G_0.

2.3.2.4 *In situ* electrical monitoring of AS-ALD

The possibility to perform *in situ* conductance measurements during FEBID and post-growth processes also at elevated temperature proved to be a key element for the characterization of the deposited material and for the monitoring of optimization processes on FEBID structures [15, 157, 174]. Considering these results, the application of electrical conductance monitoring for metal thin film growth has been considered to be a promising method for collecting a precise feedback of the growing metal nanostructure volume which, as an effect, generates a relative increase of electrical conductance. In [6], the AS-ALD monitoring technique developed in this research work is described in detail.

The conventional monitoring techniques used for ALD growth and thin film growth are, among others, UV spectroscopy [242], (spectroscopic) ellipsometry [243–245], X-ray photoelectron spectroscopy [246] and X-ray reflectivity [247, 248]. However, these monitoring techniques, in contrast to the monitoring technique proposed here, cannot be applied for nanostructures with lateral nanoscale dimensions. A further advantage of the conductance monitoring technique is that, in comparison to the common techniques where the average height increase is obtained dividing the final film thickness over the time of the ALD cycles, the *in situ* conductance monitoring is directly tracing the conductance evolution with sub-cycle time resolution. This conductance variation is directly correlated to the reactions which are taking place on the seed layer during the different reactant exposures, as well as the morphology and the thickness of the growing

sample. As a consequence, the conductance monitoring technique stands out for its versatility on providing direct and valuable information on various aspects of the growth, such as height increase and preservation of selectivity. Moreover, the advantage of an accurate time resolved feedback on the process evolution allows to evaluate the process in order to adaptively modify the nanofabrication factors. In particular, it has been demonstrated in [6] that a growth optimization can be done thanks to the direct *in situ* monitoring in a semi-automatic fashion where the conductance variation caused by different cycling time parameters is used as input to a genetic algorithm (GA) that yields improved cycling times for the ALD process.
The AS-ALD monitoring technique based on the electrical conductance measurement has been performed connecting the investigated structure in a 4-probe configuration by using a Keithley 2400 source meter and an Agilent 34420A nanovoltmeter. To improve the signal-to-noise ratio and to avoid electrical high-field breakdowns, AC 4-probe differential measurements have been performed with a Stanford Linear Research lock-in amplifier (SRS830) and a shunt resistor.

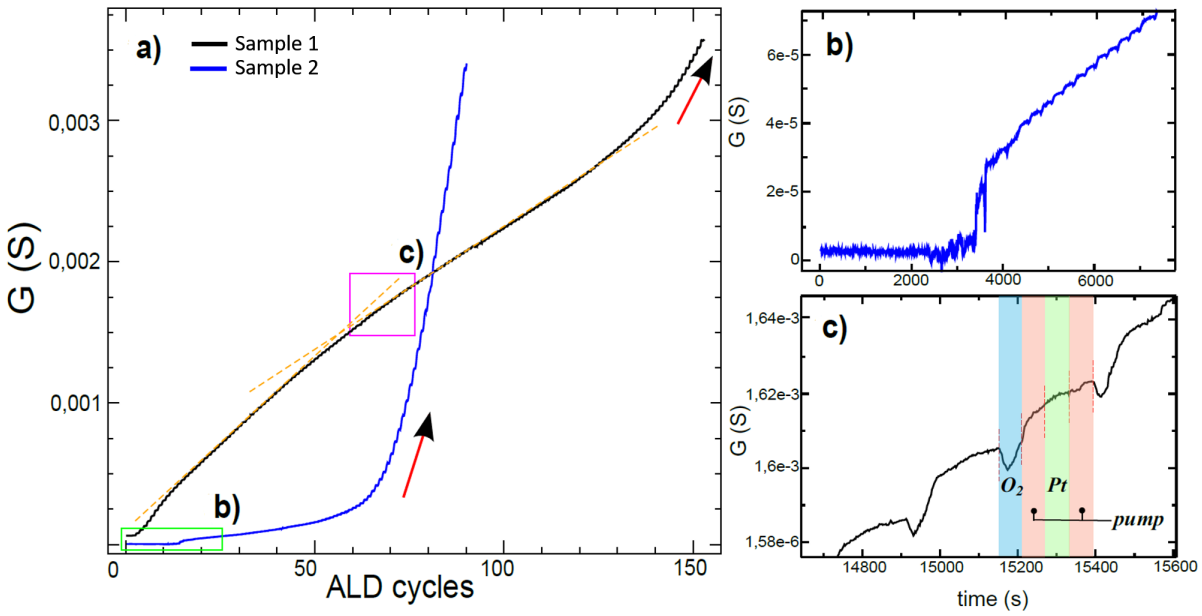

Figure 2.33: a) AC (for Sample 1) and DC (for Sample 2) conductance measurements by *in situ* electrical monitoring as a function of the number of AS-ALD cycles. b) Detail of Sample 2 time dependent conductance curve at initial stage. After the twelfth cycles, the establishment of electrical contact can be observed. c) Close look of the curve's linear region in (a) about the 63 cycle region. The action of the different reactant exposures is detectable in the conductance measurement with typical step-like features.

Examples of the conductance measurement taken during an Pt AS-ALD process are given in Figure 2.33. AC and DC conductance measurements of Sample 1 and Sample 2 are

shown, respectively. Sample 1 has been written with a FEBID dose of $0.9\,\mathrm{nC}\,\mu\mathrm{m}^{-2}$ and Sample 2 with a FEBID dose of $0.4\,\mathrm{nC}\,\mu\mathrm{m}^{-2}$ in order to provide a seed layer. After the catalytic purification, Sample 1 and Sample 2 had a thickness of about 7 nm and 2 nm, respectively. After 153 AS-ALD cycles, for which the chamber pressure during the O_2 exposure has been kept stable to $1.3 \times 10^{-5}\,\mathrm{mbar}$, Sample 1 presented an average final thickness of $11.7 \pm 1.5\,\mathrm{nm}$. In the Pt AS-ALD process of Sample 2, a higher O_2 flux has been used, maintaining the pressure of the chamber at $1.8 \times 10^{-5}\,\mathrm{mbar}$ during the O_2 exposures. SEM and AFM images of Sample 1 have been shown in Figure 2.26.
The variation of conductance taking place during the different steps of the AS-ALD cycling process do not only give information about the status of the process but also about various aspects of the growth such as electrical contact establishment, height increase and preservation of selectivity. By analysing the conductance measurements of Sample 1 and Sample 2, a detailed discussion about the information that can be extracted from the curve evolution is provided.

Process trends derived from the time-dependent electrical conductance measurement Information about the growth phases taking place during an ALD can be obtained by trend analysis of the time-dependent electrical conductance measurement.
Liang and collaborators [249] have shown that ALD consists of different phases, such as initial nucleation, grain coarsening and vertical thickening. In particular, these phases can be traced by the *in situ* conductance monitoring curve, which is characterized by different slopes corresponding to different growth regimes. An example of this is visible in Figure 2.33 (a) for Sample 1, where the orange dashed lines underline the slope changes during ALD. As a matter of fact, the height increase can vary over time, in particular for ultrathin films. Considering the different processes taking place during the formation of ALD monolayers, it is worth notice that during the initial nucleation of Pt grains on the porous Pt seed layers, a filling up of the voids rather than a simple thickening of the structures is occurring. Consequently, during the first cycles film height growth can be inhibited or slowed down. For example, from the tendency of the conductance measurement of Sample 1 in Figure 2.33 (a), it can be observed that the curve is characterized by an initial delay corresponding to the nucleation process on the very thin seed layer. In this regime, the conduction electrons are predominantly subject to scattering at grain boundaries [250] and film surface [251–253]. The initial nonlinearity of the conductance versus ALD cycles data is most probably attributed to point-contact effects and electron tunneling between the growing islands on ultra-thin seed layers.
After the initial small conductance increase, a linear trend is established lasting for 50 cycles. After the first linear regime, a second linear regime is initiated, most likely due

to a transition between island coalescence and film thickening. Finally, in the last ALD cycles of the *in situ* conductance monitoring for Sample 1, a nonlinear growth is detectable. It corresponds to loss of selectivity and it is a consequence of the prolonged exposure to the oxygen flux. Details about the loss of selectivity driven by O_2 exposure is given in the following dedicated paragraph.
Another interesting feature of the conductance monitoring technique is that the conductance measurement can give high-resolution feedback of the establishment of electrical contact. An example of that is shown in Figure 2.33 (b) for Sample 2. The sample is insulating at the beginning of the ALD process. After the 12th Pt AS-ALD cycle (2880 s) a current path is established and the sample becomes conducting. The conductance monitoring is then very useful to control electrical contact establishment driven by the proceeding growth of Pt on the monitored seed layer and, in general, of metallic materials on granular surfaces.

Conductance gain per Pt AS-ALD cycle as direct feedback of material growth
The determination of the height increase of Pt AS-ALD cycles can be directly calculated from *in situ* conductance monitoring knowing the geometry and the resistivity of the grown material.
A linear increase of the conductance during the ALD cycling is the special signature of constant growth during the process. The height increase can be, for example, extracted for Sample 1 in the linear regime of the conductance measurement during the Pt AS-ALD. An extracted closeup of the curve is given in Figure 2.33 (c). The step-wise ALD growth regime is linear, the height increase per cycle is constant and it can be accurately determined from the associated conductance increase ΔS employing the equation:

$$\Delta h = \frac{l \times \Delta S \times \rho}{b} \tag{2.8}$$

where ρ is the resistivity of Pt, and l and b are the length and width of the sample, respectively. A linear regression of the *in situ* data allows the direct extraction of the ALD growth for a single deposition run. A height increase in the range $\Delta h = 0.2\text{-}0.4$ Å has been calculated for the setup used in this work.

Direct feedback for process optimization The monitoring gives a direct feedback on the process evolution and allows the researcher to evaluate the process in order to adaptively modify the nanofabrication factors. Moreover, in [6] it has been demonstrated that a growth optimization can be done thanks to the direct *in situ* monitoring in a semi-automatic fashion where the conductance variation caused by different cycling time parameters is used as input to a Genetic Algorithm (GA) that yields improved cycling times for the ALD process.

In Figure 2.34 two sequential conductance curves are shown in black and red during purification and Pt AS-ALD at 300°C. During the elapsed time reported, different process parameters have been tested and the relative change in conductance has been evaluated as a feedback to reach a set of best performing parameters ensuring a stable and high conductance increase per ALD cycle. Initially, the conductance evolution is traced during an O_2-purification treatment (O_2 - 1 min, pause - 1 min). Afterwards, the AS-ALD process with 1 min cycle time (O_2 - 15 s; pause - 15 s ; Pt precursor - 15 s ; pause - 15 s) and O_2 flow induced chamber pressure of 8×10^{-6} mbar for 105 min has been conducted. In order to test the influence of a higher O_2 flux, the AS-ALD process with 1 min cycle time has been continued with an O_2 flux induced chamber pressure of 1.3×10^{-5} mbar. Finally, different reactant exposure and pause durations have been tested. It can be noticed that a higher O_2 flux drives an increase in conductance. Using a longer cycle time, for which every reactant exposure and pause last for 1 min, promotes also in this case a higher conductance gain over time and allows to monitor in high-resolution the effect of the reactant exposure. For instance, the optimized AS-ALD process has been performed with 4 min cycle time (O_2 - 1 min ; pause - 1 min ; Pt precursor - 1 min ; pause - 1 min) and O_2 flux induced chamber pressure of 1.3×10^{-5} mbar.
The final tested parameters have been selected as standard since the increase in conductivity associated to a cycle has been well recognisable from the particular step-like behavior (clearly visible in the inset of Figure 2.34), the conductance increase during the following 20 AS-ALD cycles has been stable and the highest for the tested set of parameters. Obviously, better parameters can be found. In [6], a direct automatic optimization of the exposures and pause durations has been shown based on the application of a Genetic Algorithm (GA) of the feedback associated to the induced conductance change. However, the loss of selectivity is a risk that has to be taken into account for long and/or high O_2 exposures.

Loss of selectivity driven by high O_2 flux From the *in situ* conductance monitoring during the AS-ALD, a direct feedback of a change of the O_2 flux is provided and the process can be optimized maximizing the relative conductance increase. In Figure 2.34, for example, it can be noticed how the conductance slope increases as soon as a higher O_2 flux is applied during the Pt AS-ALD.
Moreover, it has been observed that when the O_2 flux has been increased and the chamber of the dual-beam FIB-SEM has been maintained during the O_2 exposure at a pressure higher than 1.3×10^{-5} mbar or after longer O_2 exposure, the conductance increase suddenly becomes faster, indicating the loss of Pt growth selectivity. In Figure 2.33 (a), it can be observed that although Sample 2 had a lower starting thickness of the seed layer but higher O_2 flux has been provided to the substrate surface during ALD in

comparison with sample 1, it reached a higher conductance in a shorter period of time and developed a sharp change in the slope. On the other hand, Sample 1 shows for the last ALD cycles an abrupt change in slope, too. The loss in selectivity is then caused by higher and/or longer O_2 exposure.
Therefore, it can be summarized that with longer O_2 exposure (Sample 1) and/or higher O_2 flux (Sample 2), the risk of parasitic Pt nucleation is enhanced and the formation of additional current paths leads to a non linear increase of the conductance. The change in the conductance clearly shows the effect of metal deposition taking place on the non-seeded part of the substrate.

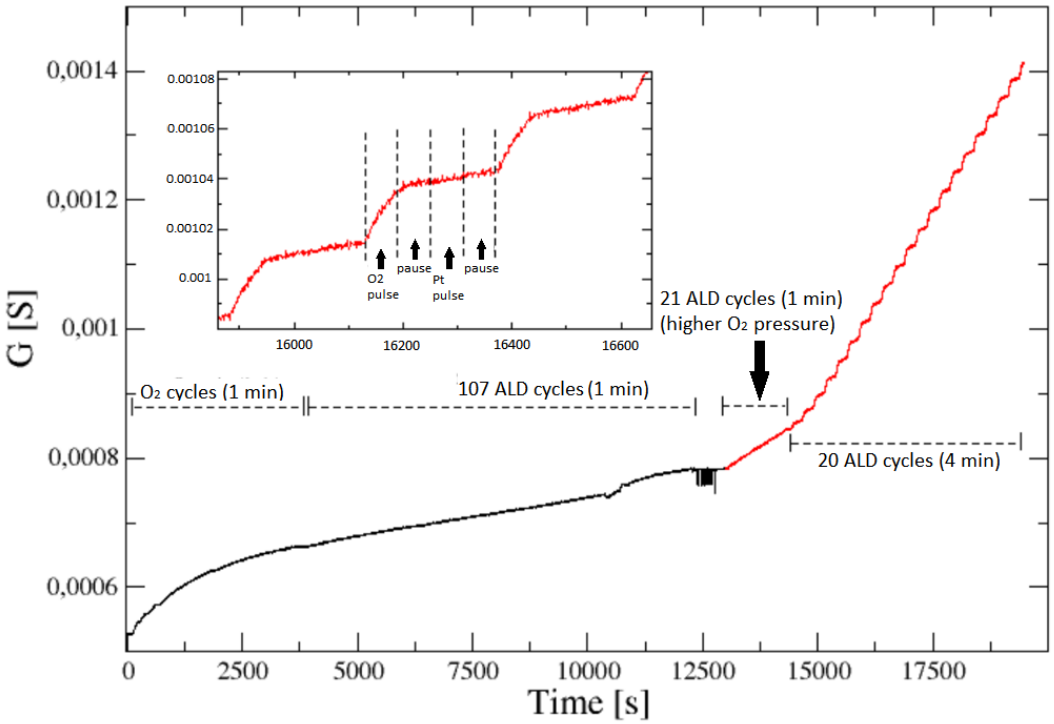

Figure 2.34: As an example of an optimization process, two sequential conductance measurements (in black and in red) are shown. Initially, the Pt-C FEBID structures have been catalytically purified. Afterwards Pt AS-ALD has been performed changing the process parameters: O_2 flux and exposure/pause duration.

Trace of chemical reactions proceeding Other important informations which can be deduced from the conductance monitoring are about the surface reactions taking place during the reactant exposures. These results can help to complete the study on the Pt ALD surface reaction mechanisms which have been extensively discussed by numerous research groups [226, 227, 230, 254]. From the detail of the ALD cycle step-like behavior of the conductance measurement shown in Figure 2.33 (c), it can be

deduced that the initial conductance drop generating the characteristic step-like shape is due to the chemisorbtion of O_2 on the catalytic Pt surface of the seed layer. More specifically, during the O_2 exposure the catalytic combustion leads to a reduction of electron density at the Pt surface [220, 230, 254] and dehydrogenates the precursor ligands on the Pt surface [220, 255, 256]. Later, the conductance increases as Pt atoms reorganize on the surface getting attached to the existing layer. The following pumping cycle is important to allow the reactions to saturate on the Pt surface and prepare the surface for the following Pt precursor adsorption. During the Pt precursor exposure and following pumping time, the molecules adsorb on the Pt surface providing ligands exchange between hydroxyl groups and methyl ligands. During this process, a slight increase in the conductance is observable.

It is important to underline that the conductance monitoring technique and the GA approach for self-optimization using the *in situ* monitoring are rather broadly applicable. For instance, Mackus, Hsu, Kaloyeros and collaborators [220, 257, 258] have shown that the catalytic action of Pt seed layers can be used for AS-ALD of other metals, like palladium and copper, making the technique eligible for different type of contacting applications, for example carbon electronics, for which palladium with its high work function and good wetting interactions with nanotubes is well suited [259]. Moreover, the method could be used for other non-selective metal deposition techniques [260] since the time-resolved feature of this growth monitoring is certainly preserved. Other applications can be forseen using the conductance monitor signal to stop the growth when a certain thickness has been reached and/or when the formation of an electrical contact has to be detected with high-resolution in time and conductance. For instance, this monitoring technique can be very useful when ALD is performed on a seed layer with nanopores and trenches, e. g. on highly porous aerogels [261–263] and on ordered nanoporous membranes and silica for biomedical applications [264–266]. If trying to contact sensitive nanoelements, like carbon nanotubes [220] and in the fabrication of microcontacts for fuel cells, hydrogen storage and pollution control applications, this method can be used in order to reduce Pt loading, thereby reducing the cost [267–269].

2.3.3 Nanoparticle drop casting

One of the approaches based on FEBID for the fabrication of SE transport devices (array and SET devices) has been carried on by the use of Au nanoparticle (Au-NP) assemblies as fundamental building blocks of the final device. Pt-purified FEBID structures, obtained with the Pt catalytic purification described in Subsection 2.3.1.4, have been used as bridge leads to connect the Cr-Au electrodes and the well-ordered Au-NP assemblies randomly distributed on the center of the SiO_2 substrate. Details of

the whole fabrication process are provided in Chapter 3. In fact, ligand capped-NP are ideal building blocks for two- and three-dimensional cluster self-assembled superlattice structures, in which the particles are arranged with long-range translational and even orientational order [270].
The Au-NP used for this approach have been provided by the group of Biophotonics of Prof. Parak at Philipps Universität Marburg [271]. The Au-NP have been synthesized following a kinetically controlled seeded growth strategy *via* the reduction of $HAuCl_4$ by sodium citrate [272]. The NP size is 12.5 nm in diameter. In order to avoid agglomeration, the Au-NP have been coated with thiol-terminated polymers (thiol-PEG). The thickness of the PEG shell depends on the molecular weight of the polymer. For the Au-NP used in this work HS-PEG-COOH polymers (MW 10kDa) have been used, providing in solution a ligand elongation of 12 nm. A picture of the received solution and a TEM image of the Au-NP are presented in Figure 2.35 (a) and (b), respectively.

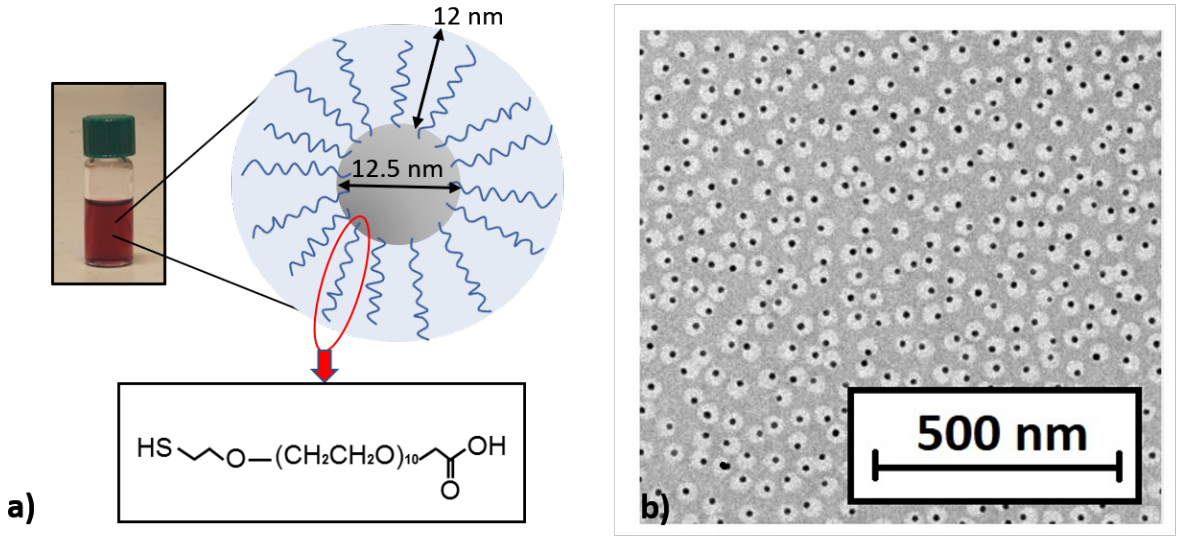

Figure 2.35: a) Picture of stock 1: concentration of 12×10^9 Au-NP/μL of DCM. Schematic of one nanoparticle with the PEG ligands attached on its surface. b) TEM image of the Au-NP received from the group of Biophotonics of Prof. Parak at Philipps Universität Marburg [271].

The excellent solubility of PEG-SH in DCM and the dual properties of PEG molecules as both hydrophilic and hydrophobic molecules allow the molecules to rapidly cover the surface of the nanoparticles in DiChloroMethane (DCM), (CH_2Cl_2), resulting in efficient phase transfer without nanoparticle aggregation.
The NP have been received in a bottle, in which after complete drying, 1 mL of DCM has been added, reaching a concentration of 12×10^9 NP/μL (stock 1). A picture of stock

1 is shown in Figure 2.35 (a). The characteristic red color of the Au-NP of this size is well recognisable. Different concentration stocks have been prepared for the two different applications (array and SET device fabrication) and will be later described in this subsection.
A micropipette with filter tips allows to provide a volume in the range of 0.1 - 2.5 μL of the solution. A droplet of 0.5 μL of a NP-concentration stock has been dropped onto the center of a SiO_2 substrate with Cr-Au contacts defined by UVL in order to deposit the NP in the area where the Cr-Au contacts have a small distance between each other (3 μm). A sketch of the drop-casting method and SEM view of the dried solution drop is visible in Figure 2.36 (a) and (b), respectively.
As a consequence of spontaneous solvent evaporation (1 - 5 s) the droplet leaves behind fractals-stain-like rings of material with lace-like patterns or clumps of particles in the inner region (Figure 2.36 (c)).

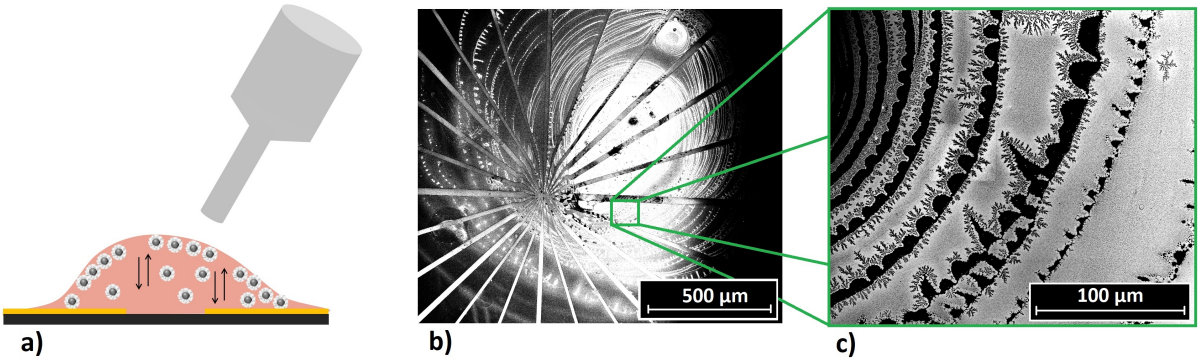

Figure 2.36: a) Sketch of the drop-casting method. b) SEM picture of the dried solution drop on the center of the substrate. c) Closeup on fractals-stain-like rings of material. These effects and the non-uniform mass distributions of drop-deposited nanoparticles are consequences of the several mechanisms taking place during droplet evaporation.

These non-uniform mass distribution and the morphology of drop-deposited nanoparticles are consequences of the evaporation kinetics, fluid convection and particle interactions with the liquid-air interface, from which nanoparticles nucleate and grow. At the molecular level, driven intermolecular forces drive the spontaneous gathering of molecules into a well-defined and stable structure. The van der Waals (vdW) force is the fundamental driving force, guiding the self-assembly process. The vdW forces are the residual attractive or repulsive forces originating from electromagnetic fluctuations due to the incessant movements of positive and negative charges within all types of atoms and molecules. The electrostatic force also plays an important role in the self-assembly process. If the nanoparticles are modified with protonation molecules, the electrostatic interaction leads to the aggregation of nanoparticles [273–275].
The self-assembly mechanism has been described by O'Mahony *et al.* [276] as an

equilibrium process by the simple Gibbs free energy equation:

$$\Delta G_{SA} = \Delta H_{SA} - T\Delta S_{SA} \tag{2.9}$$

where if ΔG_{SA} is negative, self-assembly is a spontaneous process. ΔH_{SA} is the enthalpy change of the process and is primarily determined by the potential energy/intermolecular forces between the nanoparticles. ΔS_{SA} is the change in entropy associated with the formation of the ordered arrangement. The organization is accompanied by a decrease in entropy. Under constant temperature conditions, the inner energy gain must be larger than the term associated with entropy loss. In this way, self-assembly in a closed system is the result of free energy minimization and establishment of an equilibrium state.
Another point worth mentioning is that the film thickness depends, in principle, on the volume of dispersion used and on the particle concentration, both of which can be easily varied. However, other variables affect the film structure such as how well the solvent wets the substrate, evaporation rate and capillary forces associated with drying [277].
As a result, this self-assembly mechanism can yield monolayers with long-range ordering that are compact over macroscopic areas, despite the fast evaporation process. The self-assembled lattices contain defects and dislocations which form during the assembling process and, in general, defects are never completely avoidable.
During the drop-casting deposition of nanoparticles for this work, differences in the fast evaporation rates across the substrate or concentration fluctuations led to variations in film thickness and/or internal structure. As a consequence, NP hexagonal arrays with domain sizes not larger than 1μm have been formed. This result matches well the target of the SET fabrication, where just one nanoparticle positioned between the Pt FEBID purified leads is needed.
Drop-casting does serve as a quick and accessible method to generate thin films on relatively small substrates and has a strong preference for forming monolayer films. Therefore, it stands out as an excellent candidate for the fabrication of technologically necessary ultra-thin film materials for sensors, plasmonic devices, magnetic storage and drug deliver media [278–282].

Initially, two additional NP solutions have been prepared in order to have a diluted solution suitable for the SET fabrication. Stock 2 has been prepared from 0.5 μL of stock 1 into 150 mL of DCM reaching a concentration of 4×10^4 NP/μL and for every drop-casting event a solution (stock 3) of 0.5 μL of stock 2 in 1mL of DCM has been prepared. Hence, a droplet of 0.5 μL of stock 3 with 10 NP/μL has been deposited on the substrate. Stock 3 has been disposed of after use. As it is visible from Figure 2.37(a) it has been quite difficult to find the nanoparticles on the substrate and charge drift

during the FEBID writing would make it impossible to localize the nanoparticle in the middle of the FEBID contact patterns with a resolution of 1-2 nm.
Consequently, solutions with a significantly higher concentration have been prepared. For the NP lattice fabrication, 0.5μL of stock 1 has been diluted in 0.3 mL of DCM obtaining 2×10^7 NP/μL (Solution A) delivering on the center of the substrate about 10^7 NP in 0.5 μL droplet located on the substrate center. By use of Solution A, long chains and rounded domains of ordered assemblies have been formed. A SEM picture of the obtained assemblies from a droplet of Solution A is shown in Figure 2.37 (b).

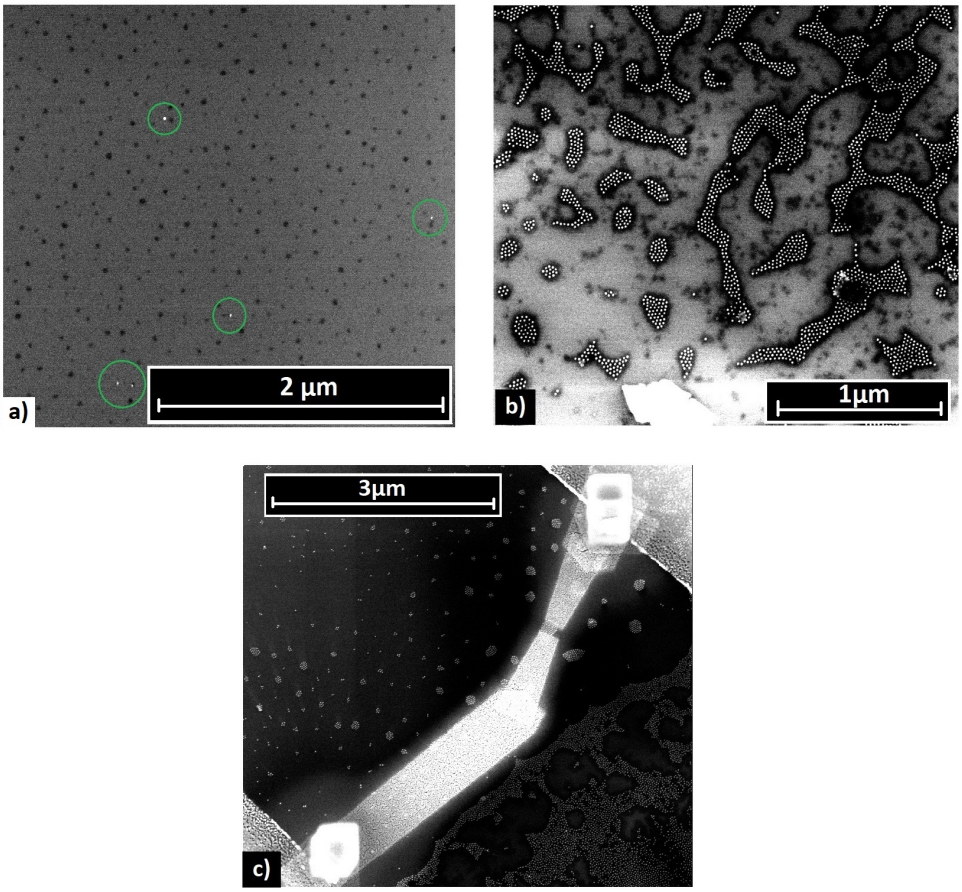

Figure 2.37: a) SEM picture of few outlined Au-NP resulting from the drop-casting of stock 3 (10 NP/μL). b) SEM picture of the substrate after Solution A (2×10^7 NP/μL) has been dropcasted on its center. The high NP-concentration leads to the deposition of few micrometers large NP assemblies. c) SEM picture of the resulted contacted structures by Pt purified FEBID leads. The results of the electrical characterization of this type of devices are reported in Chapter 3.

For the SET fabrication, 0.5μL of stock 1 has been diluted in 1 mL of DCM obtaining 6×10^6 NP/μL (Solution B). 2×10^6 NP have been then delivered on the center of the substrate in 0.5 μL droplet of solution B. With this method, smaller assemblies form

on the substrate surface. These NP-groups can be more easily recognised (than single particles) in the SEM view and contacted with FEBID.
In the obtained assemblies the PEG ligands serve as spacer between the particles leading to a perispheral distance between the nanoparticles in the range of s = 8 - 10 nm, see individual assemblies in the SEM picture in Figure 2.37 (b). This distance is slightly lower than the elongation of the ligands in solution (12 nm) probably as a consequence of the drying in air. A SEM picture of one NP assembly contacted with Pt purified FEBID leads is shown in Figure 2.37 (c). Despite the elevated temperature in the post-growth treatment, we did not observe any degradation or position change of the Au-NP in the assemblies.

2.3.4 Ion etching techniques

Ion etching is a physical dry etching technique used to remove material by exposing the material to a bombardment of ions and create high aspect ratio structures. In this section two different *in situ* ion etching methods are described. FIB milling (Subsection 2.3.4.1) and localized Ar^+-etching (Subsection 2.3.4.2) have been used in combination for this work in order to fabricate SET devices (Chapter 4).
Depending on the interaction between the ions and the atoms of the target surface, different effects can be observed, such as sputtering, swelling, redeposition, backscattering, implantation and amorphization of the near-surface layers. When enough momentum is transferred from the impinging ions to the target nuclei, one or more atoms overcome their surface binding energy and can be freed from the surface or get dislocated meanwhile the impinging ion is deflected. Ions can also penetrate into the lattice and become trapped as their energy gets dissipated. This effect is called ion implantation, and it depends mainly on the mass, energy and the angle between the surface normal and the trajectory of the colliding ions.

2.3.4.1 Focused Ion Beam (FIB) etching by Ga^+-beam

A FIB setup is a scientific instrument that resembles a SEM. However, while the SEM uses a focused beam of electrons to image the sample in a HV chamber, a FIB setup uses a focused beam of ions instead. For this reason, the two instruments use different type of source and optics. Details about the FIB used in this work can be found in Subsection 2.2.1.
FIB uses a closely focused beam of ions to form a scanning ion probe. The position and timing of the ion beam exposure are controlled by a pattern generator, which defines the fabrication strategy. The technique has maskless design machining capability, spatial resolution in the nanoscale and accessible integration capacity [283]. However, manufacturing throughput may be low since the direct writing nature of the process

undermines large-scale efficiency by high-dose FIB applications. The interaction of the primary ions with the atoms of the target sample is now discussed.
The Ga^+-ions strike the sample with high energy (typically 30 keV). The ion-sample interactions result in sputtered atoms from the surface, whereas ions are implanted into the top few nanometers of the sample surface, causing amorphization [284, 285]. In addition, a series of other effects occurs, such as backscattering, excitation, amorphization, sample heating and other chemical reactions. A representative sketch of the process is reported in Figure 2.38. Differently from the electrons in an electron gun with the same charged particle energy, the ions in a FIB have considerably higher mass (Ga atomic mass=69.723 amu and e atomic mass $= 5.488 \times 10^{-4}$ amu) and their sputtering power on the sample is several orders of magnitude higher than for electrons.

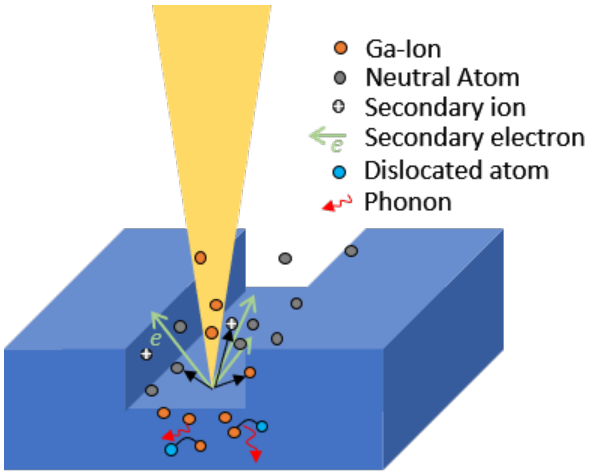

Figure 2.38: A schematic description of ion-matter interaction mechanisms. The interaction between the energetic ions and the nuclei or electrons of the solid material can produce a variety of physical and chemical phenomena. Some of the interaction results are listed in the picture.

The sputtering yield assesses the efficiency in material removal and is defined by the equation [81]:

$$Y(\theta) = \frac{Number\ of\ sputtered\ atoms}{Number\ of\ incident\ ions} \tag{2.10}$$

The sputtering yield strongly depends on the angle θ between the surface normal and the direction of the ions. However, other variables such as masses of ions and target atoms, ion energy, target temperature, and ion flux affect the sputtering yield. In addition, during sputtering, redeposition takes place into the sputtered region of a portion of the ejected atoms. Thus, it is difficult to control and estimate the amount of material actually removed by sputtering. FIB is extensively used in nanoscale machining/engineering applications such as TEM lamella sample preparation, etching of nanostructures [286], deposition [81] and doping [287].

In our setup, a Ga^+-ion beam with 30 kV acceleration voltage and 10 pA current has been used to etch the cross-region of the contacts defined by UVL in order to obtain a basic SET design with two gates [14]. The smallest gap size, that has been proven to be electrically isolated with the used setup and the mentioned FIB parameters, has been about 50 nm.

2.3.4.2 Ar^+-polishing by Beam Induced Polishing and Sputtering (BIPS)

A novel *in situ* Ar ion milling process has been used for the last step of the FEBID-based SET device fabrication described in Chapter 4.
The technique is based on the local modification of the sample surface provided by a static beam of low-energy Ar^+ ions [288]. Its applications are numerous, two of them are polishing of the top surface of a sample from the Ga-doped layer and from the redeposited material after Ga^+-FIB operation. Moreover, it can be used to clean a sample from residual hydrocarbons or FEBID co-deposit material [14, 289].
The setup consists of a Beam Induced Polishing and Sputtering (BIPS) system installed in the dual-beam FIB-SEM used for this work (FEI Nova Nanolab 600) by Thermo Fisher Scientific. By use of a Tungsten capillary with an inner radius of 17.5 μm, a localized Ar flow has been provided in close proximity to the sample. In the above mentioned application (Chapter 4), the substrate has been tilted by 45° from the *e*-beam axis, maintaining 100 μm distance in the vertical direction from the Ar gas nozzle. A bias of 100 V has been applied between the sample surface and the Ar nozzle. The Ar flux is ionized by scanning the e-beam over a slit previously cut with the Ga^+-FIB close to the nozzle aperture. In this way a plasma spark is initiated. A sketch of the setup is shown in Figure 2.39.

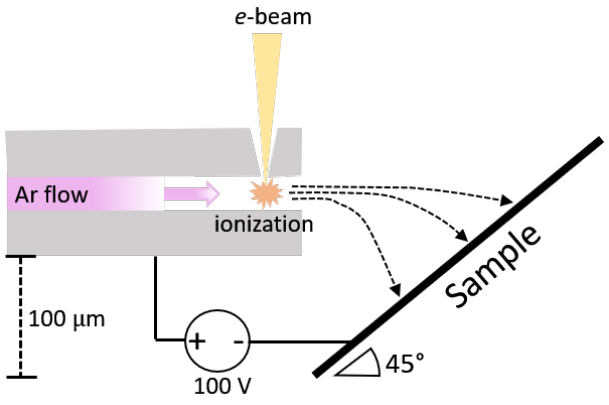

Figure 2.39: Schematic setup representation of the *in situ* localized low-energy Ar^+-polishing. The field defined by the distance sample-nozzle and the applied bias induces acceleration of ions towards the sample surface. Adapted from [288].

The area affected by the milling is a disc-like field whose width can be tuned with the

applied bias and distance to the substrate. This region is easily adjustable by changing the nozzle-to-sample distance. In Figure 2.40 (a), the Ar nozzle and the milled area on a Cr-Au electrode are visible. A close-up of the highest milling intensity and its halo is shown in Figure 2.40 (b).

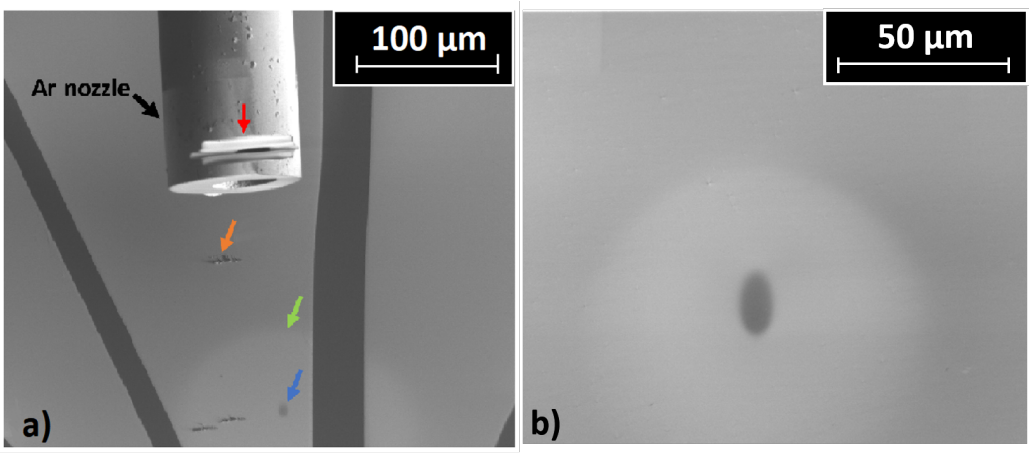

Figure 2.40: a) SEM picture of the nozzle and the substrate. The red arrow indicates the slotted hole, on which the electron beam is scanned during the polishing step. The orange arrow points to the scratch caused by the slight collision between the nozzle and the substrate during the nozzle-substrate distance (100 μm) arrangement procedure. Blue and green arrows indicate the inner and outer milled area, respectively. b) Closeup of the milled area. The milled halo diameter extends over approximately 80 μm.

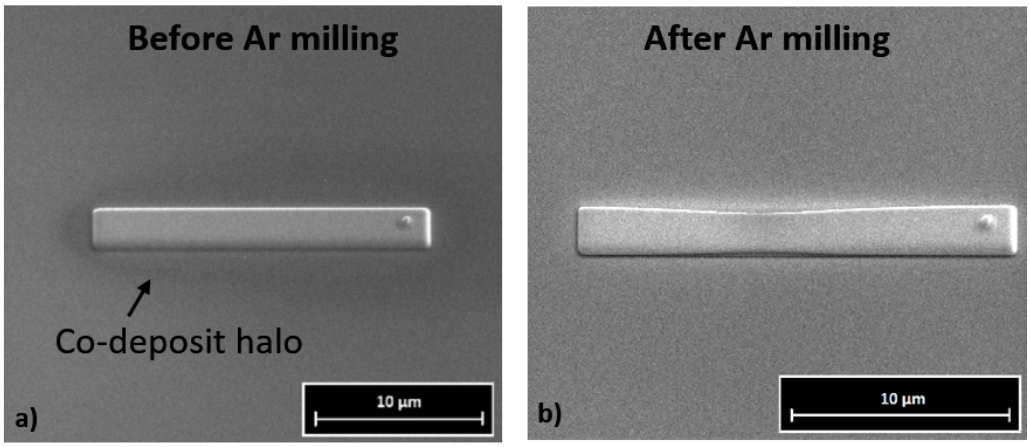

Figure 2.41: a) SEM picture of a Pt-C FEBID structure. A dark grey halo can be recognised in the area around the structure. This halo is undesired co-deposited material. b) SEM picture of the structure in (a) after Ar-etching. The co-deposit halo is removed. Moreover, the structure has been slightly milled.

This technique has been used in the present work to polish and erase the co-deposit associated with the Pt-C FEBID fabrication. The co-deposit has been found to be the

main cause of stray capacitance and background charges compromising the electrostatic environment and the consequent functioning of devices fabricated with FEBID. The detrimental effects associated with the co-deposit are reported in Appendix C.
An example of the Ar^+ polishing treatment of a Pt-C FEBID structure is shown in Figure 2.41. The co-deposit halo (dark grey) generated by FEBID with $Me_3PtCpMe$ precursor is covering the area around the defined structure about a few μm. By using the Ar^+-polishing step after the deposition, the co-deposit halo apparently is removed and the structure has been slightly thinned out by the process.

2.4 Electrical and magneto-transport characterization measurements

The characterization of samples with regard to their electronic transport behavior has been conducted at room temperature *in situ* inside the dual-beam FIB-SEM or at low temperatures inside the ^{3}He-cryostat. Different types of electrical measurements have been conducted on the various samples described in this work and are here listed:

- **Current *vs.* voltage characteristics (I(V))** have been used to measure the resistance of ohmic samples or to study the evolution of the Coulomb blockade depending on temperature and gate voltage (V_{gs}) for NP assemblies and SET devices.
- **Current *vs.* temperature (I(T))** and **Voltage *vs.* temperature (U(T))** measurements have been conducted on NP assemblies and AS-ALD samples, respectively. These measurements are particularly useful to understand the nature of the electrical transport taking place in the samples.
- **Voltage *vs.* magnetic field (U(B))** measurements of the Hall-voltage and high-resolution magneto-conductance measurements have been performed to gain information about the charge carries mobility and transport mechanism.
- **Current *vs.* time (I(t))** measurements have been carried during catalytic purification and AS-ALD as monitoring measurements of the processes.

Depending on the resistivity of the samples investigated, voltage-driven Direct Current (DC) and current driven Alternating Current (AC) measurements have been conducted. It is worth mentioning that most of the samples studied in this work are very highly resistive (for example as deposited Pt-C FEBID and contacted nanoparticles arrays have a resistivity in the range of $10^7\,\mu\Omega\,\mathrm{cm}$). In this case, the samples are measured with a DC setup since reversing polarity induces capacitance-voltage hysteresis.
For tunnel junction-based systems, like NP arrays, SET and narrow constriction, the

electric field strength becomes very high for such small dimensions and it can lead to electric arcs that may destroy the samples. For this reason, the electrical properties of the previously mentioned samples have been studied by using highly sensitive source meters in order to monitor sample currents not higher than a few nA. A Keithley source meter (model 2400), a Keithley two-channel source meter (model 2636A) and a Agilent 34420A nanovoltmeter have been used in the dual-beam FIB-SEM and ^{3}He-Cryostat setups. AC measurements have been performed with a Stanford Linear Research lock-in amplifier (SRS830) and a selectable shunt resistor.
The 2- and 4-probe techniques have been used in DC current mode. The 4-probe technique has been preferred to directly detect the voltage drop produced by the sample and eliminate the contacts' contribution. However, due to the chip configuration and knowing the measured resistivity of the setup, mostly 2-probe measurements have been carried out with negligible contact resistance contributions.
For the samples subjected to AS-ALD, two particular AC differential monitoring methods and high-resolution AC electrical magneto-transport measurements in bridge configuration are described in Subsection 2.3.2.4 and in Appendix A, respectively. Special attention is given to these two methods since they are not standard techniques and they have been developed in the laboratory during this work.

2.4.1 ^3He-cryostat system for electrical and magnetic measurements

For the sake of electrical characterization of materials and devices with particular features only observable at very low temperatures, the use of cryogenic systems is necessary. Depending on the temperature range being investigated, various cryogenic systems such as continuous flow cryostats, storage dewars, sorption pumped systems, dilution refrigerators and nuclear demagnetization systems can be used [290].
In this work, the investigation of single-electron phenomena and the temperature-dependent electrical characterization of AS-ALD nanostructures have been conducted in a ^{3}He-cryostat.
The ^{3}He-cryostat by Oxford Instruments is equipped with a vacuum sealed Inner Vacuum Chamber (IVC), a Variable Temperature Insert (VTI) (HelioxVTI), active sorption pumps, superconducting coils and electrical cables through the IVC providing the possibility to measure electrical and magnetic properties of samples in the whole temperature range from room temperature down to 300 mK [291]. In Figure 2.42, a representative sketch of the used ^{3}He-cryostat with its most important parts is shown. The cryostat has an external vacuum chamber that acts as a thermal insulation shield for the inner part of the cryostat from the outside. Inside the vacuum chamber, there is

a ^{4}He-bath containing superconducting coils. These coils can generate a magnetic field of up to 9 T. The pumping line of the cryostat is connected to a rotary pump which can pump ^{4}He from the He-bath to the IVC closed ^{4}He line through a needle valve. In addition, the rotary pump is connected to a lambda cooler. The lambda cooler is used to enhance the operation performance of the superconducting magnet that usually operates in liquid helium at 4.2 K. The lambda cooler pumps the He in its coils, which are immersed in the He-bath, leading some of the ^{4}He in the coils to evaporate and reach temperatures near the lambda point (approximately 2.17 K). In this way, the lambda cooler leads eventually to cooling the surrounding liquid, which sinks down cooling the ^{4}He below the coils.

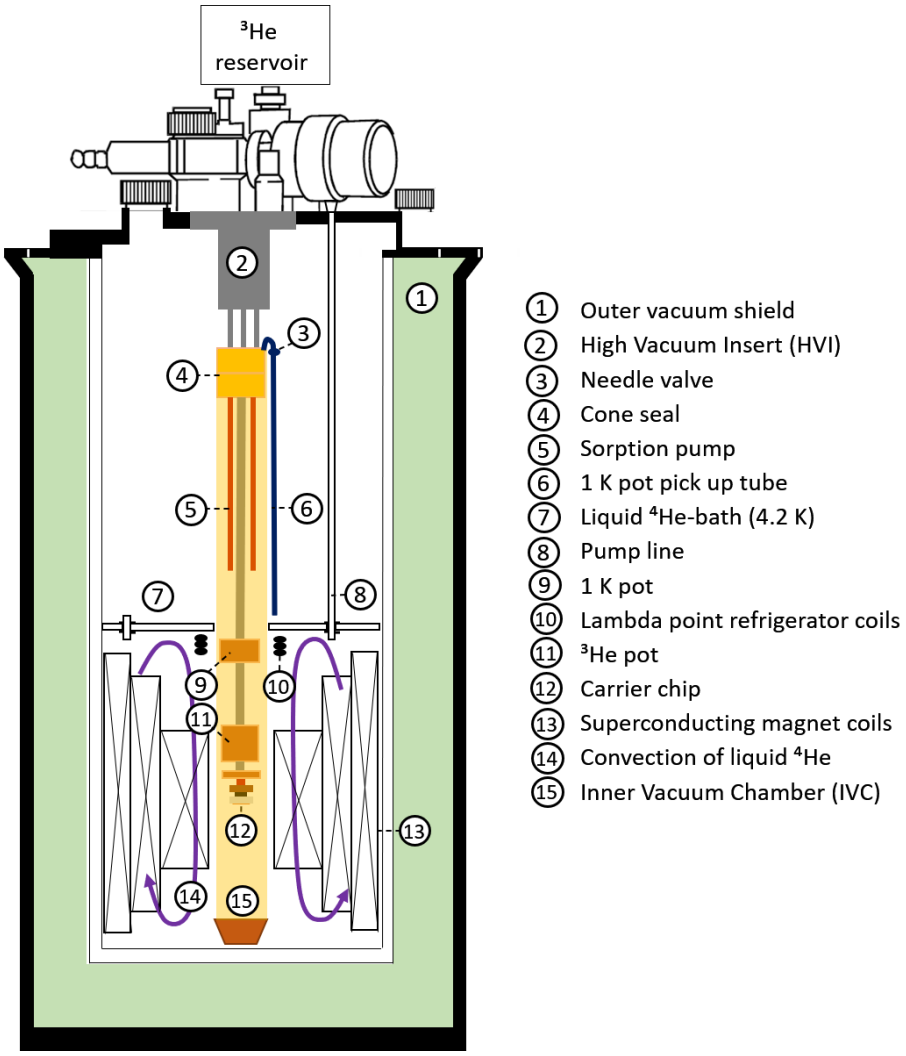

Figure 2.42: Schematic drawing of the ^{3}He-cryostat used in this work. The particularity of this cryo system is that the ^{3}He gas is safely stored within the Heliox insert at all times. In this way, the sample in the insert can reach 0.3 K and no ^{3}He refill is needed. The components of the system are indicated in the picture.

The sample is introduced in the middle of the coils inside an IVC that can be evacuated to guarantee thermal isolation from the surrounding or, contrary to the previous purpose, He gas can be inserted inside this volume and act as heating/cooling medium. The sample is mounted to the base of the ^{3}He pot placed at the end of the sample rod in vacuum. In order to establish the best thermal coupling between the sample and the ^{3}He pot, the back of the carrier chip (made of copper) is screwed and firmly pressed to the copper piece on the base of the ^{3}He pot. A photograph of a calibration sample attached to the cryostat sample rod is shown in Figure 2.4 (c).
In the ^{3}He pot, there are two temperature sensors, a ruthenium oxide and a cernox sensor used for controlling the temperature in the low-temperature mode and high-temperature mode, respectively. The IVC is then sealed by a greased cone seal and pumped. In order to faster cool the insert, a small amount of ^{4}He gas (approximately 1 cm^3) at Normal Temperature and Pressure (NTP) is allowed into the IVC. The insert may then be cooled by lowering it slowly into the liquid helium reservoir. A schematic diagram of the cooling process is shown in Figure 2.43 (a). The different components are then underlined in Figure 2.43 (b), in which a picture of the inside of the IVC (sample rod) is shown.
In the HelioxVTI a 1 K pot is present. The 1 K pot is cooled to < 2 K by pumping ^{4}He from the ^{4}He-bath through a pick-up tube and the ^{4}He flux is controlled by a programmable needle valve through a pipe inside the 1 K pot. Mounted to the 1 K pot, an exchange gas sorption pump is used to trap the ^{4}He gas inserted in the IVC for fast cooling. The temperature of the 1 K pot is monitored by a ruthenium oxide sensor. Additionally, a sorption pump for the ^{3}He is fixed in the middle of the HelioxVTI. It consists of three cylinders with active charcoal, used to store or release ^{3}He depending to the temperature. In the ^{3}He sorption pump, an Allen-Bradley temperature sensor is installed.
At the top of the HelioxVTI, 2.7 L of ^{3}He gas is stored at a pressure of approximately 2 bar (absolute) into a self-contained storage vessel. This approach avoids waste of the valuable gas. The operating temperature range of the insert is from base temperature to 300 K. However, when the insert is attached to the cryostat body, the maximum temperature is limited by the heat exchange between the liquid helium bath and the IVC. In this case, the upper limit has been observed to be around 170 K.
The insert uses two separate modes of operation, a low-temperature mode (when the ^{3}He pot temperature is lower than 1 K) and high-temperature mode (when the ^{3}He pot temperature is higher than 1 K). When the ^{3}He pot temperature is lower than the one of the 1 K pot, the insert runs as a conventional sorption pumped ^{3}He insert.
Above 1 K, the ^{3}He pot is heated directly. The temperature is controlled using a Mercury ITC temperature controller, which automatically balances the heater power against the cooling provided by the ^{4}He flowing through the 1 K pot. Once the 1 K pot temperature has cooled below 4.2 K, the ^{3}He charge must be condensed into the ^{3}He pot. This is achieved by the ^{3}He regeneration procedure. By warming the ^{3}He sorption pump to

a temperature ≈ 30 K, the ^{3}He is completely released from the sorption pump. The procedure can last up to 1 h. In the meantime, the 1 K pot is pumped and the needle valve is opened to allow a slight flow of ^{4}He. The 1 K pot cools to below 1.5 K. As a consequence, the ^{3}He is free to condense into the small tube in the 1 K pot region and runs down to cool the ^{3}He pot.
After approximately 20 minutes most of the gas is condensed into the ^{3}He pot at about 1.5 K. At this point, the ^{3}He sorption heater is switched off. The sorption pump cools down reducing the vapor pressure above the liquid ^{3}He and letting the ^{3}He pot cool further. The lowest temperature ever achieved in the ^{3}He pot has been 267 mK for 10 h before the temperature rose again, since no more liquid ^{3}He has been left inside the ^{3}He pot. Intermediate sorption temperatures are used to achieve stable sample temperatures between base temperature and 1 K without applying heat to the ^{3}He pot.

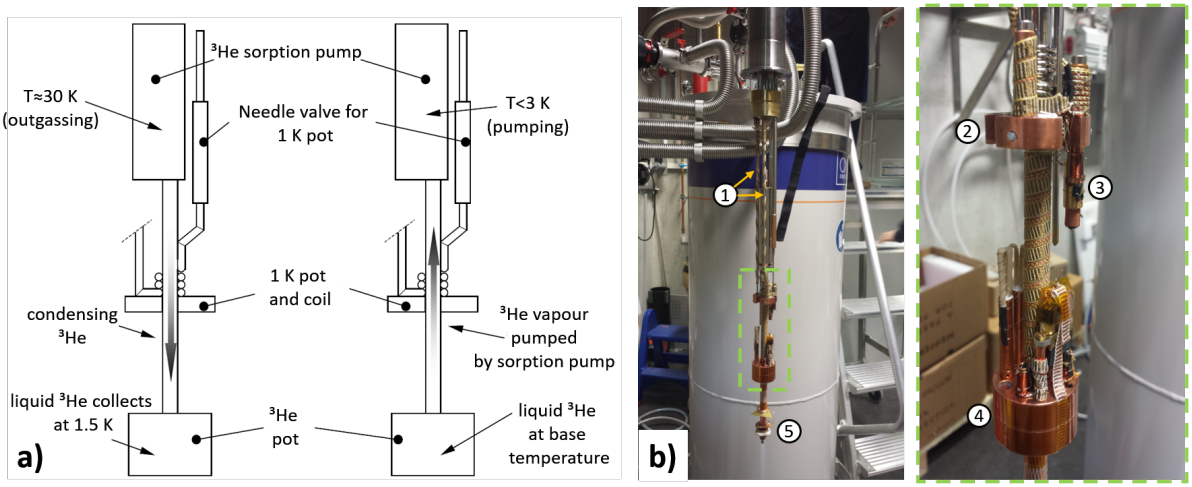

Figure 2.43: a) Operation principle of a sorption pumped ^{3}He insert. Adapted from [291]. b) Photograph of the sample rod as the IVC is opened at room temperature. Inset: Closeup of the insert part in which the ^{3}He is condensing. The indicated components are: 1) ^{3}He sorption pump: a pair of charcoal sorption elements; 2) the 1 K pot; 3) ^{4}He gas sorption pump; 4) the ^{3}He pot.

2.4.1.1 Temperature dependence of electrical conductivity

The investigation of the electrical conductivity dependence on temperature allows the researcher to investigate the characteristic conductivity properties of materials such as metals, semiconductors and superconductors. For example, impurities, cristallographic defects, phonon scattering and magnetic domain effects can be traced back as peculiar features in the material's temperature dependence of the electrical conductivity [35].
In this work, the analysis of the temperature dependence of the electrical conductivity of NP arrays (Chapter 3) and AS-ALD grown FEBID-based nanostructures (Figure 2.33)

has been a powerful tool to understand which transport mechanisms are at play in the samples from the observed conductivity trends.

2.4.1.2 SET circuit

The SET characterising measurements are Coulomb stability and Coulomb oscillation diagrams that are described in detail in Chapter 4. In order to conduct the measurements, a Keithley two-channel source meter (model 2636A) has been used in the configuration reported in Figure 2.44. I-V characteristics have been conducted sweeping the voltage until a defined limit in steps meanwhile the current has been sensed.

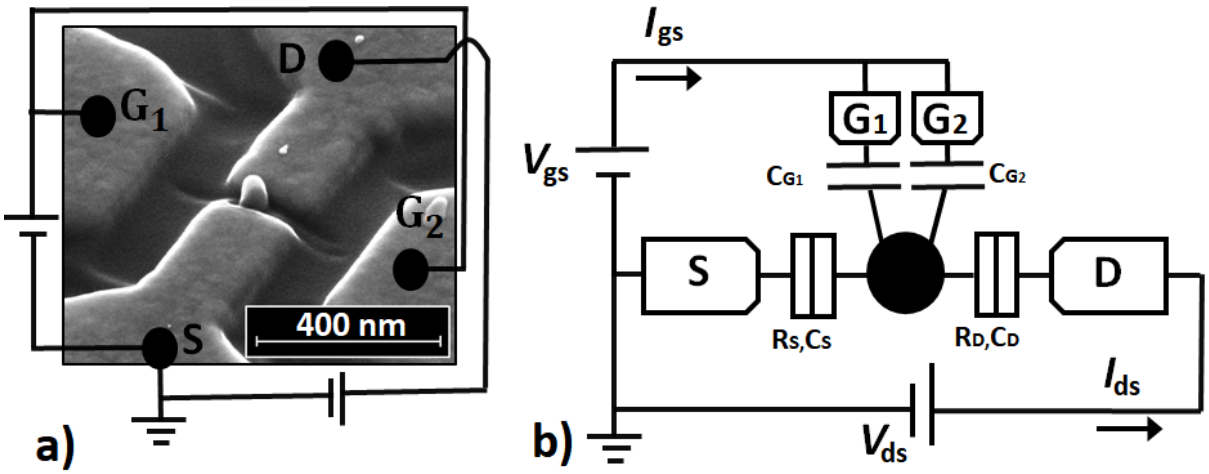

Figure 2.44: Schematic description of the SET circuit in the SEM picture of Sample A (Chapter 4). The Figure is used with permission from [14].

For Coulomb stability diagrams, a fixed V_{gs} has been applied when at the same time V_{ds} has been swept and the respective current measured. Coulomb oscillation plots have been drawn for fixed V_{ds}, measuring I_{ds} when V_{gs} has been swept. The characteristic features that are obtained by testing a functioning SET are sketched in the subsection dedicated to SET in the Theory Chapter 1.5.2 in Figure 1.18. Experimental measurements are reported in Chapter 4.

2.4.1.3 Alternating Current (AC) electrical magneto-transport measurements in bridge configuration

For the characterization of the AS-ALD nanostructures, high-resolution magneto-transport measurements have been conducted in a bridge configuration using a Stanford Linear Research lock-in amplifier(SRS830), a SR560 differential preamplifier and a ratio transformer as variable element of the bridge to null the signal at $H = 0$ [6]. The measurements have been performed at constant temperature.
The standard canceling technique has been successfully used to measure the very small resistance increase, ΔR, due to localization and electron-electron interaction effects in Pt wires and Ag films with reduced cross-sectional areas [292, 293].
In this work, the use of this technique is necessary to measure the anti-localization effect, which without filtering and amplification, would be completely masked by background noise. The setup used to perform the measurements is shown in Figure 2.45. The lock-in amplifier was sending 10^{-7} A as input at 537.6 Hz and measures the signal and noise of the output. The shunt resistor had a resistance of 9.99 MΩ and the ratio transformer has been set to the resistance value of the sample at 0 T ($R(0)$). The voltage across the sample produced by the excitation current i, $V(B) = i\,R(B)$, is measured subtracting the reference voltage that is equal to the zero-field voltage across the sample, $V(0) = i\,R(0)$ obtaining the differential resistance $\Delta R(B)$:

$$V(B) - V_0 = i\,R(B) - i\,R(0) = i\,\Delta R \tag{2.11}$$

The resulted small signal (2/100000) is then amplified ×100 and the frequencies in the range 3 - 30 kHz are filtered. The measurements carried out with this technique are reported in Appendix A Figure A.1 for Sample 1.

2.4.1.4 Hall effect measurements

In order to characterize the charge carriers of the nanostructures subjected to AS-ALD, Hall effect measurements have been conducted. The electric setup consisted of a Stanford Linear Research lock-in amplifier (SRS830), a SR560 differential preamplifier and a ratio transformer to null the signal at $H = 0$. The setup is almost the same as the one used for magneto-transport measurements. In Figure 2.45, the dashed green line indicates the different electrical connection for the Hall effect measurements. The measurements have been performed at constant temperature.

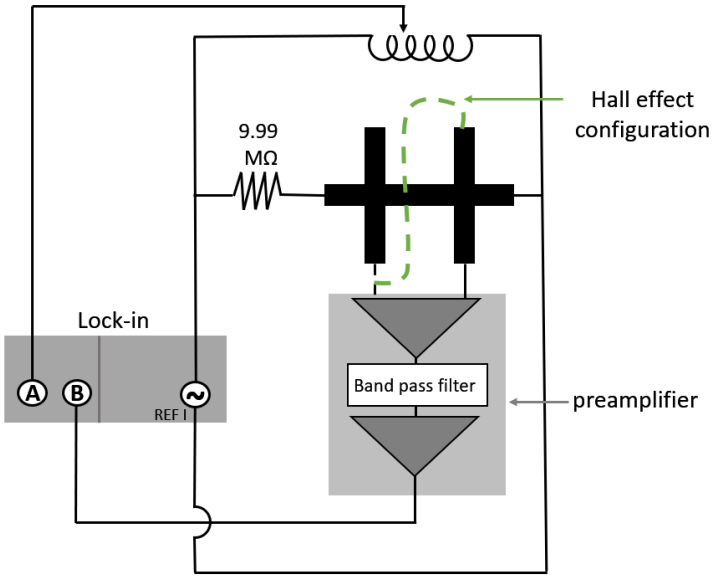

Figure 2.45: Schematic representation of the setup circuit for magneto-transport and Hall effect measurements. The dashed green line represents the electric configuration for the Hall effect measurements. Adapted from [293, 294].

Chapter 3

Single-Electron transport in Au-nanoparticle arrays contacted by Pt-FEBID purified electrodes

In the present chapter, the electrical transport properties of packed arrays of Au-nanocrystals combined with Pt-contacts, which have been realized by FEBID and subjected to a post-growth purification process, are presented.
As described in Subsection 2.3.3, the NP arrays consist of monolayers of thiol-PEG ligated gold nanoparticles (diameter = 12.5 nm), synthesized and deposited by drop-casting from solution onto Si/SiO_2 substrates in close proximity to lithographically defined gold electrodes. The Au-NP arrange in triangular lattices with domain sizes up to 1μm. The ligands serve as mechanical spacer between the particles. After the drop-casting and individuation of a suitable group of NP after SEM investigation, this domain of nanoparticles has been contacted by Pt-C FEBID and later, the assembled structure has been subjected to a catalytic purification. A SEM overview picture (a) and a closeup (b) on an exemplary contacted NP array are given in Figure 3.1.
In particular, in order to contact the gold electrodes to the NP arrays, Pt-C FEBID deposits have been written applying the precursor $Me_3PtCpMe$. The FEBID nanofabrication technique has been presented in detail in Subsubsection 2.3.1.4. Due to the typical low metal content and residual organic fragments in the deposits, the Pt-C FEBID contacts have been treated with the catalytic purification technique developed by Sachser [15]. This purification method has been described in Subsection 2.3.1.4. By using the post-growth treatment, the Pt contacts lost their carbonaceous matrix and became metallic (with a residual resistivity about 50.54 $\mu\Omega$ cm) and suitable to be used as electrodes. It is important to notice, that the arrangement of the nanoparticles in the arrays is not affected by mechanical changes connected to either the oxidation or

high-temperature treatment (250°C). Evidence of this can be found in Figure 3.2, in which the array chosen for Sample A is shown before and after the purification treatment of the FEBID electrodes. The separation, $s = 10\,\text{nm}$, that is created by the nanoparticle ligands, is maintained.

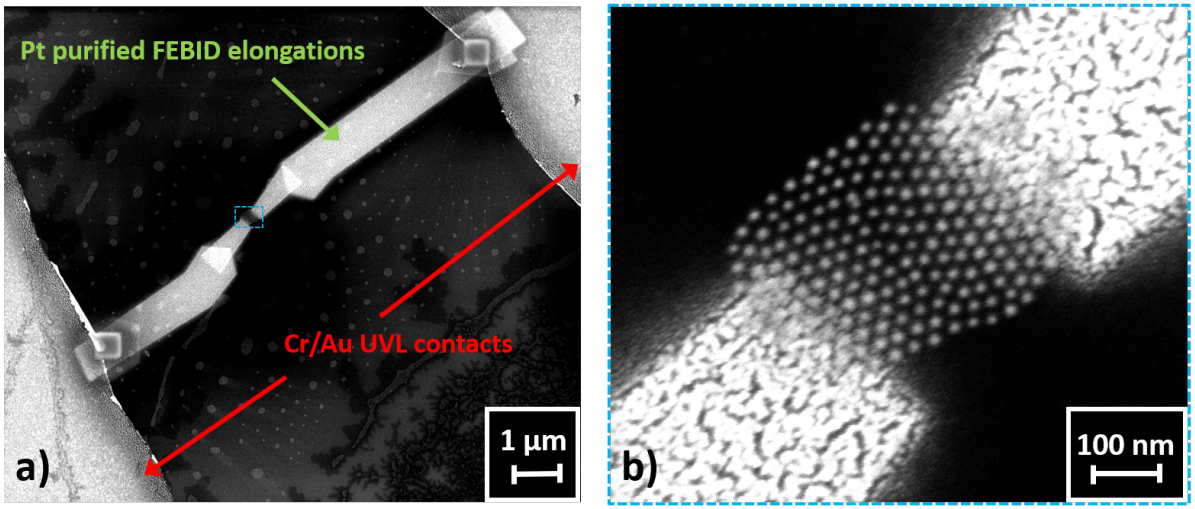

Figure 3.1: a) SEM overview of a Au NP array sample contacted by Pt-C FEBID. The FEBID leads have been purified following the Pt catalytic purification procedure described in Subsection 2.3.1.4. b) Closeup of the well-ordered NP assembly between the Pt purified FEBID contacts.

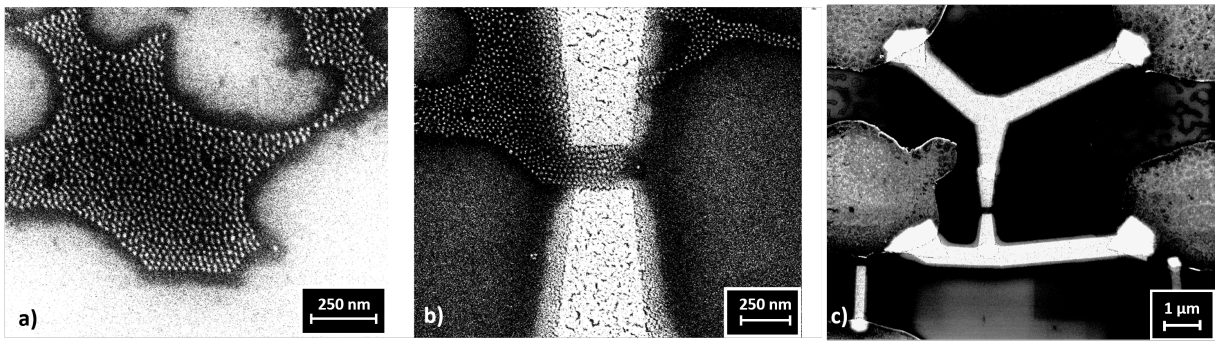

Figure 3.2: a) SEM picture of the Au-NP assembly which for form, dimension and order has been selected to be contacted. b) SEM picture of the same assembly after Pt-C FEBID catalytic purification of the electrical elongations. The contacted NP array is referenced as Sample A. c) SEM overview of Sample A. The NP array has been contacted by Pt FEBID purified leads in a 4-probe configuration to the next Cr-Au UVL pads.

Samples Four samples are presented in this section: Sample A, B, C and D.
Sample A and Sample B have been defined on the same substrate and their contacts have been written with the same FEBID parameters. An acceleration voltage of 5 kV at

a beam current of 98 pA with a pitch of 2 nm, a dwell time of 1 μs and 50 passes have been used for the FEBID process. The deposition dose of the contact elongations has been 2.45 nC/μm^2. AFM measurements, which have been conducted on the sample after executing electrical measurements inside the ^3He-cryostat, showed that the height of the contacts was 19 ± 2 nm. Sample A has been created contacting an array found in the middle of the substrate, for which 4 leads have been written on the far ends of the array by Pt-C FEBID to the next Cr-Au UVL contacts. The distance between the FEBID contacts has been set to 200 nm. Due to co-deposit expansion (during the deposition process) and lateral shrinking (during the purification treatment), the final separation is about 160 nm. In Figure 3.2 (c), a SEM overview picture of Sample A after the purification treatment is shown.

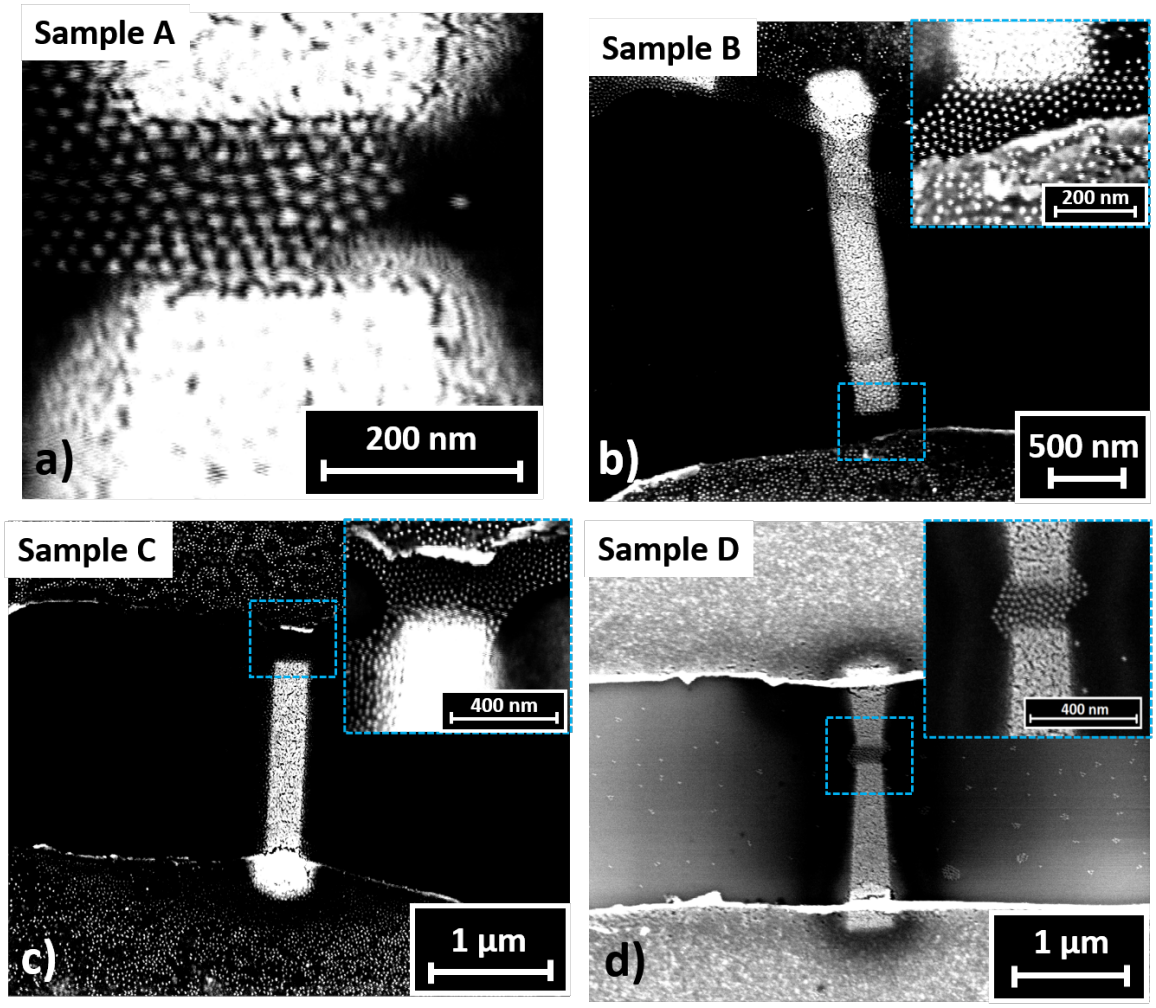

Figure 3.3: a) SEM picture of Sample A (a), Sample B (b), Sample C (c) and Sample D (d). In (b), (c) and (d) closeup SEM pictures of the contacted NP arrays are given as insets. An overview picture of Sample A is given in Figure 3.2 (c).

Sample B is defined directly contacting an ordered array between two Cr-Au UVL contacts. From one of the contacts, a metallic elongation has been fabricated using Pt-C FEBID. In this way, a reduced FEBID co-deposition on the NP array has been achieved. The separation between the FEBID and the UVL contact has been set to 250 nm. The co-deposit halo and the shrinking effect (of the electrode deposited with FEBID) reduced the separation to roughly 230 nm.
Sample C has been assembled on the same substrate as sample A and Sample B. An array found between the gap of two neighboring gold contacts has been electrically contacted to one side elongating one UVL electrode with a FEBID deposit and to the other side directly using the neighboring gold electrode as electrical lead for the NP array. The FEBID contact has been written with half the dose of Sample A and Sample B, i.e. $1.245\,\mathrm{nC}/\mu\mathrm{m}^2$. AFM measurements conducted on the sample after executing electrical measurements inside the ^3He-crystat, showed that the height of the Pt purified FEBID electrodes was about 12 nm.
Sample D has been created on another Si/SiO_2 substrate. An NP array has been contacted by using Pt purified contact elongations from two Cr-Au UVL contacts. The FEBID contacts have been written with a slightly different dose of $3.23\,\mathrm{nC}/\mu\mathrm{m}^2$ and using a dwell time of $0.250\,\mu$s. The separation gap between the contacts during the FEBID writing process has been set to 200 nm. The finally obtained separation has been approximately 180 nm. The height of the purified FEBID electrodes has been found to be 19 ± 2 nm by AFM measurements.
SEM pictures of the described samples are given in Figure 3.3.

Electrical measurements In order to analyse the electrical transport occurring in the array of nanoparticles, the capacitance and the charging energy of one nanoparticle, has been calculated.
The nanoparticles can be approximated as spheres. In the case of an isolated nanoparticle, the capacitance and the charging energy are obtained from Equations 1.2 and 1.3:

$$C_{0_1} = 4\pi\epsilon_0\epsilon_r R = 2.712\,aF \tag{3.1}$$

and

$$E_{C_{0_1}} = \frac{e^2}{2C_{0_1}} = \frac{e^2}{8\pi\epsilon_0\epsilon_r R} = 0.029\,eV \tag{3.2}$$

where $R = 6.25$ nm is the radius of the nanoparticle and $\epsilon_r = 3.9$ is the dielectric constant of the silicon oxide of the substrate [295]. In addition, the capacitance and the charging energy of the nanoparticle in the array can be theoretically calculated taking into account the single NP capacitance and the cross-capacitances. The capacitance and the charging

energy of the single NP can then be approximated using 1.27 and 1.28:

$$C_{0_2} = 4\pi\epsilon_0\epsilon_r \frac{R(R+s)}{s} = 4.407\,aF \tag{3.3}$$

and

$$E_{C_{0_2}} = \frac{e^2}{8\pi\epsilon_0\epsilon_r} \frac{s}{R(R+s)} = 0.018\,eV \tag{3.4}$$

where s is the separation between neighboring particles, $s = 10\,\text{nm}$.
In case the effect of the cross-capacitances is considered, the calculated capacitance and charging energy differ from the previous following the relations: $C_{0_1} = 0.615\,C_{0_2}$ and $E_{C_{0_1}} = 1.611\,E_{C_{0_2}}$. However, in the described system the nanoparticles are separated enough to not expect significant cross capacitances.
It is important to remember what Elteto and collaborators demonstrated [57] regarding the *coupling capacitance theory* which is reported in Section 1.3: when $d_{c-c}/R > 3$ (where d_{c-c} is the center-to-center distance) the correction of the single nanoparticle conductance as a result of coupling to nearest neighbors becomes lower than 10%. In the arrays presented in this work, the nanoparticles are separated enough ($d_{c-c}/R = 3.6$) and capacitance coupling can be ignored.
From the work of Samanta and collaborators [77] a barrier height of $E_g \approx 2.45\,eV$ [296] can be assumed for the thiol ligands. Using this energy gap in Equation 1.56 the resistance of the tunnel junction can be calculated. The equation yields an astronomical value of resistance when $E_g \approx 2.45\,\text{eV}$ and $s = 10\,\text{nm}$ are used. From this result, it can be concluded that the electrical tunnel transport among the nanoparticles proceeds via the SiO_2 substrate as dielectric mean instead of the molecular ligands. The ligands keep the nanoparticles apart from each other and they are not adding states next to the Fermi energy.

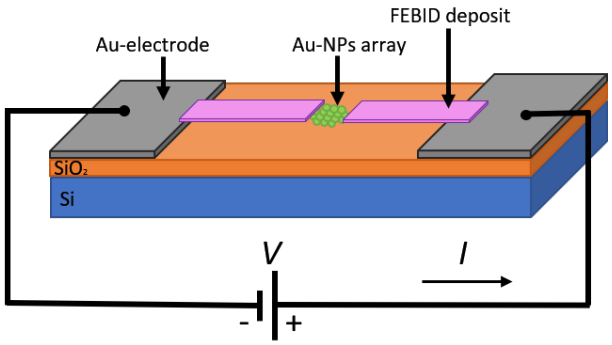

Figure 3.4: Circuit and geometrical schematic of the samples. The electrical properties of the samples have been investigated by using a DC source meter outside the HV chamber of the dual-beam FIB-SEM and of the ^{3}He-cryostat.

The NP arrays are measured in a 2- and 4-probe configuration by DC measurements. Details about the instrumentation and measurements are given in Section 2.4. A schematic of the system circuit is shown in Figure 3.4.

3.1 Current-voltage characteristics at low-temperature

The purpose of this section is to discuss the particular feature of a sharp Coulomb blockade behavior of the I-V characteristic observed for the Samples A, B, C and D. Unfortunately due to ElectroStatic Discharge (ESD) occurring on the substrate, Samples A, B and C were destroyed after the measurements shown in this section. It follows that no other I-V characteristic can be shown at other temperatures for these samples. For Sample D, the evolution of the I-V characteristic with temperature is shown and discussed in the Subsection 3.2. At very low temperature (circa 0.270 K), Sample A, B and C show non-linear current-voltage characteristics, with a well-defined threshold above which the applied bias has to be raised for conduction to occur [39].

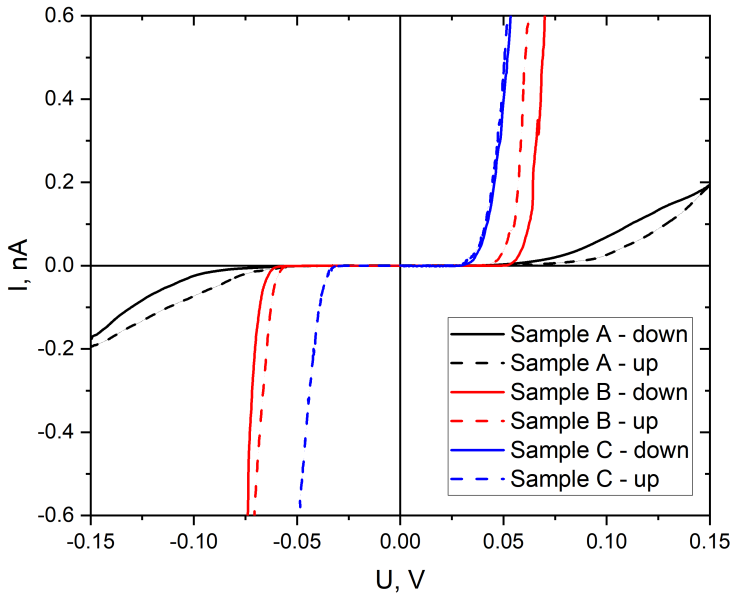

Figure 3.5: I-V characteristics of Samples A, B and C at circa 0.270 K. Sample B and Sample C show a sharper Coulomb blockade region in comparison to the one of Sample A. The current has been measured sweeping the voltage up and down between -0.15 and 0.15 V to not overcome 1 nA as current limit.

In Figure 3.5, the I-V characteristics of Samples A, B and C are shown. The diode like I-V curves of the three samples show different threshold voltages and slightly different slope of the increasing current when the voltage overcomes the threshold voltage. Considering that the increase of the current can be approximated with Equation 1.35 to $I \sim I_0(V - V_t)^{\zeta}$, the value $\zeta_{Sample\,A} = 2.67 \pm 0.03$ and $V_t(0)_{Sample\,A} = 0.055 \pm 0.004\,\mathrm{V}$ from a powerlaw fit $y = a(x - b)^c$ has been calculated for the curves measured with decreasing voltage. These curves are marked as "down" and dashed lines in Figure 3.5. The I-V characteristics of Sample B and Sample C are more similar to each other and the coefficient of the power-law and threshold voltage extracted from the fit are: $\zeta_{Sample\,B} = 5.52 \pm 0.04$, $\zeta_{Sample\,C} = 3.46 \pm 0.05$ and $V_t(0)_{Sample\,B} = 0.061 \pm 0.003\,\mathrm{V}$, $V_t(0)_{Sample\,C} = 0.037 \pm 0.002\,\mathrm{V}$. The I-V characteristics of Samples B and C are shown in detail in Figure 3.6. In the inset, a semi-log plot of the I-V curve is shown in order to better recognise the different power coefficients by a linear regression.

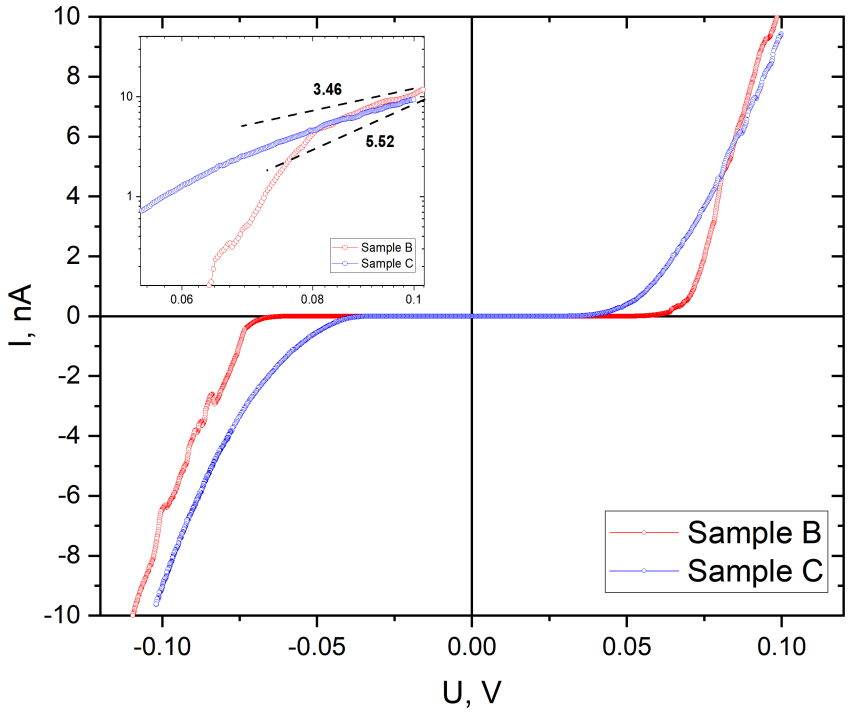

Figure 3.6: I-V characteristics of Samples B and C for decreasing voltage. Inset: Semi-log plot of the positive voltage range. With dashed lines, the value of ζ, extracted from Equation 1.35 for the corresponding sample, is reported.

3.2 Current-voltage characteristics of Sample D at different temperatures

The I-V characteristics of Sample D shows sharp Coulomb blockade behavior at 270 mK up to 20 K. The temperature evolution of the I-V characteristics of Sample D in the temperature range 0.270 - 75 K is shown in Figure 3.7.

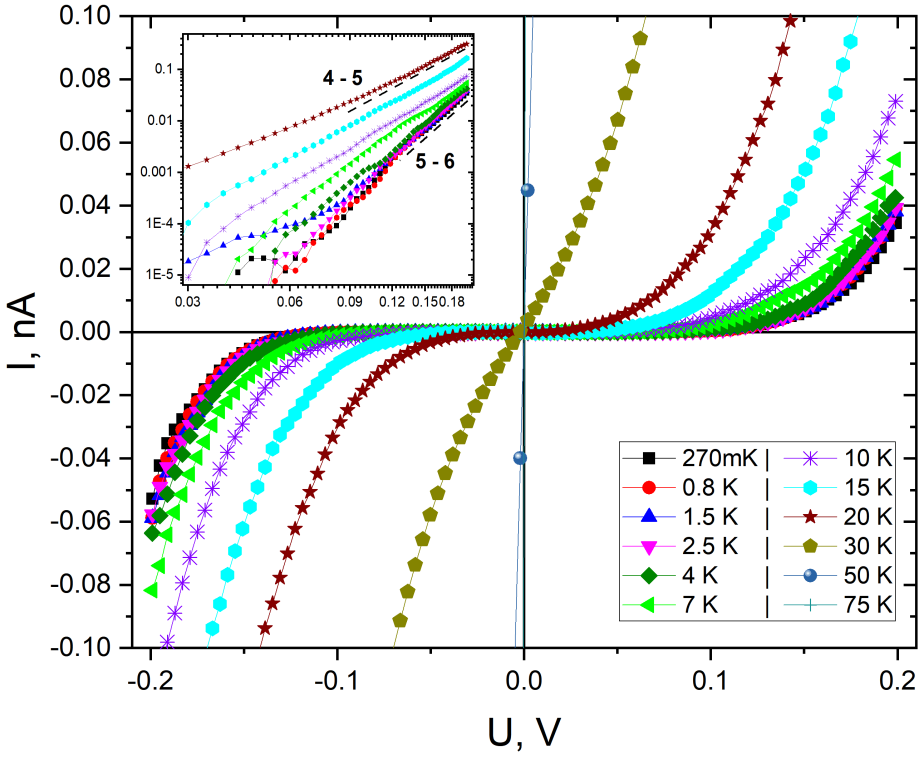

Figure 3.7: Temperature evolution of the I-V characteristics of Sample D. The measurements have been conducted inside the ^{3}He-Cryostat described in Subsection 2.4.1. Inset: Semi-log graph of the I-V curves. With dashed lines, the values $\zeta = 5 \pm 1$ are indicated corresponding to the power-law coefficient of Equation 1.35. The slope of the curves remains roughly the same for the I-V characteristics in the range 0.270 - 20 K.

Above about 20 K, the electrons overcome the charging energy due to thermal fluctuations and the arrays behave as an ohmic junction. In the inset of Figure 3.7, a semi-log plot of the I-V curves is shown. In this way, it can be easily noticed that the slope of the the curves remains roughly constant and the temperature-independent exponent extracted from the fit of Equation 3.1 is $\zeta = 5 \pm 1$ for the wide temperature range between 0.270 K and 20 K. As a consequence, the high-current powerlaw part of the I-V curves can be

mapped onto each other by voltage shift. Evidence of this behavior is shown in Figure 3.8.

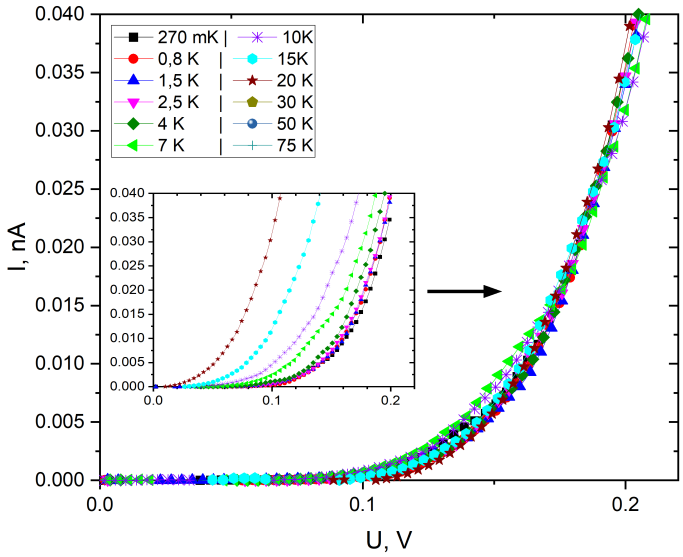

Figure 3.8: The I-V curves of sample D for positive voltages at different temperatures have been shifted on the voltage axis in order to visually show that the slope of the curve is approximately maintained and the curves collapse on one. Inset: original I-V curves measured between 0.270 K and 20 K.

The temperatures at which the I-V measurements have been conducted and the respective threshold voltages extracted from the powerlaw fit of Equation 3.1 are listed in Table 3.1. The threshold voltage can be determined for the I-V characteristics in the temperature range 0.270 - 15 K for which a well-defined Coulomb blockade is recognizable.

Temperature [K]	V_t [V]
0.270	0.071
0.800	0.072
1.5	0.061
2.5	0.066
4	0.055
7	0.045
10	0.034
15	0.024
20	0.009

Table 3.1: The extracted values of V_t are reported for the I-V measurements (Figure 3.7) conducted at different temperatures in the range 0.270 K - 20 K.

3.3 Temperature dependence of NP array electrical conductance

The samples described in this work show a distinctive single-electron charging trend in the temperature-dependent electrical conductance curve. The conductance S follows a simple activated Arrhenius behavior 1.12 in the highest temperature range. This electrical behavior crosses over into stretched exponential form described by Equation 1.36 for the lowest temperatures and it echoes ES-VRH. The temperature-dependent data of the electrical conductance for the four samples are shown in Figure 3.9, in which Arrhenius fits ($S(T) = S_0 \exp[-U/k_B T]$) of the high-temperature tendency are displayed with dashed lines next to the respective curve.

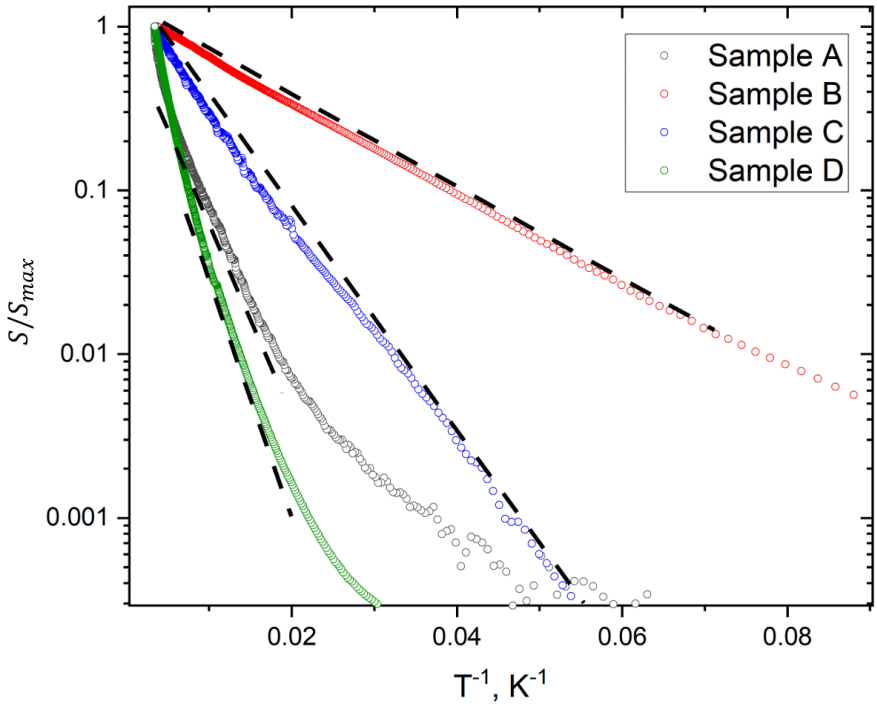

Figure 3.9: Semi-log plot of the normalized temperature-dependent conductance of Samples A, B, C and D over T^{-1}. The fits of the activated Arrhenius behavior $S(T) = S_0 \exp[-U/k_B T]$ are shown for the corresponding curve with dashed lines.

From the slopes of the semi-logarithmic plot, the characteristic energy U can be found. The U values, which have been extracted from the logarithmic fits on the respective range, are reported in the following table:

Arrhenius fit $S(T) = S_0 \exp[-U/k_B T]$		
Sample	Temperature range (±3) [K]	U (±0.0004) [eV]
Sample A	153 - 50	0.0217
Sample B	295 - 14	0.0056
Sample C	290 - 18	0.0157
Sample D	111 - 53	0.0267

Table 3.2: From the Arrhenius-like fits shown with dashed lines in Figure 3.9 the extracted U values for the corresponding sample.

The same curves can be displayed in a semi-logarithmic plot (Figure 3.10), in which the x axis is $T^{-0.5}$. Also in this graph, the slopes of the curve, extracted from a logarithmic fit, can give direct indication of the characteristic temperature T_0^{ES}.

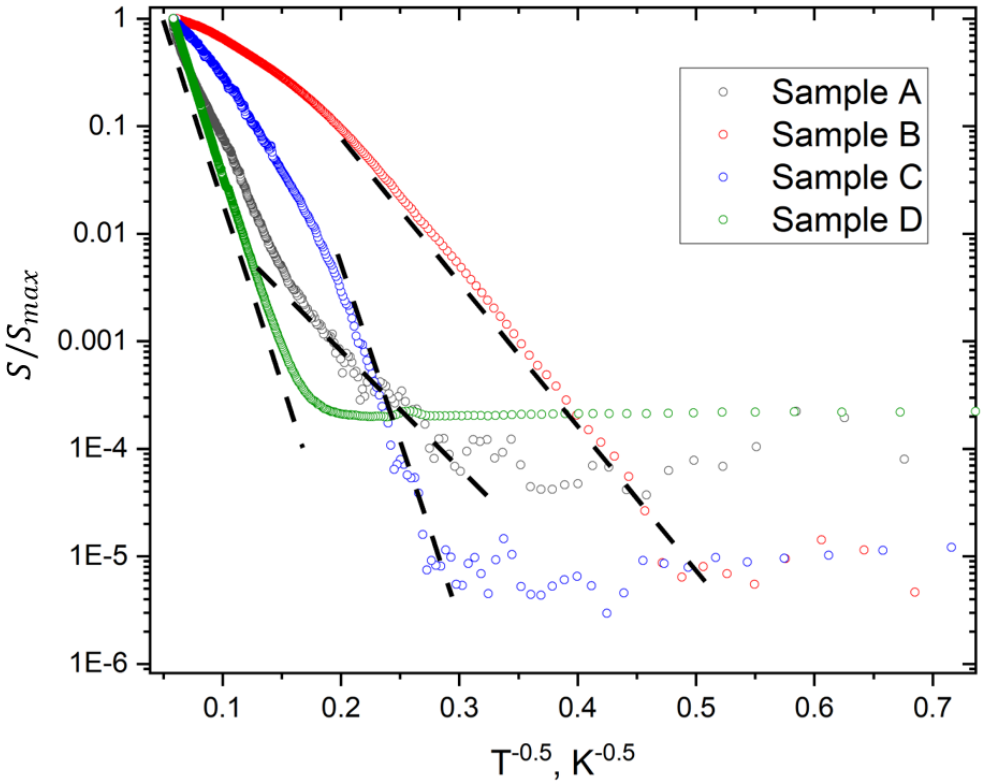

Figure 3.10: Semi-log plot of the normalized temperature-dependent conductance of Samples A, B, C and D over $T^{-0.5}$. The fits of the stretched exponential behavior $S(T) = S_0 \exp[-T_0^{ES}/T]^{1/2}$ are shown for the corresponding curve with dashed lines.

The corresponding span temperature range and the extracted T_0^{ES} are reported in the table:

ES-VRH fit $S(T) = S_0 \exp[-T_0^{ES}/T]^{1/2}$		
Sample	Temperature range (±3) [K]	T_0^{ES} (±0.4) [K]
Sample A	60 - 10	40.5
Sample B	14 - 4	31.9
Sample C	24 - 12	77.1
Sample D	290 - 40	81.7

Table 3.3: From the stretched exponential fits shown with dashed lines in Figure 3.10, temperature range and extracted T_0^{ES} value are reported for the corresponding sample.

The temperature ranges, for which the T_0^{ES} values have been extracted, for Samples A, B and C are quite small. Therefore, drawing conclusions based on these findings has to be carefully considered.
In Figure 3.10, it is possible to notice that at different low temperatures the conductance reaches a plateau. The measurements have been taken with constant voltage through the entire temperature range in order to not induce charge and temperature shifts. The applied voltage has been selected in order to monitor the wider and most stable range of current difference for the sample.
The measurements shown in this work have been taken from room temperature cooling down to 0.270 K. The plateaus correspond to the probed current achieving the resolution limit of the source meter. The localization length for the low-temperature range, ξ, can be derived from Equation 1.37. The derived values of the localization length are reported in Table 3.4.

$\xi = \frac{2.8e^2}{4\pi\epsilon_r\epsilon_0 k_B T_0^{ES}}$	
Sample	localization length, ξ [nm]
Sample A	295
Sample B	375
Sample C	155
Sample D	146

Table 3.4: Calculated values of the localization length ξ using the extracted T_0^{ES} values reported in Table 3.3.

3.4 Discussion of the results

A direct relation among charging energy, number of particles involved in the transport, geometry and threshold voltage of the Coulomb blockade of the arrays observed in I-V curves is expressed by the Equation 1.34: $V_{t,array} = \alpha N E_C$, already presented in Section 1.3. From the calculated charging energy of the Au nanoparticles ($E_C = 0.018 \,/\, 0.029\, eV$)

and from the rough estimation (from the samples images) of the number of nanoparticles ($N^* = 6 - 11$) in the triangular array involved in the transport, a threshold voltage, $V_t(0) = 0.025 - 0.072\,\mathrm{V}$ from the samples images, is expected. This result is good in agreement with the threshold voltage extracted from the fit $I \sim I_0(V - V_t)^{\zeta}$ of the experimental I-V characteristics at 0.270 mK of the four samples described in this work. In Section 1.3, it has been described that Equation 1.3: $U \approx \upsilon\, eV_t(0)$, in which $\upsilon = 0.2 - 0.5$, connects the measured high-temperature Arrhenius-type activation energy U to the array threshold voltage. From the energy gap derived by the Arrhenius fit of the temperature dependence of the electrical conductivity and the threshold voltage at $T \sim 0$, $V_t(0)$, the υ coefficient of the arrays can be extracted. The values for U, $V_t(0)$ and υ are reported in the following table:

$S(T) = S_0 \exp[-U/k_BT]$; $I \sim I_0(V - V_t)^{\zeta}$; $\upsilon = \frac{U}{V_t(0)}$			
Sample	U (± 0.0004) [eV]	$eV_t(0)$ (± 0.003)[eV]	υ
Sample A	0.0217	0.0554	0.39
Sample B	0.0056	0.061	0.092
Sample C	0.0157	0.037	0.42
Sample D	0.0267	0.071	0.38

Table 3.5: U, $V_t(0)$ and υ values extracted from the temperature-dependent conductivity curves of the relative samples.

Except for Sample B, all of the other samples (Sample A, C and D) yield $\upsilon \sim 0.4$. This result indicates that coherence has been found between the measured high-temperature Arrhenius-type activation energy U and the threshold voltage and moreover, it is consistent across three of the four samples.
In the cotunneling scenario, it has been described in Equation 1.41: $I \sim V^{2j^*-1}$ that there is a straightforward relation, $\zeta = 2j^* - 1$, between the slope of the I-V curve overcoming the Coulomb blockade and the number of junctions j^* involved in the hopping transport. It follows that the derived j^* value from the ζ coefficient extracted from the I-V characteristic fit are:

$\zeta = 2j^* - 1$		
Sample	ζ	j^*
Sample A	2.67 ± 0.03	~ 3
Sample B	5.52 ± 0.04	~ 6
Sample C	3.46 ± 0.05	~ 3
Sample D	5 ± 1	~ 5

Table 3.6: ζ and j^* values are extracted from the I-V curve slopes.

The derived values of j^* as number of junctions involved in the electrical transport are smaller than the number of the sequential junctions of neighboring nanoparticles, which

can be estimated from the sample images (6 - 11 nanoparticles). This result suggests that the current can flow by means of sequences of cotunnel events. In the theory section, it has also been described that j^* could be derived from Equation 1.39, where j^* follows a dependence on temperature like: $j^* \propto \sqrt{T}$.

Sample D is the only sample for which a temperature dependence of the I-V curves could be investigated. The I-V characteristics show that the temperature has a very small influence on ζ. This weak temperature dependence of ζ has also been observed by others [55, 57, 62]. Elteto and collaborators [57] explained that this weak temperature dependence of the nonlinear response implies that arrays are much more robust and forgiving to disorder as compared to systems with a single threshold that might be significantly affected by their local environment. The local potential is then affected by temperature and the transmission probability of single barriers is weakly modifying the overall array behavior. However, Tran, Beloborodov and collaborators [16, 26] observed and described a temperature dependence of the non-linear slope of the I-V characteristics and from this observation Equation 1.39 has been obtained.

Nevertheless, it is apparent (Figure 3.8 and Figure 3.7) that the shape of the I-V characteristics remains almost unaffected by temperature. The change of the threshold voltage has been reported in Table 3.1 and visually displayed in Figure 3.11. Evidence of the roughly constant I-V characteristic slope is shown in Figure 3.8, in which the I-V curves measured at different temperatures are shifted in voltage to overlap one another.

A polynomial (1st order) fit of the data, $y = A + Bx$ has been carried out following the Equation 1.44: $V_t(T) = V_t(0)[1 - \eta T]$. The fit coefficients $A = V_t(0) = 0.069\,\mathrm{V}$ and $B = -\eta V_t(0) = -0.0031 \pm 0.0002\,\mathrm{V/K}$ have been obtained. From B, the average of charging energies in the array, $\bar{E_C} = 0.027\,\mathrm{eV}$ is derived. Considering the classical and general formula of the charging energy of a metallic sphere (Equation 1.3), it follows that $\bar{E_C} = 0.027\,\mathrm{eV}$ is the charging energy of a nanoparticle whose radius is $R = 6.9\,\mathrm{nm}$. This finding is only 2.2% away from the actual nanoparticles radius ($R = 6.75\,\mathrm{nm}$). Thus, the temperature dependence of the measured threshold voltage provides evidence that the effective electrical transport occurs at higher temperatures by single-electron transport between neighboring nanoparticles. On the other hand, it has been observed that in the low-temperature range, Sample D (as also Samples A, B and C) shows an ES-VRH like behavior in the temperature dependence of electric conductance. It can be speculated that R- and s- disorders in the nanoparticle array are responsible for the ES-VRH trend observation. In this picture, charge carriers have a higher probability of hopping across distant sites. This behavior has been proved to be a distinct signature of grain size nonuniformity in some disordered materials [297].

The large value of the derived localization lengths in Table 3.4 is close to the separation of the FEBID designed electrodes. Typical values for weakly coupled particles are $\xi \leq 2R$. This result could suggest that there is a reduction of the barrier heights between the

nanoparticles and that charge carriers can hop between distant sites even covering almost the complete array length.
The conclusion that can be drawn from these fundings is that at high temperatures the electrical transport in the nanoparticle arrays resembles the one in well-ordered arrays by next-neighbor tunneling and Arrhenius-like behavior in the temperature-dependent conductance curve is observable. But as soon as the temperature decreases, the cotunnel range increases and a crossover to ES-VRH-type transport is taking place with effectively reduced barrier height.

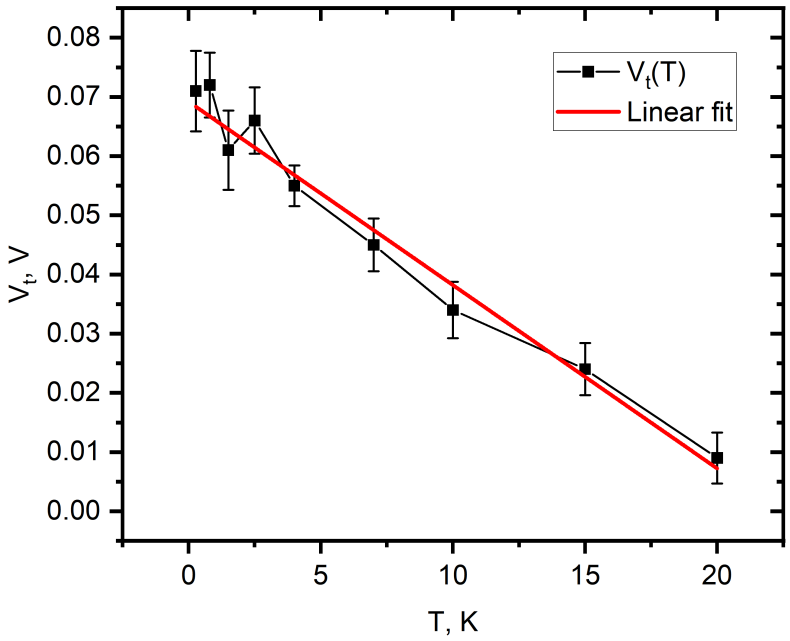

Figure 3.11: Temperature dependence of threshold voltage in the I-V characteristics of Sample D. The I-V curves and the extracted threshold voltages of Sample D at different temperatures are reported in Figure 3.7 and Table 3.1, respectively. A linear fit ($y = A + Bx$) of the data can be performed. The slope, following the results of Parthasarathy and collaborators [55] (Equation 1.44), can give direct information of the average charging energies in the array. See text for details.

Simulations of the I-V curves have been conducted with SEMSIM [298]. SEMSIM is an adaptive multiscale Simulation program for single-electron devices. Attempts to simulate the electron transport behavior of a NP array in combination with the co-deposit effect have been performed. Two types of simulated capacitance networks have been tested and the results have been compared to the I-V characteristics of Sample D at 0.270 K. The first system simulation consists of a network of tunnel junctions as capacitance-resistance system (4x4) in series with a resistor (type a). The second simulated system comprises of two parallel capacitance-resistance networks (3x3) in series with a resistor (type b).

The systems can be simulated with the software in which information about junction resistance and capacitance and node charges are provided in a parameter fit. The two simulated systems are shown in Figure 3.12.

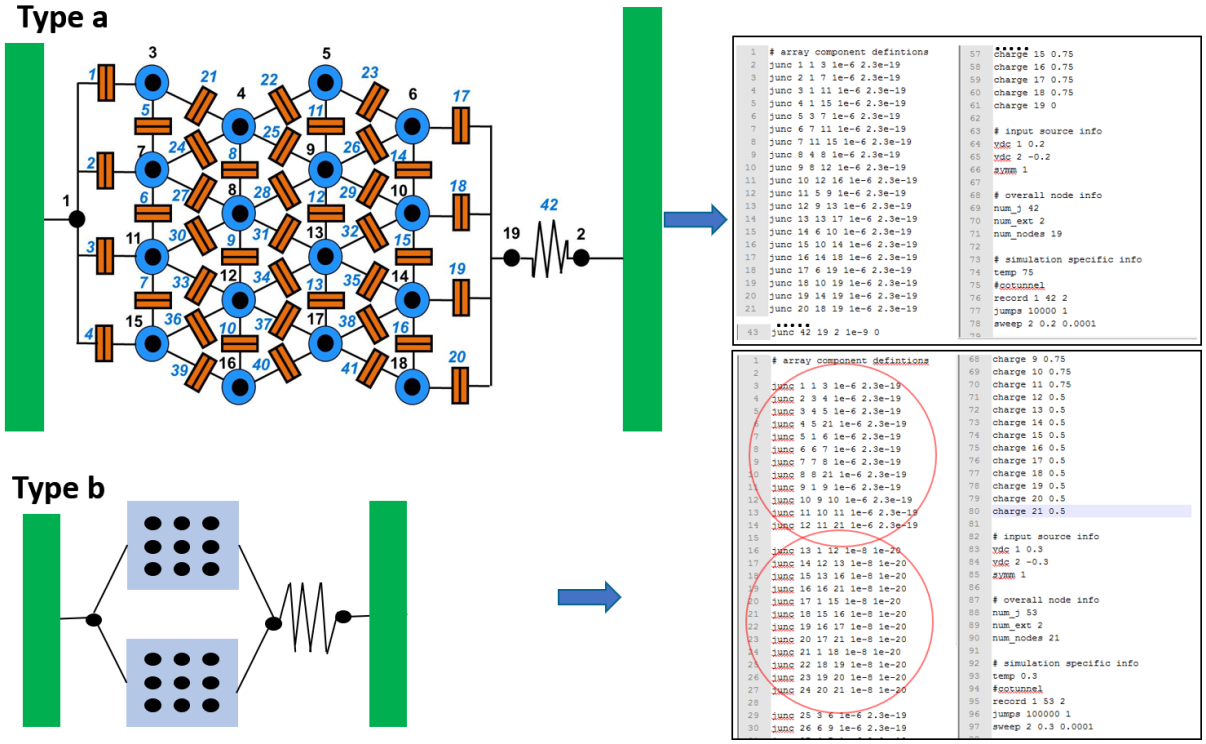

Figure 3.12: On the left, a sketch of the two types (Type a and Type b) of simulated capacitance-resistance systems by SEMSIM [298]. On the right the respective description file of the different tunnel junctions (capacitance-resistance) and single offset charges are displayed. For Type b two different junctions groups are describing the two different 3x3 tunnel junction matrices and they are outlined with red circles in the file part shown.

Two simulations (2, 3) for system type a and one simulation (4) for system type b are shown in Figure 3.13.
The simulated curves have quite different shapes outside the Coulomb blockade region. It is expected that good agreement between simulations and experimental data can be achieved by suitable model system and parameter selection. The improvement of these simulations is beyond the purpose of this analysis. However, describing these rough simulations aims to highlight that adaptive simulations of the measured system can help to understand the electrical behavior of complex arrays in which the transport can be the result of the convoluted interplay of different effects.
In the present case, the transport among nanoparticles remains the prevailing electrical transport interaction.

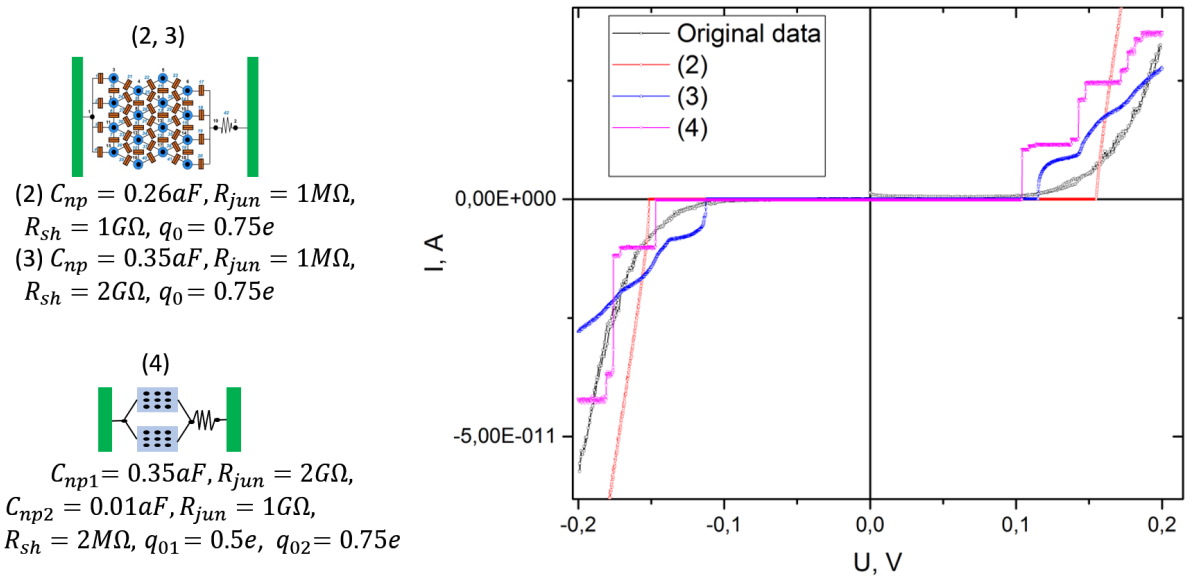

Figure 3.13: Two simulations (2, 3) for type a system and one simulation (4) for a type b system have been conducted. The parameters defining the system are reported on the left. The obtained I-V characteristics simulations are shown in comparison with the experimental I-V curve measured for Sample D at 0.270 K. The simulations yield quite different shapes of the I-V curve as soon as $I \neq 0$. It is foreseen that with further improvement of the simulated system a good match with the experimental data can be accomplished.

It is worth mentioning that in general the ES-VRH behavior has been observed in small temperature range for which the current has been very small and near to the lower current limit, maybe already compromising the measurements' truthfulness. The plateau of the conductivity curves observed in Figure 3.10 has to be traced back to the current reaching the lowest current limit measurable with the source meter. Therefore, the current values of the I-V characteristics of Sample D at lower temperature are more reliable than the ones measured during the continuous temperature dependence of current at fixed applied voltage (0.01 V). At the same time, Sample D is the only sample for which the ES-VRH behavior can be found over a larger temperature range and almost covering the complete temperature range investigated. The observation of ES-VRH can be explained as an effect of the disorder generated from the nanoparticle radius and separation disorder. However, the properties of the array prove to be robust enough to show single-electron transport through the nanoparticles.

It is important to say that a consistent number of arrays has been analysed during the research work (17) and their description is not included in this work because they showed simple metallic behavior (no Coulomb blockade in the lowest temperature range) or, on the contrary, they were not showing any tunneling current. In the first case, the co-deposit of the Pt FEBID contacts has been enough to provide favorable current percolating paths through the array producing ohmic electrical contact between the FEBID contacts. For

the second case, as a consequence of the FEBID deposit shrinking effect resulting from the purification treatment, the post-treated electrical FEBID deposits have been too porous to serve the scope of being the electrical elongation of the Cr-Au UVL contacts. However, the samples presented in this work have been the result of a FEBID contact dose optimization. The investigation served to find the right dose and patterning strategies which could provide enough Pt-material to supply a continuous electrical connection through the whole deposit elongation and, on the same time, being just enough in order to not compromise with the co-deposition of Pt the single-electron transport between the nanoparticles.
It follows that the co-deposit interference in the single-electron transport of NP arrays contacted by FEBID-based contacts is a factor that could have a significant effect. Moreover, the co-deposit effect has the complexity to be not topographically uniform since the Pt-grains in the co-deposit are different in size and their density is higher in proximity to the FEBID deposit border. Therefore, its presence increases the complexity of understanding electron transport in the analysed NP arrays.

3.5 Conclusions

The present study of NP arrays provides evidence of single-electron charging effects in temperature-dependent measurements of the electrical conductance. The electrical transport mechanism is indicated by the Arrhenius-like behavior and the Coulomb blockade observation in the I-V characteristics. Arrhenius behavior has been found over a wide temperature range for selected samples (Figure 3.9) and is typical for low-disorder granular metals.
Moreover, the extracted activation energy U of the Arrhenius-like behavior shows a strong match with the threshold voltage extracted from the I-V characteristics fit. The same accordance is kept for three of the four samples presented.
As a further result, the shape of the I-V characteristics of Sample D is weakly affected by temperature. The threshold voltage at different temperatures is shifted linearly towards smaller threshold values. The threshold vanishes and the nonlinear, Coulomb blockade-type I-V characteristic changes to ohmic behavior near zero bias once the temperature exceeds $T^* > 30\,K$. From the linear temperature dependence of the threshold voltage, confirmation has been found that the size of the grains participating in the single-electron transport agrees very well with the actual size of the nanoparticles. From this result, it is possible to speculate that the increase in the local potential disorder, which is generated from the nanoparticle radius and separation disorder, it is confirmed by the ES-VRH-like behavior for the low-temperature dependence of electrical conductance, but it is still not strongly affecting the single-electron transport through the nanoparticles. However, the co-deposit is a FEBID technique-related drawback that in the described FEBID deposit

application can have a considerable intruding effect in the single-electron transport within NP arrays as soon as the dimension of the array is becoming smaller. Evidence of this issue is reported in the next Section.

3.6 Single-Electron Transistor device fabrication by using Au-NP as island

The promising results obtained from the NP arrays encourage to use the same fabrication technique for the SET device assembly. Small groups of 2 - 3 nanoparticles, like the ones shown in Figure 3.14 inset 1, have been selected to be the center of the SET Pt-C FEBID pattern for the source-drain-gate design configuration. Pt-C FEBID deposits have been used also in this application as elongations of the UV-lithography defined contacts. The FEBID structures have been later subjected to the catalytic purification described in Subsection 2.3.1.4.

Since the SEM image is subject to a small drift in the patterning process, the selection of a small group of nanoparticles ensures that at least one of them can be found in the middle of the gap between the source and drain leads. Figure 3.14 shows one of the structures obtained. The corresponding I-V characteristic depicted in Figure 3.15 recalls the typical Coulomb staircase of not symmetric tunnel junctions. However, the current behavior for negative applied voltages differ considerably from the corresponding positive voltages. The odd behavior of the I-V measurement has been observed several times (3). Unfortunately, sweeping the voltage for a larger range (-0.7 - 0.7 V) caused electrical failure of the structure.

Although the particular I-V feature has been observed just for the structure presented in this section, this type of structures so far have not shown a clear and reproducible trend. It can be speculated that the involvement of more than one nanoparticle in the tunneling process and/or the participation of the Pt co-deposit disguise the tunneling among source, nanoparticle and drain. As a matter of fact, the most of the SET-like structures fabricated with the described method showed metallic behavior down to the lowest temperature reached with the ^{3}He-cryostat (about 0.270 K).

The Pt co-deposit is a consequence of the FEBID technique itself, giving the formation of trapped charges around the island promoting cotunneling effects that short the single electron transport through the island. Unfortunately, in the course of the Pt-FEBID based contacts optimization that guarantees that the leads are thick enough and without critical cracks in their porous topography, the minimal dose ensuring metallic leads is already enough to lead to Pt co-deposit over a few tens of nm (FEBID contacts separation in the SET configuration), disturbing the single-electron charging effect between the leads and the nanoparticle in the center.

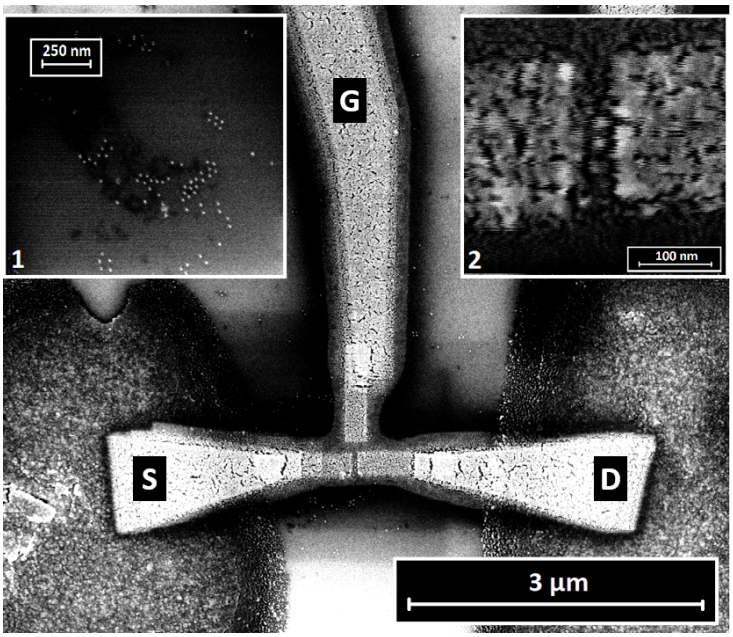

Figure 3.14: SEM picture of a SET-like structure obtained by using Au-NP as SET islands and Pt purified FEBID deposits as elongations to the Cr-Au UVL contacts. Source, drain and gate contacts as indicated. Inset 1: Example of the Au-NP groups that have been selected as center of the SET Pt-C FEBID pattern design. Inset 2: Closeup of the gap between the source and the drain lead is shown. Two nanoparticles are recognisable in the contacts separation. However, other grains are visible in their surrounding as consequence of Pt FEBID co-deposition.

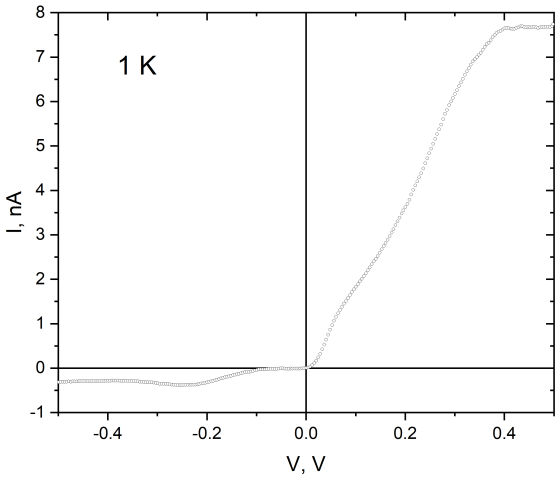

Figure 3.15: I-V characteristic of the sample shown in Figure 3.14. The electrical measurement has been conducted in a ^{3}He-cryostat at 1 K. The I-V curve resembles the trend of a Coulomb staircase. However, the current behavior does not show symmetric step shape along negative and positive applied voltages.

A 'stitching' technique of writing in separated steps has been used. In this way, better resolution and less pronounced electrostatic beam shift have been achieved in order to better match the group of nanoparticles in the middle of the contacts. First the elongations to the UV-contacts have been written and secondly the three-leads design in a restricted field of view has been written with Pt-C FEBID. Again, the shrinking effect of the deposited design generated cracks in the deposit junctions due to the carbon loss in the course of the post growth purification treatment [15]. In Figure 3.16 an indicative structure for which the effect damaged the complete structure functionality is shown. Those results demonstrate the unsuitability of this nanofabrication method to SET design applications.

For practical applications it is much more desirable to have the capability to fabricate nanostructure dots in an intentional fashion rather than relying on the random occurrence of small NP groups and the small chance to match them in the middle of the SET pattern. Moreover, it is foreseen that FEBID co-deposit effects have to be avoided. Therefore, different approaches have been tested for the SET nanofabrication. Some of them, have not been successful. A brief description of them is given in Appendix C.

The final and most promising approach for the fabrication of SET has been carried out at the end of this research work. It includes the use of Ga^+-FIB milling for the electrodes and nanogap definition. The island is fabricated by Pt-C FEBID and subjected to electrical irradiation. Finally, the island (and consequently its surrounding) is subjected to Ar-etching. By using the plasma Ar^+-etching, the thin layer of Pt co-deposit has been removed. A detailed description of the nanofabrication method is given in Chapter 4.

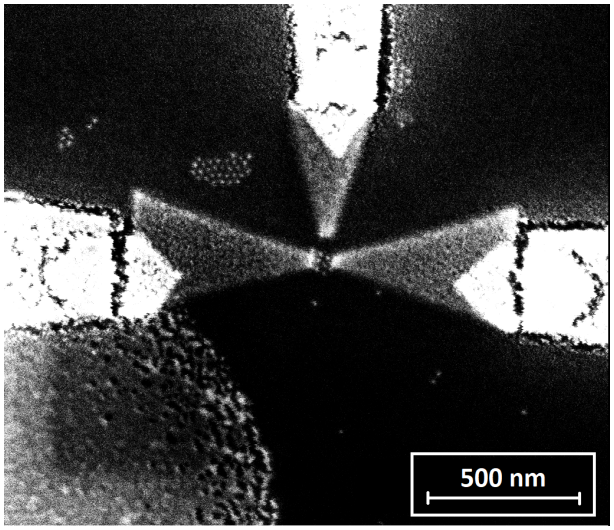

Figure 3.16: SEM picture of the center area of a typical Pt purified FEBID SET structure, in which NP have been used as islands. Few nanometer wide cracks are well visible in the overlapping areas of the 2-step fabricated FEBID deposits. The cracks prevent that the written structures serve as metallic elongations of the Cr-Au UVL contacts.

Chapter 4

SET with Pt FEBID island by localized plasma Ar^+-etching

In this chapter, a set of experiments and results on the Single-Electron Transistor (SET) device fabrication using FEBID for island definition between pre-fabricated SET electrode structures are reported.
The fabrication method presented here assures, thanks to the combination of several preparation steps, defined placing of the nanoisland and proper tuning of the island's tunnel coupling with the drain and source leads.
The particular nano-granular structure of the island and its *in situ* inter-grain tunnel coupling tunability by post-growth electron irradiation allows the proper control needed to study the interplay of the island's electronic granularity properties and the SET device performance. In addition, a novel *in situ* Argon ion etching process is used to remove FEBID-associated co-deposit in proximity of the island. The co-deposit has been detected as main counterproductive effect for the constrained single-electron tunneling through the SET island. In particular, the co-deposit generates unwanted leakage effects and undefined tunneling barriers between the metallic components of the device. In this work, several nanofabrication applications in which the co-deposit has impaired the devices functioning have been presented in Chapter 3 and Appendix C.
At the end of this chapter, the low-temperature properties and performance of the obtained SET devices are presented and shown as proof of the successful fabrication approach. The single-electron transport characterization of the devices is presented in Section 4.2. The experimental results show stable SET operation tuned by the modification of the tunnel coupling strength inside the island and between the leads. The change of the tunnel coupling is realized by accurate dosage of the electron irradiation of the SET island region. Moreover, in the article related to these findings [14], confirmation of the obtained results is provided by capacitance simulations performed

with the software Fastcap2 [299] and by complementary simulations of the SET current-voltage characteristics based on the master equation approach (see e. g. [300, 301]). The results presented in this chapter give an important contribution to the application study of using single-electron effects in SET as controlling mechanism for local potential and charge changes. Moreover, through the proposed fabrication method, it has been demonstrated how the electronic properties of the SET device can be adjusted in order to fine tune the single-electron tunneling in the sensing island.

4.1 The importance of nanoisland and nanogap definition in SET fabrication

The fabrication of SET devices for operation in the tens of Kelvin range is nowadays still challenging. Several methods have been developed in the last decades to enhance the control of the tunneling nanogaps and island fabrication to far below 100 nm.
However, for all the fabrication techniques, the biggest preparation challenges are the nanoisland placing between the electrical contacts and the high-definition establishment of nano-tunnel junctions. In general, the commonly used approaches for SET fabrication stand out in either the tunnelling junction fabrication or the island definition. For example, techniques like shadow evaporation [302–305], mechanically controlled break junctions [306, 307], electromigration [308, 309], scanning single-electron transistor microscopy [310–313] and scanning probe microscopy combined with nano-oxidation [314, 315] have, as main focus, the perfect definition and tuning of well-defined tunnel junctions. The combination of those techniques with the last decade development of nano-objects as nanoparticles [316–321], nanotubes [322, 323], fullerenes [324–326] and single-molecules [327–329] brought the tunnel junction and island definition to a new level, on which room temperature operating SET can be foreseen and thus become available for countless applications.
Considering the power of technique combinations in order to address both definition and positioning of nanogaps and nanoisland, a multistep fabrication technique has been developed during this work. The method is described in the following paragraphs.
The approch is based on the use of FEBID to provide a defined nanoisland and tunable tunneling gaps. For instance, previous experiments have demonstrated that FEBID is a suitable technique for island definition in SET fabrication [330–334]. As a matter of fact, FEBID is not only a perfectly suited technique for precise positioning and deposition of a nanometrical island but, thanks to the properties of the Pt-C FEBID material itself, a post-growth treatment, as electron irradiation, can accurately tune the tunneling rate and probability from and to the island. The effect of a post-growth electron irradiation treatment has been described in Subsection 2.3.1.4.

The fabrication steps involved in the preparation of the SET devices include:

1. Substrate preparation
2. Initial contact definition step (Ga^+-FIB milling of Cr-Au UVL contacts)
3. Pt-C FEBID island deposition in the nanogap between the source and drain contacts
4. Post growth irradiation of the Pt-C FEBID island
5. Slight plasma Ar^+-etching of the centre of the structure

In the following paragraphs, the different steps are described.

4.1.1 Substrate preparation

P-doped (100) silicon $1\times1\,cm^2$ substrates insulated with a 200 nm thick thermally grown SiO_2 layer have been used as chip base. 24 contact electrodes of circa 30 nm Cr-Au have been fabricated on the substrates by UV-lithography (the technique description can be found in Subsection 2.1.1). A closer SEM look of the chip center is shown in Figure 4.1. In the center of the chip, a maximum of 6 SET devices, indicated to the 6 crosses, indicated with orange arrows in Figure 4.1, can be prepared on the chip.
After the substrate has been mounted on a carrier holder, it is inserted in the dual-beam FIB-SEM system FEI Novananolab 600. In the chamber of the system, the following fabrication steps entailing Ga^+ ion-milling of the contacts, island deposition, post-growth irradiation and localized Ar^+-etching take place.

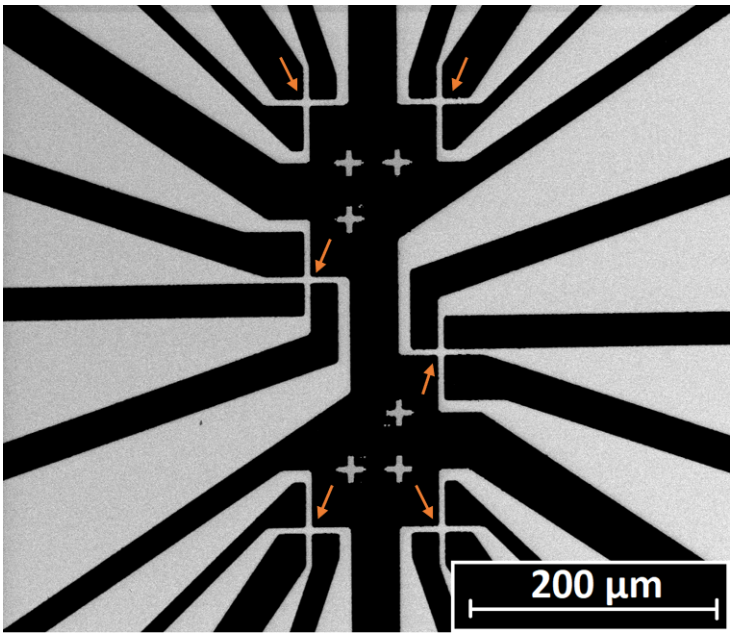

Figure 4.1: A SEM overview picture of a chip in which the 24 contacts are combined in cross-like configuration. In this way, from the crosses indicated with orange arrows, 6 SET devices can be fabricated on the same chip.

4.1.2 Electrical contact definition by Ga^+-FIB milling

As technique to provide the smallest possible gap between contacts in a reproducible and reliable manner, Ga^+-FIB milling is used to design the contacts in order to separate the cross 4-terminal Cr-Au UVL pads in 4 disconnected contacts: source, drain and two gate leads. In order to accomplish this purpose, Ga^+-FIB milling is performed by using the Ga gun installed in the dual-beam FIB-SEM microscope. Thereby, a gap of few tens of nanometers is formed between the device leads. Details about the FIB milling technique and the used system are given in Subsubsection 2.3.4.1.
Preparatory experiments on a single Cr-Au contact have been performed in order to establish the appropriate milling dose to ensure the smallest contact separation and highest electrical isolation for the following SET device design. Figure 4.2 shows a tested prototype. An initial milling step has been executed in order to separate the large electrode area and restrict the gap milling on a $1\,\mu m^2$ region. The size of this region is comparable to the one that would be used in the following SET design experiments. From later conducted AFM investigations, a recess of 40 ± 3 nm has been measured. Hence, 30 ± 1 nm of the Cr-Au contacts and 11 ± 3 nm of SiO_2 have been milled out during this first step. A second milling step has been carried out on the side of the newly defined electrodes in order to erase redeposition of material due to the first milling step. Thereby, 30 ± 6 nm hollows have been milled further in the SiO_2. As final milling step, the electrode in the middle has been milled in order to obtain two separated leads for source and drain. The final cut disconnecting the source and drain electrodes has a thickness of 50 ± 7 nm. For all the milling steps, 30 kV acceleration voltage, 10 pA beam current, dwell time 200 ns and 800 passes have been used as process parameters.
The resistance of the contact on a 2-probe configuration has been measured before and after the final cut to prove the electrical isolation after the final milling step. The resistance of the electrode before and after the final milling step has been circa $400\,\Omega$ and around $40\,M\Omega$, respectively. This preparatory test set the basic proof that the Ga^+-FIB milling technique can yield complete electrical isolation of the leads maintaining a nanometrical gap separation. Following this result and patterning strategy success, the actual SET design has been fabricated using a cross 4-terminal Cr-Au UVL structure on a 4 leads configuration design in order to separate source, drain and two gates. In Figure 4.3 the SET milling design and the obtained structure are shown. Firstly, large areas (in transparent green) have been milled with the following process parameters: acceleration voltage, 30 kV; beam current, 10 pA ; dwell time, 200 ns and 800 passes. Afterwards, deep lines (in solid green) have been milled with beam parameters: 30 kV; 10 pA ; 200 ns and 1400 passes to guarantee that redeposited material from the large area milling step did not result in a weak electrical contact.

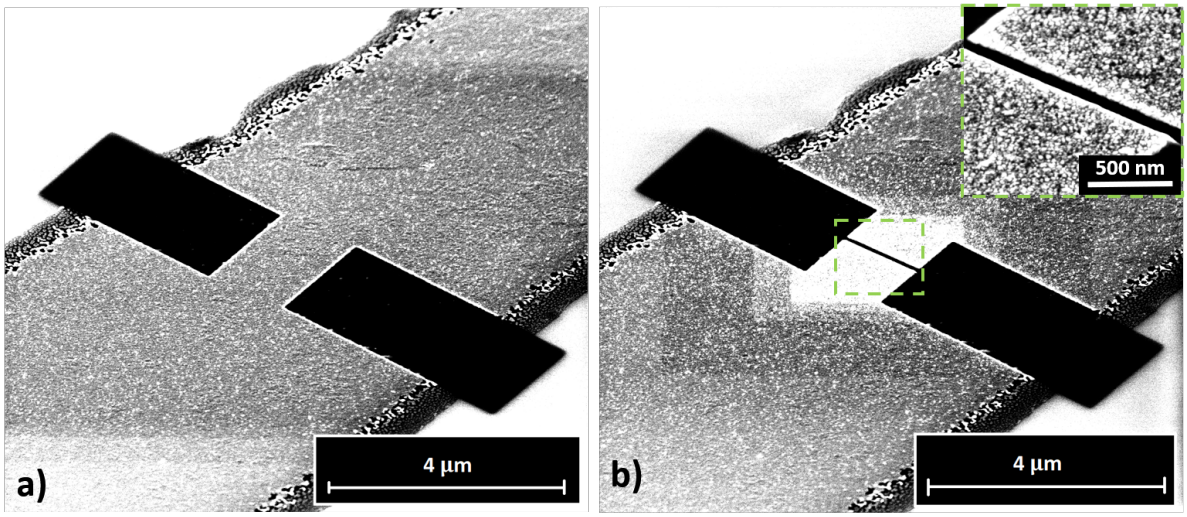

Figure 4.2: SEM pictures of a typical prototype structure on which milling doses have been tested in order to achieve the smallest gap separation and electrical isolation. a) The Cr-Au pad is shown after the first two milling steps. b) The tested structure after the final milling cut is shown. Inset: Closeup of the fabricated separation. The cut looks homogeneous and its depth by AFM measurements has been found to be about 50 nm. High-resistive measurements of the structure confirmed the electrical isolation achieved by the Ga^+-milling of the disconnected Cr-Au pads.

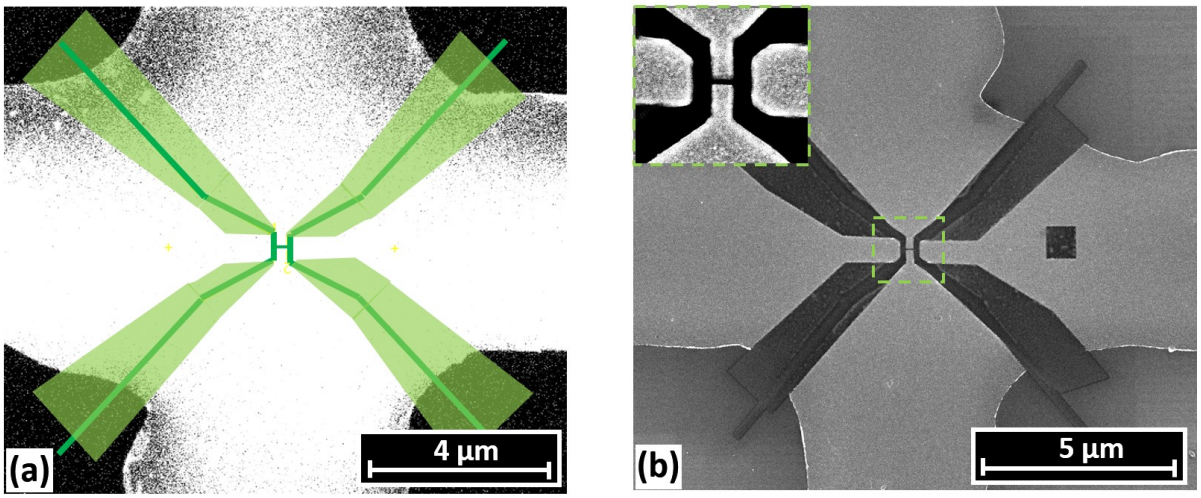

Figure 4.3: SEM pictures of the obtained structure. a) The structure is shown before the milling process. In transparent green and in solid green, the first and the second milling patters are depicted. b) The final SET design structure is shown after the complete Ga^+-milling process. Inset: Closeup of the central region of the structure. Very high definition and fast fabrication of the gaps have been obtained thanks to the Ga^+-milling fabrication strategy.

As last step, the milled line in the middle between the source and drain lead have been milled with 30 kV; 10 pA ; 200 ns and 700 passes. The gap obtained between source and drain is about 50 nm and the resistance between source and drain has been found to be in the range 20 - 40 MΩ. No evidence of appreciable leakage between source and drain contacts due to Ga^+-ions implantation [286] in the SiO_2 has been observed (0.1 pA at 2 V after Ga^+-milling). The distance between the cross center and the two gate electrodes has been around 150 nm.

4.1.3 Pt-C FEBID island deposition

The nano-granular Pt-C island has been obtained by FEBID using the precursor $Me_3PtCpMe$ (details about the precursor are given in Subsubsection 2.3.1). The deposition has been performed with patterning parameters: 15 keV (electron beam energy), 140 pA (beam current), 25 μs (dwell time) and 100 passes. The pattern with 1 pixel has been placed in the center of the narrow milled gap. The chamber pressure during deposition has been about 7.5×10^6 mbar.

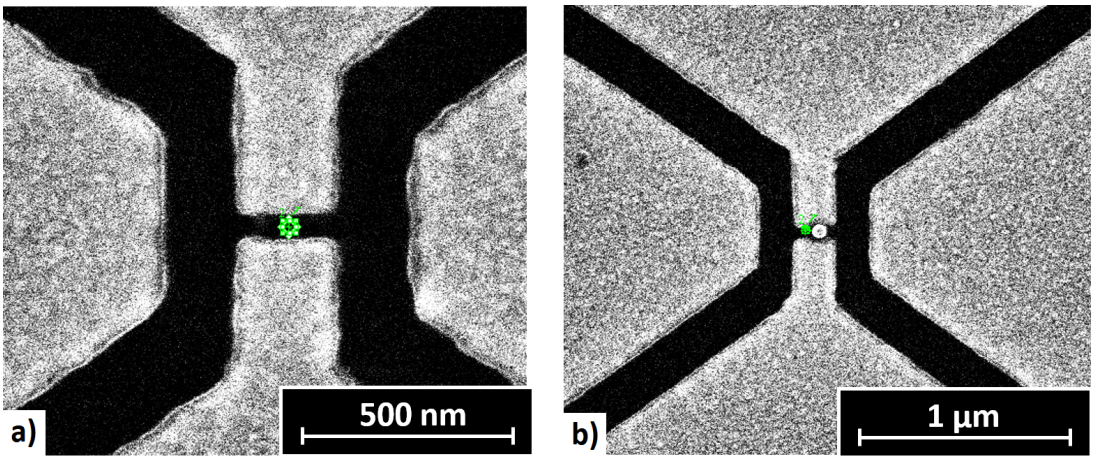

Figure 4.4: SEM pictures of a SET device before (a) and after (b) Pt-C FEBID island deposition. In green the 1-pixel pattern of the electron beam engine software is visible.

4.1.4 Post-deposition irradiation of the Pt-C FEBID island

As a result of the low metal content of the Pt-C FEBID deposit (see Section 2.3.1 for more details), no single-electron conduction mechanism can take place between the source/drain lead and the island.

Towards the electrical conductivity improvement of the Pt-C FEBID island by increasing its inter-grain tunnel coupling, the island has been subjected to a localized post-growth electron irradiation treatment. This post-growth technique has been described in Section

2.3.1.4. It has been carried out 3 h after the deposition, in order to ensure complete removal of residual precursor in the dual-beam system chamber and avoid further material deposition driven by the irradiation treatment.
Taking the irradiation results on Pt-C FEBID deposits described from Sachser *et al.* [15] and reported in Figure 2.17 into account, the SET devices have been electron irradiated with the electron doses 0.1 /0.2 /0.5 /1 / 3 μC μm^{-2}. By this means, the effect of the island irradiation doses, spanning the whole metal-insulator transition, could be investigated.
In this work, the results of two samples are presented. Sample *A* and Sample *B* have been treated with the irradiation doses 3 μC μm^{-2} and 1 μC μm^{-2}, respectively. The different electrical behaviors, associated with the distinct inter-grain tunnel coupling inside the sample islands and adjusted by the different dose, are presented in Section 4.2. It is important to mention that the samples subjected to lower irradiation doses (0.5 μC μm^{-2} and lower) did not show SET behavior.
After the electron irradiation treatment, Sample *A* and Sample *B* showed a drain-source resistance ($R_{ds} = R_D + R_S$) at room temperature of 2.7 kΩ and 6.3 kΩ, respectively.

4.1.5 Co-deposit etching by Ar-localized plasma polishing

As already described in Subsection 2.3.1.3, the result of the interaction of secondary electrons in proximity of the defined FEBID pattern with the precursors molecules leads to co-deposition of material nearby the island as a counterproductive effect of the FEBID deposition. Because of this, as the last step in the SET fabrication, the island region has been subjected to localized Ar^+-etching inside the dual-beam FIB-SEM chamber using a beam-induced polishing and sputtering system (BIPS) installed in the system by Thermo Fisher Scientific [288]. Thus the removal of the co-deposit halo in proximity of the island has been achieved. A description of the localized Ar^+-etching can be found in Paragraph 2.3.4.2.
In Figure 4.5, a SEM picture of the Ar nozzle above the SET device target is shown.
Notice in Figure 4.5, ESD can take place on the substrate and disintegrate the electrodes if, during the Ar^+ ion-etching, an additional bias is applied between the contacts and/or the etching lasts longer than 1 min. For this reason and to better monitor the resistance of the device, short etching exposures have been used and the resistance has been measured without plasma voltage application.
The plasma has been run for four times in 15 seconds intervals. In this way, the island region of the SET devices has been etched eliminating the about 1 nm thick co-deposit halo over an etching area of approximately 20 μm diameter. The island region of every structure has been exposed to 60 s overall etching time. The resistance between source and drain have been measured after every Ar^+-etching interval. The ion etching timing has been chosen so that the *in situ* measured drain-source resistance ($R_{ds} = R_D + R_S$) at

room-temperature ended up in the range of 500 kΩ to 5 MΩ. Moreover, the drain-source current in between the Ar^+ ion-milling intervals has been carefully *in situ* monitored in order to ensure the condition, for which Coulomb blockade effects occur, such as $R_{S/D} \gg 26\,k\Omega$.

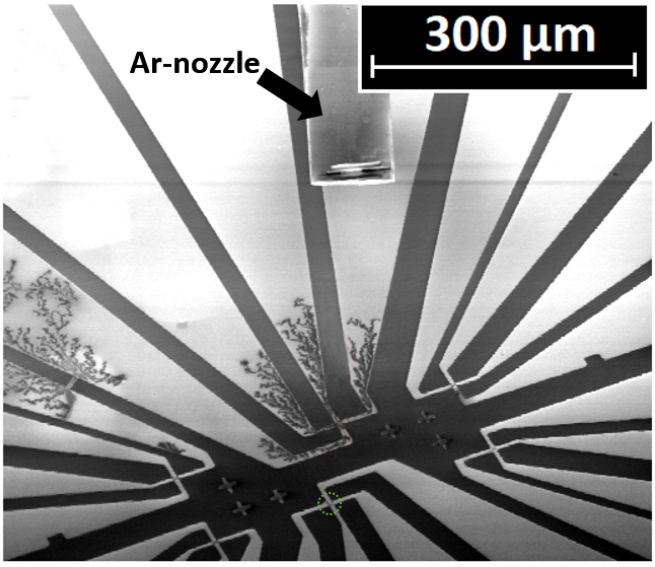

Figure 4.5: SEM overview picture of the Ar nozzle on a target structure. Distance between the nozzle and the substrate, voltage applied and etching time have to be finely tuned in order to control the process. Otherwise, discharge effects, such as the one observable in the picture, can take place.

After the etching process and still inside the dual-beam FIB-SEM chamber, Sample *A* had a total resistance of 1.6 MΩ and Sample *B* of 2.8 MΩ. No hysteresis in the current-voltage characteristics have been observed at low-temperature. This results provided a direct experimental evidence of the absence of charge traps. This outcome is quite important since it has been demonstrated that comparable devices often experience localized states that lead to hysteresis observation [335, 336].
The room temperature resistance values did not change by more than 5 - 10 % towards low-temperatures. However, junction resistances at low-temperature could be extracted by a linear fit of the I-V curve over very limited V_{ds} ranges only since the current increased steeply out of the Coulomb blockade region and could not be measured at higher V_{ds} without destroying the SET structure. It follows that accurate junction resistance values at low-temperatures can not be provided.
SEM pictures in tilted and lateral view of a typical fabricated SET are shown in Figure 4.6 (a) and (b). From the pictures, it is possible to appreciate the definition and the extraordinary island placing accuracy of the Pt-C FEBID island in the middle of the device contacts.

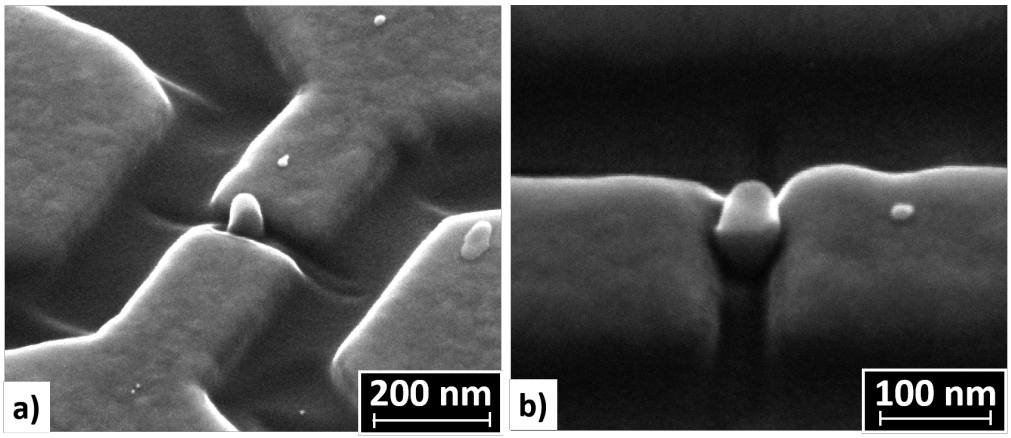

Figure 4.6: SEM pictures of a fabricated SET device in tilted view. a) Rotated closeup of the device central area. b) Closeup of the island region. Very good definition and localization of the island deposition has been achieved.

4.2 Evidence for single-electron transport

Theoretical details about the SET operation and the single-electron transport evidence in SET have been given in Subsection 1.5.2 of the theory chapter. For clarity, in Figure 4.7 a SEM picture of Sample *A* and the corresponding circuit diagram of the fabricated SET are shown. In this case, the total gate capacitance can be expressed as $C_G = C_{G_1S} + C_{G_2S} + C_0 = C_G + C_0$, where C_0 is the background capacitance formed by the gate electrodes and the p-doped Si substrate.

In order to study the single-electron transport in the devices and screen their operation from thermal energy interference, the samples need to be cooled down to very low-temperature. Electrical transport measurement of the devices in a temperature range from 270 mK and up to 160 K have been conducted after sample preparation in a ^{3}He-cryostat equipped with a vacuum-sealed insert. Particular care has been taken in keeping the time period between venting the SEM and mounting the samples in the evacuated cryostat insert as short as possible in order to minimize deposit aging effects [337, 338]. A Keithley two-channel source meter (model 2636A) has been used as voltage source and 2-probe DC current measurement instrument. The common ground for the system is the ground potential defined by the insert and in order to avoid current loops, the source contact has been forced to the same ground. Complimentary 4-probe measurements have been used to verify the contact and wiring resistance that resulted to be about 300 Ω. Current-voltage characteristics data have been gathered at 270 mK measuring I_{ds} while V_{ds} has been swept continuously between positive and negative voltages through the first

channel of the source meter. The swept V_{ds} maximal ranges have been $\pm 0.06\,\mathrm{V}$ and $\pm 0.04\,\mathrm{V}$ for Samples A and B, respectively. A constant V_{gs} voltage has been applied with the second channel of the source meter. The I-V characteristics have been collected for positive gate voltages in $0.05\,\mathrm{V}$ steps up to $5\,\mathrm{V}$.

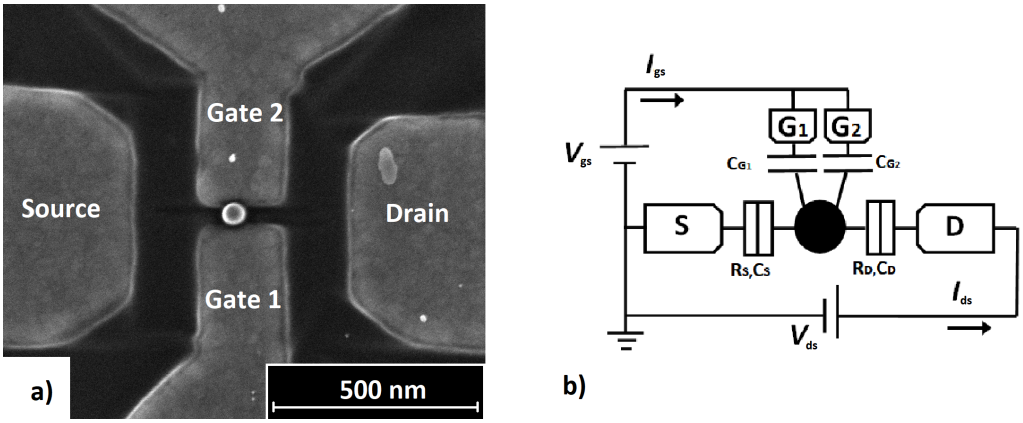

Figure 4.7: a) SEM image of Sample A. The island is placed between source and drain leads forming two tunnel junctions (J_{SI}, J_{ID}). In addition, two gates, G_1 and G_2, are used to tune the single elctron tunnelling into the island. b) SET circuit diagram of the samples. The image is used with permission from [14].

A SEM view of Sample A with the used measurement wiring configuration and the relative current-voltage characteristics observed at 270 mK in the ^{3}He-cryostat are shown in Figure 4.8.

From Figure 4.8 (b), thanks to the 3D overview, peculiar features of the I-V characteristics can be noted. Such aspects like diamond-shaped regions around zero drain-source voltage V_{ds}, as well as the step-like increase of the drain-source current I_{ds} *vs.* V_{ds} at a gate-voltage dependent threshold voltage are typical for a functional SET. In particular, by inspection of the I-V characteristics for three different gate voltages (Figure 4.9), it is possible to observe that the curves show the special staircase behavior that has been described in the dedicated paragraph of the theoretical Subsection 1.5.2.1. For those curves, it is possible to observe that for positive V_{ds} the plateaus are occurring with ΔV_{ds} separation at a comparable I_{ds} ($\sim 3\,\mathrm{nA}$ and $5\,\mathrm{nA}$). This feature is associated to the increasing probability of excess charge occupation on the island with one additional electron charge increases from 0 to a finite value ($n = \pm 1,\ 2$). From Equation 1.87, an approximate resistance value of the second tunnel junction can be derived, $R_D = 12.3\,\mathrm{M\Omega}$. This result allows to speculate that the junctions have quite different values of resistance and the lower transparency of the second junction provokes the increased probability of storing excess charges in the island. However, the plateaus appear for the other I-V characteristics ($V_{gs} = 1\,\mathrm{V}$) at different I_{ds}. Moreover, for negative V_{ds} the step is smoother and even there for the same I-V curve a different ΔI_{ds} can be calculated. For this reason, from

the step-like behavior it is not possible to extract direct information on the associated junction resistances.

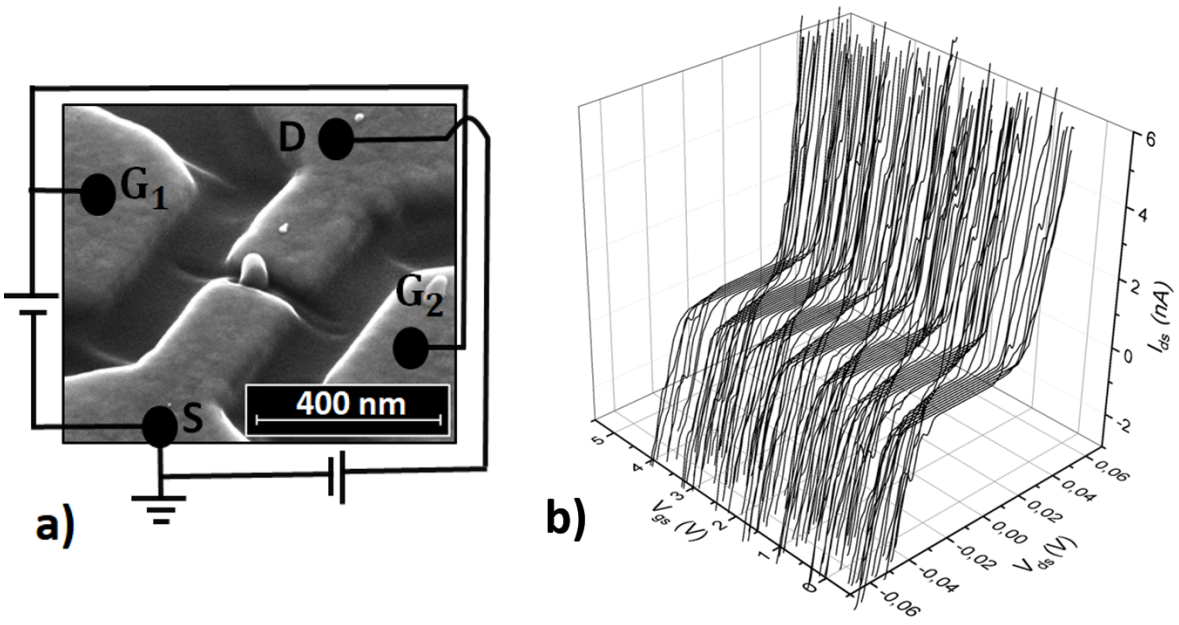

Figure 4.8: a) SEM picture of Sample A and the electrical measurement setup used in the ^{3}He Cryostat. The image has been adapted from Figure 2(a) in [14]. b) 3D representation of I-V characteristics of Sample A at 270 mK for V_{gs} up to 5 V.

The most interesting and distinct feature of the I-V characteristics recognizable from Figure 4.8 (b) are the Coulomb diamonds. Better evidence and analyses of the Coulomb diamonds can be obtained by numerical differentiation of the I-V curves shown in 4.8 (b). In this way, a color coded stability diagram of the differential conductance dI/dV for Sample A at 270 mK can be drawn for the corresponding V_{ds} and V_{gs}; such diagram is shown in Figure 4.10 (a). It appears that the Coulomb diamonds recur periodically and with constant shape along V_{gs}. Starting from $V_{gs} = 0$ V and applying positive bias, the largest Coulomb blockade is at $V_{gs} = 0.15$ V and occurs periodically with comparable extension every 0.75 V interval. As described in the Subsection 1.5.2.1, from the period extension it is possible to extract the gate capacitance as $C_G = C_{G_1} + C_{G_2} = \frac{|e|}{0.75\,V} = 0.21$ aF. A background charge, Q_0, causes the initial shift (0.15 V) of the Coulomb blockade with maximal threshold voltage on the V_{gs}-axis. Q_0 can then be calculated as $Q_0 = C_G \times (0.75 - 0.15)\,\text{V} = 0.76|e|$ using Equation 1.91.
In addition to that, the direct observation of the maximum threshold voltage $V_{ds}^{\max} = \frac{|e|}{C_\Sigma}$ with $C_\Sigma = C_D + C_S + C_G$ allows to extract the charging energy E_C and the total SET capacitance C_Σ directly from the stability diagram, $E_C = \frac{e^2}{2C_\Sigma} = 0.018$ eV and $C_\Sigma = 4.33\,aF$. Moreover, the particular symmetric shape of the diamonds discloses

that C_D and C_S are very similar and $C_G \ll C_{S/D}$. This particular case has been described in more detail at the end of the dedicated paragraph "Coulomb diamonds" in the theoretical Section 1.5.2.1. From the stability diagram the capacitance values $C_{S/D} = 2.06\,\text{aF}$ and $C_G = 0.21\,\text{aF}$ have been deduced. These capacitance values have been shown to be plausible by area iterative and adaptive multipole algorithm based simulations. The simulations have been conducted by M. Huth considering the device geometry and material property employing Fastcap2 [299] with less than 7% tolerance. Further information and details about the simulations and the obtained results can be found in the dedicated discussion subsection of [14].

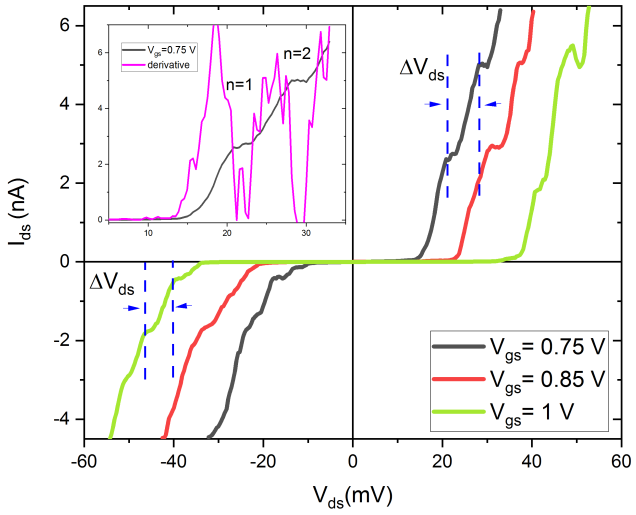

Figure 4.9: Three I-V characteristics at different V_{gs} show Coulomb staircase behavior. However, for different V_{gs} the plateus occur at different I_{ds}. Adapted from [14]. Inset: Numerical derivative of the I-V curve at $V_{gs} = 0.75\,\text{V}$. It helps to identify the occurrence of the plateaus and the corresponding charge occupation in the island.

In figure 4.10 (b), the corresponding Coulomb oscillations of Sample A for $V_{ds} = 5$, 10, 15 V are shown. The V_{gs} dependence of I_{ds} is then shown. The I_{ds} peaks correspond to the suppression of the Coulomb blockade resulting in an ohmic device behavior induced by $V_{gs} \approx 0.55 + w\,0.75$, where w is the peak number. For each peak, the total charge of the island will gain one extra electron charge, q_e. In the dedicated paragraph of Section 1.5.2.1, the Coulomb oscillation feature is described.
By resolving the tunneling rates between the island and the drain and source electrodes, the probabilities for excess charge occupation $p(n)$ on the island in the stationary case, following a master equation approach [301], can be calculated. As a result, I-V characteristics, stability diagram and Coulomb oscillations using the deduced capacitance

values and the experimental drain-island-source measured resistances can be simulated.

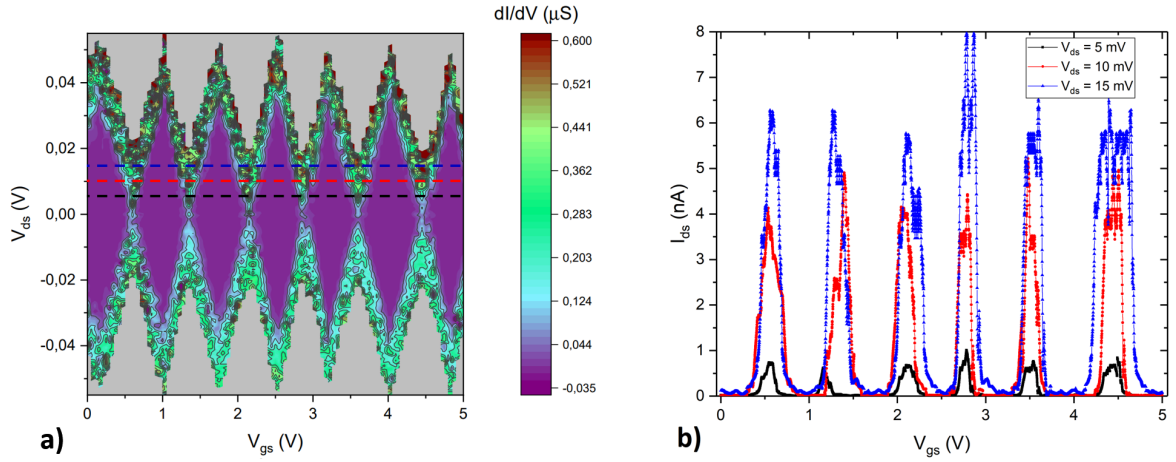

Figure 4.10: a) Charge stability diagram of Sample A at 270 mK. The symmetric and well-defined diamond shape indicates that $C_S \approx C_D$, $C_G \ll C_S$ and very reliable device performances. On the graph, dashed lines mark the V_{ds} values for which in (b) the associated Coulomb oscillations are displayed. b) The Coulomb oscillations for the reported V_{ds} voltages are shown. The peaks are periodically spaced and the height is depending on the V_{ds} applied. Adapted from Figure 4 in [14].

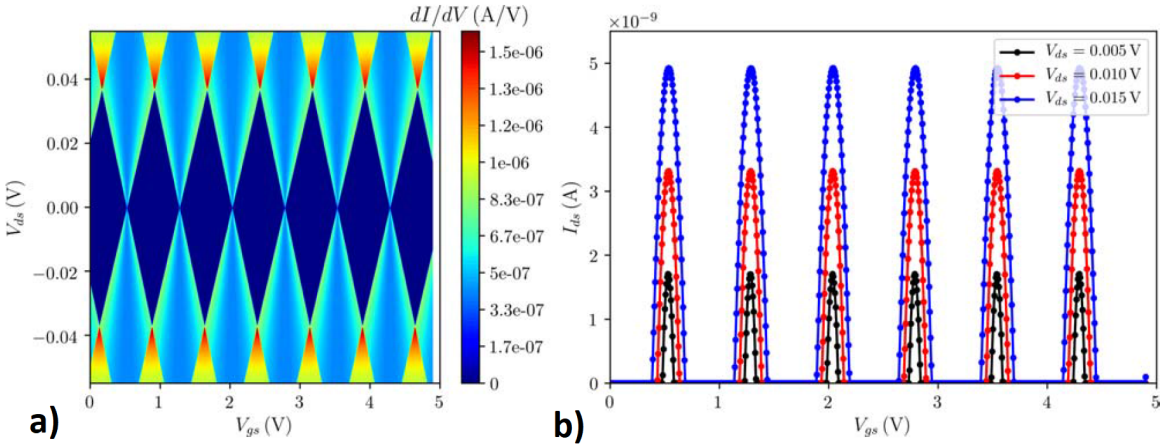

Figure 4.11: Stability diagram (a) and Coulomb oscillations (b) as obtained from simulations using the parameters: $C_S = C_D = 2.06$ aF, $C_G = 0.21$ aF, $R_S = R_D = 0.75\,\mathrm{M\Omega}$, $Q_0 = 0.76|e|$ and $T = 0.3$ K. Figure used with permission from [14].

M. Huth run simulations for $I_{ds}(V_{ds})$ and different values of $R_S = R_D$ comparing the results with the experimental I-V characteristics. Good correspondence was found for $R_S = R_D = 0.75\,\mathrm{M\Omega}$ or $R_S + R_D = 1.5\,\mathrm{M\Omega}$ which is almost identical with the measured room-temperature drain-source resistance of Sample A. The simulated stability diagrams

and the Coulomb oscillation for these device parameters are shown in Figure 4.11(a) and (b). The agreement between simulations and experimental measurements is particularly evident by directly comparing the results (device parameters, current peak positions of the Coulomb oscillations), see Figure 4.12. The values differ by less than 5%.

Values	*Experimental*	*Simulated*
$R_S + R_D$	1.6 $M\Omega$	1.5 $M\Omega$
$C_{S/D}$	2.06 aF	2.03 aF
C_G	0.21 aF	0.14 aF

a)

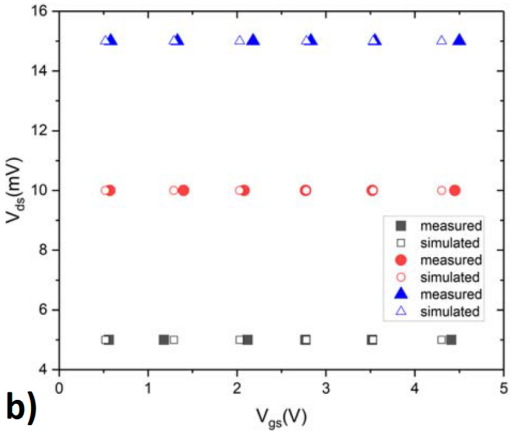

Figure 4.12: a) Table of device parameters for Sample A as deduced from experiment in comparison with the parameters deduced from the capacitance calculations and the junction resistance used for the simulations. b) Graph of current peak positions for Sample A as extracted from the measured current-voltage characteristics (full symbols, Figure 4.10) in comparison to the current peak positions as obtained from the simulations (open symbols, Figure 4.11). For maximum extraction of the experimental current peaks, $I_{ds}(V_{gs})$ was Gauss-fitted for the corresponding V_{ds}. Figure adapted from [14].

Another way to suppress the Coulomb blockade is by temperature. In Figure 4.13, the I-V characteristics of Sample A for different temperatures and fixed gate voltage ($V_{gs} = 0\,\mathrm{V}$) are shown. As a result of the higher thermally induced tunneling probability for increasing temperature, Coulomb blockade shrinkage in the device characteristics is observable. It has been found that device characteristic linearization occurs at about 160 K. This result is in good agreement with the theoretical operation range of the device if the extracted charging energy $E_C \approx 0.018\,\mathrm{eV}$, which involves about 210 K thermal energy, is taken into account. In particular, if the common criterion $E_C > 7\,k_B T_{\max}$ is considered [90], reasonable SET operation can be foreseen up to about $T_{\max} \approx 30\,\mathrm{K}$.

Although, for Sample A, a proper single-electron transport and exemplary device functioning has been displayed, the same can not be said about Sample B.
Sample A and Sample B look quite comparable from SEM images, but Sample B has been subjected to a smaller post-growth irradiation dose ($1\,\mu\mathrm{C}\,\mu\mathrm{m}^{-2}$). The different irradiation dose induces no evident change in the device shape. In Figure 4.14 (a), a SEM picture of Sample B is shown.

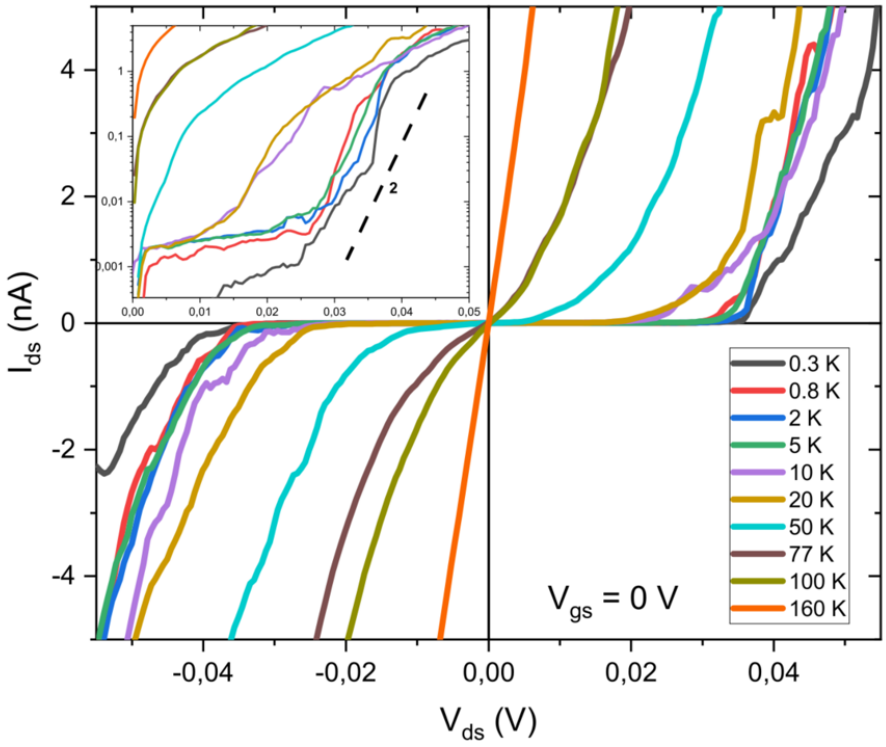

Figure 4.13: The temperature evolution of the I-V characteristics of Sample A at fixed $V_{gs} = 0\,\mathrm{V}$. The temperature increase leads to Coulomb blockade shrinkage. The Coulomb blockade is completely suppressed at 160 K, when the I-V characteristic is linear. In the inset the positive I-V characteristics are shown in a semilogaritmic graph in order to show that most of the curves have the same exponential behavior with exponent ≈ 2. The figure is adapted from [14].

The I-V characteristics of Sample B for different gate-voltages (up to 5 V) are shown as 3D graph in Figure 4.14 (b). As it can be noticed from the device I-V characteristics, Coulomb blockade regions are present also in Sample B curves. However, they are less defined than the ones of Sample A, which are shown in Figure 4.8 (a).
More evidence of the indistinct single-electron behavior can be found in the charge stability diagram of Sample B at 270 mK shown in Figure 4.15 (a) and obtained by numerical differentiation of the I-V curves of Figure 4.14 (b). Without doubt diamonds can be identified in the stability diagram. However, the diamonds show remarkable changes in the recurring shapes. The oscillation structure looks more complex and irregular if compared with the Coulomb oscillations of Sample A shown in Figure 4.10.
As it can also be noticed from the corresponding Coulomb oscillations in Figure 4.15 (b), a periodicity in the Coulomb diamonds and consequently in the Coulomb oscillations is not clearly evident. Moreover, the oscillations for $V_{ds} = 15\,\mathrm{mV}$ do not show necessarily the complete inhibition of the tunneling transport.

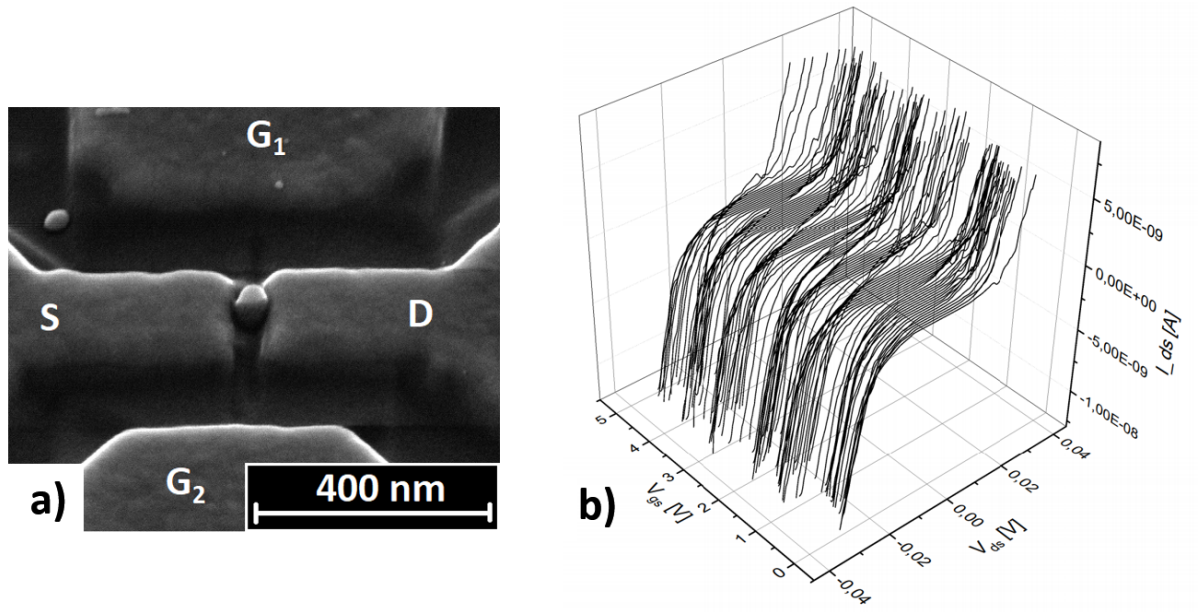

Figure 4.14: a) SEM picture of Sample B. b) Projected 3D representation of the current-voltage characteristics of Sample B for different gate voltages at 270 mK. The figure has been adapted from [14].

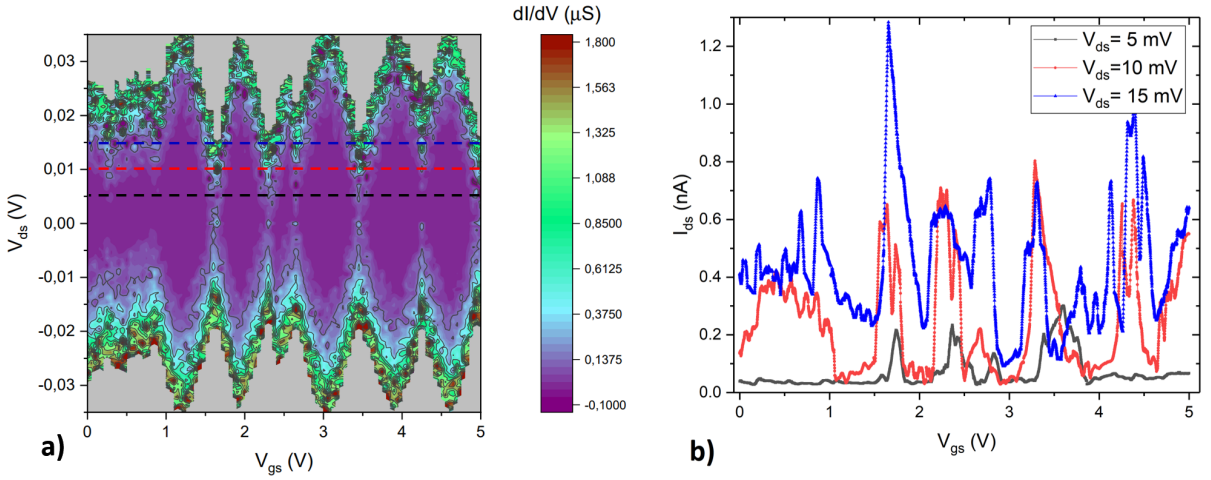

Figure 4.15: a) Charge stability diagram of Sample B at 270 mK. The diamond regions present variation in shape and periodicity. The V_{ds} voltages, for which the Coulomb oscillations in (b) are shown, are highlighted with black, red and blue lines for the values reported in the legend. b) Coulomb oscillations of Sample B for different drain-source voltages V_{ds} as indicated. Adapted from [14].

From Figure 4.16, which displays the temperature-driven device characteristic change for fixed gate voltage ($V_{gs} = 0\,\mathrm{V}$), it is directly possible to recognise that the I-V characteristics are diode-like asymmetric and that the threshold voltages reach absolute maximum values of $V_{ds,pos} = 0.023\,\mathrm{V}$ and $V_{ds,neg} = 0.015\,\mathrm{V}$ for positive and negative bias,

respectively. These results are quite different from the symmetric threshold voltage value observed for Sample A ($V_{ds,max} = 0.035$ V).
Another distinctive difference from Sample A is the device operation temperature range of Sample B. As it is clearly noticeable from Figure 4.16, the Coulomb blockade region of Sample B shrinks more rapidly with increasing temperature compared with the one of Sample A (Figure 4.13). Moreover, the Coulomb blockade disappears already at $T > 77$ K, as it is expected due to the smaller charging energy.

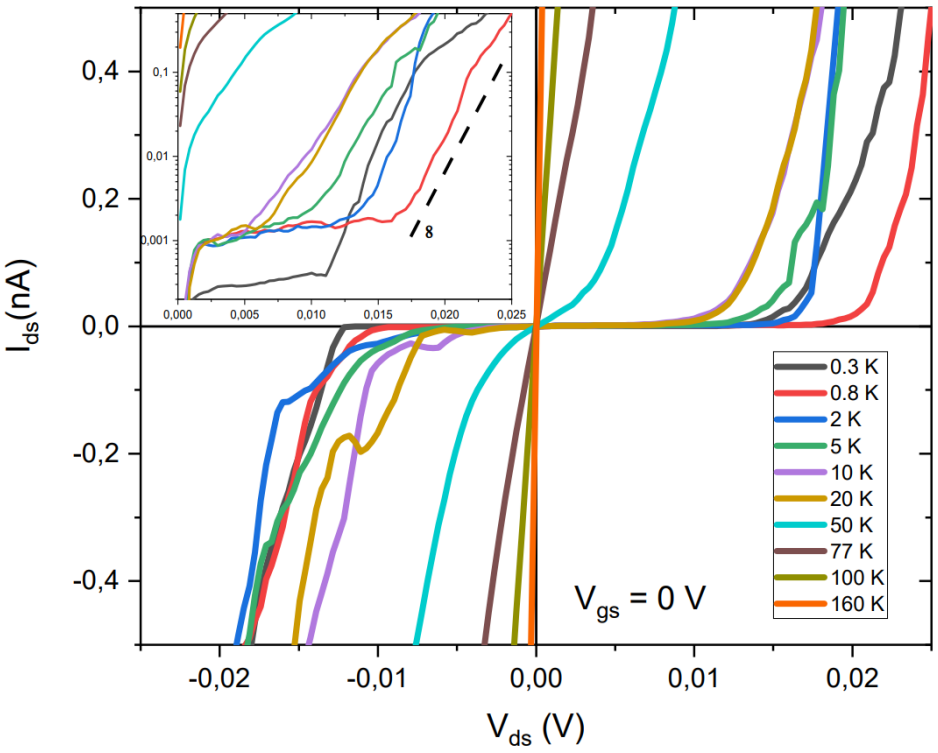

Figure 4.16: I-V characteristics of Sample B for the indicated temperatures. The device characteristics show a diode-like behavior with asymmetric threshold voltage for negative and positive applied voltage. Complete suppression of the Coulomb blockade is reached at about 77 K. Figure adapted from [14].

4.3 Modulation of the SET-performance

The advantage of using the FEBID technique for the island definition does not only derive from the direct-write nanofabrication approach that the method offers, but also of the particular composition of the material, whose electrical conductance is easy to tune. In particular, the nature of the Pt-C FEBID material, consisting of 2 - 3 nm Pt grains embedded in a carbonaceous matrix, can be especially useful for the fabrication of tunnel

junctions. Therefore, as soon as the conductance between the grains in the island is about $g \approx 0.1$ and if the number of grains is not too small, cotunneling events spanning from drain to source can be effectively blocked. Moreover, the electron transport inside the island is not negatively affected, because the conductance inside the island is still large enough to not compromise its quasi-metallic behavior.
The use of electrical irradiation to change the electrical properties of the Pt-C FEBID island is a technique that has demonstrated the capacity to increase the conductivity of the whole FEBID material changing the interplay of g_0 (intra-grain conductance) and $g\prime$ (conductance between an electrode lead and the most favorable metal grain in the island). The electron irradiation effect on Pt-C FEBID deposits has been described in Section 2.3.1.4.

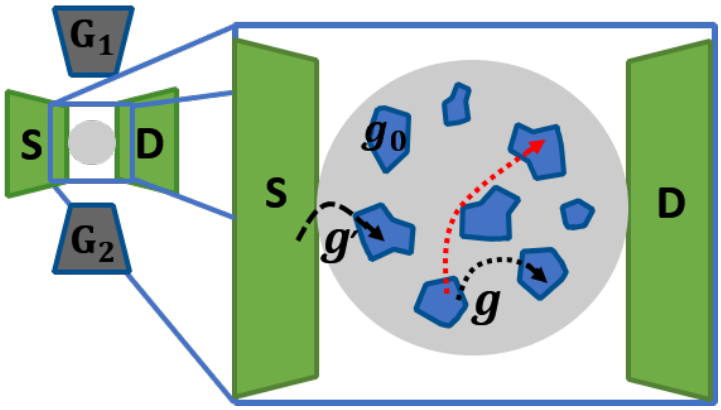

Figure 4.17: Schematic of the fabricated SET structure with highlighted nano-granular structure of the island. The electron transport through the island is described by the interplay of different tunnel conductances. The dashed red line represents a cotunneling electron transport. The figure is used with permission from [14].

It is important to point out that g is an effective quantity and may itself be written following the Landauer equation in which the final conductance is normalized to the conductance quantum G_0. It is expressed by the sum of all conductance channels, which the electron goes through when it is propagating through the nano-granular island [78]:

$$g = \sum_n T_n \,, \tag{4.1}$$

where T_n are the transmissivities of the transport channels in the conductor. However, the identification of the most important conductance channels in a nano-granular metal is not straightforward due to the large charging energies associated with the small grain size [24]. The transmission channels, described in the present discussion through different types of conductances (g, $g\prime$, g_0), are sketched in Figure 4.17.

The different behavior of the stability diagrams and temperature dependent I-V characteristics measured for Sample A and Sample B have shown that by means of the post-irradiation treatment the inter-granular tunnel coupling strength of SET devices with a Pt-C FEBID island can be modified following the results of the three-dimensional case [15]. Since no leakage currents have been measured after island irradiation between island and gates, the capacitance coupling between island and gates is maintained. In analogy with the three-dimensional case, the island can cover the full range from insulating to metallic behavior, i.e., $g \ll 1$ to $g > g_c \approx 1$. Moreover, the SET operation regime, for which the charge is quantized and localized on the island, is guaranteed if the condition $g\prime \ll 1$, of the weak lead-coupling regime, is preserved. If $g_0 \gg \max(g,\, g\prime)$ is satisfied, the different SET operation regimes can be described taking into account the ratio $g/g\prime$. For example:

a) if $\frac{g\prime}{g} \gg 1$, the electrons tunnel easily onto the island that behaves as a whole metallic system, in which the granular structure has no notable trace in the SET functionality. g is the parameter that mostly affects the device resistance.

b) if $\frac{g\prime}{g} \ll 1$, the device will not show any feature in the current-voltage characteristics. The device is too highly resistive.

c) A particular case is described by $g\prime/g \approx 1$ and $g\prime \geq 1$. In such circumstances, at least one of the junctions is in strong lead-coupling regime. In this case the quantization and localization of the charge in the island is not established and undesired leakage currents through the SET are measured [339].

Evidence of the different scenarios have been observed during the whole device optimization process. For example, scenario (a) is well describing the behavior of Sample A. As a matter of fact, the Coulomb diamonds and Coulomb oscillations of Sample A are typical of a device with metallic island. From the evidence of the features in the electrical measurements, it is then possible to conclude that the irradiation dose of Sample A, $3\,\mu\mathrm{C}\,\mu\mathrm{m}^{-2}$, promotes a quasi-metallic behavior. Comparable quasi-metallic behavior has been observed for bulk nano-granular Pt FEBID deposits irradiated with the same dose [15]. On the other hand, the irradiation dose used for Sample B, $1\,\mu\mathrm{C}\,\mu\mathrm{m}^{-2}$, does not appear to be enough to promote a fully metallic behavior of the island. The Coulomb diamonds of this sample are still clearly visible but are not as well defined as the ones measured for Sample A.
By conducting the electric transport characterization, it has been possible to investigate the fine tuning of the devices within an island irradiation range of 0.5 - $3\,\mu\mathrm{C}\,\mu\mathrm{m}^{-2}$. It follows that, case (b) can describe the transport in samples with irradiation dose lower than $1\,\mu\mathrm{C}\,\mu\mathrm{m}^{-2}$. It is interesting to point out that although the samples have comparable geometry, the used irradiation dose is the decisive factor that directly affects the dielectric

constant of the carbon matrix of the island and the island to drain/source resistance.
The scenario (c) describes the circumstances observed for the samples described in Appendix C.1. The poor definition of the tunnel junctions around the island, as a consequence of the activated co-deposit presence, caused uncontrolled island electrical shortening. As it has been described in Subsection 2.3.1.3, the application of FEBID has the side effect of a co-deposition of material in the proximity of the defined structure that with a post-growth irradiation treatment has demonstrated to promote the formation of additional conductance channels, parasitic capacitances and charge trapping nearby the island. Those effects drastically compromise the SET operation. The use of the Ar^+ ion localised etching has proven to be an essential step in the fabrication of this type of devices. Comparable structures not treated with Ar^+-etching did not show any evident conductance dependence on V_{gs} and often exhibited leakage currents between island and drain/source (scenario (c)). With the Ar^+-etching step, the circa 1 nm thick co-deposit halo (expected for nanoislands of the size fabricated in this work) is milled away. Uncritical material belonging to the island and to the leads is etched in parallel. Nevertheless, the brief milling step has shown to be enough to remove the electrostatic inhomogeneities around the island.

4.4 Outlook

The new SET fabrication technique described in this chapter lays the foundation for other single-electron applications. It is therefore the aim of the present study to develop a process, based on FEBID material for the *in situ* prototyping and further tuning of the SET functionality as base for more complex structures. The described approach can be especially useful for the highly flexible realization of single to few SE-devices.
It may be foreseen that well-calibrated prototypes can be employed in electrostatic environmental investigations. By means of the high sensibility of the island charge confinement on the electrostatic and dielectric island background, SET devices can be used as very precise electrometers. For this reason, the observation of the highly resolved features of single-electron transport (as Coulomb diamonds and oscillations) lets envision FEBID-based SET structures as on-demand charge monitor devices with high lateral positioning flexibility.
Furthermore, this special ability to accurately trace the presence of an electron in the island can be particularly interesting in the development of devices with magnetic impurities in the island for the purposes of quantum confinement investigations. Namely, the observation of quantum spin tunneling effects as Kondo effect and spin quenching could give direct information on the interaction between a confined spin (in the island) and the spins of an electronic reservoir (in the leads). Thereby, pieces of information on

the magnetic field in the vicinity of the island can be derived.
Lastly, it would be very interesting to study the stability of the charge in the island according to (not only) temperature but also time and environmental conditions. Those investigations could lead to further applications of the devices in other fields such as memory and ambient sensors. For example, the charge 'retention' of the island, as soon as the voltage is removed, has to be guaranteed if the application of the devices as memory elements is targeted.

4.5 Conclusions

The present study aims to promote the use of a combined technique based on FEBID for the fabrication of SET devices. This method takes advantage of the FEBID technique benefits, such as the precise definition and electrical tunability of the island and the tunnel junctions. Fine control of the device operation can be induced by an accurate regulation of the post-growth irradiation dose of the island.
The introduction of localized Ar^+-etching as final step in the device nanofabrication minimizes the drawback of the FEBID technique including the co-deposition halo in the vicinity of the island. The halo, if not removed, would otherwise compromise the operation of the SET, leading to leakage currents in the Coulomb blockade regime. It is additionally worth noticing that the devices can be directly *in situ* fabricated and optimized comfortably inside the chamber of the dual-beam FIB-SEM.
Finally, evidence of the tuning effect on the device conductance and the establishment of different transport regimes has been demonstrated by the observation of the Coulomb blockade in the current-voltage characteristics for different gate voltages and at different temperatures. The definition and shape of the Coulomb diamonds and oscillations, which are related to devices with different electron island irradiation doses, give a direct feedback of the quality of the obtained devices because these features are distinctive single-electron transport effects corresponding to stable SET device operations.

Conclusions

In this work by means of the observation of distinctive mesoscopic effects typical of single-electron transport, different properties such as the structure resolution, nanofabrication control, material quality and tunability have been investigated.
In particular, the focus of the study has been focused to nanostructures obtained by FEBID with the organometallic precursor $Me_3PtCpMe$. Additionally, several optimization steps of the nanofabrication technique have been conducted in order to functionalize the FEBID material and make it suitable for single-electron device fabrication.
FEBID has demonstrated in the last decades to be a compelling alternative among the established nanofabrication techniques for rapid prototyping, as EBL, focused ion beam lithography, self-assembled monolayers, etc. Some of the advantages of micro- and nanofabricated FEBID devices include the ability to control the features to the nanometer scale in a reproducible way, the faculty to miniaturize already-existing systems and the capacity of including external building blocks (as nanoparticles, nanotubes and graphene) for electronic applications.
With this work, the challenge of building extremely well-defined nanodevices as single-electron based systems by FEBID has been taken up. Two types of single-electron devices have been developed in the course of this research work for which Pt-C FEBID nanostructures have been used and functionalized in different ways. The need to treat Pt-C FEBID deposits in order to increase their electrical conductivity and use them in the applications is a consequence of the poor electrical resistivity of the as-grown material (about $10^7\,\mu\Omega\,\mathrm{cm}$). A description of the different post-growth methods is given in Subsection 2.3.1.4. By means of catalytic purification and electron irradiation, the resistivity can be reduced.
In one application, Pt-C deposits have been catalytically purified and used as elongation of the Cr-Au UVL pads in order to contact Au-NP arrays. The experimental description and electrical characterization are reported in Chapter 3. By means of the low-temperature electrical characterization of the Au-NP arrays, single-electron transport has been confirmed to take place among the nanoparticles. However, when using this approach for the SET nanofabrication, the electrical characterization of the devices

revealed some inconsistency with the theoretical behavior expected for the devices. The cause has been traced back to the presence of Pt-grains in the vicinity of the contacted Au-NP arrays working as parallel transport channel. The Pt-grains are originating from FEBID co-deposit in the proximity of the designed pattern. Unfortunately, this effect is a technique drawback and it compromised several of the attempted strategies that have been tested to fabricate single-electron transistor devices (Appendix C). For this reason, in the single-electron device application that is reported in Chapter 4 the removal of FEBID co-deposit has been addressed.

In the following application, the definition of source, drain and gate contacts has been obtained by Ga^+-FIB milling achieving a minimum gap separation of 50 nm and the Pt-C FEBID material has been used for the fabrication of the SET island. In this way, the very high and controlled tunability of the material conductivity by post-growth electron irradiation has been used to functionalize the SET island in order to well adjust the tunnel-coupling strength between the Pt-crystals in the island, as well as the junction coupling to source and drain. By means of an Ar^+-etching BIPS prototype provided from Thermo Fisher Scientific [288], the about 1 nm Pt FEBID co-deposit layer in the vicinity of the SET island has been erased. The characteristic features of Coulomb blockade diamonds and oscillations as indicators of SET behavior have been clearly defined or appeared distorted, depending on the irradiation dose applied on the Pt-C FEBID island. This result confirmed that no background charges or parallel channels are any longer present in the island environment competing with single-electron tunnelling onto and from the island. Moreover, the dependence validated the controlling effect on the tunnel-coupling tunability inside and around the island. The tuning effect is induced by the controlled post-growth electron irradiation treatment, which induces structural changes in the material. Thence, such approach is believed particularly useful for prototyping single to few SET devices with high versatility for on-demand charge monitor devices with high lateral positioning flexibility.

Additionally, in Subsection 2.3.2 a combined approach which consists of an additional Pt AS-ALD step on the catalytically purified Pt FEBID nanostructures has been described as novel approach to further functionalization of Pt-C deposits for future applications, as for example new single-electron based devices. In particular, the capability of conducting Pt-ALD on maskless patterns and the advantage of *in situ* process monitoring, which uses the electrical conductance of the growing layer as probed quantity, have been demonstrated. In the given setup a stable height increase in the range $\Delta h = 0.2\text{-}0.4$ Å per cycle has been extracted depending on the different growth conditions. The very accurate time-resolved monitoring method is a non-invasive and highly informative technique to control and optimize metal growth on a wide selection of materials. The approach is sufficiently general to be applicable to a large variety of other metal deposition setups that do not use FEBID for seeding.

The obtained results underline the huge potential of the FEBID technique as method for nanofabrication. Nevertheless, the technique has some disadvantages, as providing high-resistive deposited material for most of the precursors used so far, co-deposit formation in proximity of the defined pattern and small throughput. However, in the present work some of the technique drawbacks have been mitigated (e. g. co-deposit etching by BIPS) or used as functional parameter (e. g. conductivity improvement of the deposits by post-growth electron irradiation, seed-layer definition for promoting Pt AS-ALD, rapid prototyping of few SET devices). In this way, enhanced versatility of different approaches and ideas based on Pt-C FEBID structures has been achieved.
Moreover, by means of a powerful tool, as it is the given dual-beam system FIB-SEM, not only the nanofabrication but also material functionalization and process monitoring have been conducted *in situ*. As a result, the chamber of the dual-beam used in this work became a complete nano-laboratory suited for several purposes.

Appendices

Appendix A

Electrical and magneto-transport characterization of AS-ALD nanostructures at low-temperature

In this section the results of the electrical measurement at low-temperature for the structures fabricated by the combined technique (FEBID and AS-ALD) described in Section 2.3.2 are presented. With regard to the application of Pt nanostructures prepared by AS-ALD, a thorough characterization of their electrical transport properties is necessary.

In Figure A.1 (a), the temperature dependence of the electrical resistivity in a temperature range of 0.3 - 270 K of Sample 1 is shown. The seed layer of Sample 1 has been written with a dose of 0.9 nC μm^{-2} and it presented an average final thickness of 11.7 ± 1.5 nm after the AS-ALD process. The data are fitted by the Bloch-Grüneisen formula [340, 341] in the framework of the Boltzmann transport theory [342]:

$$\rho(T) = \rho_0 + A(\frac{T}{\Theta_D})^n \int_0^{\Theta_D/T} \frac{x^n}{(e^x - 1)(1 - e^{-x})}\, \mathrm{d}x \tag{A.1}$$

where ρ_0 is the temperature independent part of the resistivity. ρ_0 can be traced back to the residual resistivity at T $\leq$ 20 K in metallic solids. It is associated to size effects (arising mainly from the surface scattering) and the internal grain boundary scattering (along with scattering form impurities or point defects). The Residual Resistance Ratio (RRR) $= \rho(300\,\mathrm{K})/\rho(0.27\,\mathrm{K})$=1.74, is slightly larger than the one typically found for thicker Pt purified FEBID structures (RRR = 1.57) [4].

The second contribution in the equation describes a substantial part of the resistivity that is temperature dependent, where A is a constant that depends on the velocity of electrons at the Fermi surface, the Debye length and the density of electrons in the metal. Θ_D is

the Debye temperature. n is an integer that depends upon the nature of the interaction and it can assume the following values:

1. n=5 implies that the resistance is due to scattering of electrons by phonons (as for simple metals),
2. n=3 implies that the resistance is due to s-d electron scattering (as it is the case for transition metals),
3. n=2 implies that the resistance is due to electron-electron interaction.

For the fit, since Pt is a transition metal, the $n = 3$ scattering contribution has been taken into account.

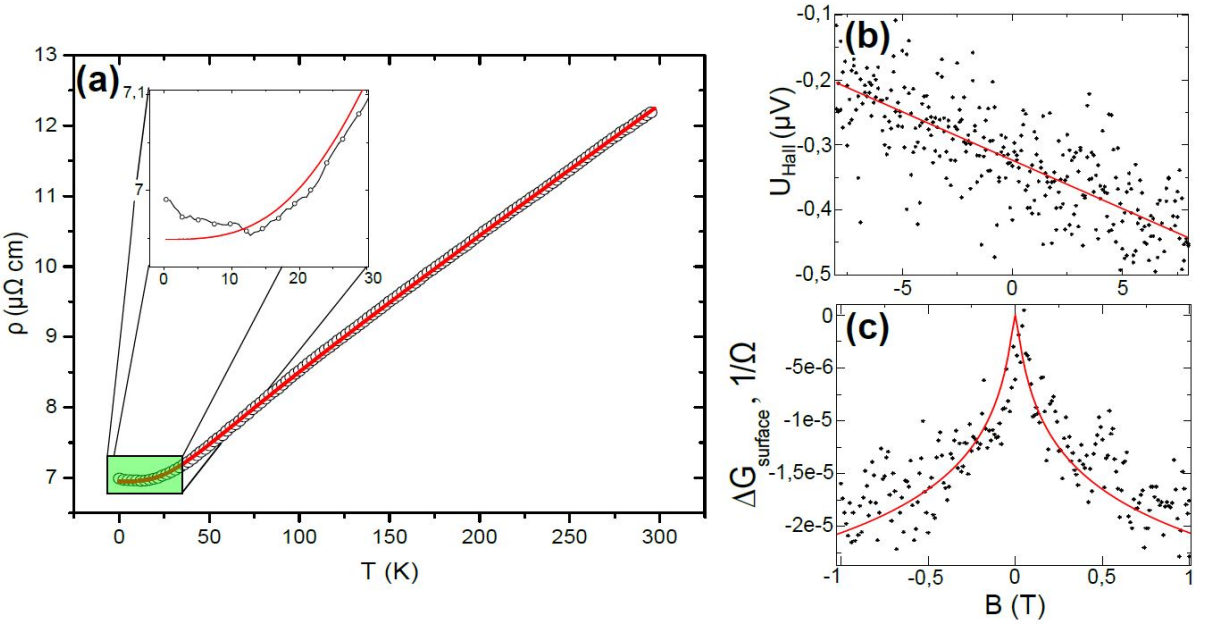

Figure A.1: a) Temperature dependence of the electrical resistivity of Sample 1. The curve can be well fit by the Bloch-Grüneisen Equation A.1. Inset: the resistivity shows a slight upturn in the lowest temperature range. This feature is typical for disordered metals. b) Magnetic field dependence of the Hall-voltage of Sample 1. (c) Magneto-conductance data of Sample 1. A coherence length of 180 nm has been extracted using a Hikami-Larkin-Nagaoka fit (Equation A.2). The data in (b) and (c) have been taken at 267 mK. The Figure is adapted from Figure 4 in [6].

The theoretical findings of Bloch, Grüneisen, Mott and Wilson give a semi-empirical relationship between the integral constant and the Debye temperature in noble metals as a function of temperature. This approach is usually used to describe the scattering mechanisms for electrons and has been extensively used in analysing the electrical resistivity of metals. The deduced Debye temperature from the fit of the curve shown in Figure A.1 (a) is 197 K. For all samples in a thickness range of 7 - 12 nm, the extracted Debye temperature is in the range of 196 - 210 K. The values for the Debye temperature

show only a modest reduction of less than 10% when compared to the bulk value (215 K) [35]. Therefore, it can be deduced that the phonon spectrum is not strongly influenced by possible size effects in the essentially two-dimensional Pt nanostripes.

Particular features of the resistivity curve can give important information on the transport mechanism in the nonostructure. If the metal is disordered, the resistivity instead of showing a constant residual value can show an upturn at low-temperatures often associated with effects such as localization [343]. A slight upturn is indeed visible in the inset on Figure A.1 (a). It presumably arises from the exchange interaction between itinerant conduction electrons and localized spin impurities leading to a weak Kondo effect [344]. Such electron scattering effects are not relevant above several Kelvin.

Hall-effect and magneto-conductance measurements have been conducted at the lowest accessible temperature of 267 mK and they are shown for Sample 1 in Figure A.1 (b) and (c), respectively. The setup used for these measurement is described in Subsection 2.4.1.3. From the linear dependence of the Hall-voltage on the magnetic field, a Hall-constant of -1.75 $\times$ 10^{11}m^{3}C^{-1} has been extracted. This value is in good agreement with the Pt bulk value of -2.13 $\times$ 10^{11}m^{3}C^{-1} [345]. In the low field magneto-conductance data, a very small enhancement of the conductivity in zero field is present. This feature is a clear signature of weak anti-localization. As a matter of fact, the obtained structures are disordered (as it is possible to be noticed from Figure 2.24). The charge transport takes place in a diffusive way and quantum interference effects between time-reversed loops formed by scattering trajectories need to be considered. In a system with large spin-orbit coupling, such as Pt, the quantum diffusion probability to return to the origin point is reduced resulting in a weak anti-localization effect. With increasing magnetic field, quantum interference effects are suppressed, giving rise to a cusp-like positive magneto-conductivity. The change in conductivity from applying a magnetic field, due to either weak localization or weak anti-localization, can be described by the Hikami-Larkin-Nagaoka (HLN) [346, 347] equation for two-dimensional systems in the limit of strong spin-orbit coupling:

$$\Delta G(B) = G(B) - G(0) = \alpha \frac{e^2}{2\pi^2 \hbar} [ln(\frac{B_\phi}{B}) - \Psi(\frac{1}{2} + \frac{B_\phi}{B})] \tag{A.2}$$

where α is the spin-orbit coupling coefficient and for weak anti-localization it is $\alpha = 0.5$. $B_\phi = \hbar/4el_\phi^2$ is the dephasing field and l_ϕ is the distance travelled by an electron before it loses phase coherence. $\Psi(x)$ denotes the digamma function: $\Psi(x) = \frac{d}{dx} ln(\Gamma(x)) = \frac{\Gamma'(x)}{\Gamma(x)}$ where $\Gamma(x) = \int_0^\infty t^{x-1} e^{-t} dt$. The solid line in the magneto-conductance data (Figure A.1 (c)) is the HLN fit. The extracted dephasing length of the obtained AS-ALD structures, having a thickness in the range of 7 - 12 nm, is between 150 and 180 nm at 267 mK. As it could be expected, the thinner samples show consistently shorter phase coherence lengths. This observation corresponds quite well with weak anti-localization effects observed in purified Pt FEBID structures of slightly higher thickness, for which a dephasing length of

234 nm has been found [4]. Overall, the causes of the modest deviation from the bulk value of the Hall-coefficient and Debye temperature and additionally the presence of localization effects are largely a consequence of finite-size effects, which are not going to undermine possible nanocontacting applications.

Appendix B

Single-Electron tunneling

This chapter introduces a theoretical background description of the single-electron tunneling transport mechanism taking place in the systems described in this work, e. g. granular metals (Section 1.1 and 1.3) and SET (Section 1.5.2). The chapter starts with the description of the tunnel junction element (Section B.1). Afterwards, the case of a double tunnel junction (Section B.2) is addressed in order to explain the electrical features of single-electron systems involving more than one tunnel junction. In the case of SET devices, the description follows the method explained in the orthodox theory [7], in which the tunneling onto and from the Coulomb island is described in terms of transition rates using tunneling probabilities (and/or the perturbation theory). It follows that a detailed balance for tunneling onto and out of the dot delineates the evolution of the charge with time in terms of tunneling current. This description is reported in literature as *transfer Hamiltonian method of tunneling*.

B.1 Tunnel junction

Elastic tunneling is a coherent quantum mechanical process in which electrons move from one side of a potential barrier to the other side preserving their energy (E). The electron tunnels through the classically forbidden region (made e. g. of dielectric material) maintaining a defined probability to be found inside the barrier. This quantum mechanical effect has been clarified by W. K. Heisenberg with his *uncertainty principle*. His principle introduces a limit on how precise the position and the momentum of an electron (having properties of wave and particle) can be determined at the same time [348].
The description of the tunnel junction problem is given considering in detail a system consisting of two closely spaced 1D metal electrodes separated by an insulator with dielectric constant ϵ_r and subjected to a potential energy difference V_b.
Since the capacitance of tunnel junctions, formed by few nanometer gaps between

electrodes, lies in the range of $10^{-15} - 10^{-18}$ F, the suppression of thermal fluctuations appears in the temperature range of a few mK [349]. In the energy diagram shown in Figure B.1 (a), the height of the potential barrier is V_0 between $x = 0$ and $x = L$ and zero everywhere else. The system can be described by the Schrödinger equations system:

$$\begin{cases} -\frac{\hbar^2}{2m}\frac{d^2\psi(x)}{dx^2} + V_0\psi(x) = E\psi(x), & \text{if } 0 \leq \text{x} \leq \text{L}, \\ -\frac{\hbar^2}{2m}\frac{d^2\psi(x)}{dx^2} = E\psi x, & \text{otherwise} \end{cases} \tag{B.1}$$

where m is the mass of the electron and $\hbar$ is the reduced Plank constant. The solutions of the equation system are the electronic wave functions ψ in the different regions. In addition, the Wentzel-Kramers-Brillouin (WKB) approximation of the tunneling probability of transmission through the barrier $V(x)$ is

$$\log|T^2| \approx \exp\left(-\frac{2}{\hbar}\int_0^L \sqrt{2m(V(x) - E)}dx\right) \text{[35]}. \tag{B.2}$$

Finding a filled energy state with energy E in a metal electrode has a probability given by the Fermi-Dirac distribution [350]:

$$f(E) = \frac{1}{1 + e^{(E-\mu)/k_BT}} \tag{B.3}$$

where μ is the chemical potential. When $T = 0\,\text{K}$ the distribution is a step function and $\mu = E_F$ (Fermi energy) is the highest occupied energy of the electrode. In order to satisfy the Pauli exclusion principle [351], the electrons leave from a filled state on one electrode and enter an empty state on the other electrode. The combined probability for identical electrodes is then $f(E) \times 1[1 - f(E)]$.
If a positive bias voltage ($V_b > 0$) is applied, the chemical potential of one of the electrode shifts to $\mu - eV_b$. The resulting Fermi-Dirac distribution is then

$$\frac{1}{1 + e^{[E-(\mu-eV_b)]/k_BT}} = \frac{1}{1 + e^{[(E+eV_b)-\mu]k_BT}} = f(E + eV_b)\,. \tag{B.4}$$

The combined probability to find a filled state on one electrode and an empty state on the other electrode becomes $f(E) \times [1 - f(E + eV_b)]$. Figure B.1 (a) and (b) shows the Fermi-Dirac probability distribution for a tunnel junction between two gold electrodes without ($V_b = 0$) and with ($V_b > 0$) an applied voltage, respectively.
In the case of a junction composed by two identical metal electrodes, where no external potential is applied ($V_b = 0$), the height of the potential barrier for a given state at energy E is

$$U = \Phi + E_F - E \tag{B.5}$$

where Φ is the work function of the metal electrode. If a voltage $V_b > 0$ is applied between the electrodes, the barrier height varies linearly with x as follows:

$$U(x) = \Phi + E_F - E - eV_b x/L\,. \tag{B.6}$$

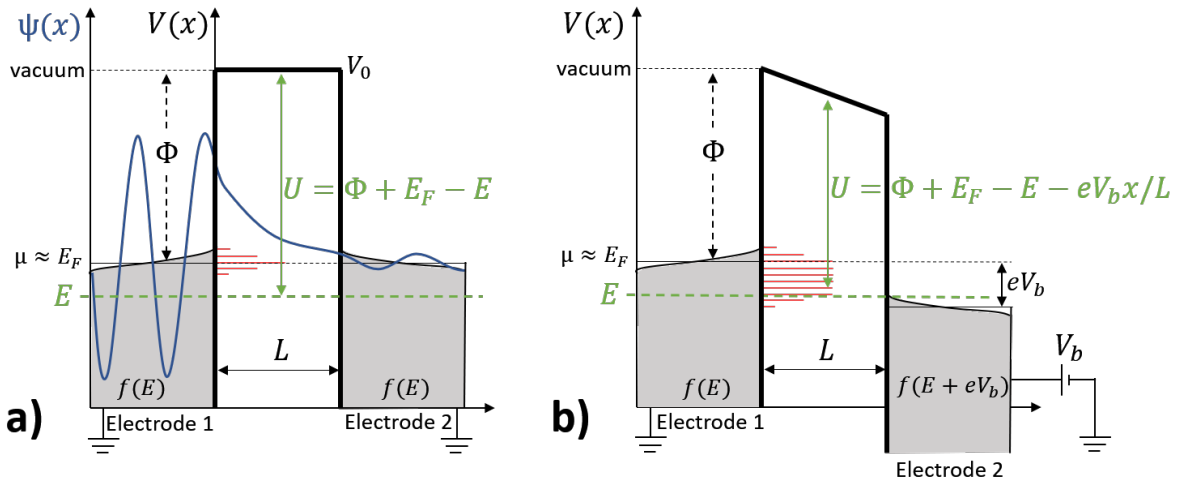

Figure B.1: Energy diagrams for a tunnel junction between two electrodes at (a) $V_b = 0$ and (b) $V_b > 0$. Blue line represents the wave function and its exponential damping within a one-dimensional potential barrier. The energy states available from electrode 1 to 2 are indicated in red. Adapted from [31].

The tunneling transmission probability decays exponentially with the barrier width (L): $|T|^2 \approx e^{-2\chi L}$ where χ is the decay constant and it depends on the barrier height as follows:

$$\chi = \frac{\sqrt{2mU}}{\hbar}\,. \tag{B.7}$$

For $E = E_F$, $V_b = 0$ and gold electrodes ($\Phi \approx 5.1eV$), χ and $|T|^2$ can be calculated and result to be $\chi \approx 1.1\,\text{Å}^{-1}$ and $|T|^2 \approx e^{-2.2L/\text{Å}} \approx 10^{-L/\text{Å}}$ with the interesting result that for every 1 Å increment on the barrier width, the tunneling transmission probability drops by about 1 order of magnitude.
Using Fermi's golden rule [352], the rate of electron tunneling from electrode 1 to 2 with energy E is:

$$\Gamma_{1\to2}(E) = 2\frac{2\pi}{\hbar}\rho(E)\rho(E+eV_b)|T(E)|^2 f(E)[1-f(E+eV_b)] \tag{B.8}$$

where the factor 2 stems from the spin degeneracy of the electrons and ρ is the density of states in the electrodes.
Considering the contributes of all energies, the total tunneling rate from electrode 1 to 2

is

$$\Gamma_{1\to2} = 2\frac{2\pi}{\hbar}\int_0^{+\infty} \rho(E)\rho(E+eV_b)|T(E)|^2 f(E)[1-f(E+eV_b)]dE \tag{B.9}$$

and thus

$$\Gamma_{1\to2}(E) = \frac{V_b}{eR_{tun}}\frac{1}{exp(eV_b/k_BT)-1}\,. \tag{B.10}$$

Here, $R_{tun} = h/(4\pi^2e^2|T|^2\rho(E)\rho(E+eV_b))$ is the tunnel resistance. $\Gamma_{2\to1}(E)$ can be similarly calculated. The total rate of electron tunneling between the two electrodes is $\Gamma = \Gamma_{1\to2}(E) - \Gamma_{2\to1}(E)$ and the respective tunneling current is

$$I = e[\Gamma_{1\to2} - \Gamma_{2\to1}] = \frac{4\pi e}{\hbar}\int_0^{+\infty} \rho(E)\rho(E+eV_b)|T(E)|^2[f(E)-f(E+eV_b)]dE\,. \tag{B.11}$$

If $eV_b << E_F$ and at room temperature, energy levels close to the Fermi level dominate in tunneling. As a result, the tunnel current can be simplified with the expression

$$I \approx \frac{g_0}{e}\int_0^{+\infty}[f(E)-f(E+eV_b)]dE \tag{B.12}$$

where $g_0 = \frac{4\pi e^2}{\hbar}\rho(E_F)^2|T(E_F)|^2$.
However, large bias reduces the barrier height and modifies $|T(E_F)|^2$. Therefore, the tunneling current depends exponentially on bias:

$$I(V_b) \propto e^{-2\chi_0 L}\sinh\left\{\frac{eV_b}{2\xi}\right\} \tag{B.13}$$

where $\chi_0 \equiv (2m\Phi)^{1/2}/\hbar$ is the decay constant at zero bias and $\xi \equiv \Phi/\chi_0 L$.
Additionally, the typical tunnel time of a tunnel junction is about 10^{-14}s. The time between tunnel events in a junction can be calculated depending on the tunnel current. Assuming currents in the nA range, the time between tunnel events is on the order of 10^{-10} s, which is much larger than the typical tunnel time [353].
It is interesting to point out that, for a classical understanding, the equivalent circuit of a tunnel junction biased by a voltage V consists of a 'leaky' capacitor, i. e. a resistor in parallel with a capacitor. This will be come important in Section 1.5, where the electrical circuit of a SET will be described.

B.2 More than one tunnel junction

Based on the model of a single tunnel junction, the transition rates for nanostructure systems, in which the charging energy is no longer a negligible contribution and more than one tunnel junction is involved in the single-electron transport, can be calculated as described in [354].

Considering a system of j^* tunnel junctions that are coupled and characterized by the number of electrons that have passed through the junction, the tunnel time through any junction is assumed to be much shorter than the time between tunnel events.
Previously, for the case of a single junction, the change in energy due to electrons tunneling through one junction has been shown in Equation 1.83. The case of the change in energy of the jth junction can be now generalized as $\Delta E_j^{\pm} = E\{n_1, n_2, ..., n_j \pm 1, ...n_{j^*}\} - E\{n_1, n_2, ..., n_j, ...n_{j^*}\}$ where the $\pm$ sign takes the tunneling process, which takes place in both transport directions (forward and backwards) across the junctions, into account.
Using the golden rule approximation and the property of the Fermi function, the tunneling rate may be written as

$$\Gamma_j^{\pm}(E) = \frac{1}{eR_{t_j}} \frac{\Delta E_j^{\pm}/e}{1 - \exp(-\Delta E_j^{\pm}/k_B T)} \,. \tag{B.14}$$

The total current flowing across the junction is still given from the difference of the left and right tunneling rates, as shown in Equation B.1. From Equation B.2, the fundamental condition of the theoretical treatment of Coulomb charging in the orthodox model is found:

$$\Gamma_j^{\pm}(E) \approx 0, \; -\Delta E_j^{\pm} \gg k_B T \,. \tag{B.15}$$

When $\Delta E_j^{\pm}$ is large and negative, tunneling is forbidden.
Thus, the qualitative explanation for Coulomb blockade is valid in the limit $|\Delta E_j^{\pm}| \gg k_B T$.
Outside the Coulomb blockade, the tunneling current is given by the equation:

$$I = \frac{e \prod_j \Gamma_j^{\pm}}{\sum_j \Gamma_j^{\pm}} \,. \tag{B.16}$$

Appendix C

Tested approaches for SET nanofabrication

As it has been pointed out in this work numerous times, the main difficulty of the nanofabrication technique in order to build a SET consists in a precise definition of both gaps and island in the range of a few nanometers. It follows that it is not easy to establish an approach able to manage the challenge. In fact, different methods have been tested in the course of this research work to overcome the obstacles and build functioning SET devices.
In this chapter, four of the not successful approaches are presented. The following nanofabrication methods, although not directly effective for the establishment of a new SET nanofabrication technique, helped in the definition of the final approach discussed in Chapter 4.

C.1 SET structures fabricated by purified Pt FEBID

One approach is the fabrication of SET structures by Pt FEBID for the definition of the island and the lead elongations to the UVL contacts. The structures have been afterwards subjected to the catalytic post growth treatment described in Subsection 2.3.1.4. Different designs have been tested and two indicative structure designs are shown in Figure C.1. The design shown in Figure C.1 (a) has been written with a one-step approach for the deposition of the elongation leads and nanoisland. The writing sequence has been: source contact, island, drain contact, gate contact. The deposits have been fabricated with a beam energy, beam current, pitch, dwell time and deposition dose of 5 keV, 180 pA, 20 nm, 1 μs and 8.3 nC μm^{-2}, respectively. For the dot a dwell time of 5 ms and 10 passes has been used.

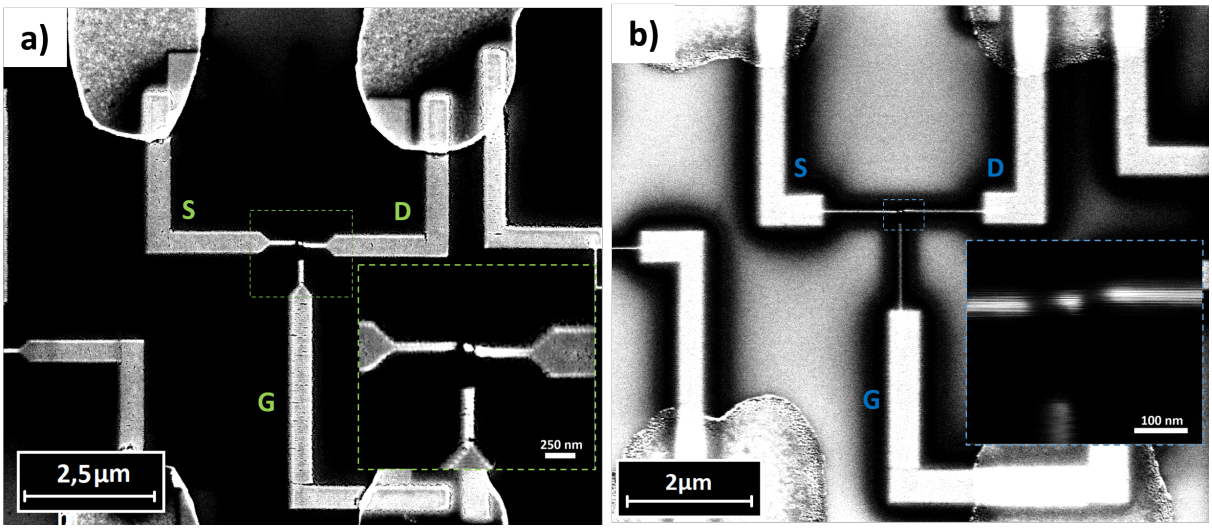

Figure C.1: SEM pictures of the structures obtained by two different FEBID writing approaches for the deposition of the contact elongations and island. a) The elongations and the island have been deposited in serial mode in a one-step deposition approach. b) Structure obtained with a two steps deposition approach with line-like contacts for the inner structure design. Insets: closeup pictures of the corresponding structure are shown for (a) and (b), respectively.

As a result of the serial writing of the deposits and relatively long deposition time (about a minute), the contacts have been subjected to beam drift. Due to charge drifting effects taking place during the deposition process, the obtained deposits do not match the structure design. For this reason, a reliable definition of the gaps between contacts and island has not been possible. In addition to this, the overlapping region of the FEBID contact elongations on the UVL contacts presented cracks originating from the shrinking effect of the carbon removal taking place during the post-growth purification treatment. The fractures do not allow to establish stable electrical contact to the SET structure.
The second attempt, of which an exemplary sample is shown in Figure C.1 (b), has been executed in two separate deposition steps. First, the elongation of the contacts have been deposited and afterwards, on the restricted central area, three line-like contacts have been written with an island in the middle of the source and drain contacts. This method has been tested in order to avoid wide co-deposit halo and drifting effects in the course of the deposition of the inner structure. For the fabrication of the outer contact elongations a beam energy, beam current, pitch, dwell time and deposition dose of 5 keV, 180 pA, 10 nm, 1 μs and 4.5 nC μm^{-2} have been used, respectively. For the lines-like deposits the pitch has been decreased to 2 nm and the dose used has been 9.2 nC μm^{-2}. The dot has been written with a dwell time of 5 ms and 10 passes. Nevertheless, difficulties have been found also in this case for the nanogaps and island definition. Gaps and island lower than 20 nm could not been obtained and, in most of the structures, the line-like contacts have

not been conductive enough.
Those fundamental nanofabrication problems restricted the feasibility of the purified Pt FEBID technique for the fabrication of both contact elongations and island.

C.2 SET structures fabricated by Fe-Co FEBID

The nanofabrication difficulties in using Pt FEBID purified deposits as metallic material for the SET design and the recent availability of the heteronuclear precursor $HFeCo_3(CO)_{12}$ in the dual-beam FIB-SEM used in this work, gave the idea to test the nanofabrication of SET devices by using FEBID with the new precursor.
$HFeCo_3(CO)_{12}$ is a heteronuclear FEBID precursor that has been proposed by Porrati *et al.* [139] as suitable precursor for the FEBID fabrication of multi-component metallic structures. In the past, other homonuclear carbonyl precursors like $Fe(CO)_5$ or $Co_2(CO)_8$, that are able to provide very high metal content (more than 70 at.% [130]) into the FEBID deposit, have been used in most applications requiring the deposition of metallic materials. However, the usability of these well-known precursors is limited by their inclination to spontaneously dissociate on activated surfaces [355, 356]. On the other hand, the carbonyl $HFeCo_3(CO)_{12}$, is very stable and yields alloy-phase nanostructures with metal content up to 84%. The compositional analysis conducted by TEM and EDX spectroscopy verified the metallic phase Co_3Fe and the formation of a residual carbon-oxide phase. As a consequence of the high metal content, Porrati *et al.* [139] reported that the electrical resistivity at room temperature of the obtained FEBID deposit is 43 $\mu\Omega\,$cm. Furthermore, the researchers showed that an improvement of the electrical conductivity of the deposits can be achieved by electron irradiation treatment (as it has been described for the $C_5H_4CH_3Pt(CH_3)_3$ precursor in Subsection 2.3.1.4). As a matter of fact, TEM analysis has shown that an amorphous-to-crystalline transformation takes place in the upper layers of the deposits, where the electron irradiation is more effective.
Accordingly, preparatory tests for the FEBID fabrication of SET devices have been performed with the precursor in 2D and in 3D.

Fe-Co 2D Line-dot-line deposits Initial tests for possible SET nanofabrication with the FEBID precursor $HFeCo_3(CO)_{12}$ have been conducted on prototyping structures as line-dot-line deposits for which an example is shown in Figure C.2.
The 2D structures have been fabricated with a beam energy, beam current, pitch, dwell time and loops number of 20 keV, 150 pA, 2 nm, 1 μs and 4000 passes, respectively. The dot has been written with 20 keV, 15 pA, 200 μs and 750 passes.
It is possible to notice from Figure C.2 (a), that the nanogap and the island look well defined even with minimal separation and island diameter (both less than 10 nm). The

asymmetric gaps have been artificially set in the FEBID design, for which the distances have been planned to be 15 nm (bottom gap) and 7.5 nm (top gap). Although the resolution of the structure is very good, it is possible to observe co-deposit grains (about 3 nm in diameter) in the surrounding background.

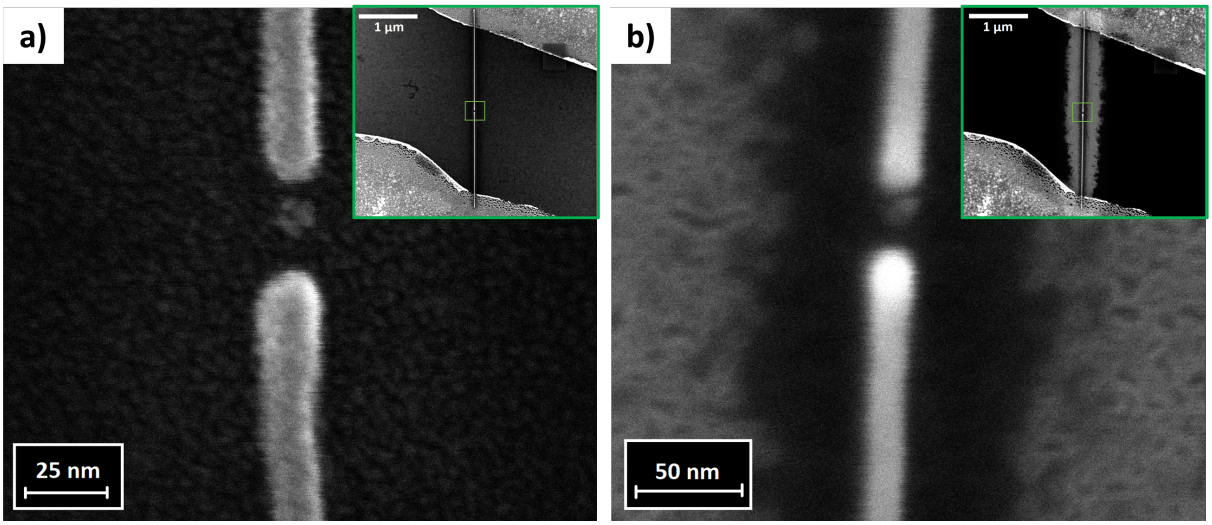

Figure C.2: SEM closeup of a line-dot-line structure fabricated by FEBID of the $HFeCo_3(CO)_{12}$ as deposited (a) and after the structure has been subjected to electron irradiation (b). Insets: overview SEM picture of the structures in (a) and (b), respectively.

Afterwards, the structures have been subjected to a post-growth irradiation step. The structures increased their resistance and a wide area next to the deposit changed its contrast. A SEM picture of the irradiated structure is shown in Figure C.2 (b). In Figure C.3, the time dependent current measurement during the post growth electron irradiation treatment is shown. The current curve shows a fast drop of conductance followed by an attenuation peak. After the deposition, from the ohmic behavior of the I-V characteristic, a resistance of 4.6 MΩ has been calculated. After subjecting the sample to electron irradiation with a dose of 0.5 μC μm^{-2}, the calculated structure resistance has been 15 MΩ.

Differently from the effect achieved on Pt-C FEBID material obtained from $MeCpPtMe_3$, the electrical irradiation treatment on the structure shown in Figure C.2 increased the 1D line-dot-line structure resistance. It can be speculated that the electron irradiation promotes the formation of an oxide phase $FeCo_2O_4$. As a matter of fact, 5 nm $FeCo_2O_4$ have been found on irradiated layers of similar FEBID deposits obtained using the same precursor and chamber [139, 357]. As a consequence of the high surface ratio of the FEBID lines and dot, the induced superficial oxidation could have undermined the electric conductive properties of the whole structure.

Line-dot-line structures with and without electron irradiation treatment, have been

electrically investigated in the ^{3}He-cryostat. Both types of structures did not show any Coulomb blockade feature in the I-V characteristics at low-temperature.

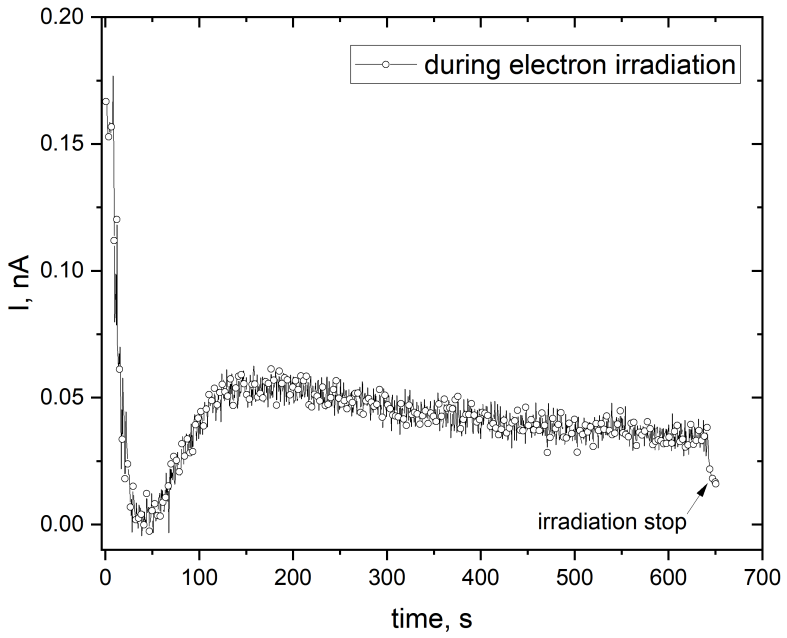

Figure C.3: Time dependence of the direct current measured during electron irradiation of the structure shown in Figure C.2 . The current reached a plateau after circa 500 sec.

Fe-Co 3D freestanding contact structures From the result of the previously discussed 2D structures, a different strategy has been tested in order to avoid the co-deposit interference in the structure function and extend the nanofabrication into the third dimension. With the collaboration of L. Keller, who has developed a software tool for the fabrication of complex FEBID 3D nanostructures [357], the fabrication of three freestanding Fe-Co 3D contacts have been tested as prototype for the fabrication of SET devices.

For the fabrication of the structures, a beam energy of 20 keV and a current of 13 pA has been used. The beam writing strategy has been translated to a pattern file. The file results from the use of an algorithm that takes precursor depletion and proximity effects into account (beam current, beam energy, pitch, dwell time, precursor molecules site depletion, etc). In this way, every deposition event has been optimized and the beam passes are treated as single depositions on horizontal slices, that are parallel to the substrate surface [357]. It follows that it is possible to transform an already powerful FEBID tool into a 3D printer on the nanometer scale. M. Huth *et al.* described in detail

the power of this 3D nanoprinting technique in their recent work [358].
The idea of the here reported 3D fabrication attempt has been to use 3D freestanding deposits as UVL contact elongations in the source-drain-gate configuration. Moreover, the superficial oxidation process of the FEBID Fe-Co deposits [139, 153] could have been used to build the interface tunnel junction between the source/drain contact and a following deposited island. In this way, the 3D fabrication of the contacts may avoid the co-deposition of material in the proximity of the two tunnel junctions. SEM pictures of the 3D SET prototype are shown in Figure C.4.

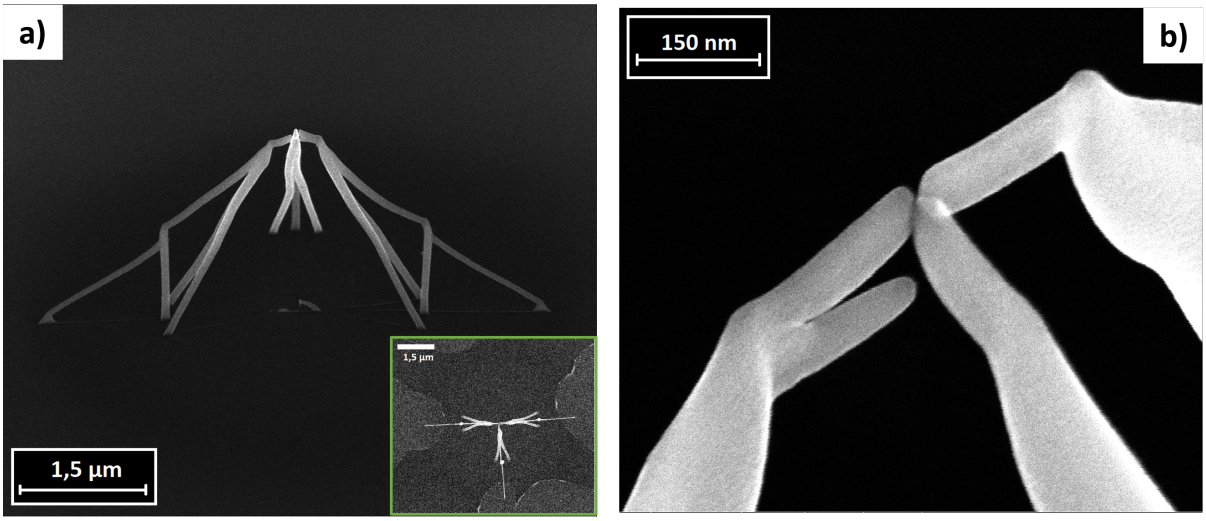

Figure C.4: a) SEM picture in tilted view of the 3D SET prototype obtained by 3D FEBID with the $HFeCo_3(CO)_{12}$ precursor using a pattern provided by the software of L. Keller [357]. Inset: standard SEM top view of the structure. b) Closeup of the structure shown in (a) by a different angle. Under the deposited lead on the left, a second branch has been deposited in parallel due to not optimized pitch.

The structure looks well defined. Nevertheless, the undesired deposition of a branch underneath one of the contacts is visible. Unfortunately, the long beam settling time on a small writing distance leads to a significant co-deposition between the anchoring feet of the contacts and even underneath the center of the structure. The mutual resistance measured between two of the three contacts has been around 1 kΩ. No significant resistance changes have been observed after 12 h from the contact elongations deposition. Furthermore, the positioning of the island in the center of the three freestanding leads in the final deposition step has not been successful. Several attempts have been tried, but due to nonsystematic beam drift effects, none of the attempts succeeded.
The 3D FEBID attempt of the SET device nanofabrication has shown its limitation in the parallel deposition of unwanted material, that compromises the single-electron based transport of the SET device, and in the unreliable two step deposition process. For

this reason, no further energy has been invested in other 3D FEBID attempts for the nanofabrication of SET prototypes.

Zusammenfassung

Über die letzten 40 Jahre hat sich der Fokus in der Entwicklung von Halbleiterprodukten auf Ultra-Low-Power und ultra-hoch-integrierte Schaltungen verschoben, um immer leistungfähigere Geräte mit sehr niedrigem Energieverbrauch herstellen zu können. Mit steigender Komplexität der integrierten Schaltungen werden immer innovativere Techniken nötig, um diese fabrizieren zu können. Dies erfordert einen starken Fokus auf die Kontrolle der Fabrikation akkurater Strukturen und der Materialreinheit, und dies im Zusammenhang mit einer skalierbaren Produktion. Hinzu kommt die nötige Kompatibilität der neuen Nanobauteile, wie zum Beispiel Nanopartikel, Graphen oder Kohlenstoffnanoröhren, mit bereits existierenden Technologien.
Bisher wurden Techniken, wie Elektronenstrahllithographie (engl. Electron-beam lithography, EBL), Microcontact und Nano-Transfer-Printing für die Kontaktierung von Nanostrukturen genutzt. Diese Techniken benötigen jedoch viele verschiedene Prozessschritte und verschiedene Chemikalien, die nicht selten zu einer Inkompatibilität mit neuartigen Oberflächen und Nanobauteilen führen.
Aus diesem Grund gelangen Techniken in den Fokus, die das direkte Erzeugen der neuartigen Nanostrukturen erlauben. Elektronenstrahlinduzierte Abscheidung (engl. Focused Electron Beam Induced Deposition, FEBID) ist eine dieser Techniken, der immer mehr Aufmerksamkeit für die Nanofabrikation geschenkt wird, da diese eine hohe Auflösung erlaubt, was für die 2D/3D-Nanostrukturierung essenziell ist. Mit dieser Technik sind hochauflösende Formen im Nanometer-Maßstab möglich, die dem vorgegebene Design sehr genau entsprechen. Insbesondere können die Strukturen durch den Bottom-Up-Ansatz von FEBID aus einer Vielzahl verschiedener Materialien mit einer hohen Auflösung (besser als 10 nm laterale Auflösung) und minimaler Beschädigung der Oberfläche erzeugt werden.
Der FEBID-Prozess basiert auf dem lokalen Befüllen der Vakuumkammer eines Rasterelektronenmikroskops (engl. Scanning Electron Microscope, SEM) mit einem Präkursor in direkter Nähe zu einem Substrat. Im Fokus des Elektronenstrahls werden Präkursorsmoleküle in flüchtige und nicht flüchtige Komponenten zersetzt. Die nicht flüchtigen Komponenten bilden das Deponat. Bei der unvollständigen Zersetzung metallorganischer Präkursoren lagern sich organische Bestandteile auf dem Substrat ab.

Als Beispiel sei hier der Präkursor $Me_3PtCpMe$ angeführt. Das auf dem Substrat abgelagerte Material besteht aus kleinen Pt-Kristalliten mit einem Durchmesser von 2 - 3 nm, welche in einer Matrix aus amorphem Kohlenstoff eingebettet sind. Die amorphe Kohlenstoff-Matrix verhält sich hier wie ein Halbleiter. Die gewachsenen Pt-C FEBID Ablagerungen sind nano-granulare Metalle, deren elektrische Transporteigenschaften die Folge des Zusammenspiels von diffusivem Transport von Ladungen innerhalb der Pt-Kristalliten und temperaturabhängigen Tunneleffekten sind [2].
Neben den vielen offenen Fragen zu diesen Typen von nano-granularen Metallen liegt das größte Interesse an diesen Materialien an der Möglichkeit, Strukturen für technische Anwendungen im Nanometerbereich herstellen zu können. Die Möglichkeit, diese Strukturen im Nanometerbereich zu erzeugen, legt Anwendungen, die auf Einzelelektroneneffekten beruhen, nahe. Um Einzelelektronentransport zu ermöglichen, der auf dem Tunneln einzelner Elektronen basiert, müssen alle Parameter, wie Grösse und Abstände der Strukturen, genauestens definiert sein.
Im Rahmen dieser Arbeit wurden Einzelelektronenbausteine entwickelt, die auf zwei unterschiedlichen Anwendungen des Pt-C FEBID-Prozesses basieren. Die beiden Anwendungen sind:

1. Arrays von Gold-Nanopartikeln (Au-NP), welche mittels Pt-Strukturen kontaktiert wurden, die mit FEBID präpariert und anschließend aufgereinigt wurden

2. Einzelelektronentransistoren (engl. single-electron transistors, SET), deren Inseln aus elektronennachbestrahlten Pt-C FEBID Deponate bestehen

Im Rahmen dieser Arbeit wurden die elektrischen Eigenschaften der präparierten Nanostrukturen charakterisiert und mit der erzielten Auflösung und Materialqualität in Relation gesetzt. Es wurden Optimierungen an der Präparationsmethode durchgeführt, welche direkt die Leitfähigkeit des Pt-C FEBID Materials erhöhen. Dies kann durch die Änderung der Kohlenstoff-Matrix oder die Erhöhung des metallischen Gehalts der Struktur geschehen.
Pt-C Deponate können nach der Präparation mittels FEBID nachbehandelt werden. In dieser Arbeit wurden Pt-C Deponate O_2-Gas ausgesetzt und gleichzeitig erhitzt. Das Prozessgas konnte sehr lokal in die Nähe der Probe geleitet werden. Diese Nachbehandlungen basieren auf der katalytischen Eigenschaft von Pt und haben in zwei unterschiedlichen Anwendungen den Kohlenstoff erfolgreich aus den Deponaten entfernt. Die Methode wurde von Sachser *et al.* [4] entwickelt. Die Handhabung sieht vor, dass ein erhitztes Substrat in Zyklen O_2 ausgesetzt wird. Dieser Prozess kann lokal überwacht werden, indem die Leitfähigkeit einer Pt-C FEBID Struktur zwischen zwei UV-Lithographie (UVL) präparierten Cr-Au Kontakten gemessen wird. Mit dieser Methode kann Kohlenstoff aus dem Deponat komplett entfernt werden, wodurch Strukturen aus

reinem Pt für die weitere Nutzung zur Verfügung stehen.
Zum einen wurden die aufgereinigten Strukturen als Keimschicht für die nachfolgende ortsgenaue Atomlagenabscheidung (engl. Area-Selective Atomic Layer Deposition, AS-ALD) von Pt-Dünnschichten genutzt. Zum anderen wurde diese Technik dafür genutzt, Metallbrücken zwischen den bereits durch Auftropfen zufällig auf dem Substrat aufgebrachten NP-Gruppen und den zuvor aufgebrachten Cr-Au Kontakten zu erzeugen. Eine NP-Gruppe ist ein periodisches, granulares Array von Partikeln, welche uniform in Größe und Form sind und einen unterschiedlichen Grad von Ordnung inne haben. Durch die Art des Aufbringens kann die Anordnung der Nanopartikel durch Lösen und Erzeugen der Verbindungen beeinflusst werden. Die Liganden der Moleküle übernehmen die Rolle von mechanischen inter-NP-Abstandshaltern und erlauben eine präzise Steuerung der elektronischen Kopplung. Diese Systeme zeigen ein Verhalten wie Tunnelkontakte mit Coulombblockade und eine Verteilung der Schwellspannung. Die NP-Arrays bestehen aus Monolagen mit Thiol-PEG verbundenen Gold-Nanopartikeln (Durchmesser = 12,5 nm). Diese werden in der Nähe zu Gold-Elektroden auf einem Si/SiO_2 Substrat durch Auftropfen zufällig aufgebracht. Die Au-NP formieren sich dabei in einem Dreiecksgitter in Domänen mit einem Durchmesser von bis zu 1μm.
Die elektrischen Messungen der Au-NP-Arrays bestätigen den Einzelelektronentransport durch die Nanopartikel in einem typischen Elektronentransportregime mit schwacher Kopplung. Die Größe der am Transport beteiligte Partikel entspricht die Größe der Nanopartikel. Trotz dieser Ergebnisse war die Anwendung dieser Technik für die SET Nanostrukturierung nicht erfolgreich. Die Ursache konnte auf das Vorhandensein von Pt-Partikeln in der Nähe der Kontakte der Au-NP Arrays zurückgeführt werden. Diese führten zu parallelen Transportkanälen, oder zu elektrostatischen Ladungen um die Nanopartikel, welche durch Co-Tunnel-Effekte den Einzelelektronentransport durch das gesamte Array stören können. Die Pt-Partikel sind durch den FEBID Fertigungsprozess in der Nähe der vorgegebenen Struktur entstanden. Dieser Effekt ist ein Nachteil dieser Technik, welcher viele der versuchten Techniken zur Erstellung von Einzelelektronenbausteinen betroffen hat. Aus diesem Grund wurde das FEBID Co-Deponat in der folgenden SET-Nanofabrikation entfernt.
Ein SET basiert auf einer Nano-Insel, welche durch Tunnelkontakte mit Source- und Drain-Elektroden verbunden ist. Darüber hinaus besteht eine kapazitive Verbindung zu einer oder mehreren Gate-Elektrode(n). Innerhalb der Insel gibt es eine feste Anzahl von Überschuss-Elektronen. Der Strom durch diese Insel kann durch eine Änderung der Spannung am Gate beeinflusst werden. Im Herstellungsprozess besteht die Herausforderung darin, die Insel sehr präzise in einem Bereich kleiner als 100 nm zu platzieren und die Tunnelkontakte zu Drain und Source entsprechend anzupassen. In dieser Arbeit wurden die Source-, Drain- und Gate-Kontakte erzeugt, indem 50 nm breite Spalte in zuvor kurzgeschlossene Au-Kontakte mithilfe eines fokussierten

Gallium-Strahls geätzt wurden. Die Insel des SETs wurde aus Pt-C FEBID-Material nachträglich präpariert. Die Leitfähigkeit der Insel aus Pt-C wurde mit anschließender Elektronenbestrahlung erhöht. Dieses Verfahren kann genutzt werden, um Kohlenstoff zu reduzieren, die Kohlenstoff-Matrix zu graphitisieren und die Koaleszenz von Pt-Körnern hervorzurufen. Durch diese Technik kann die Leitfähigkeit durch die Verringerung der Tunnelbarrieren zwischen gekoppelten Pt-Kristalliten erhöht werden. Darüber hinaus wurde für mikroskopische Strukturen gezeigt, dass die Leitfähigkeit über drei Größenordnungen fein abgestimmt werden kann, was einen fließenden Übergang zwischen metallischem und isolierendem Verhalten bewirkt [15, 21].
Als letzte Präparationsmethode wurde ein neueartiges Argon-Ätzverfahren genutzt, um die durch FEBID erzeugten Co-Ablagerungen in der direkten Umgebung der Insel zu entfernen. Das Ätzen wurde schrittweise durchgeführt, um den elektrischen Widerstand während des Prozesses überwachen zu können. Dieser Finalisierungsschritt minimiert das Problem der Co-Ablagerungen rund um die Insel, welche im FEBID-Herstellungsprozess entstehen. Diese Ablagerungen können die Funktion des SET durch Leckströme im Bereich der Coulombblockade negativ beeinflussen. Dies wurde als größtes Problem beim Einzelelektronentunneln durch die Insel beobachtet.
Durch die Elektronennachbestrahlung kann die Kopplung zwischen den einzelnen metallischen Kristalliten angepasst werden. Die Auswirkungen unterschiedlich starker Tunnelkontakte auf die elektronischen Eigenschaften der Insel und die daraus resultierende Performanz des SETs wurden in dieser Arbeit untersucht. Im Speziellen wurde die hohe Kontrollierbarkeit der Leitfähigkeit durch die Elektronennachbestrahlung genutzt, um die Tunnelkopplung zwischen den Pt-Kristalliten in der Insel, sowie die Kopplung zu Source und Drain fein abzustimmen. Der Nachweis des Effekts des Tunings auf die Leitfähigkeit des Bauelements und auf das Erreichen verschiedener Transportregime wurde durch die Beobachtung bei sehr niedrigen Temperaturen (bis zum 0,3 K) von charakteristischen Merkmalen wie Coulombblockade, -Diamanten und -Oszillationen erbracht. Dieses Ergebnis bestätigt, dass keine Ladungen mehr im Hintergrund oder noch parallele elektrische Kanäle in der Umgebung der Insel vorhanden sind, die das Einzelelektronentunneln negativ beinflussen. Der Unterschied in der Definition und Form der Merkmale der Coulombblockade, die für unterschiedliche Elektronenbestrahlungsdosen auf die Pt-C FEBI-Insel beobachtet wurden, geben direkten Aufschluss über die Qualität der geschaffenen Bauelemente, da diese Merkmale charakteristische Einzelelektronentransporteffekte im Zusammenhang mit stabilen SET-Bauelementen sind [14].
Darüber hinaus wurde ein kombinierter Ansatz beschrieben, der aus einem zusätzlichen Pt AS-ALD-Schritt auf den katalytisch gereinigten Pt FEBID-Nanostrukturen besteht. Mit diesem neuartigen Ansatz wurde die Funktionalisierung von Pt-C-Ablagerungen für Anwendungen, wie z. B. neue Bauelemente auf Einzelelektronenbasis, untersucht. Bei

AS-ALD ist das Substrat bei hoher Temperatur der zyklischen Einwirkung von zwei Reaktionsgasen, $Me_3PtCpMe$ und O_2, ausgesetzt. Auf diese Weise kann bei jedem Zyklus eine Abscheidung einer reinen Pt-Schicht im Sub-Nanometerbereich erreicht werden.
Mit dieser Technik können beliebig komplizierte Strukturen maskenlos bearbeitet werden. Sie bietet außerdem eine räumliche Auflösung im Nanometerbereich und ist einfache in andere Prozesse zu integrieren.
Insbesondere wurde in dieser Arbeit gezeigt, dass der Pt-ALD-Prozess mithilfe der Messung des elektrischen Leitwertes / Widerstands der entstehenden Schicht überwacht werden kann. In dem verwendeten Aufbau wurde eine stabile Wachstumsrate im Bereich $\Delta h = 0{,}2\text{-}0{,}4\,\text{Å}$ pro Zyklus in Abhängigkeit verschiedener Wachstumsbedingungen gemessen.
Weitere wichtige Informationen können aus Leitwertsmessungen im laufenden Prozess abgeleitet werden und umfassen Oberflächenreaktionen, die während der Reaktantenexposition stattfinden, die Erhaltung der Selektivität und die Herstellung eines elektrischen Kontakts. Darüber hinaus ermöglicht ein zeitlich genaues Fortschritts monitoring des Prozesses eine Bewertung und eine Anpassung der Faktoren der Nanofabrikation, um den Prozess zu optimieren.
Diese zeitaufgelöste Überwachungsmethode ist eine nicht-invasive Technik zur Kontrolle und Optimierung des Metallwachstums von und auf einer großen Auswahl von Materialien. Der Ansatz ist sehr allgemein, sodass er bei einer Vielzahl anderer Metallabscheidungstechniken anwendbar ist, die nicht FEBID zur Präparation der Keimschicht verwenden [6].

Bibliography

[1] H. S. Nalwa and R. E. Smalley. *Encyclopedia of Nanoscience and Nanotechnology*. Journal of Nanoscience and Nanotechnology, 2011. 1

[2] M. Huth, F. Porrati, C. Schwalb, M. Winhold, R. Sachser, M. Dukic, J. Adams, and G. Fantner. Focused electron beam induced deposition: A perspective. *Beilstein Journal of Nanotechnology*, 3:597–619, 2012. 2, 8, 70, 73, 188

[3] E. Villamor, F. Casanova, P. H. F. Trompenaars, and J. J. L. Mulders. Embedded purification for electron beam induced Pt deposition using $MeCpPtMe_3$. *Nanotechnology*, 26(9):095303, 2015. 3, 79

[4] R. Sachser, H. Reizh, D. Huzel, M. Winhold, and M. Huth. Catalytic purification of directly written nanostructured Pt microelectrodes. *ACS Applied Materials and Interfaces*, 6(18):15868, 2014. 5, 77, 79, 81, 82, 90, 171, 174, 188

[5] B. Geier, C. Gspan, R. Winkler, R. Schmied, J. D. Fowlkes, H. Fitzek, S. Rauch, J. Rattenberger, P. D. Rack, and H. Plank. Rapid and Highly Compact Purification for Focused Electron Beam Induced Deposits: A Low Temperature Approach Using Electron Stimulated H_2O Reactions. *The Journal of Physical Chemistry C*, 118(25): 14009, 2014. 3, 79

[6] G. Di Prima, R. Sachser, P. Gruszka, M. Hanefeld, T. Halbritter, A. Heckel, and M. Huth. In situ conductance monitoring of Pt thin film growth by area-selective atomic layer deposition. *Nano Futures*, 1(025001), 2017. 3, 69, 84, 90, 102, 103, 105, 106, 123, 172, 191

[7] K. K. Likharev. Single-electron devices and their applications. *Proceedings of the IEEE*, 87(4):606–632, 1999. 3, 8, 11, 32, 35, 36, 175

[8] Y. Nakamura, C. Chen, and J. Tsai. 100-K Operation of Al-Based Single-Electron Transistors. *Japanese Journal of Applied Physics*, 35(11A):L1465, 1996. 36

[9] K. Yano, K. T. Ishii, T. Hashimoto, T. Kobayashi, F. Murai, and T. Seki. Room-temperature single-electron memory. *IEEE Transactions on Electron Devices*, 9 (41):1628, 1994.

[10] R. H. Chen and K. K. Likharev. Multiple-junction single-electron transistors for digital applications. *Applied Physics Letters*, 72(1):61, 1998. 36

[11] A. N. Korotkov, R. H. Chen, and K. K. Likharev. Possible performance of capacitively coupled single-electron transistors in digital circuits. *Journal of Applied Physics*, 78(4):2520, 1995.

[12] H. Inokawa, A. Fujiwara, and Y. Takahashi. A Merged Single-Electron Transistor and Metal-Oxide-Semiconductor Transistor Logic for Interface and Multiple-Valued Functions. *Japanese Journal of Applied Physics*, 41(4S):2566, 2002. 3, 36

[13] J. M. De Teresa, R. Córdoba, A. Fernández-Pacheco, O. Montero, P. Strichovanec, and M. R. Ibarra. Origin of the difference in the resistivity of as-grown focused-ion- and focused-electron beam-induced Pt nanodeposits. *Journal of Nanomaterials*, 2009(936863), 2009. 3, 76, 98

[14] G. Di Prima, R. Sachser, P. H. F. Trompenaars, J. J. L Mulders, and M. Huth. Direct-write single electron transistors by focused electron beam induced deposition. *Nano Futures*, 1(18):183109, 2019. 4, 115, 122, 146, 155, 156, 157, 158, 159, 160, 161, 162, 163, 190

[15] R. Sachser, F. Porrati, C. H. Schwalb, and M. Huth. Universal conductance correction in a tunable strongly coupled nanogranular metal. *Physical Review Letters*, 107(20):1–5, 2011. 5, 8, 69, 79, 80, 102, 125, 145, 152, 164, 190

[16] I. S. Beloborodov, A. V. Lopatin, V. M. Vinokur, and K. B. Efetov. Granular electronic systems. *Review of Modern Physics*, 79(2):469–518, 2007. 7, 8, 11, 12, 15, 23, 24, 138

[17] B. Abeles, P. Sheng, M. D. Coutts, and Y. Arie. Structural and electrical properties of granular metal films. *Advances in Physics*, 24(3):407–461, 1975. 8

[18] C. P. Collier, T. Vossmeyer, and J. R. Heath. Nanocrystal Superlattices. *Annual Review of Physical Chemistry*, 49(1):371–404, 2002. 8

[19] C. B. Murray, R. Kagan, and M. G. Bawendi. Synthesis and Characterization of Monodisperse Nanocrystals and Close-Packed Nanocrystal Assemblies. *Annual Review of Material Science*, 30:545–610, 2006. 8

[20] M. Huth, F. Porrati, and O. V. Dobrovolskiy. Focused electron beam induced deposition meets materials science. *Microelectronic Engineering*, 185:9, 2018. 8, 12, 16, 31, 69, 70, 71, 76

[21] F. Porrati, R. Sachser, C. H. Schwalb, A. S. Frangakis, and M. Huth. Tuning the electrical conductivity of Pt-containing granular metals by postgrowth electron irradiation. *Journal of Applied Physics*, 109(6):063715, 2011. 8, 78, 79, 190

[22] I. S. Beloborodov, A. V. Lopatin, and V. M. Vinokur. Universal description of granular metals at low temperatures: Granular Fermi liquid. *Physical Review B - Condensed Matter and Material Physics*, 70(20):1–5, 2004. 8, 12

[23] K. B. Efetov and A. Tschersich. Transition from insulating to non-insulating temperature dependence of the conductivity in granular metals. *Europhysics Letters*, 59(1):114–120, 2002. 11, 12, 18

[24] I. S. Beloborodov, A. V. Lopatin, and V. M. Vinokur. Coulomb effects and hopping transport in granular metals. *Physical Review B - Condensed Matter and Material Physics*, 72(12):1–20, 2005. 15, 17, 23, 163

[25] T. B. Tran, I. S. Beloborodov, X. M. Lin, T. P. Bigioni, V. M. Vinokur, and H. M. Jaeger. Multiple cotunneling in large quantum dot arrays. *Physical Review Letters*, 95(7):10–13, 2005. 15, 24

[26] T. B. Tran, I. S. Beloborodov, J. Hu, X. M. Lin, T. F. Rosenbaum, and H. M. Jaeger. Sequential tunneling and inelastic cotunneling in nanoparticle arrays. *Physical Review B - Condensed Matter and Material Physics*, 78(7):22–24, 2008. 11, 15, 23, 24, 25, 138

[27] R. Parthasarathy, X. Lin, and H. M. Jaeger. Electronic Transport in Metal Nanocrystal Arrays: The Effect of Structural Disorder on Scaling Behavior. *Physical Review Letters*, 87(18):186807, 2001. 13, 23, 26

[28] D. V. Averin and K. K. Likharev. *Possible Applications of the Single Charge Tunneling*, page 311. Springer US, 1992. 13, 32, 36

[29] N. F. Mott. Electrons in disordered structures. *Advances in Physics*, 16(61):49–144, 1967. 14

[30] A. L. Efros and B. I. Shklovskii. Coulomb gap and low temperature conductivity of disordered systems. *Journal of Physics C: Solid State Physics*, 8(4):1–4, 1975. 15

[31] A. Zabet-Khosousi and A. Dhirani. Charge transport in nanoparticle assemblies. *Chemical Reviews*, 108(10):4072–4124, 2008. 15, 19, 28, 177

[32] D. V. Averin and Y. V. Nazarov. Virtual electron diffusion during quantum tunneling of the electric charge. *Physical Review Letters*, 65(19):2446–2449, 1990. 15, 23, 24

[33] M. Dukic, M. Winhold, C. H. Schwalb, J. D. Adams, V. Stavrov, M. Huth, and G. E. Fantner. Direct-write nanoscale printing of nanogranular tunnelling strain sensors for sub-micrometre cantilevers. *Nature Communications*, 7(12487), 2016. 16

[34] M. Huth. Granular metals: From electronic correlations to strain-sensing applications. *Journal of Applied Physics*, 107:113709, 2010. 17

[35] C. Kittel. *Introduction to Solid State Physics*. John Wiley and Sons, 2004. 18, 82, 91, 121, 173, 176

[36] I. Beloborodov, K. Efetov, A. Lopatin, and V. Vinokur. Transport Properties of Granular Metals at Low Temperatures. *Physical Review Letters*, 91(24):246801, 2003. 18, 19

[37] I. S. Beloborodov, A. V. Lopatin, G. Schwiete, and V. M. Vinokur. Tunneling density of states of granular metals. *Physical Review B - Condensed Matter and Material Physics*, 70(7):2–5, 2004. 19

[38] B. L. Altshuler and A. G. Aronov. Zero bias anomaly in tunnel resistance and electron-electron interaction. *Solid State Communications*, 30(3):115–117, 1979. 19

[39] G. Di Prima, D. Friedl, P. Del Pino, W. Parak, and M. Huth. Electrical studies of nanoparticle arrays contacted by Pt–FEBID deposits. *Abstract for Focused Electron Beam Induced Processes FEBIP2006 Conference*, 2016. 19, 130

[40] E. Katz, I. Willner, and J. Wang. Electroanalytical and bioelectroanalytical systems based on metal and semiconductor nanoparticles. *Electroanalysis*, 16(1–2):19–44, 2004. 20

[41] J. P. Wolfgang, D. Gerion, T. Pellegrino, D. Zanchet, C. Micheel, Williams S. C., Boudreau R., M. A. Le Gros, C. A. Larabell, and A. P. Alivisatos. Biological applications of colloidal nanocrystals. *Nanotechnology*, 14(7):R15–R27, 2003. 20

[42] Y. Suganuma and A. Dhirani. Gating of enhanced electron-charging thresholds in self-assembled nanoparticle films. *The Journal of Physical Chemistry B*, 109(32): 15391–15396, 2005. 20

[43] G. Schmid and B. Corain. Nanoparticulated gold: Syntheses, structures, electronics, and reactivities. *European Journal of Inorganic Chemistry*, 2003(17):3081–3098, 2003. 20

[44] R. P. Andres, J. D. Bielefeld, J. I. Henderson, D. B. Janes, V. R. Kolagunta, C. P. Kubiak, W. J. Mahoney, and R. G. Osifchin. Self-Assembly of a Two-Dimensional Superlattice of Molecularly Linked Metal Clusters. *Science*, 273(5282):1690–1693, 1996. 20

[45] G. B. Khomutov, A. Yu Obydenov, S. A. Yakovenko, E. S. Soldatov, A. S. Trifonov, V. V. Khanin, and S. P. Gubin. Synthesis of nanoparticles in Langmuir monolayer. *Materials Science and Engineering: C*, 8–9:309–318, 1999. 20

[46] M. Brust, D. J. Schiffrin, D. Bethell, and C. J. Kiely. Novel gold-dithiol nano-networks with non-metallic electronic properties. *Advanced Materials*, 7(9):795–797, 1995. 20

[47] J. H. Fendler. Self-assembled nanostructured materials. *Chemistry of Materials*, 8 (8):1616–1624, 1996. 20

[48] M. A. Mangold, A. W. Holleitner, J. S. Agustsson, and M. Calame. *Nanoparticle Arrays*, pages 1–31. Springer International Publishing, 2015. 20

[49] A. A. Middleton and N. S. Wingreen. Collective transport in arrays of small metallic dots. *Physical Review Letters*, 71(19):3198–3201, 1993. 20, 21, 22, 23, 24, 26, 27, 28

[50] A. Zabet-Khosousi, P.-E. Trudeau, Y. Suganuma, A.-A. Dhirani, and B. Statt. Metal to insulator transition in films of molecularly linked gold nanoparticles. *Physical Review Letters*, 96:156403, 2006. 28

[51] G. R. Wang, L. Wang, Q. Rendeng, J. Wang, J. Luo, and C. Zhong. Correlation between nanostructural parameters and conductivity properties for molecularly-mediated thin film assemblies of gold nanoparticles. *Journal of Material Chemistry*, 17:457, 2007. 20, 21

[52] R. H. Terrill, T. A. Postlethwaite, C. Chen, C. Poon, A. Terzis, A. Chen, J. E. Hutchison, M. R. Clark, G. Wignall, J. D. Londono, R. Superfine, M. Falvo, E. T. Samulski, and R. W. Murray. Monolayers in three dimensions: NMR, SAXS, thermal, and electron hopping studies of alkanethiol stabilized gold clusters. *Journal of American Chemical Society*, 117:12537, 1995. 21

[53] W. P. Wuelfing, S. J. Green, J. J. Pietron, D. E. Cliffel, and R. W. Murray. Electronic conductivity of solid-state, mixed-valent, monolayer-protected au clusters. *Journal of American Chemical Society*, 122:11465, 2000. 21

[54] A. S. Cordan, Y. Leroy, A. Goltzené, A. Pépin, C. Vieu, M. Mejias, and H. Launois. Temperature behavior of multiple tunnel junction devices based on disordered dot arrays. *Journal of Applied Physics*, 87(1):345–352, 2000. 21

[55] R. Parthasarathy, X. Lin, K. Elteto, T. F. Rosenbaum, and H. M. Jaeger. Percolating through networks of random thresholds: Finite temperature electron tunneling in metal nanocrystal arrays. *Physical Review Letters*, 92(7):076801, 2004. 21, 23, 24, 26, 138, 139

[56] U. Geigenmüller and G Schön. Single-electron effects in arrays of normal tunnel junctions. *Europhysics Letters*, 10(8):765–770, 1989. 22

[57] K. Elteto, E. G. Antonyan, T. T. Nguyen, and H. M. Jaeger. Model for the onset of transport in systems with distributed thresholds for conduction. *Physical Review B - Condensed Matter and Materials Physics*, 71(6):1–13, 2005. 22, 23, 24, 26, 27, 129, 138

[58] K.H. Müller and M. M. A. Yajadda. Electron transport in discontinuous gold films and the effect of coulomb blockade and percolation. *Journal of Applied Physics*, 111 (12):123705, 2012. 23

[59] F. Ruffino, A. M. Piro, G. Piccitto, and M. G. Grimaldi. Electronic collective transport in disordered array of C_{49}-phase $TiSi_2$ nanocrystals in Si. *Journal of Applied Physics*, 101(2):024316, 2007.

[60] L. Clarke, M. N. Wybourne, L. O. Brown, J. E. Hutchison, M. Yan, S. X. Cai, and J. F. W. Keana. Room-temperature coulomb-blockade-dominated transport in gold nanocluster structures. *Physical Review Letters*, 92(7):076801, 2004. 23

[61] L. J. Geerligs, D. V. Averin, and J. E. Mooij. Observation of macroscopic quantum tunneling through the Coulomb energy barrier. *Physical Review Letters*, 65(24): 3037–3040, 1990. 24

[62] M. G. Ancona, W. Kruppa, R. W. Rendell, A. W. Snow, D. Park, and J. B. Boos. Coulomb blockade in single-layer Au nanocluster films. *Physical Review B*, 64(3): 033408, 2001. 24, 26, 138

[63] H. E. Romero and M. Drndic. Coulomb blockade and hopping conduction in PbSe quantum dots. *Physical Review Letters*, 95(15):156801, 2005. 24

[64] A. Bezryadin, R. M. Westervelt, and M. Tinkham. Self-assembled chains of graphitized carbon nanoparticles. *Applied Physical Letters*, 74(18):2699–2701, 1999. 25, 26

[65] P. E. Trudeau, A. Escorcia, and A. A. Dhirani. Variable single electron charging energies and percolation effects in molecularly linked nanoparticle films. *The Journal of Chemical Physics*, 119(10):5267–5273, 2003. 28

[66] D. J. Wold and C. D. Frisbie. Fabrication and characterization of metal-molecule-metal junctions by conducting probe atomic force microscopy. *Journal of the Americal Chemical Society*, 123(23):5549–5556, 2001. 28

[67] N. J. Tao. Electron transport in molecular junctions. *Nature Nanotechnology*, 1: 173–181, 2006.

[68] S. Datta. Electrical resistance: an atomistic view. *Nanotechnology*, 15(7):S433–S451, 2004.

[69] Y. Xue and M. A. Ratner. Theoretical principles of single-molecule electronics: A chemical and mesoscopic view. *International Journal of Quantum Chemistry*, 102 (5):911–924, 2005. 28

[70] P. Beecher, A. J. Quinn, E. Shevchenko, H. Weller, and G. Redmond. Insulator-to-metal transition in nanocrystal assemblies driven by in situ mild thermal annealing. *Nano Letters*, 4(7):1289–1293, 2004. 28

[71] A. J. Quinn, P. Beecher, D. Iacopino, L. Floyd, G. De Marzi, E. V. Shevchenko, H. Weller, and G. Redmond. Manipulating the charging energy of nanocrystal arrays. *Small*, 1(6):613–618, 2005. 28

[72] Y. Liu, Y. Wang, and R. O. Claus. Layer-by-layer ionic self-assembly of Au colloids into multilayer thin-films with bulk metal conductivity. *Chemical Physics Letters*, 298(4):315–319, 1998. 28

[73] A. Salomon, D. Cahen, S. Lindsay, J. Tomfohr, V. B. Engelkes, and C. D. Frisbie. Comparison of electronic transport measurements on organic molecules. *Advanced Materials*, 15(22):1881–1890, 2003. 29

[74] H. M. McConnell. Intramolecular charge transfer in aromatic free radicals. *The Journal of Chemical Physics*, 35(2):508–515, 1961. 29

[75] A. Nitzan. A relationship between electron-trasfer rate and molecular conduction. *Journal of Physical Chemistry A*, 105(26):2677, 2001. 30

[76] D. M. Adams, L. Brus, C. E. D. Chidsey, S. Creager, C. Creutz, C. R. Kagan, P. V. Kamat, M. Lieberman, S. Lindsay, R. A. Marcus, R. M. Metzger, M. E. Michel-Beyerle, J. R. Miller, M. D. Newton, D. R. Rolison, O. Sankey, K. S. Schanze, J. Yardley, and X. Zhu. Charge transfer on the nanoscale: Current status. *Journal of Physical Chemistry B*, 107(28):6668–6697, 2003. 30

[77] M. P. Samanta, W. Tian, S. Datta, J. I. Henderson, and C. P. Kubiak. Electronic conduction through organic molecules. *Physical Review B*, 53(12):R7626–R7629, 1996. 30, 129

[78] R. Landauer. Spatial variation of currents and fields due to localized scatterers in metallic conduction. *IBM Journal of Research and Development*, 1(3):223–231, 1957. 30, 163

[79] H. W. P. Koops, C. Schossler, A. Kaya, and M. Weber. Conductive dots, wires, and supertips for field electron emitters produced by electron-beam induced deposition on samples having increased temperature. *Journal of Vacuum Science and Technology B: Microelectronics and Nanometer Structures*, 14(6):4105–4109, 1996. 31

[80] Z. M. Liao, J. Xun, and D. P. Yu. Electron transport in an array of platinum quantum dots. *Physics Letters, Section A: General, Atomic and Solid State Physics*, 345(4–6):386–390, 2005. 31

[81] I. Utke, S. Moshkalev, and P. Russell. *Nanofabrication using focused ion and electron beams: principles and applications*. New York: Oxford University Press, 2012. 31, 69, 72, 114

[82] I. Utke, P. Hoffmann, and J. Melngailis. Gas-assisted focused electron beam and ion beam processing and fabrication. *Journal of Vacuum Science and Technology B: Microelectronics and Nanometer Structures*, 26(1197), 2008. 31, 71, 75

[83] J. J. L. Mulders, L. M. Belova, and A. Riazanova. Electron beam induced deposition at elevated temperatures: compositional changes and purity improvement. *Nanotechnology*, 22(5):55302, 2010. 31, 75

[84] G. C. Arena, B. Kleinsorge, F. R. J. Robertson, I. W. Milne, and E. M. Welland. Electronic properties of tetrahedral amorphous carbon investigated by scanning tunneling microscopy. *Journal of Applied Physics*, 85(3):1609–1615, 1999. 31

[85] V. Prasad. Magnetotransport in the amorphous carbon films near the metal-insulator transition. *Solid State Communications*, 145(4):186–191, 2008. 31

[86] H. Grabert and M. H. Devoret. *Single Charge Tunneling*. Springer Netherlands, 1992. 32, 35, 38

[87] Z. A. K. Durrani. *Single-electron devices and circuits in silicon*. Imperial College Press, 01 2009. 32, 34, 38

[88] T. A. Fulton and G. J. Dolan. Observation of single-electron charging effects in small tunnel junctions. *Physical Review Letters*, 59(1):109–112, 1987. 36

[89] A. N. Korotkov, D. V. Averin, and K. K. Likharev. Single-electron charging of the quantum wells and dots. *Physica B: Condensed Matter*, 165–166:927–928, 1990. 36

[90] L. P. Kouwenhoven, C. M. Marcus, P. L. McEuen, S. Tarucha, R. M. Westervelt, and N. S. Wingreen. *Electron Transport in Quantum Dots*, pages 105–214. Springer Netherlands, 1997. 36, 159

[91] Y. Y. Wei, J. Weis, K. v. Klitzing, and K. Eberl. Single-electron transistor as an electrometer measuring chemical potential variations. *Applied Physics Letters*, 71 (17):2514, 1997. 36

[92] R. J. Schoelkopf, P. Wahlgren, A. A. Kozhevnikov, P. Delsing, and D. E. Prober. The Radio-Frequency Single-Electron Transistor (RF-SET): A Fast and Ultrasensitive Electrometer. *Science*, 280(5367):1238, 1998.

[93] V. A. Krupenin, D. E. Presnov, A. B. Zorin, and J. Niemeyer. Aluminium Single Electron Transistors with Islands Isolated from the Substrate. *Journal of Low Temperature Physics*, 287(118), 2000.

[94] P. Lafarge, H. Pothier, E. R. Williams, D. Esteve, C. Urbina, and M. H. Devoret. Direct observation of macroscopic charge quantization. *Physik B - Condensed Matter*, 327(85):327, 1991. 36

[95] S. J. Kim, J. J. Lee, H. J. Kang, J. B. Choi, Y. S. Yu, Y. Takahashi, and D. G. Hasko. One electron-based smallest flexible logic cell. *Applied Physics Letters*, 101 (18):183101, 2012. 36

[96] H. H. Pothier, P. Lafarge, C. Urbina, D. Esteve, and M. H. Devoret. Single-Electron Pump Based on Charging Effects. *Europhysics Letters*, 17(3):249, 1992.

[97] R. L. Kautz, M. W. Keller, and J. M. Martinis. Leakage and counting errors in a seven-junction electron pump. *Physical Review B*, 60(11):8199, 1999.

[98] L. Guo, E. Leobandung, and S. Y. Chou. A room-temperature silicon single-electron metal–oxide–semiconductor memory with nanoscale floating-gate and ultranarrow channel. *Applied Physics Letters*, 70(7):850, 1997.

[99] S. Tiwari, F. Rana, H. Hanafi, A. Hartstein, E. F. Crabbé, and K. Chan. A silicon nanocrystals based memory. *Applied Physics Letters*, 68(10):1377, 1996.

[100] L. P. Kouwenhoven. Quantized current in a quantum dot turnstile. *Physica Scripta*, 1992(T42):133, 1992.

[101] M. H. Devoret and R. J. Schoelkopf. Amplifying quantum signals with the single-electron transistor. *Nature*, 406(6799):1039, 2000.

[102] K. Maeda, N. Okabayashi, S. Kano, S. Takeshita, D. Tanaka, M. Sakamoto, T. Teranishi, and Y. Majima. Logic Operations of Chemically Assembled Single-Electron Transistor. *ACS Nano*, 6(3):2798–2803, 2012.

[103] L. Zhuang, L. Guo, and S. Y. Chou. Silicon single-electron quantum-dot transistor switch operating at room temperature. *Applied Physics Letters*, 72(10):1205, 1998. 36

[104] P. S. K. Karre, M. Acharya, W. R. Knudsen, and P. L. Bergstrom. Single Electron Transistor-Based Gas Sensing With Tungsten Nanoparticles at Room Temperature. *IEEE Sensors Journal*, 8(6):797, 2008. 36

[105] B. Jain, K. Vinod Kumar, B. Santhi Bhushan, K. Gaurav, M. Pattanaik, and A. Srivastava. A tetracene-based single-electron transistor as a chlorine sensor. *Journal of Computational Electronics*, 17(4):1515, 2018. 36

[106] J. J. Henderson, C. M. Ramsey, E. Del Barco, A. Mishra, and G. Christou. Fabrication of nanogapped single-electron transistors for transport studies of individual single-molecule magnets. *Journal of Applied Physics*, 9(101):E102, 2007. 36

[107] W. Liang, M. P. Shores, M. Bockrath, J. R. Long, and H. Park. Kondo resonance in a single-molecule transistor. *Nature*, 417(6890):725, 2002. 36

[108] J. Weis. *Single-Electron Devices*, pages 87–121. Springer Berlin Heidelberg, 2005. 42

[109] H. J. Levinson. *Principles of Lithography*. SPIE Press, 2005. 48

[110] Ar-U Negative Photoresists. *Positive and Negative Photoresists AR-U 4000, image reversal resist series*. ALLRESIST, 2016. 50

[111] D. M. Mattox. Physical Sputtering and Sputter Deposition. In *Handbook of Physical Vapor Deposition (PVD) Processing*, pages 343–405. William Andrew Publishing, 1998. 51

[112] K. Wasa, M. Kitabatake, and H. Adachi. *Thin Film Materials Technology*. William Andrew Publishing, 2004.

[113] P. J. Kelly and R. D. Arnell. Magnetron sputtering: A review of recent developments and applications. *Vacuum*, 56(3), 2000. 51, 52

[114] M. A. Lieberman and J. A. Lichtenberg. *Principles of Plasma Discharges and Materials Processing: Second Edition*, volume 30. Hoboken, N.J.: Wiley-Interscience, 09 2003. 51

[115] Sterling Sensors. RTD Sensors including Pt100 and Pt1000 Elements (PRT). *RTD Sensor (Pt100, Pt1000)*, 1:1–10, 2019. 55

[116] Manfred von Ardenne. Das elektronen-rastermikroskop. *Zeitschrift für Physik*, 109 (9):553–572, 1938. 57

[117] J. I. Goldstein, D. E. Newbury, P. Echlin, D. C. Joy, A. D. Romig, C. E. Lyman, C. Fiori, and E. Lifshin. *Scanning Electron Microscopy and X-Ray Microanalysis*. Springer, Boston, MA, 1992. 57, 65

[118] J. Orloff. *Handbook of Charged Particle Optics*. CRC Press Inc, Taylor and Francis Group, 2008. 57

[119] C. Benvenuti. Molecular surface pumping: the getter pumps. *CERN Accelerator School on Vacuum Technology*, 1, 1999. 57

[120] J. I. Goldstein, D. E. Newbury, Joseph R. Michael, Nicholas W. M. Ritchie, John Henry J. Scott, and David C. Joy. *Electron Beam–Specimen Interactions: Interaction Volume*, pages 1–14. Springer New York, 2018. 59

[121] L. Reimer. *Scanning Electron Microscopy*. Springer-Verlag, Berlin, 1998. 59, 61

[122] K. Kanaya and S. Okayama. Penetration and energy-loss theory of electrons in solid targets. *Journal of Physics D Applied Physics*, 5:43–58, 1972. 59

[123] D. A. Moncrieff and P. R. Barker. Secondary electron emission in the scanning electron microscope. *Scanning*, 1(3):195–197, 1978. 60

[124] A. Suri, A. Pratt, S. Tear, C. Walker, C. Kincal, U. Kamber, O. Gurlu, and M. El-Gomati. Analysis and detection of low-energy electrons in scanning electron microscopes using a bessel box electron energy analyser. *Journal of Electron Spectroscopy and Related Phenomena*, 241:146823, 2020. 60

[125] D. Drouin, A. R. Couture, D. Joly, X Tastet, V. Aimez, and R. Gauvin. CASINO V2.42: a fast and easy-to-use modeling tool for scanning electron microscopy and microanalysis users. *Scanning*, 3(29):92–101, 2007. 62

[126] H. G. J. Moseley. The High-Frequency Spectra of the Elements. *The London, Edinburgh and Dublin Philosophical Magazine and Journal of Science*, 26(6):1024–1034, 1913. 66

[127] EDAX. *EDAX EDS Manual*. EDAX Press, 2012. 66

[128] Y. Seo and W. Jhe. Atomic force microscopy and spectroscopy. *Reports on Progress in Physics*, 71, 2008. 66

[129] Nanosurf. *Nanosurf Easyscan 2 Manual*. Nanosurf Press, 2010. 68

[130] W. F. Van Dorp and C. W. Hagen. A critical literature review of focused electron beam induced deposition. *Journal of Applied Physics*, 104(8):1–42, 2008. 69, 71, 72, 182

[131] W. F. Van Dorp, B. Van Someren, C. W. Hagen, P. Kruit, and P. A. Crozier. Approaching the resolution limit of nanometer-scale electron beam-induced deposition. *Nano Letters*, 5(7):1303–1307, 2005. 69, 77

[132] W. F. Van Dorp, X. Zhang, B. L. Feringa, T. W. Hansen, J. B. Wagner, and J. T. M. De Hosson. Molecule-by-molecule writing using a focused electron beam. *ACS Nano*, 6(11):10076–10081, 2012.

[133] M. Tanaka, M. Shimojo, M. Han, K. Mitsuishi, and K. Furuya. Ultimate sized nano-dots formed by electron beam-induced deposition using an ultrahigh vacuum transmission electron microscope. *Surface and Interface Analysis*, 37(2):261–264, 2005. 69

[134] L. van Kouwen, A. Botman, and C. W. Hagen. Focused electron-beam-induced deposition of 3 nm dots in a scanning electron microscope. *Nano Letters*, 5(9):2149, 2009. 69

[135] J. C. van Oven, F. Berwald, K. K. Berggren, P. Kruit, and C. W. Hagen. Electron-beam-induced deposition of 3-nm-half-pitch patterns on bulk Si. *Journal of Vacuum Science and Technology B, Nanotechnology and Microelectronics: Materials, Processing, Measurement, and Phenomena*, 29(6):06F305, 2011. 69, 77

[136] M. Winhold, C. H. Schwalb, F. Porrati, R. Sachser, A. S. Frangakis, B. Kämpken, A. Terfort, N. Auner, and M. Huth. Binary Pt-Si nanostructures prepared by focused electron-beam-induced deposition. *ACS Nano*, 5(12):9675–9681, 2011. 69

[137] F. Porrati, E. Begun, M. Winhold, C. H. Schwalb, R. Sachser, A. S. Frangakis, and M. Huth. Room temperature L_{10} phase transformation in binary copt nanostructures prepared by focused-electron-beam-induced deposition. *Nanotechnology*, 23(18):185702, 2012.

[138] F. Porrati, B. Kämpke, A. Terfort, and M. Huth. Fabrication and electrical transport properties of binary Co-Si nanostructures prepared by focused electron beam-induced deposition. *Journal of Applied Physics*, 053707(113), 2013.

[139] F. Porrati, M. Pohlit, J. Müller, S. Barth, F. Biegger, C. Gspan, H. Plank, and M. Huth. Direct writing of CoFe alloy nanostructures by focused electron beam induced deposition from a heteronuclear precursor. *Nanotechnology*, 26(47):475701, 2015. 69, 182, 183, 185

[140] N. Silvis-Cividjian. *Electron Beam Induced Nanometer Scale Deposition*. PhD thesis, Universitatea din Craiova, 2002. 69

[141] C. T. H. Heerkens, M. J. Kamerbeek, W. F. van Dorp, C. W. Hagen, and J. Hoekstra. Electron beam induced deposited etch masks. *Microelectronic Engineering*, 86(4-6):961–964, 2009. 69

[142] M. G. Lassiter, T. Liang, and P. D. Rack. Inhibiting spontaneous etching of nanoscale electron beam induced etching features: Solutions for nanoscale repair of extreme ultraviolet masks. *Journal of Vacuum Science and Technology B: Microelectronics and Nanometer Structures*, 26(3):963–967, 2008. 69

[143] T. Liang, E. Frendberg, B. Lieberman, and A. Stivers. Advanced photolithographic mask repair using electron beams. *Journal of Vacuum Science and Technology B: Microelectronics and Nanometer Structures*, 23(6):3101, 2005. 69

[144] K. Edinger, H. Becht, J. Bihr, V. Boegli, M. Budach, T. Hofmann, W.P. Koops, P. Kuschnerus, J. Oster, P. Spies, and B. Weyrauch. Electron-beam-based photomask repair. *Journal of Vacuum Science Technology B: Microelectronics and Nanometer Structures*, 22(6):2902–2906, 2004. 69

[145] S. Kasap and P. Capper. *Springer Handbook of Electronic and Photonic Materials*. Prentice Hall, Upper Saddle River, 2007. 69

[146] J. F. Waters, L. Riester, M. Jouzi, P. R. Guduru, and J. M. Xu. Buckling instabilities in multiwalled carbon nanotubes under uniaxial compression. *Applied Physics Letters*, 85(10):1787–1789, 2004. 69

[147] A. Perentes, A. Bachmann, M. Leutenegger, I. Utke, C. Sandu, and P. Hoffmann. Focused electron beam induced deposition of a periodic transparent nano-optic pattern. *Microelectronic Engineering*, 73-74:412–416, 2004. 69

[148] I. Utke, M. G Jenke, C. Rooooling, P. H. Thiesen, V. Iakovlev, A. Sirbu, A. Mereuta, A. Caliman, and E. Kapon. Polarisation stabilisation of vertical cavity surface emitting lasers by minimally invasive focused electron beam triggered chemistry. *Nanoscale*, 3(7):2718–2722, 2011.

[149] R. Winkler, F. Schmidt, U. Haselmann, J. D. Fowlkes, and B. B. Lewis. Direct-Write 3D Nanoprinting of Plasmonic Structures. *ACS Applied Materials and and Interfaces*, 9(9):8233, 2016. 69

[150] M. Gavagnin, H. D Wanzenboeck, D. Belić, and E. Bertagnolli. Synthesis of individually tuned nanomagnets for nanomagnet logic by direct write focused electron beam induced deposition. *ACS Nano*, 7(1):777–784, 2013. 69

[151] L. Serrano-Ramón, R. Cordóba, L. A. Rodríguez, C. Magén, E. Snoeck, C. Gatel, I. Serrano, M. R. Ibarra, and J. M. De Teresa. Ultrasmall functional ferromagnetic nanostructures grown by focused electron-beam-induced deposition. *ACS Nano*, 5 (10):7781–7787, 2011.

[152] M. S. Gabureac, L. Bernau, G. Boero, and I. Utke. Single superparamagnetic bead detection and direct tracing of bead position using novel nanocomposite nano-hall sensors. *IEEE Transactions on Nanotechnology*, 12(5):668–673, 2013.

[153] L. Keller and M. Huth. Pattern generation for direct-write three-dimensional nanoscale structures via focused electron beam induced deposition. *Beilstein Journal of Nanotechnology*, 9:2581, 2018. 69, 185

[154] I. Utke, P. Hoffmann, R. Berger, and L. Scandella. High-resolution magnetic Co supertips grown by a focused electron beam. *Applied Physics Letters*, 80(25):4792–4794, 2002. 69

[155] K. Edinger, T. Gotszalk, and I. W. Rangelow. Novel high resolution scanning thermal probe. *Journal of Vacuum Science and Technology B: Microelectronics and Nanometer Structures Processing, Measurement, and Phenomena*, 19(6):2856–2860, 2001. 69

[156] S. Sengupta, C. Li, C. Baumier, A. Kasumov, S. Gueeeron, H. Bouchiat, and F. Fortuna. Superconducting nanowires by electron-beam-induced deposition. *Applied Physics Letters*, 106(4):042601, 2015. 69

[157] M. Winhold, P. M. Weirich, C. H. Schwalb, and M. Huth. Superconductivity and metallic behavior in $Pb_xC_yO_\delta$ structures prepared by focused electron beam induced deposition. *Applied Physics Letters*, 105(16):162603, 2014. 69, 102

[158] A. J. M. Mackus, J. J. L. Mulders, M. C. M. van de Sanden, and W. M. M. Kessels. Local deposition of high-purity Pt nanostructures by combining electron beam induced deposition and atomic layer deposition. *Journal of Applied Physics*, 107(11):21–23, 2010. 69, 84, 92

[159] C. H. Schwalb, C. Grimm, M. Baranowski, R. Sachser, F. Porrati, H. Reith, P. Das, J. Muuuuller, F. Vooolklein, A. Kaya, and M. Huth. A tunable strain sensor using nanogranular metals. *Sensors*, 10(11):9847, 2010. 69, 79

[160] M. Moczala, K. Kwoka, T. Piasecki, P. Kunicki, A. Sierakowski, and T. Gotszalk. Fabrication and characterization of micromechanical bridges with strain sensors deposited using focused electron beam induced technology. *Microelectronic Engineering*, 176:111, 2017. 69

[161] F. Kolb, K. Schmoltner, M. Huth, A. Hohenau, J. Krenn, A. Klug, E. J. W. List, and H. Plank. Variable tunneling barriers in FEBID based PtC metal-matrix nanocomposites as a transducing element for humidity sensing. *Nanotechnology*, 24 (30), 2013. 69

[162] M. Huth, F. Kolb, and H. Plank. Dielectric sensing by charging energy modulation in a nano-granular metal. *Applied Physics A: Materials Science and Processing*, 117 (4):1689–1696, 2014. 69

[163] I. Utke, V. Friedli, M. Purrucker, and J. Michler. Resolution in focused electron- and ion-beam induced processing. *Journal of Vacuum Science and Technology B: Microelectronics and Nanometer Structures Processing, Measurement, and Phenomena*, 25(6):2219–2223, 2007. 70, 72, 76

[164] R. M. Thorman, T. P. Ragesh Kumar, D. Howard Fairbrother, and O. Ingooolfsson. The role of low-energy electrons in focused electron beam induced deposition: Four case studies of representative precursors. *Beilstein Journal of Nanotechnology*, 6(1): 1904–1926, 2015. 71, 72

[165] N. Silvis-Cividjian, C. W. Hagen, and P. Kruit. Spatial resolution limits in electron-beam-induced deposition. *Journal of Applied Physics*, 98(8):1–12, 2005.

[166] D. a Smith, J. D. Fowlkes, and P. D. Rack. A nanoscale three-dimensional Monte Carlo simulation of electron-beam-induced deposition with gas dynamics. *Nanotechnology*, 18(26):265308, 2007. 76

[167] J. D. Fowlkes, S. J. Randolph, and P. D. Rack. Growth and simulation of high-aspect ratio nanopillars by primary and secondary electron-induced deposition. *Journal of Vacuum Science and Technology B: Microelectronics and Nanometer Structures Processing, Measurement, and Phenomena*, 23(6):2825, 2005. 76

[168] K. T. Kohlmann von Platen, J. Chlebek, M. Weiss, K. Reimer, H. Oertel, and W. H. Brünger. Resolution limits in electron-beam induced tungsten deposition. *Journal of Vacuum Science and Technology B: Microelectronics and Nanometer Structures Processing, Measurement, and Phenomena*, 11(6):2219–2223, 1993.

[169] N. Silvis-Cividjian, C. W. Hagen, L. H. A. Leunissen, and P. Kruit. The role of secondary electrons in electron-beam-induced-deposition spatial resolution. *Microelectronics Engineering*, 61-62:693–699, 2002. 72

[170] T. E. Allen. Monte Carlo calculation of low-energy electron emission from surfaces. *Journal of Vacuum Science and Technology B: Microelectronics and Nanometer Structures Processing, Measurement, and Phenomena*, 6(1988):2057, 1988. 72

[171] E. Bohler, J. Warneke, and P. Swiderek. Control of chemical reactions and synthesis by low-energy electrons. *Chemical Society reviews*, 42(24):9219–31, 2013. 72, 73

[172] W. F. Van Dorp, J. D. Wnuk, J. M. Gorham, D. H. Fairbrother, T. E. Madey, and C. W. Hagen. Electron induced dissociation of trimethyl (methylcyclopentadienyl) platinum(IV): Total cross section as a function of incident electron energy. *Journal of Applied Physics*, 106(7):1–9, 2009. 72, 76

[173] R. Winkler, A. Szkudlarek, J. D. Fowlkes, P. D. Rack, I. Utke, and H. Plank. Toward ultraflat surface morphologies during focused electron beam induced nanosynthesis: Disruption origins and compensation. *ACS Applied Materials and Interfaces*, 7(5): 3289–3297, 2015. 73

[174] M. Winhold, P. M. Weirich, C. H. Schwalb, and M. Huth. Identifying the crossover between growth regimes via in-situ conductance measurements in focused electron beam induced deposition. *Nanofabrication*, 1(1):86–95, 2014. 73, 102

[175] G. Arnold, R. Timilsina, J. D. Fowlkes, A. Orthacker, G. Kothleitner, P. D. Rack, and H. Plank. Fundamental resolution limits during electron induced direct write synthesis. *ACS Applied Materials and Interfaces*, 6:7380–7387, 2014. 73, 74, 77

[176] R. Schmied, J. D. Fowlkes, R. Winkler, P. D. Rack, and H. Plank. Fundamental edge broadening effects during focused electron beam induced nanosynthesis. *Beilstein Journal of Nanotechnology*, 6(1):462–471, 2015. 73, 76, 77, 78

[177] Jmol. An open-source java viewer for chemical structures in 3d. *http://www.jmol.org/*, 2016. 75

[178] C. Thurier and P. Doppelt. Platinum OMCVD processes and precursor chemistry. *Coordination Chemistry Reviews*, 252(1-2):155–169, 2008. 75

[179] T. Aaltonen, M. Ritala, T. Sajavaara, J. Keinonen, and M. Leskelä. Atomic layer deposition of platinum thin films. *Chemistry of Materials*, 15(9):1924–1928, 2003. 75, 84, 87

[180] Z. Xue, M. J. Strouse, D. K. Shuh, C. B. Knobler, H. D. Kaesz, R. F. Hicks, and R. S. Williams. Characterization of (methylcyclopentadienyl)trimethylplatinum and low-temperature organometallic chemical vapor deposition of platinum metal. *Journal of the American Chemical Society*, 111(24):8779, 1989. 75

[181] G. Spessard. *Organometallic chemistry*. Prentice Hall, Upper Saddle River, 1997. 75

[182] J. D. Wnuk, J. M. Gorham, S. G. Rosenberg, W. F. Van Dorp, T. E. Madey, C. W. Hagen, and D. H. Fairbrother. Electron induced surface reactions of the organometallic precursor trimethyl(methylcyclopentadienyl)platinum(IV). *Journal of Physical Chemistry C*, 113(6):2487–2496, 2009. 75, 76

[183] S. Engmann, M. Stano, S. Matejčík, and O. Ingólfsson. Gas phase low energy electron induced decomposition of the focused electron beam induced deposition (FEBID) precursor trimethyl (methylcyclopentadienyl) platinum(IV) ($MeCpPtMe_3$). *Physical Chemistry Chemical Physics*, 14(42):14611–14618, 2012. 75

[184] A. Botman, D. A. M. de Winter, and J. J. L. Mulders. Electron-beam-induced deposition of platinum at low landing energies. *Journal of Vacuum Science and Technology B: Microelectronics and Nanometer Structures*, 26(6):2460, 2008. 76

[185] D. Beaulieu, Y. Ding, Z. L. Wang, and W. J. Lackey. Influence of process variables on electron beam chemical vapor deposition of platinum. *Journal of Vacuum Science and Technology B: Microelectronics and Nanometer Structures*, 23(5):2151–2159, 2005. 76

[186] H. Plank, C. Gspan, M. Dienstleder, G. Kothleitner, and F. Hofer. The influence of beam defocus on volume growth rates for electron beam induced platinum deposition. *Nanotechnology*, 19(48):485302, 2008. 76

[187] A. Botman, M. Hesselberth, and J. J. L. Mulders. Improving the conductivity of platinum-containing nano-structures created by electron-beam-induced deposition. *Microelectronic Engineering*, 85(5-6):1139–1142, 2008. 76, 78

[188] J. R. V. Garcia and T. Goto. Chemical Vapor Deposition of Iridium , Platinum , Rhodium and Palladium. *Materials Transactions*, 44(9), 2003. 76

[189] S. G. Rosenberg, K. Landheer, C. W. Hagen, and D. H. Fairbrother. Substrate temperature and electron fluence effects on metallic films created by electron beam induced deposition. *Journal of Vacuum Science and Technology B: Microelectronics and Nanometer Structures*, 30(2012):051805, 2012. ISSN 21662746. 77

[190] H. Plank, D. A. Smith, T. Haber, P. D. Rack, and F. Hofer. Fundamental proximity effects in focused electron beam induced deposition. *ACS Nano*, 6(1):286–294, 2012. 77

[191] P. A. Crozier. Proximity effects in nanoscale patterning with high resolution electron beam induced deposition. *Journal of Vacuum Science and Technology B: Microelectronics and Nanometer Structures Processing, Measurement, and Phenomena*, 26(1):249, 2008. 77

[192] T. Bret, I. Utke, P. Hoffmann, M. Abourida, and P. Doppelt. Electron range effects in focused electron beam induced deposition of 3D nanostructures. *Microelectronics Engineering*, 83(4-9 SPEC. ISS.):1482–1486, 2006. 77

[193] K. Kanaya, S. Ono, F. Ishigaki, K. Kanaya, H. Kawakatsu, and K. Kanaya. The energy dependence of secondary emission based on the range-energy retardation power formula. *Journal of Physics D: Applied Physics*, 1979. 77

[194] N. Silvis-Cividjian, C. W. Hagen, P. Kruit, M. A. J. v.d. Stam, and H. B. Groen. Direct fabrication of nanowires in an electron microscope. *Applied Physics Letters*, 82(20):3514–3516, 2003. 78

[195] M. G. Stanford, B. B. Lewis, J. H. Noh, J. D. Fowlkes, N. A. Roberts, H. Plank, and P. D. Rack. Purification of Nanoscale Electron-Beam-Induced Platinum Deposits via a Pulsed Laser-Induced Oxidation Reaction. *ACS Applied Materials and Interfaces*, 6(23):21256, 2014. 79

[196] H. Plank, G. Kothleitner, F. Hofer, S. G. Michelitsch, C. Gspan, A. Hohenau, and J. Krenn. Optimization of postgrowth electron-beam curing for focused electron-beam-induced Pt deposits. *Journal of Vacuum Science and Technology B: Microelectronics and Nanometer Structures*, 29(5):051801, 2011. 79

[197] S. Frabboni, G. C. Gazzadi, L. Felisari, and A. Spessot. Fabrication by electron beam induced deposition and transmission electron microscopic characterization of sub-10-nm freestanding Pt nanowires. *Applied Physics Letters*, 88(21):213116, 2006. 79, 80

[198] A. Botman, J. J. L. Mulders, R. Weemaes, and S. Mentink. Purification of platinum and gold structures after electron-beam-induced deposition. *Nanotechnology*, 17(15): 3779–3785, 2006. 79

[199] M. Shimojo, M. Takeguchi, K. Mitsuishi, M. Tanaka, and K. Furuya. Formation of nanoscale platinum and iron oxide structures using electron beam induced deposition techniques. *Journal of Physics, Conference Series*, 100(5):052016, 2008. ISSN 1742-6596. 79

[200] S. Mehendale, J. J. L. Mulders, and P. H. F. Trompenaars. A new sequential EBID process for the creation of pure Pt structures from $MeCpPtMe_3$. *Nanotechnology*, 24(14):145303, 2013. 79, 96

[201] Z. Warneke, M. Rohdenburg, J. Warneke, J. Kopyra, and P. Swiderek. Electron-driven and thermal chemistry during water-assisted purification of platinum nanomaterials generated by electron beam induced deposition. *Beilstein Journal of Nanotechnology*, 9(1):77–90, 2018. 79

[202] M. J. Perez-Roldan, J. J. L. Mulders, and P. H. F. Trompenaars. Oxygen-assisted purification of platinum structures deposited by ion and electron beam induced processes. *Journal of Physics D: Applied Physics*, 50(20):205307, 2017. 79

[203] B. B. Lewis, R. Winkler, X. Sang, P. R. Pudasaini, M. G. Stanford, H. Plank, R. R. Unocic, J. D. Fowlkes, and P. D. Rack. 3D Nanoprinting via laser-assisted electron beam induced deposition: Growth kinetics, enhanced purity, and electrical resistivity. *Beilstein Journal of Nanotechnology*, 8(1):83, 2017. 79

[204] A. Möbius. Comment on Critical behavior of the zero-temperature conductivity in compensated silicon, Si:(P,B). *Physical Review B - Condensed Matter and Materials Physics*, 40(6):4194–4195, 1989. 79

[205] L. Reimer and H. Kohl. *Transmission Electron Microscopy*. Springer, Berlin, 2008. 79

[206] E. Smith and G. Dent. *Modern Raman Spectroscopy - A Practical Approach*. John Wiley and Sons, Ltd, 2005. 79

[207] A. C. Ferrari and J. Robertson. Interpretation of Raman spectra of disordered and amorphous carbon. *Physical Review B*, 61(20):95–107, 2000. 79

[208] I. Utke, J. Michler, P. Gasser, C. Santschi, D. Laub, M. Cantoni, P. Buffat, C. Jiao, and P. Hoffmann. Cross section investigations of compositions and sub-structures of tips obtained by focused electron beam induced deposition. *Adv. Eng. Mater.*, 7 (5):323–331, 2005. 80

[209] S. J. Randolph, J. D. Fowlkes, and P. D. Rack. Effects of heat generation during electron-beam-induced deposition of nanostructures. *Journal of Applied Physics*, 97 (12):1–8, 2005. 80

[210] F. Banhart. Irradiation effects in carbon nanostructures. *Reports on Progress in Physics*, 62(8):1181, 1999. 80

[211] L. Keller. Charakterisierung kooperativer Transportphänomene an den mittels FEBID präparierten inhomogenen Systemen FeSi und WGa. Master's thesis, Johann Wolfgang Goethe Universät in Frankfurt am Main, 2014. 82

[212] M. Ishigami, J. H. Chen, W. G. Cullen, M. S. Fuhrer, and E. D. Williams. Atomic structure of graphene on SiO_2. *Nano Letters*, 7(6):1643–1648, 2007. 83

[213] S. Kumar, N. Peltekis, K. Lee, H. Kim, and G. S. Duesberg. Reliable processing of graphene using metal etchmasks. *Nanoscale Research Letters*, 6(1):390, 2011.

[214] J. Fan, J. M. Michalik, L. Casado, S. Roddaro, M. R. Ibarra, and J. M. De Teresa. Investigation of the influence on graphene by using electron-beam and photo-lithography. *Solid State Communications*, 151(21):1574–1578, 2011. 83

[215] S. M. George. Atomic layer deposition: An overview. *Chemical Reviews*, 110(1): 111–131, 2010. 83, 92

[216] H. C. M. Knoops, A. J. M. Mackus, M. E. Donders, M. C. M. van de Sanden, P. H. L. Notten, and W. M. M. Kessels. Remote Plasma ALD of Platinum and Platinum Oxide Films. *Electrochemical and Solid-State Letters*, 12(7):G34, 2009. 84, 90, 91, 92

[217] M. J. Biercuk, D. J. Monsma, C. M. Marcus, J. S. Becker, and R. G. Gordon. Low-temperature atomic-layer-deposition lift-off method for microelectronic and nanoelectronic applications. *Applied Physics Letters*, 83(12):2405–2407, 2003. 84

[218] R. Chen, H. Kim, P. C. McIntyre, D. W. Porter, and S. F. Bent. Achieving area-selective atomic layer deposition on patterned substrates by selective surface modification. *Applied Physics Letters*, 86(19):191910, 2005. 84

[219] A. J. M. Mackus, W. M. M. Kessels, and J. J. L. Mulders. Selective in-situ atomic layer deposition on structures created with EBID. *Microscopy and Analysis*, 25(4): 5, 2011. 84, 92

[220] A. J. M. Mackus, S. A. F. Dielissen, J. J. L. Mulders, and W. M. M. Kessels. Nanopatterning by direct-write atomic layer deposition. *Nanoscale*, 4(15):4477, 2012. 91, 108

[221] A. J. M. Mackus, N. F. W. Thissen, J. J. L. Mulders, P. H. F. Trompenaars, M. A. Verheijen, A. A. Bol, and W. M. M. Kessels. Direct-write atomic layer deposition of high-quality Pt nanostructures: Selective growth conditions and seed layer requirements. *Journal of Physical Chemistry C*, 117(20):10788–10798, 2013. 84, 92, 93, 94

[222] V. Friedli. *Focused electron- and ion-beam induced processes: In situ monitoring, analysis and modeling*. PhD thesis, Ecole Polytechnique Fédérale de Lausanne, Switzerland, 2008. 86, 95

[223] Blender. The free and open source 3D creation suite. *http://www.blender.org/*, 2016. 86

[224] S. Ding, H. Chen, X. Cui, S. Chen, Q. Sun, P. Zhou, H. Lu, D. W. Zhang, and S. Shen. Atomic layer deposition of high-density Pt nanodots on Al_2O_3 film using $MeCpPtMe_3$ and O_2 precursors for nonvolatile memory applications. *Nanoscale Research Letters*, 8(1):1, 2013. 87

[225] W. M. M. Kessels, H. C. M. Knoops, S. A. F. Dielissen, A. J. M. Mackus, and M. C. M. van de Sanden. Surface reactions during atomic layer deposition of Pt derived from gas phase infrared spectroscopy. *Applied Physics Letters*, 95(1):013114, 2009. 88

[226] S. T. Christensen, J. W. Elam, F. A. Rabuffetti, Q. Ma, S. J. Weigand, B. Lee, S. Seifert, P. C. Stair, K. R. Poeppelmeier, M. C. Hersam, and M. J. Bedzyk. Controlled growth of platinum nanoparticles on strontium titanate nanocubes by atomic layer deposition. *Small*, 5(6):750–757, 2009. 107

[227] S. D. Elliott. Mechanism, products, and growth rate of atomic layer deposition of noble metals. *Langmuir*, 26(12):9179–9182, 2010. 107

[228] T. J. Larrabee, T. E. Mallouk, and D. L. Allara. An atomic layer deposition reactor with dose quantification for precursor adsorption and reactivity studies. *Review of Scientific Instruments*, 84(1), 2013. 87

[229] P. Shrestha, D. Gub, N. Tranc, K. Tapilyd, H. Baumgarte, and G. Namkoong. Investigation of Volmer-Weber Growth during the Nucleation Phase of ALD Platinum Thin Films and Template Based Platinum Nanotubes. *ECS Transactions*, 33(2):127–134, 2010. 90

[230] W. M. M. Kessels, H. C. M. Knoops, S. A. F. Dielissen, A. J. M. Mackus, and M. C. M. van de Sanden. Surface reactions during atomic layer deposition of Pt derived from gas phase infrared spectroscopy. *Applied Physics Letters*, 95(1):1–4, 2009. ISSN 00036951. 92, 107, 108

[231] C. T. Campbell. Ultrathin metal films and particles on oxide surfaces: structural, electronic and chemisorptive properties. *Surface Science Reports*, 27(1-3):1–111, 1997. 92

[232] W. Setthapun, W. D. Williams, S. M. Kim, H. Feng, J. W. Elam, F. A Rabuffetti, K. R. Poeppelmeier, P. C. Stair, E. A. Stach, F. H. Ribeiro, J. T. Miller, and C. L. Marshall. Genesis and evolution of surface species during Pt atomic layer deposition on oxide supports characterized by in situ XAFS analysis and water-gas shift reaction. *Journal of Physical Chemistry C*, 114(21):9758–9771, 2010. 92

[233] J. W. Clancey, A. S. Cavanagh, R. S. Kukreja, A. Kongkanand, and S. M. George. Atomic layer deposition of ultrathin platinum films on tungsten atomic layer deposition adhesion layers: Application to high surface area substrates. *Journal of Vacuum Science Technology A*, 33(1):A130, 2015. 92

[234] J. A. Floro, E. Chason, R. C. Cammarata, and D. J. Srolovitz. Physical origins of intrinsic stresses in volmer-weber thin films. *MRS Bulletin*, 27(1):19–25, 2002. 92

[235] I. J. M. Erkens, A. J. M. Mackus, H. C. M. Knoops, P. Smits, T. H. M. van de Ven, F. Roozeboom, and W. M. M. Kessels. Mass Spectrometry Study of the Temperature Dependence of Pt Film Growth by Atomic Layer Deposition. *Ecs Journal of Solid State Science and Technology*, 1(6):255–262, 2012. 92

[236] A. J. M. Mackus, M. A. Verheijen, N. Leick, A. A. Bol, and W. M. M. Kessels. Influence of oxygen exposure on the nucleation of platinum atomic layer deposition: Consequences for film growth, nanopatterning, and nanoparticle synthesis. *Chemistry of Materials*, 25(9):1905–1911, 2013. 92

[237] HDMS YES. Yes HDMS Vapor Prime Process Application Note. *Process Solutions, Equipment and Services*, pages 1–6, 2016. 96

[238] H. Makino, S. Kishimoto, T. Yamada, A. Miyake, N. Yamamoto, and T. Yamamoto. Effects of surface pretreatment on growth of ZnO on glass substrate. *Physica Status Solidi A*, 205(8):1971–1974, 2008. 96

[239] J. J. L. Mulders, J. M. Veerhoek, E. G. T. Bosch, and P. H. F. Trompenaars. Fabrication of pure gold nanostructures by electron beam induced deposition with Au(CO)Cl precursor: deposition characteristics and primary beam scattering effects. *Journal of Physics D: Applied Physics*, 45(47):475301, 2012. 96

[240] B. J. van Wees, H. van Houten, C. W. J. Beenakker, J. G. Williamson, L. P. Kouwenhoven, D. van der Marel, and C. T. Foxon. Quantized conductance of point contacts in a two-dimensional electron gas. *Physical Review Letters*, 60(9):848–850, Feb 1988. 100

[241] Pr. Dr. Michael Huth. Thin Films and Nanostructures Laboratories, Goethe Universität, Frankfurt am Main. *http://nano.physik.uni-frankfurt.de/*, 2021. 101

[242] R. Zhao, Y. Gao, Z. Guo, Y. Su, and X. Wang. Interface energy alignment of atomic-layer-deposited VO_x on pentacene: an in situ photoelectron spectroscopy investigation. *ACS Applied Materials and Interfaces*, 9(2):1885–1890, 2017. 102

[243] S. B. S. Heil, E. Langereis, A. Kemmeren, F. Roozeboom, M .C. M. van de Sanden, and W. M. M. Kessels. Plasma-assisted atomic layer deposition of TiN monitored by in situ spectroscopic ellipsometry. *Journal of Vacuum Science and Technology A*, 23(4):L5–L8, 2017. 102

[244] E. Langereis, S. B. S. Heil, H. C. M. Knoops, W. Keuning, M. C. M. van de Sanden, and W. M. M. Kessels. In situ spectroscopic ellipsometry as a versatile tool for studying atomic layer deposition. *Journal of Physics D Applied Physics*, 42(7): 73001, 2009.

[245] N. Leick, J. W. Weber, A. J. M. Mackus, M. J. Weber, M. C. M. van de Sanden, and W. M. M. Kessels. In situ spectroscopic ellipsometry during atomic layer deposition of Pt, Ru and Pd. *Journal of Physics D Applied Physics*, 49(11):115504, 2016. 102

[246] S. M. Geyer, R. Methaapanon, B. Shong, P. A. Pianetta, and S. F. Bent. In Vacuo Photoemission Studies of Platinum Atomic Layer Deposition Using Synchrotron Radiation. *The Journal of Physical Chemistry Letters*, 4(1):176–179, 2012. 102

[247] D. D. Fong, J. A. Eastman, S. K. Kim, T. T. Fister, M. J. Highland, P. M. Baldo, and P. H. Fuoss. In situ synchrotron x-ray characterization of ZnO atomic layer deposition. *Applied Physics Letters*, 97(19), 2010. 102

[248] S. M. Geyer, R. Methaapanon, R. Johnson, S. Brennan, M. F. Toney, B. Clemens, and S. Bent. Structural evolution of platinum thin films grown by atomic layer deposition. *Journal of Applied Physics*, 116(6):4905, 2014. 102

[249] G. Liang, H. Cheng, Z. Zhiwei, Z. Wei, W. Dongping, and Z. Shili. Influence of surface preparation on atomic layer deposition of Pt films. *Journal of Semiconductors*, 33(8):2–6, 2012. 104

[250] A. F. Mayadas, M. Shatzkes, and J. F. Janak. Electrical resistivity model for polycrystalline films: The case of specular reflection at external surfaces. *Applied Physics Letters*, 14(11):345–347, 1969. 104

[251] K. Fuchs. The conductivity of thin metallic films according to the electron theory of metals. *Mathematical Proceedings of the Cambridge Philosophical Society*, 34(1): 100–108, 1938. 104

[252] E. H. Sondheimer. The mean free path of electrons in metals. *Advance Physics*, 1 (1):1–42, 1952.

[253] W. Steinhögl, G. Schindler, G. Steinlesberger, M. Traving, and M. Engelhardt. Comprehensive study of the resistivity of copper wires with lateral dimensions of 100 nm and smaller. *Journal of Applied Physics*, 97(2), 2005. 104

[254] T. Aaltonen, A. Rahtu, M. Ritala, and M. Leskelä. Reaction Mechanism Studies on Atomic Layer Deposition of Ruthenium and Platinum. *Electrochemical and Solid-State Letters*, 6(9):C130, 2003. 107, 108

[255] N. Leick, S. Agarwal, A. J. M. Mackus, and W. M. M. Kessels. Dehydrogenation Reactions during atomic layer deposition of Ru using O_2. *Chemistry of Materials*, 24(19):3696–3700, 2012. 108

[256] I. J. M. Erkens, A. J. M. Mackus, H. C. M. Knoops, P. Smits, T. H. M. van de Ven, F. Roozeboom, and W. M. M. Kessels. Mass Spectrometry Study of the Temperature Dependence of Pt Film Growth by Atomic Layer Deposition. *ECS Journal of Solid State Science and Technology*, 1(6):P255–P262, 2012. 108

[257] I. J. Hsu, B. E. McCandless, C. Weiland, and B. G. Willis. Characterization of ALD copper thin films on palladium seed layers. *Journal of Vacuum Science and Technology A*, 27(4):660–667, 2009. 108

[258] A. Kaloyeros, Y. Zhu, K. Dunn, R. Mayti, C. Miller, and M. Breslin. Copper electroplating on zero-thickness ald platinum for nanoscale computer chip interconnects. *MRS Proceedings*, 914(0914-F05-08), 2006. 108

[259] A. Javey, J. Guo, Q. Wang, M. Lundstrom, and H. Dai. Ballistic carbon nanotube field-effect transistors. *Nature*, 424(6949):654–657, 2003. 108

[260] J. An, Y. Kim, and F. B. Prinz. Ultra-thin platinum catalytic electrodes fabricated by atomic layer deposition. *Physical Chemistry Chemical Physics*, 15(20):7520–7525, 2013. 108

[261] T. F. Baumann, J. Biener, Y. M. Wang, S. O. Kucheyev, E. J. Nelson, J. H. Satcher, J. W. Elam, M. J. Pellin, and A. W. Hamza. Atomic Layer Deposition of Uniform Metal Coatings on Highly Porous Aerogel Substrates. *Chemistry of Materials*, 18 (26):6106–6108, 2006. 108

[262] J. Biener, T. F. Baumann, Y. Wang, E. J. Nelson, S. O. Kucheyev, A. V. Hamza, M. Kemell, M. Ritala, and M. Leskelä. Ruthenium/aerogel nanocomposites via atomic layer deposition. *Nanotechnology*, 18(5):055303, 2007.

[263] J. S. King, A. Wittstock, J. Biener, S. O. Kucheyev, Y. M. Wang, T. F Baumann, S. K. Giri, A. V. Hamza, M. Baeumer, and S. F. Bent. Ultralow loading Pt nanocatalysts prepared by atomic layer deposition on carbon aerogels. *Nano Letters*, 8(8):2405–2409, 2008. 108

[264] R. J. Narayan, S. P. Adiga, M. J. Pellin, L. A. Curtiss, A. J. Hryn, S. Stafslien, B. Chisholm, C. C. Shih, C. M. Shih, S. J. Lin, Y. Y. Su, C. Jin, J. Zhang, N. A. Monteiro-Riviere, and J. W. Elam. Atomic layer deposition-based functionalization of materials for medical and environmental health applications. *Philosophical Transactions of the oyal Society A*, 368:2033–2064, 2010. 108

[265] S. P. Sree, J. Dendooven, L. Geerts, R. K. Ramachandran, E. Javon, F. Ceyssens, E. Breynaert, C. E. A. Kirschhock, R. Puers, T. Altantzis, G. Van Tendeloo, S. Bals, C. Detavernierb, and J. A. Martens. 3D porous nanostructured platinum prepared using atomic layer deposition. *Journal of Material Chemistry A*, 5:19007–19016, 2017.

[266] F. Ceyssens, S. Pulinthanathu, J. Martens, and R. Puers. Fabrication of nanostructured platinum with multilevel porosity for low impedance biomedical recording and stimulation electrodes. *Procedia Engineering*, 120:355–359, 2015. 108

[267] N. Cheng, J. Liu, M. Norouzi, and X. Sun. ScienceDirect High stability and activity of Pt electrocatalyst on atomic layer deposited metal oxide / nitrogen-doped graphene hybrid support. *International Journal of Hydrogen Energy*, 39(28): 15967–15974, 2014. 108

[268] M. Inaba, T. Suzuki, T. Hatanaka, and Y. Morimoto. Fabrication and Cell Analysis of a Pt/SiO_2 Platinum Thin Film Electrode. *Journal of the Electrochemical Society*, 162(7):634–638, 2015.

[269] X. Jiang, H. Huang, F. B. Prinz, and S. F. Bent. Application of Atomic Layer Deposition of Platinum to Solid Oxide Fuel Cells. *Chemistry of Materials*, 20(12): 3897–3905, 2008. 108

[270] Z. L. Wang. Structural analysis of self-assembling nanocrystal superlattices. *Advanced Materials*, 10(1):13–30, 1998. 109

[271] P. Del Pino, F. Yang, B. Pelaz, Q. Zhang, K. Kantner, R. Hartmann, N. Martinez De Baroja, M. Gallego, M. Müller, B. B. Manshian, S. J. Soenen, R. Riedel, N. Hampp, and W. J. Parak. Basic Physicochemical Properties of Polyethylene Glycol Coated Gold Nanoparticles that Determine Their Interaction with Cells. *Angewandte Chemie - International Edition*, 55(18):5483–5487, 2016. 109

[272] N. G. Bastús, J. Comenge, and V. Puntes. Kinetically Controlled Seeded Growth Synthesis of Citrate-Stabilized Gold Nanoparticles of up to 200 nm: Size Focusing versus Ostwald Ripening. *Langmuir*, 27(11):11098–11105, 2011. 109

[273] J. Chen, L. Guo, B. Qiu, Z. Lin, and T. Wang. Application of ordered nanoparticle self-assemblies in surface-enhanced spectroscopy. *Materials Chemistry Frontiers*, 2 (5):835–860, 2018. 110

[274] K. J. M. Bishop, C. E. Wilmer, S. Soh, and B. A. Grzybowski. Nanoscale forces and their uses in self-assembly. *Small*, 5(14):1600–630, 2009.

[275] D. Luo, C. Yan, and T. Wang. Interparticle forces underlying nanoparticle self-assemblies. *Small*, 11(45):5984–6008, 2015. 110

[276] C. T. O'Mahony, R. A. Farrell, T. Goshal, J. D. Holmes, and M. A. Morris. *The Thermodynamics of Defect Formation in Self-Assembled Systems*, chapter 13. IntechOpen, 2011. 110

[277] T. P. Bigioni, X. Lin, T. T. Nguyen, E. I. Corwin, T. Witten, and H. M. Jaeger. Kinetically driven self assembly of highly ordered nanoparticle monolayers. *Nature Materials*, 5(4):26–270, 2006. 111

[278] Z. Nie, A. Petukhova, and E. Kumacheva. Properties and emerging applications of self-assembled structures made from inorganic nanoparticles. *Nature Nanotechnology*, 5(1):15–25, 2010. 111

[279] C. Sönnichsen, B. M. Reinhard, J. Liphardt, and A. P. Alivisatos. A molecular ruler based on plasmon coupling of single gold and silver nanoparticles. *Nature Biotechnology*, 23(6):741–745, 2005.

[280] J. Lee, P. Hernandez, J. Lee, A. O. Govorov, and N. A. Kotov. Exciton-plasmon interactions in molecular spring assemblies of nanowires and wavelength-based protein detection. *Nature Materials*, 6(4):291–295, 2007.

[281] B. Warne, O. I. Kasyutich, E. L. Mayes, J. A. L. Wiggins, and K. K. W. Wong. Self assembled nanoparticulate Co:Pt for data storage applications. *IEEE Transactions on Magnetics*, 36(5):3009–3011, 2000.

[282] J. Kim, J. Kim, and R. Deaton. Programmable construction of nanostructures: Assembly of nanostructures with various nanocomponents. *IEEE Nanotechnology Magazine*, 6(1):19–23, 2012. 111

[283] P. Li, S. Chen, H. Dai, Z. Yang, Z. Chen, Y. Wang, Y. Chen, W. Peng, W. Shan, and H. Duan. Recent advances in focused ion beam nanofabrication for nanostructures and devices: fundamentals and applications. *Nanoscale*, 13(3):1529–1565, 2021. 113

[284] L. A. Giannuzzi. Reducing fib damage using low energy ions. *Microscopy and Microanalysis*, 12(02):1260–1261, 2006. 114

[285] A. Bolker, J. Salzman, B. Meyler, C. Cytermann, I. Bayn, V. Richter, and R. Kalish. Diamond processing by focused ion beam-surface damage and recovery. *Applied Physics Letters*, 99(18):183109, 2011. 114

[286] L. A. Giannuzzi. *Introduction to Focused Ion Beams*. Springer US, 2005. 114, 151

[287] G. P. S. Balasubramanian and R. Hull. Mechanisms of Focused Ion Beam Implantation Damage and Recovery in Si. *Journal of Electronic Materials*, 45(6): 3236–3243, 2016. 114

[288] J. J. L. Mulders and P. H. F. Trompenaars. An in-situ Low Energy Argon Ion Source for Local Surface Modification. *European Microscopy Congress 2016: Proceedings, Instrumentation and Methods*, 1, 2016. 115, 152, 168

[289] M. J. Perez-Roldan, J. J. L Mulders, and P. H. F. Trompenaars. C-FEBID etching mask and C-FEBID in-situ removal; enabling a new micro- and nano fabrication route. *Microelectronic Engeneering*, 201:22–25, 2018. 115

[290] R. F. Barron. *Cryogenic Systems*. Oxford University Press, 1985. 118

[291] Oxford Instruments. *HelioxVL Insert Manual*. Oxford Instruments NanoScience, 2013. 118, 121

[292] J. T. Masden and N. Giordano. Localization and electron-electron interaction effects in thin Pt wires. *Physical Review B Condens Matter*, 15(31):6395–6401, 1985. 123

[293] A. D. Beyer, M. Koesters, K. G. Libbrecht, and E. D. Black. Macroscopic coherence effects in a mesoscopic system: Weak localization of thin silver films. *American Journal of Physics*, 73(11):1014, 2005. 123, 124

[294] M. Kompaniiets. *Superconducting proximity effect in ferromagnetic and diamagnetic nanowire-structures*. PhD thesis, Johann Wolfgang Goethe Universät in Frankfurt am Main, 2014. 124

[295] P. R. Gray. *Analysis and Design of Analog Integrated Circuits*. Wiley Publishing, 2009. 128

[296] V. Yarzhemsky and C. Battocchio. The structure of gold nanoparticles and Au based thiol self-organized monolayers. *Russian Journal of Inorganic Chemistry*, 56: 2147–2159, 12 2011. 129

[297] B. Abeles, P. Sheng, M. D. Coutts, and Y Arie. Structural and electrical properties of granular metal films. *Advances in Physics*, 24(3):407–461, 1975. 138

[298] N. Allec, R. G. Knobel, and L. Shang. Semsim: Adaptive multiscale simulation for single-electron devices. *IEEE Transactions on Nanotechnology*, 7(3):351–354, 2008. 139, 140

[299] K. Nabors, S. Kim, and J. White. Fast capacitance extraction of general three-dimensional structures. *IEEE Transactions on Microwave Theory and Techniques*, 40(7):1496, 1992. 147, 157

[300] I. O. Kulik and I. Shekhter. Kinetic phenomena and charge discreteness effects in granulated media. *Soviet Physics - Journal of Experimental and Theoretical Physics*, 41(2):308–316, 1975. 147

[301] D. V. Averin and K. K. Likharev. Coulomb blockade of single-electron tunneling, and coherent oscillations in small tunnel junctions. *Journal of Low Temperature Physics*, 62(3):345, 1986. 147, 157

[302] J. R. Tucker. Complementary digital logic based on the Coulomb blockade. *Journal of Applied Physics*, 72(9):4399, 1992. 147

[303] T. Weimann, H. Wolf, H. Scherer, J. Niemeyer, and V. A. Krupenin. Metallic single electron devices fabricated using a multilayer technique. *Applied Physics Letters*, 71(5):713, 1997.

[304] M. A. Sillanpää and P. J. Hakonen. Titanium single-electron transistor fabricated by electron-beam lithography. *Physica E: Low-Dimensional Systems and Nanostructures*, 15(1):41, 2002.

[305] R. Dolata, H. Scherer, A. B. Zorin, and J. Niemeyer. Single electron transistors with Nb/AlO_x/Nb junctions. *Journal of Vacuum Science and Technology B: Microelectronics and Nanometer Structures Processing, Measurement, and Phenomena*, 21(2):775–780, 2003. 147

[306] J. J. Parks, A. R. Champagne, G. R. Hutchison, S. Flores-Torres, H. D. Abruña, and D. C. Ralph. Tuning the Kondo Effect with a Mechanically Controllable Break Junction. *Physical Review Letters*, 99(2):026601, 2007. 147

[307] Z. Bai, X. Liu, Z. Lian, K. Zhang, G. Wang, S. Shi, X. Pi, and F. Song. A silicon cluster based single electron transistor with potential room-temperature switching. *Chinese Physics Letters*, 35(3):037301, 2018. 147

[308] K. I. Bolotin, F. Kuemmeth, A. N. Pasupathy, and D. C. Ralph. Metal-nanoparticle single-electron transistors fabricated using electromigration. *Applied Physics Letters*, 84(16):3154, 2004. 147

[309] H. Park, A. K. L. Lim, A. P. Alivisatos, J. Park, and P. L. McEuen. Fabrication of metallic electrodes with nanometer separation by electromigration. *Applied Physics Letters*, 75(2):301, 1999. 147

[310] S. H. M. Persson, L. Olofsson, L. Hedberg, D. Sutherland, and E. Olsson. A self-assembled single-electron tunneling device. *Annals of the New York Academy of Sciences*, 852:188, 1998. 147

[311] M. Brink. *Imaging single-electron charging in nanostructures by low-temperature scanning force microscopy*. PhD thesis, Cornell University, 2007.

[312] M. J. Yoo, T. A. Fulton, H. F. Hess, R. L. Willett, L. N. Dunkleberger, R. J. Chichester, L. N. Pfeiffer, and K. W. West. Scanning single-electron transistor microscopy: Imaging individual charges. *Science*, 276(5312):579–582, 1997.

[313] H. Brenning, S. Kubatkin, D. Erts, S. Kafanov, T. Bauch, and P. Delsing. A single electron transistor on an atomic force microscope probe. *Nano letters*, 6:937, 06 2006. 147

[314] R. Moriya, H. Kobayashi, K. Shibata, S. Masubuchi, K. Hirakawa, S. Ishida, Y. Arakawa, and T. Mac Hida. Fabrication of single-electron transistor composed of a self-assembled quantum dot and nanogap electrode by atomic force microscope local oxidation. *Applied Physics Express*, 3:035001, 2010. 147

[315] K. Matsumoto, M. Ishii, K. Segawa, Y. Oka, B. J. Vartanian, and J. S. Harris. Room temperature operation of a single electron transistor made by the scanning tunneling microscope nanooxidation process for the TiO_x/Ti system. *Applied Physics Letters*, 68(1):34, 1996. 147

[316] L. C. Tsai, I. C. Cheng, M. C. Tu, C. D. Chen, and H. Y. Lin. Formation of single-electron-transistors using self-assembly of nanoparticle chains. *Journal of Nanoparticle Research*, 12(8):2859, 2010. 147

[317] Y. Azuma, S. Suzuki, K. Maeda, N. Okabayashi, D. Tanaka, M. Sakamoto, T. Teranishi, M. R. Buitelaar, C. G. Smith, and Y. Majima. Nanoparticle single-electron transistor with metal-bridged top-gate and nanogap electrodes. *Applied Physics Letters*, 99(7):1, 2011.

[318] T. Junno, M. H. Magnusson, S. B. Carlsson, K. Deppert, J. O. Malm, L. Montelius, and L. Samuelson. Single-electron devices via controlled assembly of designed nanoparticles. *Microelectronic Engineering*, 47(1):179, 1999.

[319] N. Okabayashi, K. Maeda, T. Muraki, D. Tanaka, M. Sakamoto, T. Teranishi, and Y. Majima. Uniform charging energy of single-electron transistors by using size-controlled Au nanoparticles. *Applied Physics Letters*, 100(3):1, 2012.

[320] Y. S. Gerasimov, V. V. Shorokhov, and O. V. Snigirev. Electron Transport Through Thiolized Gold Nanoparticles in Single-Electron Transistor. *Journal of Superconductivity and Novel Magnetism*, 28(3):781, 2015.

[321] O. Bitton, D. B. Gutman, R. Berkovits, and A. Frydman. Multiple periodicity in a nanoparticle-based single-electron transistor. *Nature Communications*, 8(1):8, 2017. 147

[322] H. W. Ch. Postma, T. Teepen, Z. Yao, M. Grifoni, and C. Dekker. Carbon nanotube single-electron transistors at room temperature. *Science*, 293(5527):76, 2001. 147

[323] K. Seike, Y. Kanai, Y. Ohno, K. Maehashi, K. Inoue, and K. Matsumoto. Carbon nanotube single-electron transistors with single-electron charge storages. *Japanese Journal of Applied Physics*, 54(6), 2015. 147

[324] V. Khademhosseini, , D. Dideban, M. T. Ahmadi, R. Ismail, and H. Heidari. Single Electron Transistor Scheme Based on Multiple Quantum Dot Islands: Carbon Nanotube and Fullerene. *ECS Journal of Solid State Science Technology*, 7(10): M145, 2018. 147

[325] H. Park, J. Park, A. K. L. Lim, E. H. Anderson, A. P. Alivisatos, and P. L. McEuen. Nanomechanical Oscillations in a Single-C60 Transistor. *Nature*, 407:57, 2000.

[326] A. Nasri, A. Boubaker, B. Hafsi, W. Khaldi, and A. Kalboussi. High-Sensitivity Sensor Using C_{60}-Single Molecule Transistor. *IEEE Sensors Journal*, 18(1):248, 2018. 147

[327] M. A. Reed, C. Zhou, C. J. Muller, T. P. Burgin, and J. M. Tour. Conductance of a Molecular Junction. *Science*, 278(5336):252, 1997. 147

[328] T. Liang and A. R. Stivers. Damage-free mask repair using electron-beam-induced chemical reactions. *Emerging Lithographic Technologies VI*, 4688, jul 2002.

[329] S. Kubatkin, A. Danilov, M. Hjort, J. Cornil, J. Brédas, N. Stuhr-Hansen, P. Hedegård, and Thomas Bjørnholm. Single-electron transistor of a single organic molecule with access to several redox states. *Nature*, 425:698–701, 11 2003. 147

[330] M. Komuro and H. Hiroshima. Fabrication and properties of dot array using electron-beam-induced deposition. *Microelectronic Engineering*, 35(1):273, 1997. 147

[331] N. Miura, T. N. Umaguchi, A. Y. Amada, M. K. Onagai, and J. S. Hirakashi. Room Temperature Operation of Amorphous Carbon-Based Single-Electron Transistors Fabricated by Beam-Induced Deposition Techniques. *Japanese Journal of Applied Physics*, 37(4):423, 1998.

[332] J. Fang, S. Qin, X. Zhang, D. Liu, and S. Chang. Annealing effect of platinum-incorporated nanowires created by focused ion/electron-beam-induced deposition. *Chinese Physics B*, 23(8):088111, 2014.

[333] H. C. George, T. A. Orlova, A. O. Orlov, and G. L. Snider. Novel method for fabrication of nanoscale single-electron transistors: Electron beam induced deposition of Pt and atomic layer deposition of tunnel barriers. *Journal of Vacuum Science Technology B: Microelectronics and Nanometer Structures*, 29(6):06FB01, 2011.

[334] Z. A. K. Durrani, M. E. Jones, C. Wang, M. Scotuzzi, and C. W. Hagen. Electron transport and room temperature single-electron charging in 10 nm scale Pt-C nanostructures formed by electron beam induced deposition. *Nanotechnology*, 28 (47):474002, 2017. 147

[335] G. Kalon, Y. Jun Shin, V. Giang Truong, A. Kalitsov, and H. Yang. The role of charge traps in inducing hysteresis: Capacitance-voltage measurements on top gated bilayer graphene. *Applied Physics Letters*, 99(8):083109, 2011. 153

[336] S. B. Mitta, M. S. Choi, A. Nipane, F. Ali, C. Kim, J. T. Teherani, J. Hone, and W. J. Yoo. Electrical characterization of 2D materials-based field-effect transistors. *2D Materials*, 8(1):012002, 2020. 153

[337] A. Botman, M. Hesselberth, and J. J. L. Mulders. Improving the conductivity of platinum-containing nano-structures created by electron-beam-induced deposition. *Microelectronic Engineering*, 85(5):1139, 2008. 154

[338] M. Winhold. *Focused electron-beam-induced deposition, From process optimization to cantilever-based strain-sensing applications using nanogranular tunneling resistors*. PhD thesis, Johann Wolfgang Goethe Universät in Frankfurt am Main, 2015. 154

[339] A. Furusaki and K. A. Matveev. Coulomb Blockade Oscillations of Conductance in the Regime of Strong Tunneling. *Physical Review Letters*, 75(4):709, 1995. 164

[340] D. B. Poker and C. E. Klabunde. Temperature dependence of electrical resistivity of vanadium, platinum, and copper. *Physical Review B*, 26(12):7012–7014, 1982. 171

[341] H. L. Stormer, L. N. Pfeiffer, K. W. Baldwin, and K. W. West. Observation of a Bloch-Grüneisen regime in two-dimensional electron transport. *Physical Review B*, 41(2):1278–1281, 1990. 171

[342] J. M. Ziman. *Electrons and Phonons*. Clarendon Press, Oxford, 1960. 171

[343] G. Bergmann. Weak localization in thin films a time-of-flight experiment with conduction electrons. *Physics Reports*, 107(1):1–58, 1984. 173

[344] I. E. Smolyarenko and N. S. Wingreen. Kondo effect in systems with spin disorder. *Physical Review B*, 60(13):9675–9689, 1999. 173

[345] D. Greig and D. Livesey. The Hall coefficient of dilute palladium and platinum alloys. *Journal of Physics F: Metal Physics*, 2(4):699, 1972. 173

[346] S. Hikami, A. I. Larkin, and Y. Nagaoka. Spin-Orbit Interaction and Magnetoresistance in the Two Dimensional Random System. *Progress of Theoretical Physics*, 63(2):707–710, 2005. 173

[347] F. Xiu, T. A. Lograsso, P. Zhang, L. He, N. Meyer, X. Kou, L. Bao, T. M. Riedemann, K. L. Wang, J. Zou, G. Tuttle, A. V. Fedorov, and Z. Chen. Weak Anti-localization and Quantum Oscillations of Surface States in Topological Insulator Bi_2Se_2Te. *Scientific Reports*, 2(1):1–7, 2012. 173

[348] W. Heisenberg. Über den anschaulichen Inhalt der quantentheoretischen Kinematik und Mechanik. *Zeitschrift für Physik*, 43(3):172–198, 1927. 175

[349] M. H. Devoret and H. Grabert. *Single Charge Tunneling - Coulomb Blockade Phenomena in Nanostructures*, volume 294. Springer, New York, 1992. 176

[350] E. Fermi. Sulla quantizzazione del gas perfetto monoatomico. *Rendiconti Accademia Lincei*, 3:145–149, 1926. 176

[351] W. Pauli. Über den Zusammenhang des Abschlusses der Elektronengruppen im Atom mit der Komplexstruktur der Spektren. *Zeitschrift für Physik*, 31:765–783, 1925. 176

[352] E. Fermi. *Nuclear Physics: A Course Given by Enrico Fermi at the University of Chicago*. University of Chicago Press, 1950. 177

[353] N. Pala. Coulomb blockade and single-electron transistors. *Introduction to Nanotechnology Course*, 1:16, 2015. 178

[354] D. Ferry and S. M. Goodnick. *Transport in Nanostructures*. Cambridge University Press, 1997. 178

[355] M.-M. Walz, M. Schirmer, F. Vollnhals, T. Lukasczyk, H.-P. Steinrück, and H. Marbach. Electrons as invisible ink: Fabrication of nanostructures by local electron beam induced activation of SiO_x. *Angewandte Chemie International Edition*, 49(27):4669–4673, 2010. 182

[356] K. Muthukumar, H. O. Jeschke, R. Valenti, E. Begun, J. Schwenk, F. Porrati, and M. Huth. Spontaneous dissociation of $Co_2(CO)_8$ and autocatalytic growth of Co on SiO_2: A combined experimental and theoretical investigation. *Beilstein Journal of Nanotechnology*, 3:546–555, 2012. 182

[357] L. Keller, M. K. I. Al Mamoori, J. Pieper, C. Gspan, I. Stockem, C. Schröder, S. Barth, R. Winkler, H. Plank, M. Pohlit, J. Müller, and M. Huth. Direct-write of free-form building blocks for artificial magnetic 3D lattices. *Scientific Reports*, 8 (1):1–13, 2018. 183, 184, 185

[358] M. Huth, L. Keller, H. Plank, and R. Winkler. Kleingedrucktes mit grossem effekt. *Physik in unserer Zeit*, 51(2):64–71, 2020. 185

Publications

1. **G. Di Prima**, R. Sachser, P. H. F. Trompenaars, J. J. L Mulders, and M. Huth. Direct-write single electron transistors by focused electron beam induced deposition. Nano Futures, 1(18):183109, 2019.

2. M. S. Seifner, M. Sistani, F. Porrati, **G. Di Prima**, P. Pertl, M. Huth, A. Lugstein, S. Barth. Direct Synthesis of Hyperdoped Germanium Nanowires. ACS Nano, 12(2):1236-1241, 2018.

3. **G. Di Prima**, R. Sachser, P. Gruszka, M. Hanefeld, T. Halbritter, A. Heckel, and M. Huth. In situ conductance monitoring of Pt thin film growth by area-selective atomic layer deposition. Nano Futures, 1(025001), 2017

Erklärung und Versicherung

Erklärung

Hiermit erkläre ich durch meine Unterschrift an Eides statt, dass ich mich bisher keiner Doktorprüfung im mathematischnaturwissenschaftlichen Bereich unterzogen habe.

Frankfurt am Main, den _____

_____

Giorgia Di Prima

Versicherung

Ich erkläre hiermit, dass ich die eingereichte Dissertation mit dem Titel:
Single-Electron transport effects in Focused Electron Beam Induced Deposition (FEBID)-based nanostructures

selbständig und ohne fremde Hilfe verfasst habe. Alle Zitate und Entlehnungen geistigen Eigenturms aus anderen Schriften sind unter Angabe der betreffenden Schrift gekennzeichnet.
Ich versichere, dass die Dissertation ohne Hinzuziehung einer kommerziellen Promotionsberatung erstellt wurde.
Frankfurt am Main, den _____

_____

Giorgia Di Prima